UNIVERSITAT DE BARCELONA

Advanced Characterization of Interfaces of the Chalcogenide-Based Absorbers for the Thin Film Photovoltaic Technologies

Robert Fonoll i Rubio

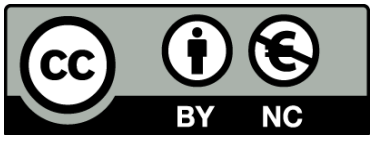

PhD Thesis

Advanced Characterization of Interfaces of the Chalcogenide-Based Absorbers for the Thin Film Photovoltaic Technologies

Robert Fonoll i Rubio

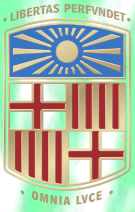

UNIVERSITAT DE BARCELONA

Advanced Characterization of Interfaces of the Chalcogenide-Based Absorbers for the Thin Film Photovoltaic Technologies

Programa de doctorat en Física

Autor: Robert Fonoll i Rubio

Directors: Dr. Víctor Izquierdo Roca, Dr. Maxim Guc

Tutor: Prof. Dr. Blas Garrido Fernández

Lloc on s'ha dut a terme la tesi: Institut de Recerca en Energia de Catalunya (IREC), Universitat de Barcelona (UB)

UNIVERSITAT DE BARCELONA

A la Jhoy, els meus pares i els meus germans

Table of Contents

Acknowledgments

It has been four years since I started this stage of my life, a period full of experiences and shared with wonderful people. This thesis has one author, but it was possible thanks to the work and support of many people that I would like to acknowledge.

First of all, I thank Víctor for opening the doors of IREC to me, for giving me the opportunity of developing this PhD, for your confidence along the years, and for your guidance. I value that even if you had no time, you did not disengage from being my director and that you found moments for supervising and discussing my work, and for teaching me how to be a researcher.

I thank Max for your infinite patience, for your dedication as my director, and for teaching me all I know about Raman measurements. I knew nothing when I first met you, you took me to the lab, and you have stayed at my side since then guiding me. You answered every question I asked and reviewed all the work I presented without losing time, including the hundreds of pages of this thesis. You did not start officially as my director, but it is the right thing that at the end you are, since you were a *de facto* director of this work from the beginning.

Alejandro, you showed us that being a good group leader is compatible with being a kind person. I thank you for all your support and advices, but especially for the ones involving the MasterPV experiments that resulted in one of the pillars of this thesis and for the final revision of this manuscript.

Alex H., you treated me as a friend from the first second and made me feel a part of the group from the beginning. There was an IREC with you and another completely different without you, which means that you make a difference.

Alex L., you are a great guy and I always enjoy your company. I remember with joy being teammates at foosball and billiards in Les Houches and IREC parties, thanking your patience for my lack of skills at those games. You are also a great researcher that had to work in new and difficult materials, I am glad that I could collaborate with the characterization of some of your samples.

Angélica, you always included me in the group plans and opened the doors of your home to me, which I really value, and I always had a good time there. I had fun when we

did calisthenics and you were a constant at lunch time, where I liked talking with you. You are an amazing person, IREC is not the same without you.

Diouldé, you always greet me with a smile and treat me with tenderness. Even if you are busy, you have helped me every time I asked you. The Fridays are not Fridays without our "¡Buen fin de semana!".

Enric, you expanded the abilities of IREC and it was great working together, this thesis has been improved thanks to your work. Your company was charming and I save the good moments, like the ones in Les Houches.

Fabien, you are a fun guy and many times you broke the monotony of the working day. It is pleasant talking with you and I thank you for every time you invited me to climb; when I went, I always had a great time.

Jacob, we had a strong collaboration during my first years at IREC and, without you, this thesis would have less value. You are a great researcher and a better person; I always like talking with you, specially when we do it in Catalan.

Laia, I was supposed to teach you about Raman and solar cells stuff, but at the end it was I who learned from you. My colleague and partner in crime during the last year of this thesis, you are everything a researcher should be and, frankly, we are the best work team that IREC has seen.

Marcel, you started as my thesis director and you were a good one. You gave me your support and you were crucial in many works included in this thesis. And, more important, you are a kind person and it is always nice seeing you.

Mohamed, you were always in a good mood and working together characterizing your samples was a nice and successful experience, I was happy to see you achieving the PhD title.

Nacho, you also taught me how to move in the lab and you helped me in many experiments, articles, and presentations. You feel like a third, unofficial director to me. I liked our conversations during lunch time, specially the ones in Catalan, your departure to Austria left a void in IREC.

Pedro, you are a wonderful guy to whom I can always talk. I find it funny when you ask me about C(V) because it was you who taught me how the system worked. Thank

you for the good moments, remembering particularly the ones in Uppsala and Les Houches, and also for your help with the writing and administrative questions of this thesis.

Rafael, it is impressive what you built in the lab, which makes our jobs easier. It is good every time we coincide at IREC because the conversations with you are pleasing and interesting.

Thanos, your time at IREC was short but it left a mark. You always had interesting topics for conversation and it was really funny see your Žižek imitations.

Yude, you were always full of joy and had a smile for me. Every time I went to the synthesis lab, where I was lost, you helped me. And, of course, a have the good memories of being tourist in Nice together, you made my first IREC travel easier.

David, Gustavo, Victoria; being the last incorporations to IREC means that we did not share so many moments, but I hope we do in the future. And Fernando, a last incorporation too, but you were one of my best friends at school, I am glad to see you again.

Edgardo, you always had nice words for me and I always felt valued by you. I enjoy talking with you and I thank you for the good moments in Nice, Les Houches, and Philadelphia; those travels would have been less funny without you. In addition, my wardrobe is grateful for the visit to the outlet.

Kunal, Sergio, and Zach; we shared good conversations during the coffee breaks when you were at IREC. It was nice working with you and I thank you for your help and guidance in the experiments that improved this thesis.

Alejandro, Alex J., Axel, Ivan, and Maykel; I shared few moments with you, but those ones were good and fun. Every one of you have been kind to me and it would have been nice to spend more time together.

A thought for the people that made an internship at IREC, specially Esteban, Ikram, Nada, and Roberto, which are the ones to whom I collaborated the most.

To my friends of elementary and high school: time and my lack of social skills have distanced us, but I remember you and I thank you for all the good moments. And thanks to my physicist friends, specially to the ones that are also my callisthenic friends: Bonet,

Carlos, David, Isaac, Oscar, and, of course, El Dragón; we grew together both personally and physically.

I would like to thank all my family, with a special mention to Carmen, Empar, Jeroni, Joan, Pau, and Rafel. And thanks mom, dad, Josep, Xavier, and Víctor; you are the nucleus of my life and you gave me everything, growing up in our home was a dream. And last, but not least, my thanks to Jhoy: you were there before I started the thesis and you are here after I finish it. As times goes by, it's becoming harder to think about my life without thinking about you. Or, in other words, from now on, when someone says "This man is having a stroke! Is there some doctor in the room?" and I say "Yes, I am", you will be the one saying "My darling, you are a doctor *in Physics*".

List of acronyms, abbreviations and physical quantities

A	Diode quality factor or solar cell area
AC	Alternating current
AES	Auger electron spectroscopy
AFM	Atomic force microscopy
ALD	Atomic layer deposition
ARC	Anti-reflective coating
a-Si	Amorphous silicon
AVT	Average visible transmittance
AZO	Aluminum-doped zinc oxide
B	Susceptance
BF	Bright-field
BIPV	Building-integrated photovoltaics
c	Speed of light in vacuum
C	Capacitance
CB	Conduction band
CBD	Chemical bath deposition
CCD	Charge-coupled device
CIGSe	$CuIn_{1-x}Ga_xSe_2$
CIS	$CuInS_2$
CISe	$CuInSe_2$
CGS	$CuGaS_2$
CGSe	$CuGaSe_2$
CZTS	Cu_2ZnSnS_4

CZTSe	$Cu_2ZnSnSe_4$
CZTSSe	$Cu_2ZnSn(S_{1-x}Se_x)_4$
DC	Direct current
DF	Dark-field
$\vec{E}$	Electric field vector
E_{bi}	Built-in electric field
EDX	Energy dispersive X-ray spectroscopy
EELS	Electron energy-loss spectroscopy
E_g	Band gap
EHP	Electron-hole pairs
f	Frequency
FIB	Focused ion beam
FF	Fill factor
FTO	Fluorine-doped tin oxide
G	Carriers generation rate
h	Planck constant
HAADF	High-angle annular dark-field
HRTEM	High-resolution transmission electron microscopy
i	Imaginary unit
I	Intensity
ISS	Ion scattering spectroscopy
ITO	Indium tin oxide
J	Current density
J_0	Reverse saturation current

J_{mpp}	Current density at the maximum power point
J_{ph}	Photocurrent
J_{SC}	Short-circuit current density
$\vec{k}$	Wavevector
k_B	Boltzmann's constant
L_N	Electron diffusion length
L_P	Hole diffusion length
MBE	Molecular bean epitaxy
ML	Machine learning
n	Concentration of electrons
N	Number of atoms in the crystal base
NA	Numerical aperture
N_A	Acceptor doping concentration
N_{CV}	Apparent doping concentration from capacitance–voltage profiling
N_D	Donor doping concentration
NIR	Near-infrared
OVC	Ordered vacancy compound
p	Concentration of holes
$\vec{P}$	Polarization density vector
PCE	Power conversion efficiency
PDT	Post-deposition treatment
P_{in}	Incident power on the solar cell
PL	Photoluminescence
P_{max}	Maximum power generated by a solar cell

PR	Photonic response
P_{theo}	Maximum theoretical power that a solar cell can produce
PV	Photovoltaics
q	Electric charge
$\vec{q}$	Wavevector of the atomic oscillations
$\vec{Q}$	Atomic oscillations vector
q_e	Elementary charge
QY	Quantum yield
$\vec{r}$	Position vector
R	Resistance
R_p	Parallel resistance
R_s	Series resistance
R_{sh}	Shunt resistance
S	Solar photon flux
SCR	Space charge region
SEM	Scanning electron microscopy
SIMS	Secondary ion mass spectroscopy
SLG	Soda-lime glass
SPM	Scanning probe microscopy
STEM	Scanning transmission electron microcopy
t	Time
T	Temperature
TCO	Transparent conductive oxide
TEM	Transmission electron microscopy

TOF-SIMS	Time-of-flight secondary ion mass spectroscopy
T_{opt}	Optical transmittance
V	Voltage
VB	Valence band
V_{bi}	Built-in voltage
VIPV	Vehicles-integrated photovoltaics
V_{mpp}	Voltage at the maximum power point
V_{OC}	Open-circuit voltage
W_{SCR}	Width of the space charge region
X	Electrical reactance
XPS	X-ray photoelectron spectroscopy
XRD	X-ray diffraction
XRF	X-ray fluorescence
Z	Atomic number or impedance
ε_0	Vacuum permittivity
ε_s	Semiconductor dielectric constant
η	Energy conversion efficiency
θ	Angle
λ	Wavelength
φ	Phase difference
χ	Electrical susceptibility
ω	Angular frequency or Raman shift

Table of Figures

Preface: Publications and summary of the thesis

The work presented in this thesis has been carried out at the Catalonia Institute for Energy Research (IREC) in the Solar Energy Materials and Systems (SEMS) research group, located in Sant Adrià de Besòs (Spain), during the period 2018-2022 in the framework of the MasterPV (PCI 2018-092945) and In4CIS (PCI 2019-111837-2) projects. The main goal of this thesis is the identification of the main physicochemical mechanisms that occur at the interfaces (back and front) of the chalcogenide absorber layers characteristic of the thin film solar cell architecture. These interfaces have a relevant impact on the device performance, which justifies the strong interest in the development of methodologies suitable for their deep analysis. The comprehensive approach in the interfaces analysis, that is also complemented with the analysis of the bulk properties of the layers, has also resulted in the development of new methodologies for the non-destructive characterization of the thin film solar cells based on optical techniques and compatible with in-line industrial process monitoring.

This thesis is based on the following six articles that are published in high impact factor peer-reviewed journals from the first quartile (Q1), which satisfies the main requirement for the conferment of the title of Doctor of Philosophy in Physics at the University of Barcelona. The articles are presented in chronological order of appearance:

- **R. Fonoll-Rubio**, J. Andrade-Arvizu, J. Blanco-Portals, I. Becerril-Romero, M. Guc, E. Saucedo, F. Peiró, L. Calvo-Barrio, M. Ritzer, C. S. Schnohr, M. Placidi, S. Estradé, V. Izquierdo-Roca, A. Pérez-Rodríguez. "Insights into interface and bulk defects in a high efficiency kesterite-based device". **Energy Environ. Sci.**, vol. 14, no. 1, p. 507, January 2021, DOI: 10.1039/D0EE02004D. IMPACT FACTOR (IF): 39.714 (Q1).
- K. J. Tiwari, **R. Fonoll Rubio**, S. Giraldo, L. Calvo-Barrio, V. Izquierdo-Roca, M. Placidi, Y. Sanchez, A. Pérez-Rodríguez, E. Saucedo, Z. Jehl Li-Kao. "Defect depth-profiling in kesterite absorber by means of chemical etching and surface analysis". **Appl. Surf. Sci.**, vol. 540, no. 2, p. 148342, February 2021, DOI: 10.1016/j.apsusc.2020.148342. IMPACT FACTOR (IF): 7.392 (Q1).

- S. Giraldo, **R. Fonoll-Rubio**, Z. Jehl Li-Kao, Y. Sánchez, L. Calvo-Barrio, V. Izquierdo-Roca, A. Pérez-Rodríguez, E. Saucedo. "Rear interface engineering of kesterite $Cu_2ZnSnSe_4$ solar cells by adding $CuGaSe_2$ thin layers". **Prog Photovolt Res Appl.**, vol. 29, no. 3, p. 334, March 2021, DOI: 10.1002/pip.3366. IMPACT FACTOR (IF): 8.490 (Q1).
- J. Andrade-Arvizu, **R. Fonoll Rubio**, V. Izquierdo-Roca, I. Becerril-Romero, D. Sylla, P. Vidal-Fuentes, Z. Jehl Li-Kao, A. Thomere, S. Giraldo, K. Tiwari, S. Resalati, M. Guc, M. Placidi. "Controlling the Anionic Ratio and Gradient in Kesterite Technology". **ACS Appl. Mater. Interfaces**, vol. 14, no. 1, p. 1177, January 2022, DOI: 10.1021/acsami.1c21507. IMPACT FACTOR (IF): 10.383 (Q1).
- **R. Fonoll-Rubio**, S. Paetel, E. Grau-Luque, I. Becerril-Romero, R. Mayer, A. Pérez-Rodríguez, M. Guc, V. Izquierdo-Roca. "Insights into the Effects of RbF-Post-Deposition Treatments on the Absorber Surface of High Efficiency $Cu(In,Ga)Se_2$ Solar Cells and Development of Analytical and Machine Learning Process Monitoring Methodologies Based on Combinatorial Analysis". **Adv. Energy Mater.**, vol. 12, no. 8, p. 2103163, February 2022, DOI: 10.1002/aenm.202103163. IMPACT FACTOR (IF): 29.698 (Q1).
- **R. Fonoll-Rubio**, M. Placidi, T. Hoelscher, A. Thomere, Z. Jehl Li-Kao, M. Guc, V. Izquierdo-Roca, R. Scheer, A. Pérez-Rodríguez. "Characterization of the Stability of Indium Tin Oxide and Functional Layers for Semitransparent Back-Contact Applications on $Cu(In,Ga)Se_2$ Solar Cells". **Sol. RRL**, vol. 6, no. 7, p. 2101071, July 2022, DOI: 10.1002/solr.202101071. IMPACT FACTOR (IF): 9.173 (Q1).

This thesis is divided into four chapters: introduction, methodology, results, and conclusions.

The first chapter provides an introduction into photovoltaics. It starts with a presentation of the main primary energy sources and an explanation of the problems associated with fossil fuels, which illustrates the need for the further development of renewable energy sources such as photovoltaics. Then, the fundamental processes that undergo in a solar cell and their main parameters are described, including the photovoltaic effect, the electronic band structure of semiconductor materials, the p–n junction effect,

the typical structure of a p–n solar cell, and the basic parameters that characterize a functional photovoltaic device. The different generations of solar cells are briefly presented with a main focus on high efficiency chalcopyrite and emerging sustainable kesterite-based technologies, since these are the technologies that have been studied in the present thesis. After this, the main principles of the different characterization techniques suitable for analyzing the interfaces of solar cells are explained. A special emphasis is made on Raman spectroscopy, since it is the main characterization technique employed in this thesis due to several advantages explained in the corresponding section. Finally, the first chapter concludes with the presentation of the main objectives of the present thesis.

The second chapter describes the details about the samples preparation, with a short description of the processes used for the fabrication of the solar cells, and the techniques and characterization methodologies employed during the development of this thesis are also reviewed. First, a brief description of the manufacturing processes of the solar cells is given. Then, a detailed description of the equipment and the experimental conditions selected for the different characterization techniques used in the experiments involved in this thesis is presented.

The third chapter describes and reviews the main results obtained in the thesis.. A general introduction is provided to give the general context of the performed experiments. This is followed by a summary of the obtained results and a general discussion. Then, the six scientific articles of the thesis are presented. The first article, *Insights into interface and bulk defects in a high efficiency kesterite-based device*, presents a detailed analysis of a high efficiency $Cu_2ZnSnSe_4$ device using a combination of advanced electron microscopy and spectroscopy techniques, so a full picture of the different defects present at the interfaces of the device and in the bulk of the absorber is achieved. The second article, *Defect depth-profiling in kesterite absorber by means of chemical etching and surface analysis*, describes a method to probe the depth morphology, defect profile, and possible secondary phases in $Cu_2ZnSnSe_4$ absorbers based on a controlled Methanol-Br_2 chemical etching and the employment of different characterization techniques such as scanning electron microscopy, 3D optical profilometry, X-ray photoelectron spectroscopy, and Raman spectroscopy. The third article, *Rear interface engineering of kesterite $Cu_2ZnSnSe_4$ solar cells by adding $CuGaSe_2$ thin layers*, focuses on an innovative approach using ultrathin CuGa layers at the rear interface to promote the formation of

wide-bandgap $CuGaSe_2$, and on the detailed analysis of the changes induced by this layer at the back interface of the kesterite absorber. The fourth article, *Controlling the Anionic Ratio and Gradient in Kesterite Technology*, presents a simple and reliable technique that allows to achieve anionic compositional profiles and gradients for $Cu_2ZnSn(S_{1-x}Se_x)_4$ and $Cu_2ZnGe(S_{1-x}Se_x)_4$ kesterite absorbers, and proposes a fast and robust methodology for the assessment of chemical compositional at the front and back interfaces. The fifth article, *Insights into the Effects of RbF-Post-Deposition Treatments on the Absorber Surface of High Efficiency Cu(In,Ga)Se_2 Solar Cells and Development of Analytical and Machine Learning Process Monitoring Methodologies Based on Combinatorial Analysis*, performs a high statistics analysis on high efficiency $CuIn_{1-x}Ga_xSe_2$ solar cells submitted to different RbF post-deposition treatments conditions, revealing the impact of the PDT processes in the absorber surface region, which in turn has a relevant impact on optoelectronic parameters such as the open-circuit voltage. Additionally, an industry-compatible methodology for the assessment of the RbF processes and the non-destructive prediction of the open-circuit voltage of the final devices is proposed. The sixth article, *Characterization of the Stability of Indium Tin Oxide and Functional Layers for Semitransparent Back-Contact Applications on Cu(In,Ga)Se_2 Solar Cells*, presents a detailed study of the stability of different indium tin oxide-based back contacts under the co-evaporation processes developed for the synthesis of high-efficiency semi-transparent $CuIn_{1-x}Ga_xSe_2$ solar cells, showing that the application of functional layers such as $MoSe_2$ and MoS_2 on the surface of indium tin oxide is required to avoid a degradation of the optical transparency and of the device performance at high co-evaporation process temperatures.

The fourth and final chapter of this thesis presents the conclusions and outlook of the work.

Finally, the following articles, which are co-authored by Robert Fonoll i Rubio, contributed to the preparation of this thesis, but are not included as the main results of the author:

- J. Andrade-Arvizu, V. Izquierdo-Roca, I. Becerril-Romero, P. Vidal-Fuentes, **R. Fonoll-Rubio**, Y. Sánchez, M. Placidi, L. Calvo-Barrio, O. Vigil-Galán, E. Saucedo. "Is It Possible To Develop Complex S–Se Graded Band Gap Profiles in Kesterite-Based Solar Cells?". **ACS Appl. Mater.**

Interfaces, vol. 11, no. 36, p. 32945, September 2019, DOI: 10.1021/acsami.9b09813. IMPACT FACTOR (IF): 8.758 (Q1).

- N. Benhaddou, S. Aazou, **R. Fonoll-Rubio**, Y. Sánchez, S. Giraldo, M. Guc, L. Calvo-Barrio, V. Izquierdo-Roca, M. Abd-Lefdil, Z. Sekkat, E. Saucedo. "Uncovering details behind the formation mechanisms of $Cu_2ZnGeSe_4$ photovoltaic absorbers". **J. Mater. Chem. C**, vol. 8, no. 12, p. 4003, March 2020, DOI: 10.1039/C9TC06728K. IMPACT FACTOR (IF): 7.393 (Q1).
- E. Ojeda-Durán, K. Monfil-Leyva, J. Andrade-Arvizu, I. Becerril-Romero, Y. Sánchez, **R. Fonoll-Rubio**, M. Guc, Z. Jehl, J.A. Luna-López, A.L. Muñoz-Zurita, J.A.D. Hernández-de la Luz, V. Izquierdo-Roca, M. Placidi, E. Saucedo. "CZTS solar cells and the possibility of increasing V_{OC} using evaporated Al_2O_3 at the CZTS/CdS interface". **Sol. Energy**, vol. 198, p. 696, March 2020, DOI: 10.1016/j.solener.2020.02.009. IMPACT FACTOR (IF): 5.742 (Q2).
- A.J. Lopez-Garcia, A. Bauer, **R. Fonoll Rubio**, D. Payno, Z. Jehl Li-Kao, S. Kazim, D. Hariskos, V. Izquierdo-Roca, E. Saucedo, A. Pérez-Rodríguez. "UV-Selective Optically Transparent Zn(O,S)-Based Solar Cells". **Sol. RRL**, vol. 4, no. 11, p. 2000470, November 2020, DOI: 10.1002/solr.202000470. IMPACT FACTOR (IF): 8.582 (Q1).
- M.O. Salem, **R. Fonoll**, S. Giraldo, Y. Sanchez, M. Placidi, V. Izquierdo-Roca, C. Malerba, M. Valentini, D. Sylla, A. Thomere, D.O. Ahmedou, E. Saucedo, A. Pérez-Rodríguez, Z. Jehl Li-Kao. "Over 10% Efficient Wide Bandgap CIGSe Solar Cells on Transparent Substrate with Na Predeposition Treatment". **Sol. RRL**, vol. 4, no. 11, p. 2000284, November 2020, DOI: 10.1002/solr.202000284. IMPACT FACTOR (IF): 8.582 (Q1).
- J. Andrade-Arvizu, **R. Fonoll-Rubio**, Y. Sánchez, I. Becerril-Romero, C. Malerba, M. Valentini, L. Calvo-Barrio, V. Izquierdo-Roca, M. Placidi, O. Vigil-Galán, A. Pérez-Rodríguez, E. Saucedo, Z. Jehl Li-Kao. "Rear Band gap Grading Strategies on Sn–Ge-Alloyed Kesterite Solar Cells". **ACS Appl. Energy Mater.**, vol. 3, no. 11, p. 10362, November 2020, DOI: 10.1021/acsaem.0c01146. IMPACT FACTOR (IF): 6.024 (Q2).

- E. Ojeda-Durán, K. Monfil-Leyva, J. Andrade-Arvizu, I. Becerril-Romero, Y. Sánchez, **R. Fonoll-Rubio**, M. Guc, Z. Jehl Li-Kao, J.A. Luna-López, E. Saucedo. "High efficiency Cu_2ZnSnS_4 solar cells over FTO substrates and their CZTS/CdS interface passivation via thermal evaporation of Al_2O_3". **J. Mater. Chem. C**, vol. 9, no. 16, p. 5356, April 2021, DOI: 10.1039/D1TC00880C. IMPACT FACTOR (IF): 8.067 (Q1).
- E. Grau-Luque, I. Anefnaf, N. Benhaddou, **R. Fonoll-Rubio**, I. Becerril-Romero, S. Aazou, E. Saucedo, Z. Sekkat, A. Perez-Rodriguez, V. Izquierdo-Roca, M. Guc. "Combinatorial and machine learning approaches for the analysis of $Cu_2ZnGeSe_4$: influence of the off-stoichiometry on defect formation and solar cell performance". **J. Mater. Chem. A**, vol. 9, no. 16, p. 10466, April 2021, DOI: 10.1039/D1TA01299A. IMPACT FACTOR (IF): 14.511 (Q1).
- I. Anefnaf, S. Aazou, Y. Sánchez, P. Vidal-Fuentes, **R. Fonoll-Rubio**, K.J. Tiwari, S. Giraldo, Z. Jehl Li-Kao, J. Andrade-Arvizu, M. Guc, E. Saucedo, Z. Sekkat. "Insights on the limiting factors of $Cu_2ZnGeSe_4$ based solar cells". **Sol. Energy Mater. Sol. Cells**, vol. 227, p. 111106, August 2021, DOI: 10.1016/j.solmat.2021.111106. IMPACT FACTOR (IF): 7.305 (Q1).
- M. Guc, E. Bailo, **R. Fonoll-Rubio**, F. Atlan, M. Placidi, P. Jackson, D. Hariskos, X. Alcobe, P. Pistor, I. Becerril-Romero, A. Perez-Rodriguez, F. Ramos, V. Izquierdo-Roca. "Evaluation of defect formation in chalcopyrite compounds under Cu-poor conditions by advanced structural and vibrational analyses". **Acta Mater.**, vol. 223, p. 117507 January 2022, DOI: 10.1016/j.actamat.2021.117507. IMPACT FACTOR (IF): 9.209 (Q1).
- **R. Fonoll-Rubio**, I. Becerril-Romero, P. Vidal-Fuentes, E. Grau-Luque, F. Atlan, A. Perez-Rodriguez, V. Izquierdo-Roca, M. Guc. "Combinatorial Analysis Methodologies for Accelerated Research: The Case of Chalcogenide Thin-Film Photovoltaic Technologies", **Sol. RRL**, p. 2200235, 2022. DOI: 10.1002/solr.202200235. IMPACT FACTOR (IF): 9.173 (Q1).

A a final remark, the results obtained during this thesis have contributed to the development and successful achievement of the goals of several national and European projects such as In4CIS, MasterPV, INFINITE-CELL, IGNITE, CELL2WIN, and

WINCOST. Moreover, new national and European projects were successfully submitted allowing to continue both Advanced characterization and Process monitoring lines of the SEMS group. The articles included in this thesis accumulate 32 citations (according to SCOPUS database on October 2022) in high impact factor journals, which indicates the interest and value of the performed research for the scientific community. In addition, the work carried out during this thesis was presented in several international conferences such as E-MRS, EU PVSEC and IEEE PVSC, and widened or deepened collaboration of SEMS group of IREC with different research groups from the worldwide leading institutes, as Zentrum für Sonnenenergie- und Wasserstoff-Forschung Baden-Württemberg (ZSW), Martin Luther University (MLU), University of Barcelona (UB), and Friedrich Schiller University (FSU). Finally, this thesis contributed to the development of a process monitoring system based on Raman and PL spectroscopy for evaluating the V_{OC} of CIGSe-based solar cells treated by RbF-PDT at the early production stages, which was installed at pilot production line of ZSW.

Prefaci: Publicacions i resum de la tesi

El treball presentat en aquesta tesi s'ha realitzat a l'Institut de Recerca en Energia de Catalunya (IREC) a l'equip d'investigació de Materials i Sistemes per a l'Energia Solar (SEMS), situat a Sant Adrià de Besòs (Espanya), durant el període 2018-2022 en el marc dels projectes MasterPV (PCI 2018-092945) i In4CIS (PCI 2019-111837-2). El principal objectiu d'aquesta tesi és identificar els principals mecanismes fisicoquímics que ocorren a les interfícies (anterior i posterior) de les capes absorbidores calcogenures característiques de l'arquitectura de cèl·lules solars de capa prima. Aquestes interfícies tenen un impacte rellevant en el rendiment del dispositiu, fet que justifica el gran interès en el desenvolupament de metodologies adients per a aquesta profunda anàlisi. L'enfocament integral en l'anàlisi d'interfícies, que també es complementa amb l'anàlisi del cos de l'absorbidor, també produeixen el desenvolupament de noves metodologies per a la caracterització no-destructiva de cèl·lules solars de capa fina basades en tècniques òptiques i compatibles amb processos de monitoratge industrial en línia.

Aquesta tesi està basada en els sis articles següents que han estat publicats en revistes d'alt factor d'impacte del primer quartil (Q1), fet que satisfà el principal requisit per a la concessió del títol de Doctor de Filosofia en Física a la Universitat de Barcelona. Els articles es presenten en ordre cronològic d'aparició:

- **R. Fonoll-Rubio**, J. Andrade-Arvizu, J. Blanco-Portals, I. Becerril-Romero, M. Guc, E. Saucedo, F. Peiró, L. Calvo-Barrio, M. Ritzer, C. S. Schnohr, M. Placidi, S. Estradé, V. Izquierdo-Roca, A. Pérez-Rodríguez. "Insights into interface and bulk defects in a high efficiency kesterite-based device". **Energy Environ. Sci.**, vol. 14, no. 1, p. 507, January 2021, DOI: 10.1039/D0EE02004D. IMPACT FACTOR (IF): 39.714 (Q1).
- K. J. Tiwari, **R. Fonoll Rubio**, S. Giraldo, L. Calvo-Barrio, V. Izquierdo-Roca, M. Placidi, Y. Sanchez, A. Pérez-Rodríguez, E. Saucedo, Z. Jehl Li-Kao. "Defect depth-profiling in kesterite absorber by means of chemical etching and surface analysis". **Appl. Surf. Sci.**, vol. 540, no. 2, p. 148342, February 2021, DOI: 10.1016/j.apsusc.2020.148342. IMPACT FACTOR (IF): 7.392 (Q1).

- S. Giraldo, **R. Fonoll-Rubio**, Z. Jehl Li-Kao, Y. Sánchez, L. Calvo-Barrio, V. Izquierdo-Roca, A. Pérez-Rodríguez, E. Saucedo. "Rear interface engineering of kesterite $Cu_2ZnSnSe_4$ solar cells by adding $CuGaSe_2$ thin layers". **Prog Photovolt Res Appl.**, vol. 29, no. 3, p. 334, March 2021, DOI: 10.1002/pip.3366. IMPACT FACTOR (IF): 8.490 (Q1).
- J. Andrade-Arvizu, **R. Fonoll Rubio**, V. Izquierdo-Roca, I. Becerril-Romero, D. Sylla, P. Vidal-Fuentes, Z. Jehl Li-Kao, A. Thomere, S. Giraldo, K. Tiwari, S. Resalati, M. Guc, M. Placidi. "Controlling the Anionic Ratio and Gradient in Kesterite Technology". **ACS Appl. Mater. Interfaces**, vol. 14, no. 1, p. 1177, January 2022, DOI: 10.1021/acsami.1c21507. IMPACT FACTOR (IF): 10.383 (Q1).
- **R. Fonoll-Rubio**, S. Paetel, E. Grau-Luque, I. Becerril-Romero, R. Mayer, A. Pérez-Rodríguez, M. Guc, V. Izquierdo-Roca. "Insights into the Effects of RbF-Post-Deposition Treatments on the Absorber Surface of High Efficiency $Cu(In,Ga)Se_2$ Solar Cells and Development of Analytical and Machine Learning Process Monitoring Methodologies Based on Combinatorial Analysis". **Adv. Energy Mater.**, vol. 12, no. 8, p. 2103163, February 2022, DOI: 10.1002/aenm.202103163. IMPACT FACTOR (IF): 29.698 (Q1).
- **R. Fonoll-Rubio**, M. Placidi, T. Hoelscher, A. Thomere, Z. Jehl Li-Kao, M. Guc, V. Izquierdo-Roca, R. Scheer, A. Pérez-Rodríguez. "Characterization of the Stability of Indium Tin Oxide and Functional Layers for Semitransparent Back-Contact Applications on $Cu(In,Ga)Se_2$ Solar Cells". **Sol. RRL**, vol. 6, no. 7, p. 2101071, July 2022, DOI: 10.1002/solr.202101071. IMPACT FACTOR (IF): 9.173 (Q1).

Aquesta tesi es divideix en quatre capítols: introducció, metodologia, resultats i conclusions.

El primer capítol proporciona una introducció a la fotovoltaica. Comença amb la presentació de les principals fonts d'energia primàries i una explicació dels problemes associats amb els combustibles fòssils, fet que demostra la necessitat de desenvolupar les fonts d'energia renovable com la fotovoltaica. Després, es descriuen els processos fonamentals que succeeixen en una cèl·lula solar i els seus paràmetres principals, incloent-hi l'efecte fotovoltaic, l'estructura de bandes electròniques de materials

semiconductors, l'efecte de la junció p–n, l'estructura típica d'una cèl·lula solar p–n, i els paràmetres bàsics que caracteritzen un dispositiu fotovoltaic funcional. Les diferents generacions de cèl·lules solars es presenten breument amb un enfocament en les cèl·lules solars basades en calcopirites d'alta eficiència i en kesterites sostenibles, ja que aquestes tecnologies són les estudiades en aquesta tesi. A continuació, s'explica el principi bàsic de diferents tècniques de caracterització adients per a l'anàlisi d'interfícies de cèl·lules solars. Es posa un èmfasi especial en l'espectroscòpia Raman, ja que aquesta és la tècnica de caracterització principal emprada en aquesta tesi a causa de diversos avantatges detallats en la secció corresponent. Finalment, el primer capítol conclou amb la presentació dels principals objectius de la present tesi.

El segon capítol descriu els detalls sobre la preparació de mostres, amb una breu descripció dels processos de fabricació de les cèl·lules solars, i les tècniques i les metodologies de caracterització emprades durant el desenvolupament d'aquesta tesi també són explicades. Primer, es proporciona una breu descripció del procés de fabricació de les cèl·lules solars. Després, s'ofereix una descripció detallada dels equips i condicions experimentals seleccionades per a les diferents tècniques de caracterització utilitzades en els experiments implicats en aquesta tesi.

El tercer capítol descriu i examina els resultats principals obtinguts durant la preparació de la tesi. S'ofereix una introducció general per a contextualitzar els experiments duts a terme, seguits per un resum dels resultats aconseguits i una discussió general. A continuació, es presenten els sis articles científics de la tesi. El primer article, *Insights into interface and bulk defects in a high efficiency kesterite-based device*, presenta una anàlisi detallada d'un dispositiu $Cu_2ZnSnSe_4$ d'alta eficiència utilitzant una combinació de tècniques avançades d'espectroscòpia i de microscòpia electrònica, així que s'aconsegueix una imatge completa dels diferents defectes presents a les interfícies del dispositiu i al cos de l'absorbidor. El segon article, *Defect depth-profiling in kesterite absorber by means of chemical etching and surface analysis*, descriu un mètode per a analitzar la morfologia en profunditat, el perfil de defectes i les possibles fases secundàries en absorbidors $Cu_2ZnSnSe_4$ basat en un gravat químic controlat de metanol-Br_2 i en l'ús de diferents tècniques de caracterització com microscòpia electrònica d'escaneig, perfilometria òptica 3D, espectroscòpia fotoelectrònica de raigs X i espectroscòpia Raman. El tercer article, *Rear interface engineering of kesterite $Cu_2ZnSnSe_4$ solar cells by adding $CuGaSe_2$ thin layers*, se centra en un enfocament

innovador utilitzant capes ultrafines de CuGa a la interfície posterior per a fomentar la formació de $CuGaSe_2$ de banda prohibida ampla, la qual actua com a un reflector d'electrons eficient i com una capa intermèdia efectiva que millora la cristal·linitat de la kesterita a la interfície posterior. El quart article, *Controlling the Anionic Ratio and Gradient in Kesterite Technology*, presenta una tècnica simple i segura que permet aconseguir perfils composicionals aniònics i gradients per als absorbidors de kesterita$Cu_2ZnSn(S_{1-x}Se_x)_4$ and $Cu_2ZnGe(S_{1-x}Se_x)_4$. El cinquè article, *Insights into the Effects of RbF-Post-Deposition Treatments on the Absorber Surface of High Efficiency Cu(In,Ga)Se_2 Solar Cells and Development of Analytical and Machine Learning Process Monitoring Methodologies Based on Combinatorial Analysis*, du a terme una anàlisi d'alta estadística sobre cèl·lules solars $CuIn_{1-x}Ga_xSe_2$ d'alta eficiència sotmeses a diferents condicions de tractaments de postdeposició de RbF, el qual revela l'impacte dels processos PDT en la regió superficial de l'absorbidor, que al seu torn té un gran impacte en els paràmetres optoelectrònics com el voltatge de circuit obert. Addicionalment, es desenvolupa una metodologia compatibles amb la indústria per a l'avaluació del procés de RbF i la predicció no-destructiva del voltatge de circuit obert dels dispositius finals. El sisè article, *Characterization of the Stability of Indium Tin Oxide and Functional Layers for Semitransparent Back-Contact Applications on Cu(In,Ga)Se_2 Solar Cells*, presenta un estudi detallat de l'estabilitat de diferents contactes posteriors basats en òxid d'estany i indi sota els processos de coevaporació desenvolupats per a la síntesi de cèl·lules solars semitransparents $CuIn_{1-x}Ga_xSe_2$ d'alta eficiència, el qual mostra que es requereix l'aplicació de capes funcionals com $MoSe_2$ i MoS_2 a la superfície de l'òxid d'estany i indi per a evitar la degradació de la transparència òptica i del rendiment del dispositiu a temperatures altes del procés de coevaporació.

El quart i últim capítol d'aquesta tesi presenta les conclusions i els pronòstics del treball.

Finalment, els articles següents, dels quals Robert Fonoll i Rubio és coautor, han contribuït a la preparació d'aquesta tesi, però no s'hi inclouen com a resultats principals de l'autor:

- J. Andrade-Arvizu, V. Izquierdo-Roca, I. Becerril-Romero, P. Vidal-Fuentes, **R. Fonoll-Rubio**, Y. Sánchez, M. Placidi, L. Calvo-Barrio, O. Vigil-Galán, E. Saucedo. "Is It Possible To Develop Complex S–Se Graded

Band Gap Profiles in Kesterite-Based Solar Cells?". **ACS Appl. Mater. Interfaces**, vol. 11, no. 36, p. 32945, September 2019, DOI: 10.1021/acsami.9b09813. IMPACT FACTOR (IF): 8.758 (Q1).

- N. Benhaddou, S. Aazou, **R. Fonoll-Rubio**, Y. Sánchez, S. Giraldo, M. Guc, L. Calvo-Barrio, V. Izquierdo-Roca, M. Abd-Lefdil, Z. Sekkat, E. Saucedo. "Uncovering details behind the formation mechanisms of $Cu_2ZnGeSe_4$ photovoltaic absorbers". **J. Mater. Chem. C**, vol. 8, no. 12, p. 4003, March 2020, DOI: 10.1039/C9TC06728K. IMPACT FACTOR (IF): 7.393 (Q1).
- E. Ojeda-Durán, K. Monfil-Leyva, J. Andrade-Arvizu, I. Becerril-Romero, Y. Sánchez, **R. Fonoll-Rubio**, M. Guc, Z. Jehl, J.A. Luna-López, A.L. Muñoz-Zurita, J.A.D. Hernández-de la Luz, V. Izquierdo-Roca, M. Placidi, E. Saucedo. "CZTS solar cells and the possibility of increasing V_{OC} using evaporated Al_2O_3 at the CZTS/CdS interface". **Sol. Energy**, vol. 198, p. 696, March 2020, DOI: 10.1016/j.solener.2020.02.009. IMPACT FACTOR (IF): 5.742 (Q2).
- A.J. Lopez-Garcia, A. Bauer, **R. Fonoll Rubio**, D. Payno, Z. Jehl Li-Kao, S. Kazim, D. Hariskos, V. Izquierdo-Roca, E. Saucedo, A. Pérez-Rodríguez. "UV-Selective Optically Transparent Zn(O,S)-Based Solar Cells". **Sol. RRL**, vol. 4, no. 11, p. 2000470, November 2020, DOI: 10.1002/solr.202000470. IMPACT FACTOR (IF): 8.582 (Q1).
- M.O. Salem, **R. Fonoll**, S. Giraldo, Y. Sanchez, M. Placidi, V. Izquierdo-Roca, C. Malerba, M. Valentini, D. Sylla, A. Thomere, D.O. Ahmedou, E. Saucedo, A. Pérez-Rodríguez, Z. Jehl Li-Kao. "Over 10% Efficient Wide Bandgap CIGSe Solar Cells on Transparent Substrate with Na Predeposition Treatment". **Sol. RRL**, vol. 4, no. 11, p. 2000284, November 2020, DOI: 10.1002/solr.202000284. IMPACT FACTOR (IF): 8.582 (Q1).
- J. Andrade-Arvizu, **R. Fonoll-Rubio**, Y. Sánchez, I. Becerril-Romero, C. Malerba, M. Valentini, L. Calvo-Barrio, V. Izquierdo-Roca, M. Placidi, O. Vigil-Galán, A. Pérez-Rodríguez, E. Saucedo, Z. Jehl Li-Kao. "Rear Band gap Grading Strategies on Sn–Ge-Alloyed Kesterite Solar Cells". **ACS Appl. Energy Mater.**, vol. 3, no. 11, p. 10362, November 2020, DOI: 10.1021/acsaem.0c01146. IMPACT FACTOR (IF): 6.024 (Q2).

- E. Ojeda-Durán, K. Monfil-Leyva, J. Andrade-Arvizu, I. Becerril-Romero, Y. Sánchez, **R. Fonoll-Rubio**, M. Guc, Z. Jehl Li-Kao, J.A. Luna-López, E. Saucedo. "High efficiency Cu_2ZnSnS_4 solar cells over FTO substrates and their CZTS/CdS interface passivation via thermal evaporation of Al_2O_3". **J. Mater. Chem. C**, vol. 9, no. 16, p. 5356, April 2021, DOI: 10.1039/D1TC00880C. IMPACT FACTOR (IF): 8.067 (Q1).
- E. Grau-Luque, I. Anefnaf, N. Benhaddou, **R. Fonoll-Rubio**, I. Becerril-Romero, S. Aazou, E. Saucedo, Z. Sekkat, A. Perez-Rodriguez, V. Izquierdo-Roca, M. Guc. "Combinatorial and machine learning approaches for the analysis of $Cu_2ZnGeSe_4$: influence of the off-stoichiometry on defect formation and solar cell performance". **J. Mater. Chem. A**, vol. 9, no. 16, p. 10466, April 2021, DOI: 10.1039/D1TA01299A. IMPACT FACTOR (IF): 14.511 (Q1).
- I. Anefnaf, S. Aazou, Y. Sánchez, P. Vidal-Fuentes, **R. Fonoll-Rubio**, K.J. Tiwari, S. Giraldo, Z. Jehl Li-Kao, J. Andrade-Arvizu, M. Guc, E. Saucedo, Z. Sekkat. "Insights on the limiting factors of $Cu_2ZnGeSe_4$ based solar cells". **Sol. Energy Mater. Sol. Cells**, vol. 227, p. 111106, August 2021, DOI: 10.1016/j.solmat.2021.111106. IMPACT FACTOR (IF): 7.305 (Q1).
- M. Guc, E. Bailo, **R. Fonoll-Rubio**, F. Atlan, M. Placidi, P. Jackson, D. Hariskos, X. Alcobe, P. Pistor, I. Becerril-Romero, A. Perez-Rodriguez, F. Ramos, V. Izquierdo-Roca. "Evaluation of defect formation in chalcopyrite compounds under Cu-poor conditions by advanced structural and vibrational analyses". **Acta Mater.**, vol. 223, p. 117507 January 2022, DOI: 10.1016/j.actamat.2021.117507. IMPACT FACTOR (IF): 9.209 (Q1).
- **R. Fonoll-Rubio**, I. Becerril-Romero, P. Vidal-Fuentes, E. Grau-Luque, F. Atlan, A. Perez-Rodriguez, V. Izquierdo-Roca, M. Guc. "Combinatorial Analysis Methodologies for Accelerated Research: The Case of Chalcogenide Thin-Film Photovoltaic Technologies", **Sol. RRL**, p. 2200235, 2022. DOI: 10.1002/solr.202200235. IMPACT FACTOR (IF): 9.173 (Q1).

Contribution of the author to the thesis publications

R. Fonoll-Rubio, J. Andrade-Arvizu, J. Blanco-Portals, I. Becerril-Romero, M. Guc, E. Saucedo, F. Peiró, L. Calvo-Barrio, M. Ritzer, C. S. Schnohr, M. Placidi, S. Estradé, V. Izquierdo-Roca, A. Pérez-Rodríguez. "Insights into interface and bulk defects in a high efficiency kesterite-based device". **Energy Environ. Sci.**, vol. 14, no. 1, p. 507, January 2021, DOI: 10.1039/D0EE02004D. IMPACT FACTOR (IF): 39.714 (Q1).

In this work, Robert Fonoll i Rubio was actively involved in the development and coordination of most of the experiments, including the preparation of the samples for the analysis by the different techniques, and in the analysis of the obtained data, including preliminary and more advanced analysis. Namely, he has participated in the sample preparation for TEM observation at CCiTUB and at UB facilities, and in the analysis of the TEM images. He performed the mechanical lift-off for SEM observation of the CZTSe back interface and the acquisition of SEM micrographs at the IREC facilities, and the corresponding analysis of such micrographs. He also performed the impedance measurements at IREC facilities and the analysis of the derived capacitance data. He participated in the analysis of the experimental data acquired by Raman spectroscopy. Finally, he participated in the results discussion, wrote the first draft of the paper and revised the article manuscript at the final stage, including the preparation of the report to address the Reviewers comments.

K. J. Tiwari, **R. Fonoll Rubio**, S. Giraldo, L. Calvo-Barrio, V. Izquierdo-Roca, M. Placidi, Y. Sanchez, A. Pérez-Rodríguez, E. Saucedo, Z. Jehl Li-Kao. "Defect depth-profiling in kesterite absorber by means of chemical etching and surface analysis". **Appl. Surf. Sci.**, vol. 540, no. 2, p. 148342, February 2021, DOI: 10.1016/j.apsusc.2020.148342. IMPACT FACTOR (IF): 7.392 (Q1).

In this work, Robert Fonoll i Rubio was responsible for the Raman scattering analysis of the kesterite thin films after different etching stages. He has performed the measurements of the spectra under λ_{exc} = 325 nm using IREC facilities, and made the analysis of the corresponding experimental data. Robert discussed the results with the other co-authors and participated in defining the model that allows to explain the obtained data. He also participated in the investigation of the different samples by means of 3D

Optical Profilometry applying IREC facilities. Finally, he participated in the preparation of the manuscript being quite active at all the preparation steps.

S. Giraldo, **R. Fonoll-Rubio**, Z. Jehl Li-Kao, Y. Sánchez, L. Calvo-Barrio, V. Izquierdo-Roca, A. Pérez-Rodríguez, E. Saucedo. "Rear interface engineering of kesterite $Cu_2ZnSnSe_4$ solar cells by adding $CuGaSe_2$ thin layers". **Prog Photovolt Res Appl.**, vol. 29, no. 3, p. 334, March 2021, DOI: 10.1002/pip.3366. IMPACT FACTOR (IF): 8.490 (Q1).

In this work, Robert Fonoll i Rubio coordinated the Raman scattering analysis of the samples, performing the Raman measurements with different excitation wavelengths (λ_{exc} = 532 and 785 nm) using the IREC facilities, and was responsible for the analysis of the corresponding experimental data. He also performed the mechanical lift-off that allowed making the measurements of the Raman spectra at the back interface of the CZTSe absorber. All these lead to significant results that composed a core of the article and allowed to conclude about the main findings of the present study. Finally, Robert participated in the results discussion and in the redaction of the manuscript.

J. Andrade-Arvizu, **R. Fonoll Rubio**, V. Izquierdo-Roca, I. Becerril-Romero, D. Sylla, P. Vidal-Fuentes, Z. Jehl Li-Kao, A. Thomere, S. Giraldo, K. Tiwari, S. Resalati, M. Guc, M. Placidi. "Controlling the Anionic Ratio and Gradient in Kesterite Technology". **ACS Appl. Mater. Interfaces**, vol. 14, no. 1, p. 1177, January 2022, DOI: 10.1021/acsami.1c21507. IMPACT FACTOR (IF): 10.383 (Q1).

In this work, Robert Fonoll i Rubio was responsible for the Raman scattering analysis of these processes, making the measurements of Raman spectra under different excitation wavelengths (532 and 785 nm) using IREC facilities, and coordinated the analysis of the corresponding experimental data. The mechanical lift-off of the studied thin films, also performed by Robert, allowed him to make the measurements of the Raman spectra at the back interface of the CZTSSe and CZGSSe absorber layers. He was actively involved in the discussion of the obtained results of Raman spectroscopy which allowed to propose a model for the estimation of the [S]/([S]+[Se]) compositional ratio at

different depth of the thin films. Finally, he participated in the preparation of the manuscript and in the review of its final version.

R. Fonoll-Rubio, S. Paetel, E. Grau-Luque, I. Becerril-Romero, R. Mayer, A. Pérez-Rodríguez, M. Guc, V. Izquierdo-Roca. "Insights into the Effects of RbF-Post-Deposition Treatments on the Absorber Surface of High Efficiency Cu(In,Ga)Se_2 Solar Cells and Development of Analytical and Machine Learning Process Monitoring Methodologies Based on Combinatorial Analysis". **Adv. Energy Mater.**, vol. 12, no. 8, p. 2103163, February 2022, DOI: 10.1002/aenm.202103163. IMPACT FACTOR (IF): 29.698 (Q1).

As the main author of this article, Robert Fonoll i Rubio was involved in all the steps of the analysis leading to the publication. Namely, he was participating in the preliminary planning of the study in general and of the coordination of the experiments. Robert was responsible for the planning and definition of the Raman analysis, which involved Raman scattering measurements performed under 638 and 785 nm excitation wavelengths, and for the interpretation of the experimental data. He also performed the measurements of all photoluminescence spectra under λ_{exc} = 638 nm and the analysis of the obtained data. The analysis of both Raman and PL data also included studying the correlation between them and the optoelectronic parameters of the solar cells. Robert was also in charge of the impedance measurements and the analysis of the derived capacitance data, which allowed to complete a deep study on the impact of the PDT processes and the mechanisms related to the observed improvement of the solar cells efficiency. For this study, all measurements were performed using IREC facilities. Finally, Robert participated in the discussion of the obtained results and in the development of the physical model explaining them. He wrote the first draft of the manuscript and coordinated its revision with the other co-authors.

R. Fonoll-Rubio, M. Placidi, T. Hoelscher, A. Thomere, Z. Jehl Li-Kao, M. Guc, V. Izquierdo-Roca, R. Scheer, A. Pérez-Rodríguez. "Characterization of the Stability of Indium Tin Oxide and Functional Layers for Semitransparent Back-Contact Applications on Cu(In,Ga)Se_2 Solar Cells". **Sol. RRL**, vol. 6, no. 7, p. 2101071, July 2022, DOI: 10.1002/solr.202101071. IMPACT FACTOR (IF): 9.173 (Q1).

Being the first and the corresponding author of this article, Robert Fonoll i Rubio was one of the leading researchers at all the steps of its preparation. He coordinated the main characterization experiments (measurements of the transmittance and reflectance spectra, of Raman scattering spectra under different excitation wavelengths and from different sides of the sample), and was in charge of the interpretation of the experimental data from these measurements. Analysis of the obtained data leaded to the main conclusions of the article, which allowed to report for the first time in the literature a detailed study on the impact of the technological processes on the transparency and electrical quality of ITO based back transparent contacts for semi-transparent devices. All these measurements were performed applying IREC facilities. In addition, Robert performed the analysis of the optoelectronic parameters of the solar cells measured at the Martin-Luther University in Halle (Germany) (partner organization in this study). Finally, he participated in the results discussion, he was in charge of the writing of the first draft of the paper and coordinated its revision with all the co-authors.

Chapter 1: Introduction

1.1. Primary energy sources

World population has been growing during centuries and different projections predict that this growth will not stop until the end of the current century,[1] which means that the energy demand to sustain the significantly growing population will also increase in the next decades. Combustion of fossil fuels such as oil, coal, and natural gas is the traditional process that our society employs to obtain energy and, in the year 2020, this represented 83.1% of the global energy consumption, as shown in Figure 1.[2] However, fossil fuels have several critical problems that compromise their use as primary energy sources. First, they are limited resources and they will be exhausted at some time. At the current consumption rate, the depletion of the proven oil and gas reserves will occur in less than 50 years, while the coal reserves depletion will occur in approximately 100 years.[3] Second, the extraction of fossil fuels becomes more difficult as readily accessible reserves are consumed, which increases the cost of their extraction both in terms of money and energy. Therefore, even before the complete depletion of these reserves, there will be a point where the energy invested in extracting fossil fuels will be higher than the energy obtained from those fuels. This will lead to an unsustainable discrepancy between the prices that companies need to cover their extraction costs and the fuel prices that society can afford to pay.[4] Third, inhomogeneous distribution of the fossil fuels in the Earth crust leads to a possibility of local governments to use them as means of influence against the other territories. Finally, combustion of fossil fuels emits large amounts of CO_2, a greenhouse gas that accumulates in the atmosphere and traps heat. The energy balance of the Earth is maintained between the incoming shortwave radiation from the Sun and the outgoing longwave radiation from the Earth. CO_2 accumulated in the atmosphere absorbs a portion of the outgoing infrared radiation emitted by the Earth and, then, it reemits the absorbed radiation in all directions, some of which returns to the terrestrial surface as heat.[5] Thus, fossil fuels contribute to the global warming and climate change, which will produce catastrophic consequences in ecosystems, freshwater supplies, and human health.[6] In addition to CO_2, other gases such as NO_x, SO_2, and CO are also released when burning fossil fuels, and they are gaseous pollutants that cause adverse effects on human health.[7] Taking into account the presented disadvantages, it is necessary a transition from fossil fuels to cleaner, decentralized, and efficient energy systems.

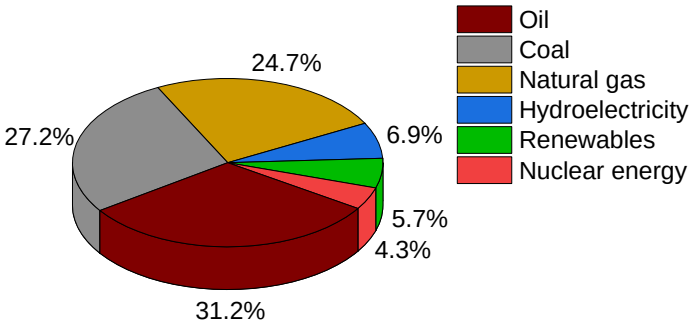

Figure 1. *World energy consumption by fuel during 2020.*[2]

Nuclear fission is an energy source that does not generate greenhouse gases or air pollutants; however, it is also a limited resource and it produces a radioactive waste that has to be isolated from the environment for thousands of years to avoid endangering human life.[8] Then, nuclear fusion promises the same benefits than fission while producing a higher amount of energy and a considerably lower radioactive waste, but the technical challenges that it entails prevent its commercial viability for the moment.[9]

An alternative to fossil fuels and nuclear energy are renewable energies, which include solar power, wind, hydroelectricity, bioenergy, and geothermal energy. These sources are virtually inexhaustible, and most of them do not emit greenhouse gases. Despite these clear advantages, renewable energies have not replaced fossil fuels yet due to current limitations such as a high dependency on the geographic location and on the weather, and a higher economic cost with respect to fossil fuel and/or the need for high initial investments.[10] Nevertheless, the contribution of renewables to the world energy consumption has increased over the years and, as shown in Figure 1, it surpassed that of nuclear energy in 2020 even when excluding hydroelectricity.[2] This indicates that renewable energies are becoming the main alternative to fossil fuels and that their development has to continue to guarantee a sustainable society and to reverse, or at least to slow down, climate change.

1.2. Photovoltaic technologies

Among all renewable energy sources, sunlight is the most abundant one; each day, the sun provides 10000 times the energy needed on the planet,[10,11] which makes solar energy the renewable source with the greatest potential to satisfy the existing and future energy demand.[12] Thus, research on photovoltaic (PV) technologies, which convert light into electricity, is fundamental to substitute fossil fuels by a clean and inexhaustible

resource. This research has to overcome real-life limitations that counter the potential of PV. First, solar irradiance has an unequal global distribution, so PV depends on the latitude and the climate.[13] Then, it is an intermittent source due to day-night cycles and variable weather.[10] These limitations could be solved by efficient electrical grids to transport the energy and by efficient energy storage systems, but currently there exists a lack of economically viable large-scale storage and grid technologies.[14] It is also worth to note that the extraction of raw materials for solar panels and their manufacturing depend on fossil fuels, so developing PV technologies contributes to the depletion of such sources. Finally, abundance and properties of the materials that constitute the solar panels has also to be taken into account. A material with optimal properties has a limited applicability if it is scarce, and an abundant one cannot be employed in PV if it lacks the optimal properties. This last limitation can be solved by studying and optimizing the materials and compounds that constitute the solar cells, which is the aim of the present thesis.

1.2.1. Fundamentals of solar cells

The main working principle of a solar cell is based on the PV effect, which occurs when a photon hits a material and generates an electron-hole pair that can be further separated to obtain a potential difference or a voltage. In most cases, a semiconductor material is used in solar cells for absorbing the photons. Generally, semiconductors are crystalline materials, which means that their atoms are arranged following a periodic order. Due to its positively charged nucleus, each atom of a crystal generates a potential well that attracts the electrons and that depends on the distance between the electron and the atomic nucleus; this contrasts with the case of a free electron, which is one that does not interact with the environment, so it moves in a region where the potential is constant. While a free electron can take any energy value in a continuous manner, an electron that is attracted by a single atom can only occupy discrete energy levels determined by the geometry of the potential wells. When multiple atoms approach to a form of crystal, however, their atomic orbitals overlap and different electrons try to occupy the same level. So, due to the Pauli exclusion principle that states that only two electrons of opposite spin can occupy the same level, there is a splitting of each discrete energy level into different levels that are very close, but with different energies, as shown in Figure 2a. The higher the number of atoms present in the crystal, the higher the number of levels into which each discrete energy level splits. In practice, the energy difference between the levels

resulting from the splitting process is so small that it can be considered that they form a quasi-continuum of permitted levels, which are called energy bands. Inside each of these bands, the behavior of electrons resembles that of a free electron, but between the different bands there are forbidden regions with no electronic states for them to occupy. The bands with the highest energy values, which are the ones farther from the atomic nucleus, contain no electrons at $T = 0$ K. The bands with the lowest energy values, which are the ones closest to the atomic nucleus, contain core electrons that are tightly bounded to the nucleus and do not participate in the bonding with other atoms. Then, the last band that contains electrons is called valence band (VB) and its electrons form the bonds between different atoms, as shown in Figure 2b. The permitted energy band directly above the VB is called conduction band (CB), and the energy difference between the top of the VB and the bottom of the CB is the band gap (E_g). If an amount of energy equal or higher to E_g is transferred to an electron, it jumps from the VB to the CB, where the electron is no longer attracted by the atom and it can move freely throughout the crystal, which produces an electric current. Thus, PV effect is based on the optical absorption of photons with energy higher than E_g that excite valence electrons to the CB, a process that breaks the bond between the different atoms and leaves a free electron in the CB and a hole in the VB, as shown in Figure 2. This hole corresponds to an empty electronic state (i.e. is a lack of an electron), so it is quasiparticle that is associated to a positive charge that moves in the crystal to fill the empty space left by an electron.[15–17]

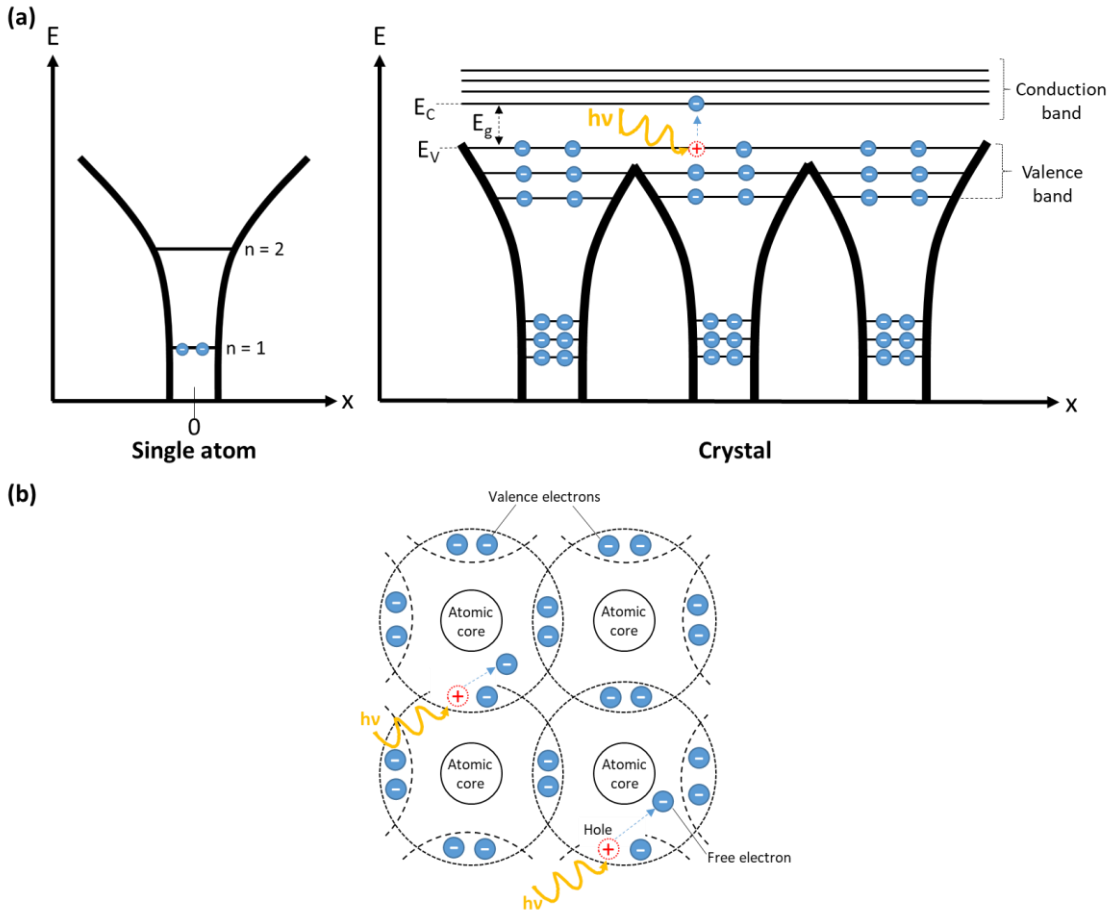

Figure 2. *(a) Permitted energy levels of a single atom and a crystal. In the case of the crystal, absorption of photons with energies higher than the band gap is represented using the energy band model for semiconductors. Blue-filled circles represent electrons, while red-dashed circles represent holes. E_C, E_V, and E_g are the energy values of the conduction band minimum, the valence band maximum, and the band gap of the material, respectively. h is the Planck constant and ν is the frequency of the incident photon. (b) Schematic representation of the photovoltaic effect in a two-dimensional crystal lattice. Valence electrons correspond to the electrons in the E_V energy level in (a), while the free electron corresponds to the electron in the conduction band.*

The electron-hole pairs (EHP) generated by photons act as charge carriers that conduct the electric current; but if they are not separated and extracted, the electron and the hole recombine after some time and loss the energy acquired from the incident photon, which is released as a new photon (radiative recombination) or as phonons that increase the temperature of the crystal (non-radiative recombination). Thus, a p–n junction is used in solar cells to create a built-in electric field that separates the EHP before recombination. The p–n junction is the interface between an n-type and a p-type semiconductor that are in contact. In an intrinsic semiconductor, the concentration of electrons in the CB (n) is equal to the concentration of holes in the VB (p), and these carriers are mainly generated

by thermal energy; in this case, the Fermi level, which is the level that has a 50% probability of being filled with electrons if an available energy state is present, is close to the middle of the band gap. In extrinsic semiconductors, carriers are mainly generated by impurities or dopants, which are atoms of another element that replace crystal atoms. Thus, a n-type semiconductor contains donor impurities that introduce extra electrons in the crystal lattice, which results in a higher *n* than *p* (electrons are the majority carriers and holes are the minority carriers) and a Fermi level is located in the band gap closer to the CB; a p-type semiconductor contains acceptor impurities that generate extra holes in the crystal lattice, which results in a higher *p* than *n* (holes are the majority carriers and electrons are the minority ones) and the Fermi level is located in the band gap closer to the VB.

When n-type and p-type semiconductors are first put together to form the p–n junction, the carrier concentration gradient generates a diffusion force that moves holes of the p-type semiconductor into the n-type one, while electrons of the n-type semiconductor diffuse into the p-type one. Diffused holes leave ionized impurity atoms with a negative charge in the p-type region and diffused electrons leave ionized impurity atoms with a positive charge in the n-type one, which generates an electric field from the n-type side to the p-type one; this built-in electric field produces a drift force that moves holes back to the p-type semiconductor and electrons back to the n-type one. Eventually, the diffusion and drift forces reach an equilibrium where the Fermi levels of the p-type and n-type semiconductors are equal. This process, shown in Figure 3, results in a region free of mobile carriers around the p–n interface, which is called depletion region or space charge region (SCR); this region is charged by the ionized donor and acceptor ions, while the region beyond the SCR is electrically neutral. Thus, in a solar cell, photons generate EHP and, if they are generated within a distance smaller than the diffusion length from the edge of the SCR, they are able to reach the SCR, where they are separated by the drift force produced by the built-in electric field, which results in an electric photocurrent.[15,16,18]

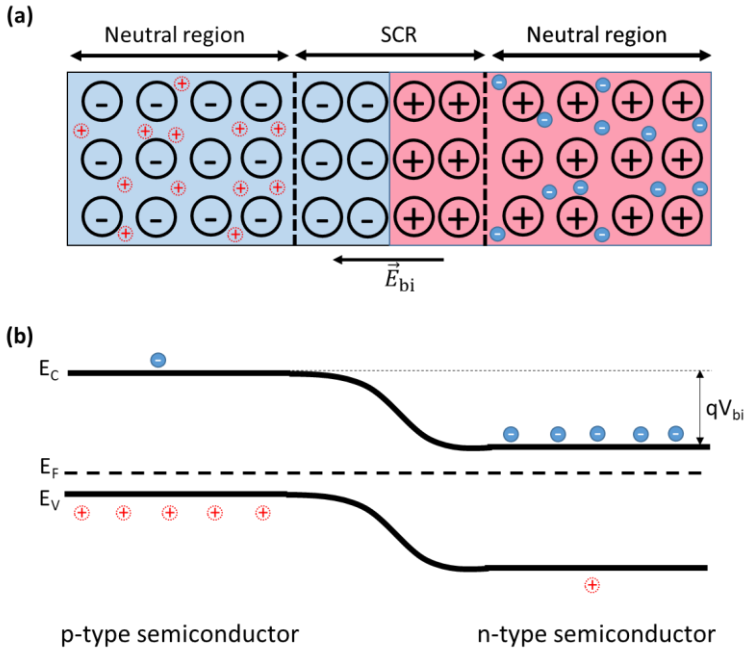

Figure 3. *(a) Schematic representation of a p–n junction. Blue-filled circles represent free electrons, while red-dashed circles represent holes. Black circles with – symbol represent negative ions from filled holes, while black circles with + symbol represent positive ions from removed electrons. Neutral regions, space charge regions (SCR), and direction of the built-in electric field (E_{bi}) are indicated. (b) Energy band diagram of a p–n junction. E_C and E_V are the energy values of the conduction band minimum and the valence band maximum, respectively, while E_F is the Fermi energy level. Q is the electric charge and V_{bi} is the built-in potential.*

Once EHP are generated and separated, they have to be collected and extracted from the solar cell to generate power. This is achieved by means of the different layers that constitute the structure of a solar cell. Figure 4 shows the typical structured of a p–n heterojunction thin film solar cell using a substrate configuration. First, the absorber is the photoactive layer that absorbs most of the light and generates most of the carriers. Then, the buffer layer is a highly-doped semiconductor of opposite type than that of the absorber to form the p–n junction, and it should have a high band gap so it does not absorb the sunlight that has to reach the absorber. On top of the absorber a window layer is deposited. This layer acts as front contact to extract the charge, and it is usually a transparent conductive oxide (TCO) that can collect carriers without shading the absorber layer. For the back contact, usually metal contacts are used due to their high conductivity, but they must have an appropriate work function to avoid the formation of a resistive barrier. Finally, the substrate provides mechanical and thermal stability. In addition to these layers, a metal grid can be deposited on top of the front contact to compensate the high sheet resistance of the TCO and to improve the current collection for large-area cells,

and the front contact can also be coated by anti-reflective coatings to reduce reflection losses.[18,19]

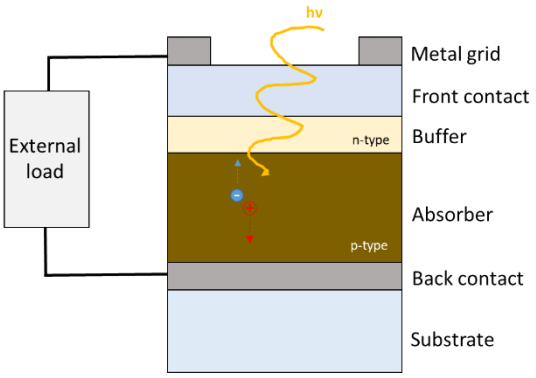

Figure 4. *Schematic representation of a typical p–n heterojunction thin film solar cell structure with substrate configuration. Blue-filled circles represent free electrons, while red-dashed circles represent holes.*

Since the absorber layer is central to the energy conversion process, it has to be carefully selected according to its properties. For a proper light absorption and carrier generation, it should have a direct band gap, a high absorption coefficient (> 10^4 cm^{-1}), a high carrier mobility, and low recombination rates. Focusing on the band gap, an absorber with a small E_g allows to maximize the number of absorbed photons, but the generated EHPs will relax quickly to empty states to E_C and E_V, and the excess energy will be lost as heat. An absorber with a high E_g allows to maximize the available energy per absorbed photon, but it will not absorb photons with smaller energies. In addition, it has to be taken into account the photon flux and the spectral irradiance of the Sun; which is composed by about 5% of UV light, 43% of visible light, and 52% of IR light. Thus, there exists an optimal E_g that leads to a maximum photovoltaic conversion efficiency, which is given by the Shockley–Queisser limit. This optimal E_g range is between 1.1 and 1.4 eV with maximum theoretical conversion efficiencies around 33%.[18,19]

In order to understand the concept of the photovoltaic conversion efficiency, some parameters that characterize a functional solar device must be introduced. First, the current density–voltage (J–V) characteristics indicate the net current flowing through the device and, in real conditions, it is defined by:[20]

$$J(V) = J_0 \cdot \left[exp\left(\frac{q_e \cdot V - q_e \cdot J \cdot R_S}{A \cdot k_B \cdot T}\right) - 1\right] + \frac{V - J \cdot R_S}{R_{sh}} - J_{ph} \quad (1)$$

where V is the voltage across the output terminals, J_0 is the reverse saturation current of the PN junction, q_e is the elementary charge, k_B is Boltzmann's constant, T is the temperature, and J_{ph} is the photocurrent. R_s is the series resistance that models all resistive losses due to the electrical resistance of the different layers and the contacts, and R_{sh} is the shunt resistance that models losses determined by alternative current paths or shunts in the device. Finally, A is the diode quality factor.

The maximum current density that can provide the solar cell is the short-circuit current density (J_{SC}), corresponding to the current achieved with short circuited terminals ($V = 0$). In the case of an ideal diode (no losses due to resistances or non-radiative recombination), it is equal to the photocurrent. The critical material parameter that determine J_{SC} is the diffusion length of the minority carriers, which is the average distance that minority carriers can travel before they recombine. The photocurrent, and thus the J_{SC} of an ideal solar cell, is given by:[21]

$$J_{ph} = q_e \cdot G \cdot (L_N + W_{SCR} + L_P) \quad (2)$$

where G is the carriers generation rate, L_N and L_P are the minority carriers diffusion lengths, and W_{SCR} is the width of the SCR.

The open-circuit voltage (V_{OC}) is the maximum voltage that can provide the solar cell, and corresponds to the voltage obtained when the device terminals are in open circuit ($J = 0$). In the case of an ideal device without resistive losses, the open circuit voltage is given by:[16]

$$V_{OC} = \frac{A \cdot k_B \cdot T}{q_e} \cdot ln\left(\frac{J_{ph}}{J_0} + 1\right) \quad (3)$$

The fill factor (FF) is the ratio between the maximum power that can be generated by the solar cell (P_{max}) and the maximum theoretical power (P_{theo}) defined by the product of the maximum current (J_{SC}) and the maximum voltage (V_{OC}):[16]

$$FF = \frac{P_{max}}{P_{theo}} = \frac{J_{mpp} \cdot V_{mpp}}{J_{SC} \cdot V_{OC}} \quad (4)$$

where J_{mpp} and V_{mpp} are the current density and the voltage corresponding to the optimal operation point with maximum power P_{max}.

Finally, the photovoltaic conversion efficiency (PCE) or energy conversion efficiency (η) is defined as the ratio between the maximum power generated by the solar cell and the incident illumination power (P_{in}). It indicates the performance of the solar cell, so it is the main parameter used for comparing different PV devices and for evaluating their quality as power generators. It can be expressed as:[16]

$$\eta = \frac{P_{max}}{P_{in}} = \frac{J_{SC} \cdot V_{OC} \cdot FF}{P_{in}} \quad (5)$$

In standard measuring conditions, P_{in} corresponds to the power extracted from the integration of the solar spectrum AM1.5G (~1000 W/m^2).

1.2.2. Existing photovoltaic technologies

Among the different PV technologies, the one based on crystalline silicon wafers dominates the market, and it is known as the first generation of solar cells.[22,23] In this technology, p–n homojunctions are usually formed by diffusing phosphorus (donor impurity) into the surface of a silicon wafer doped with boron (acceptor impurity), or vice versa. Silicon can be monocrystalline, which has a higher crystalline quality but it is more expensive, or multicrystalline, which is cheaper but it has a higher density of defects that reduce the performance.[23] The advantages of the crystalline silicon technology are its high energy conversion efficiencies (current record is 26.7%)[24], ease of fabrication, environmentally friendly traits, longevity, and resistance to rough ambient conditions.[22] However, silicon has an indirect band gap, which means that its VB top and its CB bottom have a different momentum value, and this leads to a low absorption coefficient; in consequence, thick absorber layers about 150-300 μm are required, which increases the fabrication costs due to the high amount of material employed and, in addition, increases the weight of the PV modules, something that makes it unsuitable for certain applications requiring low weight, mechanical flexibility and ability for adaptation to specific customized designs as required in advanced PV integration applications.[22,23]

These limitations of crystalline silicon technology promoted the development of thin film PV technology, also known as second generation PV technology, which is based on materials with direct band gap such as CdTe, amorphous silicon (a-Si), $CuIn_{1-x}Ga_xSe_2$ (CIGSe), and $Cu_2ZnSn(S_{1-x}Se_x)_4$ (CZTSSe).[11,22,23] Thanks to their high absorption coefficient, the thickness of the absorber layer can be reduced to less than 5 μm, which reduces the material consumption and, thus, the manufacturing costs. In addition, thin

film PV allows to employ a wide range of absorber materials, substrates, and deposition techniques, which opens the way for innovative applications requiring a higher degree of technological flexibility such as building-integrated PV (BIPV), vehicles-integrated PV (VIPV), space flight, wearables, or Internet of things, among others.[11,23,25] In the case of chalcogenide technologies, CIGSe and CdTe are already at industrial production stages and have achieved high efficiency record values at cell level (23.35% for CIGS, 22.1% for CdTe) which are comparable to the values achieved with Si technologies.[11,22–24] The current disadvantages of these technologies are related to the existence of a relatively high gap between the efficiencies achieved at cell and module level,[26] and the use of scarce and/or toxic elements as In, Ga, Cd, Te. Emerging kesterite technologies as those based on CZTSSe compounds have been proposed as a more sustainable alternative to CIGSe and CdTe as they avoid the use of critical raw materials, but they are in a less matures level of development, with a record efficiency value of 13.6%.[24] The potential of these technologies for the development of high efficiency devices with lower fabrication costs and a high technological flexibility justifies the strong interest in their research.

The will for increasing the efficiency of solar cells and reducing the cost per Watt resulted in a third generation of PV technology based on novel concepts, materials and device architectures, such as tandem and multi-junction solar cells, quantum dots, concentrator systems, hot carrier cells, and perovskite-based cells, among others. Tandem and multijunction technologies have the potential to achieve energy conversion efficiencies that exceed the single junction Shockley–Queisser limit, even up to 66%, but current technologies are based on the use of very expensive molecular bean epitaxy (MBE) processes and the combination of thin film low cost processes with tandem/multi-junction device concepts is still in an immature stage of development.[27,28]

1.2.3. Details on thin film solar cells

This thesis is focused on thin film chalcogenide PV technologies due to their potential advantages with respect to the traditional crystalline silicon technologies and because the further improvement of these technologies and the full exploitation of their efficiency and low cost potential can only be achieved with an intensive and systematic research on the current main limitations of the device performance.

The typical structure of a chalcogenide thin film solar cells is represented in Figure 5. Usually, soda-lime glass (SLG) of 3–4 mm thickness is employed as substrate, as it is

thermally stable, chemically inert, has a similar thermal expansion coefficient as the absorber, a smooth surface, and insulating properties suitable for monolithic interconnection. It can also supply alkali doping elements to the absorber, something required for achieving high efficiencies.[25] SLG is a rigid substrate, but flexible substrates can also be employed such as metal foils or polymer films.[22,25] Then, molybdenum layer is the mostly used back contact, which is normally partially selenized during the absorber synthesis and originates an intermediate $Mo(Se/S/S,Se)_2$ layer. Thus, metallic Mo acts as a reflector of most unabsorbed light, while chalcogenided part serves as a quasi-ohmic contact with the absorber.[22,25] Alternatively, TCOs such as fluorine-doped tin oxide (FTO), or indium tin oxide (ITO) can be employed as transparent back contacts for specific applications such as BIPV, bifacial solar cells, or tandem solar cells.[29] Regarding the absorber, the main materials employed for thin film PV devices are chalcopyrites (such as CIGSe), CdTe, kesterites (such as CZTSSe), and Sb_2Se_3; and there are various physical or chemical methods to grow them.[11,22] Afterwards, the buffer layer is typically deposited by chemical bath deposition (CBD) or atomic layer deposition (ALD). The mostly used buffer layer is CdS (with the typical thickness of ~50 nm), since it offers a suitable conduction band alignment to the most of absorbers used in thin film solar cells, but its relatively narrow band gap (~2.4 eV) produces J_{SC} losses due to parasitic absorption of the light, and it employs toxic Cd and thiourea (CH_4N_2S) for some deposition processes.[22,25] Consequently, Cd-free alternatives such as $Zn(S,O,OH)_x$, $Zn_{1-x}Mg_xO$, In_2S_3, $Zn_{1-x}Sn_xO$, ZnO, ZnS, $ZnO_{1-x}S_x$, and $Zn_{1-x}Cd_xS$ have been studied.[25,29] In fact, the current efficiency record for thin film chalcogenide solar cells was achieved by means of a double buffer layer of $Zn(O,S,OH)_x$ (~50 nm) deposited by CBD and $Zn_{0.75}Mg_{0.25}O$ (~50 nm) deposited by atomic layer deposition (ALD).[30] Finally, the front contact usually consists of an intrinsic ZnO layer covered by a transparent conductive oxide layer (Al-doped ZnO (AZO), ITO, etc.), which are commonly deposited by sputtering.[22,25,29] The role of the intrinsic ZnO layer consists in avoiding possible shunt paths in the solar cell that would produce power losses. If the absorber surface is not smooth, there might be regions where the CdS does not cover the absorber properly. In this case, the TCO layer directly deposited on the CdS would result in regions with a direct contact between the absorber and the front contact, which would result in a large band gap discontinuity and V_{OC} losses. Thanks to the high resistance of intrinsic ZnO, its deposition prevents the circulation of the electric current from the absorber directly to the TCO layer, and this mitigates the V_{OC} losses. In addition, intrinsic ZnO also protects the

CdS layer during the TCO sputtering deposition.[31,32] Regarding the TCO layers, it acts as front contact for conducting the current to the external circuit. One of the most used TCOs is AZO, but it has relatively low mobility (<30 $cm^2V^{-1}s^{-1}$), so it has to be heavily doped to achieve the necessary conductivity, which originates optical losses in the visible and near-infrared (NIR) by free carrier absorption.[25] Alternative front contacts are boron-doped ZnO (which is the one employed in the solar cell with the current efficiency record for thin film chalcogenides), hydrogenated indium oxide, indium zinc oxide, FTO, and ITO.[22,25,29,30] Additionally, a metallic electrode such as Al and an anti-reflective coating (ARC) such as MgF_2 can be applied on top of the solar cells, which improves the charge extraction efficiency and reduces the light loss due to reflections, respectively.[22,29]

Taking into account the structure of a thin film solar cell, carriers generated in the absorber must cross the interfaces between the different layers before they are extracted and power is generated, so the properties of such interfaces play a critical role in the performance of the devices. Specifically, the absorber interfaces determine the separation, transport, extraction, and recombination of the carriers, which are controlled by interface properties such as the band alignment, the position of the VB maximum and the CB minimum, the elemental intermixing, and the presence of secondary phases, among others.[33,34] The front interface between the absorber and the buffer layer acts as the p–n junction that separates the carriers to prevent their recombination. The main limitations that affect the device performance located at this interface are non-optimum band alignment,[35–39] Fermi level pinning due to antisite point defects,[40] incomplete buffer layer coverage,[41–43] high density of interface defects,[44,45] as well as secondary phase formation.[46] Then, the back interface between the absorber and the back contact is responsible for extracting the charge carriers to the back contact. The main limitations at this interface are related to a defective coupling with the back contact,[47,48] chemical instability,[49,50] as well as an unfavorable back band alignment.[51–53] In thin film solar cells, the density of interface defect states at the interfaces is high due to the combination of dissimilar materials, which results in high recombination velocities at such regions.[34] While some studies indicate that the device performance in different thin film solar cells is dominated by the properties of the absorber bulk,[54,55] other studies defend that it is dominated by the properties of the interfaces or the region near them.[56–59] In fact, studies that report record efficiencies for chalcopyrite and kesterite-based solar cells suggest that optimizing the interfaces is the best strategy to further improving the device

efficiency.[30,60] In addition, the properties at the interfaces differ from the absorber bulk properties in terms of stoichiometry, presence of secondary phases, and presence of unexpected elements that may diffuse from other layers, which means that a special attention should be paid to the solar cell interfaces together with the bulk analysis, and the study should be made using techniques that allow to directly probe these specific regions.[33] Thus, after an initial understanding of the bulk properties of the absorber layers, this thesis is focused on the study of the absorber interfaces due to the important impact of their properties on the solar cells performance, which implies the need for the development of suitable characterization methodologies allowing the high sensitivity analysis of the interfaces.

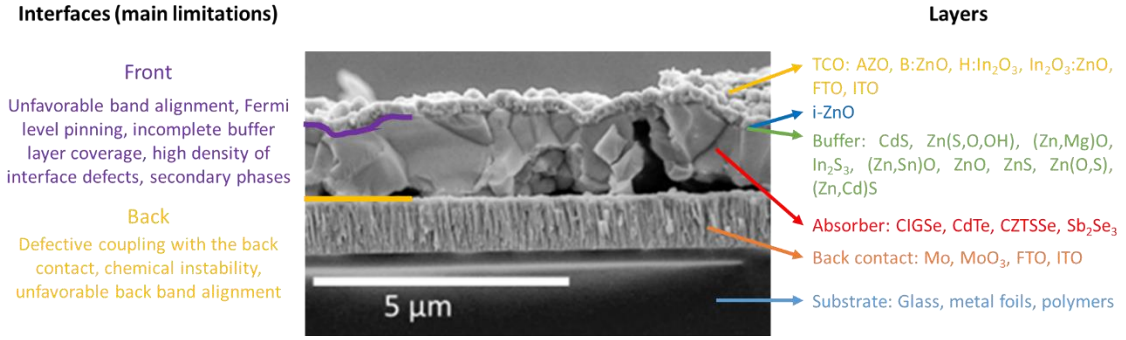

Figure 5. *Typical structure of a chalcogenide thin film solar cell. Absorber interfaces and their main limitations influencing the device performance (left), and the possible materials for the different layers (right) are indicated.*

In this thesis the study of thin film solar cells is focused on chalcogenide absorbers; specifically, solar cells based on chalcopyrite and kesterite absorbers. Both chalcopyrite and kesterite structures derive from the zinc-blende structure. For example, chalcopyrite $CuInSe_2$ (CISe) structure can be derived from the ZnSe one by alternately replacing Zn^{2+} cations by Cu^{+} and In^{3+} cations,[23] while kesterite $Cu_2ZnSnSe_4$ (CZTSe) structure can be derived from CISe structure by alternately replacing In^{3+} cations by Zn^{2+} and Sn^{4+} cations.[61] Both chalcopyrite and kesterite absorbers can be doped with native defects (usually using the off-stoichiometric chemical compositions) without introducing extrinsic impurities, something that silicon does not offer. In consequence, both materials present mainly p-type electrical conductivity due to typical intrinsic defects in their structure. Regarding the band gap, it can be tuned for both absorbers by partial or total replacement of some of the elements. For example, chalcopyrite compounds such as CISe, $CuInS_2$ (CIS), $CuGaSe_2$ (CGSe), and $CuGaS_2$ (CGS) present band gaps of 1.04 eV, 1.5 eV, 1.7 eV, and 2.4 eV, respectively;[23] while the band gaps of kesterite compounds

such as CZTSe and Cu_2ZnSnS_4 (CZTS) are 1.0 eV and 1.5 eV, respectively.[62,63] In addition to being tunable, both materials present a direct band gap, which produces a high absorption coefficient in the order of 10^4–10^5 cm^{-1} in the visible range, which allows to keep the absorber thicknesses between 1 and 2 μm, about 100 times smaller than in the case of crystalline silicon.[23,64,65] This opens the way to the deposition of chalcopyrite and kesterite absorbers on flexible substrates, which has advantages for manufacturing (large area roll-to-roll deposition is possible) and allows the development of solar modules with a customized design suitable to advanced integration applications in different fields such as BIPV, VIPV, Internet of things, and others. In addition to flexible substrates, solar modules based on these absorbers can be laminated directly onto metallic building elements. Thus, flexibility in shape, power rating, and form factor are the main advantages of chalcopyrite and kesterite technologies with respect to traditional rigid and heavier Si-based PV technology.[23,25] Additional applications have been demonstrated for these materials such as top cell in tandem devices, photocatalyst, photodetector, thermoelectric device, and gas sensor.[64]

Despite their similarities, chalcopyrite and kesterite-based solar cells present some notable differences. First of all, chalcopyrite is part of the I-III-VI_2 semiconductor materials and kesterite belongs to the I_2-II-IV-VI_4 family.[23,66] Chalcopyrite technology is in a more mature stage, since the first CISe-based solar cell was fabricated in 1976,[22] while the first CZTS-based solar cell was fabricated in 1997.[67] This is translated in different device performances between both materials. CIGSe absorber has produced the highest energy conversion efficiency among thin film chalcogenide solar cells (23.35%)[24], but the record efficiency of kesterite-based solar cells is 13.6%.[24] In consequence, chalcopyrite technology has been commercialized and it represented 1.9% of the global PV production in 2019,[22] with commercial modules in the order of 14% efficiency,[23] while kesterite technology has not been commercialized yet.[63] In spite of the previous advantages, chalcopyrite presents the limitation of containing indium and gallium, which are scarce materials, so their availability is lower and their cost higher.[11,22,63] In contrast, kesterite absorbers are composed of earth-abundant and non-toxic elements, which represents a benefit in terms of economical cost and environmental impact.[63,64]

Taking into account the previous characteristics, the study of chalcopyrite-based solar cells is important because they have achieved the highest device performance among

thin film solar cell technologies, so they hold the lead as alternative materials to silicon in terms of performance and they can open new markets for PV, related to their higher technological flexibility. Regarding kesterite-based solar cells, they are a promising earth-abundant and non-toxic alternative, so their study is important to improve their energy conversion efficiency to levels similar to those achieved with CIGSe and CdTe. This implies the need for an intense activity in the advanced characterization of the materials and devices, including the detailed characterization of the device interfaces that are critical for device performance.

1.3. Techniques for characterizing interfaces of thin film solar cells

For both chalcopyrite and kesterite-based solar cells, one of the employed strategies for improving the device performance is related to the modification of the regions near the absorber interfaces, which are the front interface between the absorber and the buffer layer and the back interface between the absorber and the back contact. As already indicated, these regions play an important role in the device operation since the separation and extraction of carriers takes place in there. In consequence, characterization techniques that allow the study of such interfaces are fundamental to the research and further development of these technologies.

The possibility of obtaining information from the absorber interfaces depends on the analysis depth of the characterization technique, which is represented in Figure 6 for some common techniques. Atomic force microscopy (AFM) and scanning probe microscopy (SPM) offer the lowest analysis depths, around 0.1 Å.[68] The sampling depths for time-of-flight secondary ion mass spectroscopy (TOF-SIMS) and ion scattering spectroscopy (ISS) are lower than 3 Å.[68] In the case of Auger electron spectroscopy (AES) and X-ray photoelectron spectroscopy (XPS), the analysed depths are up to 10 nm.[68,69] These characterization techniques are considered to be able to provide information from just the actual interfaces. Characterization techniques with an analysis depth in the order of 100 nm can provide information from both the interfaces and from the regions of the layers close to these interfaces. This is the case of scanning electron microscopy (SEM), energy dispersive X-ray spectroscopy (EDX), and Raman spectroscopy.[68,69] Then, there are techniques such as X-ray diffraction (XRD), X-ray fluorescence (XRF), and SIMS, that have sampling depths typically larger than 1 μm. These techniques are not considered to be useful for studying the absorber interfaces since the information coming from there is negligible compared to the one coming from the bulk of the absorber.[68,69] Nevertheless,

it has to be taken into account that the presented values are average values; the analysis depth of a technique varies depending on the experimental conditions such as the accelerating voltage of the electron beam, the excitation wavelength, or the sample properties like density and absorption coefficient, among others.[68,69]

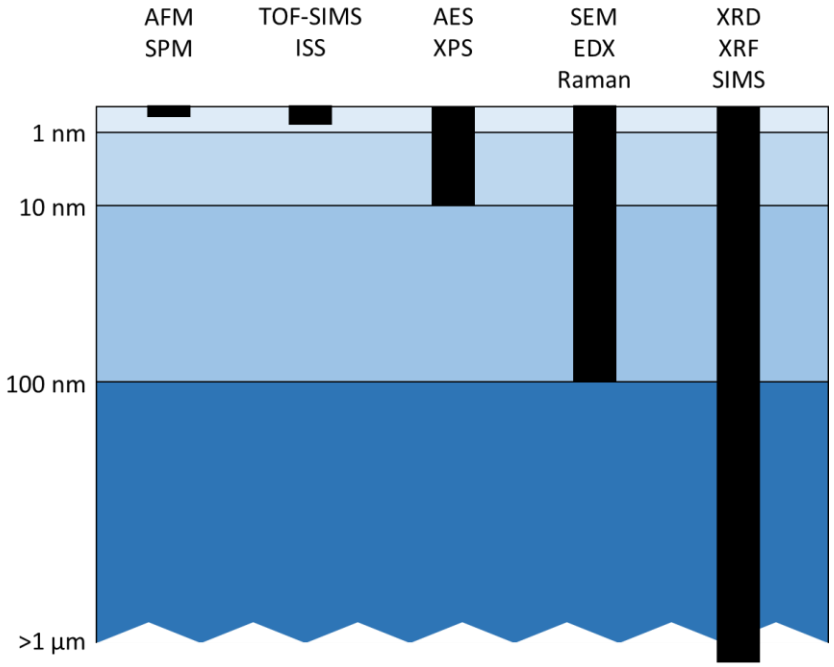

***Figure 6**. Typical analysis depths for common materials characterization techniques: atomic force microscopy (AFM), scanning probe microscopy (SPM), time-of-flight secondary ion mass spectroscopy (TOF-SIMS), ion scattering spectroscopy (ISS), Auger electron spectroscopy (AES), X-ray photoelectron spectroscopy (XPS), scanning electron microscopy (SEM), energy dispersive X-ray spectroscopy (EDX), Raman spectroscopy, X-ray diffraction (XRD), X-ray fluorescence (XRF), and SIMS.*

The above discussions clearly show that there is a variety of techniques that allow assessing the absorber interfaces due to their different penetration depth. However, to define the depth of an interface or the depth that has a relevant contribution to the specific parameters of an interface is not that straightforward. In this thesis, the term "interface" is referred mainly to a region around 100 nm from the actual edge of the absorber, and most of the obtained results show that the performance of the solar cells is strongly influenced by the properties of this region. Taking this into account, the main characterization technique employed in this work is Raman spectroscopy, since, in addition to other advantages described in the next Sub-Section, its analysis depth is comparable to 100 nm for most of the used excitation wavelengths (from UV and visible ranges), so it provides information from the region of interest, including the actual interface. Data acquired by SEM, AES, and XPS are also analyzed in this work, since

they allow measurements in the region of interest, as shown in Figure 6. Other techniques able to characterize actual interfaces such as AFM, SPM, TOF-SIMS and ISS are not employed in this work due to lack of access to the systems required for such measurements. Then, capacitance spectroscopy is extensively applied in this thesis since it provides information regarding the electronic properties of the SCR, which is also an important region of the absorber.[70,71] Transmittance techniques such as optical transmittance spectroscopy and transmission electron microscopy (TEM) are also applied because, with a proper sample preparation, they can also provide relevant information of the absorber interfaces. Finally, photoluminescence (PL) spectroscopy, *J–V* characteristics, XRF and XRD are applied because they provide global information about the material and the devices that can complement the interface information obtained by other techniques; in addition, the correlation between the data acquired by different techniques is fundamental to achieve a deeper understanding of the impact of the interfaces properties on the global properties of the solar cell.

1.3.1. Raman spectroscopy

Raman spectroscopy consists in exciting the sample with photons with a specific wavelength and, then, measuring the frequency variation of the photons inelastically scattered by the sample. It is the main characterization technique employed in this thesis due to several advantages. First, it is a fast and non-destructive technique that does not require any specific sample preparation, which makes it compatible with both laboratory and industrial scales, and allows to perform measurements of statistically relevant number of samples. Then, it offers a high lateral resolution (by performing mappings and/or by applying a macro configuration) and a relatively high depth resolution (by applying different excitation wavelengths). Finally, it provides information related to the structural, compositional, phase and even electrical properties of the sample. The frequency, intensity and shape of the Raman bands are associated to the atoms vibrations in the crystalline lattice, which indirectly depend on physical and chemical factors such as the chemical composition, the crystallographic structure, the presence of impurities, the stress, or crystalline defects.[72] In the field of thin film solar cells, it the use of Raman spectroscopy has been extensively reported for evaluating the composition,[73–80] the lateral homogeneity,[81] the crystalline quality,[82,83] and the presence of structural defects[78,83–85] of the absorber and other layers for different materials. In addition, presence of peaks characteristic of different phases allows the identification of secondary phases.[72,81,86] The

employment of different excitation wavelengths allows to selectively enhance Raman modes of different phases due to resonant effect,[87–91] which represents an advantage with respect to other standard techniques such as XRD; moreover, resonant Raman spectroscopy allows to detect secondary phases located at the absorber surface in very low concentrations that would not be detected by XRD.[84] With a proper analysis, information about the formation mechanism of the compounds can be obtained from Raman spectra,[88,92,93] as well as the optimum synthesis conditions and post-deposition treatments (PDTs).[81,83,94–96] In consequence, Raman spectroscopy is a powerful technique that can be employed for optimizing the material properties and, thus, improving the performance of thin film solar cells.

In addition to the advanced characterization, Raman spectroscopy can also be employed for developing process monitoring methodologies. The objective of process monitoring is to detect deviations of a characteristic parameter from its acceptable behavior before they produce failures or malfunctions in the final products so the necessary correction can be applied in the process.[97] In order to detect the deviations, data-based methods are developed consisting in collecting high statistics of data from the monitored process and applying analytical or machine learning (ML) methods to develop a reference empirical model that mimics the expected behavior of the process. Finally, this model is used for detecting deviations in new data, and this can be done quantitatively or qualitatively.[97] The fabrication of thin film solar cells involves many production steps and monitoring these steps would help to increase production yield, reduce production cost, and lead to a tight control on product specifications. However, the techniques employed in the process monitoring of PV devices must fulfill some requirements. First, the technique must be compatible with large-area measurements, since solar modules at the industrial scale have areas in the order of m^2 and the influence of inhomogeneities must be taken into account. Then, the rough and textured surface of solar cells prevents to apply specular measurements. In addition, the measurement systems must be simple and low cost, and the measurements must be fast and in real time conditions.[98] Taking into account the previous requirements, contactless and non-destructive optical techniques such as Raman spectroscopy are the most suitable ones for monitoring the production of PV devices.

1.3.1.1. Classical theory

The understanding of Raman spectroscopy according to the classical theory starts with the fact that light is an electromagnetic radiation. When the photons of the excitation light interact with atoms of a semiconductor material, these atoms redistribute their electrical charge due to the presence of the externally applied electric field of the light. This creates an internal electric field (polarization) to compensate the external field. Additionally, in a semiconductor crystal at temperatures above 0 K, atoms oscillate around their equilibrium positions with a characteristic frequency ω_{phon}, and such periodic oscillations produce radiative polarization fields oscillating at a frequency different to the one of the external electric field. In consequence, the polarization density generated by the excitation light when interacting with the atoms can be expressed as:

$$\vec{P} = \vec{P}_{elastic} + \vec{P}_{anti-Stokes} + \vec{P}_{Stokes} \tag{6}$$

being $\vec{P}_{\text{elastic}}$ the contribution due to the elastic scattering of the light, $\vec{P}_{\text{anti-Stokes}}$ the contribution due to the anti-Stokes scattered light, and $\vec{P}_{\text{Stokes}}$ the contribution due to the Stokes scattered light. These contributions can be expressed as:[72,99]

$$\vec{P}_{elastic} = \chi \cdot \vec{E}^0_{exc} \cdot \cos\left(\vec{k}_{exc} \cdot \vec{r} - \omega_{exc} \cdot t\right) \tag{7}$$

$$\vec{P}_{anti-Stokes} = \left(\frac{\partial \chi}{\partial Q^j}\right) \cdot Q^j \cdot \vec{E}^0_{exc} \cdot \cos\left[\left(\vec{k}_{exc} + \vec{q}\right) \cdot \vec{r} - \left(\omega_{exc} + \omega_{phon}\right) \cdot t\right] \tag{8}$$

$$\vec{P}_{Stokes} = \left(\frac{\partial \chi}{\partial Q^j}\right) \cdot Q^j \cdot \vec{E}^0_{exc} \cdot \cos\left[\left(\vec{k}_{exc} - \vec{q}\right) \cdot \vec{r} - \left(\omega_{exc} - \omega_{phon}\right) \cdot t\right] \tag{9}$$

where χ is the electrical susceptibility of the sample, which may be interpreted as the density of electric dipoles per unit volume. $\vec{E}^0_{\text{exc}}$ is the amplitude of the electric field from the incident electromagnetic wave (excitation light) with wavevector $\vec{k}_{\text{exc}}$ and frequency ω_{exc}. $\vec{r}$ is the atom position and t is the time. Then, Q^j are the coordinates of the plane wave $\vec{Q}$ over the three crystallographic directions. This $\vec{Q}$ vector is associated to the collective oscillation modes of the atoms, also known as phonons, and it has a wavevector $\vec{q}$ and a frequency ω_{phon}. In addition, the electrical susceptibility and the atomic oscillations vector can be expressed as:[72,99]

$$\chi = \chi_0 + \left(\frac{\partial \chi}{\partial Q^j}\right) \cdot Q^j \tag{10}$$

$$\vec{Q} = \vec{Q}^0 \cdot \cos\left(\vec{q} \cdot \vec{r} - \omega_{phon} \cdot t\right) \quad (11)$$

As seen in Equation 6, light scattered by the atoms contains an elastic contribution, also called Rayleigh scattering, and two inelastic contributions, which are the ones responsible for the Raman scattering. Typically, the Raman signal is 10^6–10^9 times less intense than the Rayleigh signal. Regarding the two inelastic contributions (Stokes and anti-Stokes), they are symmetrically shifted in frequency with respect to the frequency of the excitation light, as shown in Figure 7. Since the information that they provide is redundant, usually only the Stokes component is analyzed, because its intensity is higher than the anti-Stokes one. For both Stokes and anti-Stokes scattering, the magnitude of the shift (ω) with respect to the Rayleigh or excitation wavelength value is known as Raman shift, and it is equal to the vibration frequency of the atoms in the crystal. The Raman shift is usually expressed as a wave number in cm^{-1}:[72]

$$\omega = \frac{1}{\lambda_{scatt}} - \frac{1}{\lambda_{exc}} \quad (12)$$

where λ_{exc} is the wavelength of the excitation light and λ_{scatt} is the wavelength of the scattered light, both of them expressed in cm.

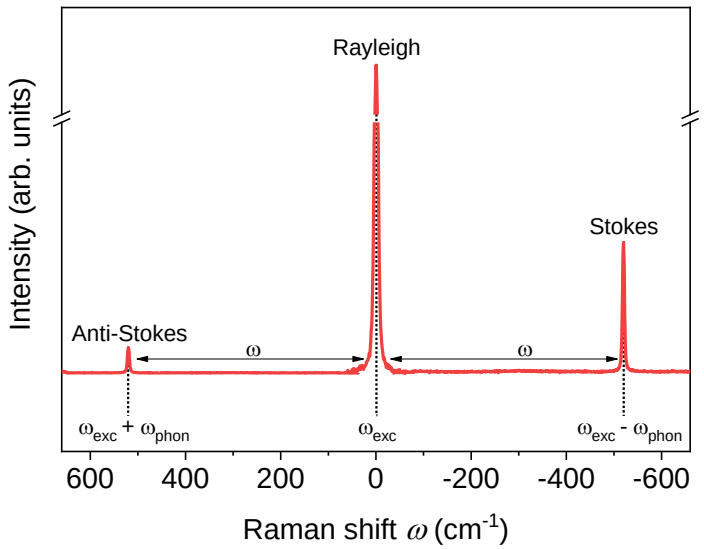

Figure 7. *Example of Raman spectra indicating the different contributions: the Rayleigh one corresponds to elastic scattering with the same frequency as the excitation light (ω_{exc}); the anti-Stokes and Stokes ones correspond to inelastic scattering with increase and decrease of frequency, respectively, equal to the vibration frequency of the atoms in the crystal (ω_{phon}). This frequency shift is known as Raman shift (ω).*

In Equations 7, 8, and 9, it is assumed that all the atoms in the crystal oscillate at the same frequency, but, in real crystals, there exist multiple collective oscillation modes or phonons. Consequently, the band structure of Raman spectra is usually complex, although some restrictions reduce such complexity. First, the energy balance in the scattering process must be preserved due to the energy conservation law. Then, the conservation of the crystalline quasi-momentum imposes that the difference between the wavevectors of the excitation and scattered photons must be equal to the wavevector of the phonon involved in the process. Furthermore, the energy of visible photons is about three orders of magnitude greater than the typical phonon energy, so inelastic scattering usually occurs without significant changes in the photon energy and in its wavevector module. Thus, phonons involved in inelastic scattering processes must have a wavevector module close to zero ($|\vec{q}| = 0$). According to these conservation laws, the Stokes process is interpreted as the creation of a phonon by the incident photon, and this results in a scattered photon with lower energy, while the anti-Stokes process corresponds to the annihilation of a phonon by the incident photon, resulting in a scattered photon with higher energy, as shown in Figure 8.[72]

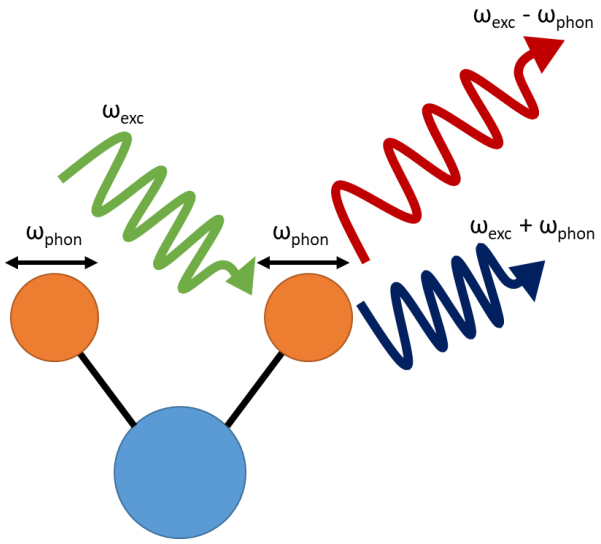

Figure 8. *Schematic representation of the Raman scattering according to the classical theory. ω_{exc} is the frequency of the incident photon, while ω_{phon} is the vibrational frequency of the atom. Photons with lower (ω_{exc} - ω_{phon}) and higher (ω_{exc} + ω_{phon}) frequencies are produced by Stokes and anti-Stokes scattering, respectively.*

In addition, the previous conservation laws allow predicting the number of optically active bands for any crystalline structure. Raman active phonons correspond to long-wave oscillation modes (or Brillouin zone-center phonons), which involves the displacement

of all the equivalent atomic positions in the crystal. Therefore, the number of optical vibrational modes in three-dimensional crystalline structures is $3N - 3$, where N is the number of atoms in the crystal base or unit cell. Further restrictions can be applied depending on the symmetry characteristics of the crystalline structure. For example, optically active modes that are symmetrically equivalent produce Raman modes with the same frequency, which are called degenerate modes. Then, if atoms are displaced, the terms in the derivative of the electrical susceptibility are null $\left(\frac{\partial \chi}{\partial Q^j} = 0\right)$ or they cancel each other, and the corresponding vibrational modes present no Raman activity. Furthermore, asymmetric displacements of ions in the lattice, known as polar oscillation modes, originate a net electric field over the crystal and, in turn, a splitting of the phonons with propagation vector parallel (longitudinal) and perpendicular (transverse) to the electric field. This splitting is known as LO–TO splitting, and it produces two bands for each polar mode occurring at different frequencies.[72]

Taking into account the dependency of the Raman spectrum with the frequency and the selection rules due to the conservation laws, the intensity of Raman bands originated by Stokes scattering depends on molecular and experimental parameters as follows:[99]

$$I_{Stokes} \propto \left(\frac{\partial \chi}{\partial Q^j}\right)^2 \cdot \left(\omega_{exc} - \omega_{phon}\right)^4 \cdot (E^0_{exc})^2 \qquad (13)$$

Equation 13 shows that the intensity of Raman bands provides molecular information such as $\left(\frac{\partial \chi}{\partial Q^j}\right)$ and ω_{phon}, while it can be controlled by experimental parameters such as ω_{exc} and E^0_{exc}. In consequence, increasing the frequency (shorter wavelengths) and the power of the excitation light results in more intense bands in the Raman spectrum.

1.3.1.2. Quantum theory

So far, Raman spectroscopy has been discussed according to the classical theory, but this approach does not offer a connection between the Raman scattering tensor and the transition dipole moments, the molecular Hamiltonian, and the frequency of the incident field. Thus, a quantum theory approach has to be considered. In this approach, the vibrational energy of a molecule is quantized as:[100]

$$E_{phon} = h \cdot \omega_{phon} \cdot \left(v + \frac{1}{2}\right) \qquad (14)$$

where *h* is the Planck constant and *v* is the vibrational quantum number having values of 0, 1, 2, 3, etc.

The quantum approach applies perturbations to the ground state molecular wavefunctions. The transition from ground state is achieved via a perturbing wavefunction, which is the sum of the applied perturbations. This perturbing wavefunction has a corresponding energy, so the vibrational transitions occur via this virtual energy level, as shown in Figure 9, which is characterized by an unmeasurably small life time ($<10^{-15}$ s). According to this, the Rayleigh scattering corresponds to transitions that start and finish at the same vibrational energy level, so the scattered photon has the same frequency than the incident one. Stokes scattering corresponds to transitions that start at the ground state vibrational energy level and finish at a higher level, while anti-Stokes scattering involves transitions from a higher to a lower vibrational energy level. In consequence, the scattered photon has a lower frequency than the incident one for Stokes scattering, while for anti-Stokes scattering the frequency of the scattered photon is higher. At room temperature, most molecular vibrations are at the ground state (v = 0), so anti-Stokes transitions are less likely to occur than the Stokes ones, which explains the higher signal intensity of the latter.[100]

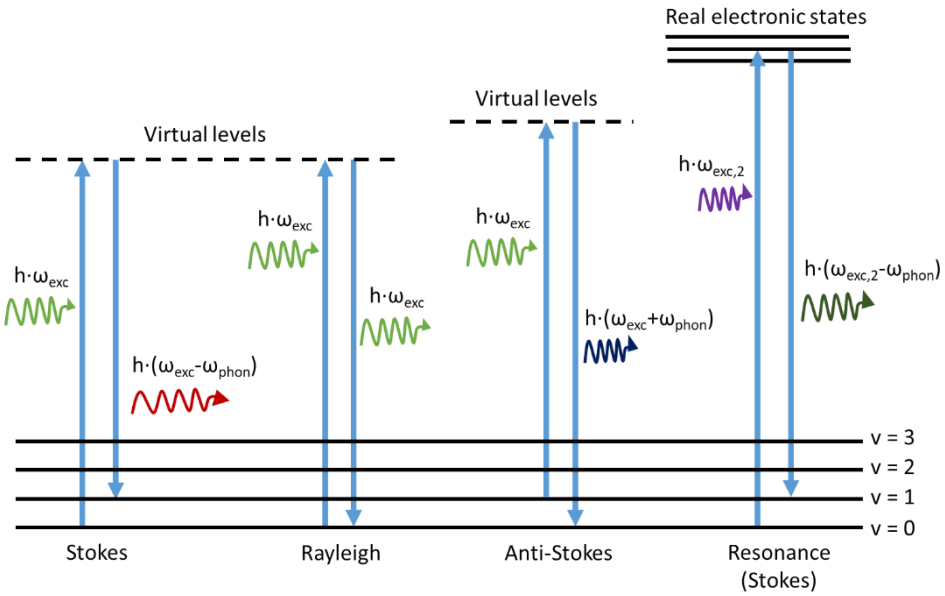

Figure 9. *Schematic representation of the Raman scattering according to the quantum theory. All vibrational energy levels have the same frequency (ω_{phon}), but different vibrational quantum number (v). h is the Planck constant, ω_{exc} is the frequency of the incident photon, and $\omega_{exc,2}$ is the frequency of an incident photon with enough energy for promoting an electron to excited electronic states.*

This quantum approach allows to explain the resonant Raman scattering, where the excitation wavelength falls within an electronic absorption of the sample. Thus, instead of a virtual level, the vibrational transition is achieved via real electronic states, as shown in the right part of Figure 9. While non-resonant Raman involves only vibrational transitions (different vibrational energy levels of the same electronic state), resonant Raman involves also electronic transitions. In consequence, non-resonant Raman is limited to the study of ground-state structures of molecules, but resonant Raman allows the study of electronically excited states, thus providing information about the electron-phonon interaction, the electron-radiation interaction, and the electron band structure. Additionally, resonance increases the intensity of the scattered light by up to eight orders of magnitude with respect to the non-resonant signal. This improves considerably the signal-to-noise ratio and allows the detection of phases present in very low concentrations that would not be detected by other techniques such as XRD.[99]

The explanation of Raman spectroscopy by the quantum theory approach provided here is elementary and a deeper understanding of it is outside the scope of this thesis. However, detailed discussions can be found in Refs. 101 and 102, among other books.

1.3.1.3. Mulliken notation

As previously said, Raman active bands, which involve modes at the Brillouin zone center (Γ point), can be predicted by applying the different selection rules. The irreducible representation of the optical Γ-point modes is usually expressed by applying the Mulliken notation.[103,104] This notation has been introduced for easier presentation of different vibrations in the crystalline system and consists of letters (*A*, *B*, *E* or *F* (*T* in the old notations)), subscript (numbers or letters) and superscript (prime or double prime) signs. According to this notation, *A* and *B* represent non-degenerate, one-dimensional modes, so only one set of atom displacements exists for a given frequency ω; *E* represents doubly degenerate, two-dimensional modes, so two sets of atom displacements exist for a given frequency ω; and *F* represent triply degenerate, three-dimensional modes, so three sets of atom displacements exist for a given frequency ω. Regarding the non-degenerate modes, *A* represents symmetric modes with respect to the principal rotation axis, while *B* represents antisymmetric modes with respect to such axis. Then, *g* and *u* subscripts indicate symmetric and antisymmetric modes with respect to a center of symmetry (inversion), respectively. In addition, symmetric modes with respect to an axis that is perpendicular to the principal rotation axis are indicated by a subscripted number 1; when

there is no such axis, the subscript indicates that reflection in a plane of symmetry is symmetric. If the modes are antisymmetric with respect to an axis that is perpendicular to the principal rotation axis, they are indicated by a subscripted number 2; when there is no such axis, the subscript indicates that reflection in a plane of symmetry is antisymmetric. Finally, prime (′) and double prime (″) symbols indicate symmetric and antisymmetric modes, respectively, with respect to reflection in a horizontal plane of symmetry.[105]

For example, the unit cell in chalcopyrite structures such as CISe, CIS, or CGSe is occupied by two formula units (N = 8), leading to a total of 21 optical vibrational modes according to $3N - 3$. These modes are classified according to the symmetry of the atomic displacements, and expressed in group theory notation as:[72]

$$\Gamma_{opt} = A_1 \oplus 2A_2 \oplus 3B_1 \oplus 3B_2 \oplus 6E \quad (15)$$

Therefore, in this case, the 21 optical vibrational modes are grouped into nine non-degenerate modes and six double degenerate modes. In addition, there are three symmetric modes and six anti-symmetric modes with respect to the principal rotation axis. There are also four symmetric modes and five anti-symmetric modes with respect to an axis that is perpendicular to the principal rotation axis or there is a plane where the reflections are symmetric and anti-symmetric, respectively.

In the case of kesterite structures such as CZTSe or CZTS, the unit cell also contains 8 atoms and the irreducible representation for the corresponding 21 zone-center phonon modes is:[106]

$$\Gamma_{opt} = 3A \oplus 6B \oplus 6E \quad (16)$$

So, kesterite presents nine non-degenerate modes and six double degenerate modes. Three modes are symmetric and six are anti-symmetric. In order to make a more facile use of the Mulliken notation and present more detailed explanations of the vibrations that occur in the crystalline materials, as well as indication of LO-TO splitting of the modes, the detailed tables have been proposed and published by Porto et al. in Ref. 107.

1.3.1.4. Experimental setup

Generally, the setup of a Raman spectroscopy system consists of a light source, focusing and collection optics, a monochromator, and a detector.[72]

The light source in Raman spectroscopy usually emits coherent light. Since Raman is a scattering effect, the light is not absorbed by the sample and, in consequence, the source does not need to provide any broadband tunable light for matching the absorption features. In addition, due to the weaker signal of Raman effect with respect to the Rayleigh signal, sources with a high photon flux are needed to maximize the signal intensity. In consequence, continuous gas lasers and highly temperature stabilized solid-state lasers are the usual light sources.[72]

In order to focus the light on the sample and to collect the resulting scattered light, optical systems based either on conventional optical discrete elements or fiber optics are used, commonly in conjunction with beam-splitting optics.[72] Depending on the geometry of this optical system, different Raman spectroscopic configurations exist. In backscattering configuration, scattered light is collected at an angle of 180º with respect to the incident excitation light, and it offers a high reproducibility and efficiency.[108] In right angle (or transverse) configuration, the angle between the collected and the excitation light is 90º, and it offers a lower impact of parasitic signals from the system components and the atmosphere.[108] Angles between 180º and 90º can be used, for example in wide-angle illumination, to cover a wider surface area and to obtain a better representation of the sample.[109] In spatially offset Raman spectroscopy, the excitation and collected lights are parallel and there is a lateral distance between them, so surface interference is avoided.[109] Finally, in transmission Raman spectroscopy, the sample is illuminated on one side and the light is collected on the opposite side, and it offers a better representation of the bulk composition.[109] Additionally, the used optical components define the size of the measured spot, which can be in the range of 1 – 2 μm (micro-Raman) up to hundreds of microns (macro-Raman). In case of thin film solar cells that are formed by polycrystalline layers, this has a critical importance as collected information can be from a single grain (in case of micro-Raman) or an averaged information from the surface of tens or hundreds of grains (in case of macro-Raman).

The collected light is passed into a monochromator that disperses the light into its constituent wavelengths. The dispersive elements can be a diffraction grating, a prism or a simple bandpass filter. A single or a series of dispersion elements can be applied in a monochromator.[110] Then, the spectrum of the dispersed light can be detected by a photomultiplier or all at once using an array detector, which can be a charge-coupled device (CCD) or an indium gallium arsenide (InGaAs) detector. CCD detectors are based

on silicon and include several thousand active pixels for the light detection arranged in a rectangular shape, and they have a high responsivity from the near-ultraviolet to the NIR region of the spectrum (200 – 1100 nm).[111] Photons with longer wavelengths have less energy than the silicon band gap, so CCDs cannot detect them. However, since III-V materials have a lower band gap, InGaAs detectors are suitable for detecting photons in the 900 – 1700 nm range.[111] Due to its very weak signal, very sensitive detectors are required for Raman spectroscopy. A cooling of the active elements of the detectors is usually employed in order to increase the signal-to-noise ratio.

1.3.2. Additional techniques

In this thesis, the characterization by Raman spectroscopy of the device interfaces is complemented by additional techniques that provide information that allow improving our level of understanding of the materials and/or devices properties. Each one of these additional techniques is very powerful and, despite playing a supporting role in this thesis, they are equally important and useful for the scientific community as Raman spectroscopy. In fact, a proper characterization must not be limited to just one technique, but it has to employ several techniques that provide different information that complement and reinforce the data obtained by the other techniques. This statement makes a core of most of the articles collecting the results of this thesis.

1.3.2.1. Current density–voltage characteristics

J–*V* characteristics consists in applying a voltage sweep to the sample under illumination and measuring the voltage and the current. Thus, a *J*–*V* curve is obtained and its analysis provides the optoelectronic parameters that define the performance of the solar cell such as the V_{OC}, the J_{SC} and the FF, as shown in Figure 10, and from them the photovoltaic conversion efficiency η is derived. Illuminated *J*–*V* curves are usually measured at room temperature using simulated AM1.5 illumination (~1000 W/m^2) with a four-point probe geometry, where the current measurement is connected in series with a load resistance, while the voltage measurement are performed by using two separate probes.[21] By fitting a one- or two-diode model, or by comparing dark and illuminated *J*–*V* curves, it is possible to determine the series resistance and the diode quality factor of the device. In addition, performing temperature-dependent *J*–*V* measurements allows to distinct between the different recombination mechanisms occurring in the device.[21]

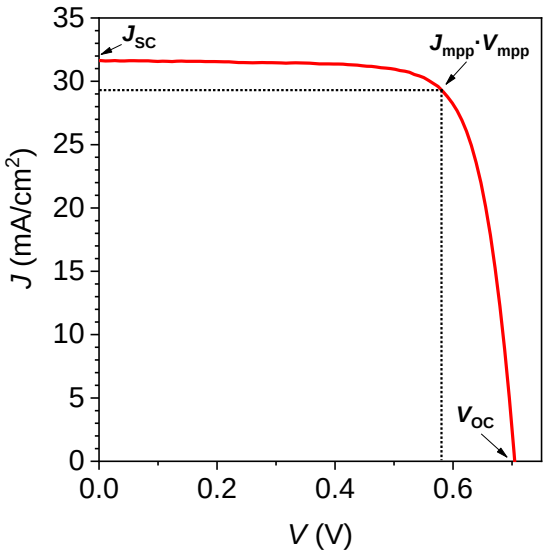

Figure 10. *Example of a current density–voltage curve. Short-circuit current density (J_{SC}), open-circuit voltage (V_{OC}), and current density and voltage at the maximum power point (J_{mpp} and V_{mpp}, respectively) are indicated.*

1.3.2.2. Photoluminescence spectroscopy

PL spectroscopy consists in disturbing the thermal equilibrium state of the sample by means of excitation light that is absorbed by the material and then by measuring the light emitted by the sample. PL radiation is caused by the transition of electrons from higher occupied electronic states into lower unoccupied states, which produces the emission of photons. In consequence, the energy of the excitation photons has to be sufficiently large to produce electronic transitions, something that was not required for non-resonant Raman spectroscopy.[112]

PL emissions can be of different types or related to different type of transitions shown in Figure 11. These are free exciton transitions, bound exciton transitions, donor–acceptor pair transitions, free-to-bound transitions, and band–band transitions. If the band structure is distorted by potential fluctuations due to local variations in the fixed space charge, transitions with significantly smaller energy than that of donor–acceptor pair and free-to-bound transitions can occur.[112] Evaluating the previous transitions require temperature-dependent PL measurements, since the characteristics of the associated emission bands depend on the temperature. However, at room temperature, the PL yield allows to estimate the V_{OC} of the solar cell, so PL spectroscopy can be employed for evaluating the electronic quality of the material without need of electrical contacts or

electrical measurement. In addition, spatial inhomogeneities of the sample can be investigated by means of PL performed with microscopic spatial resolution.[112]

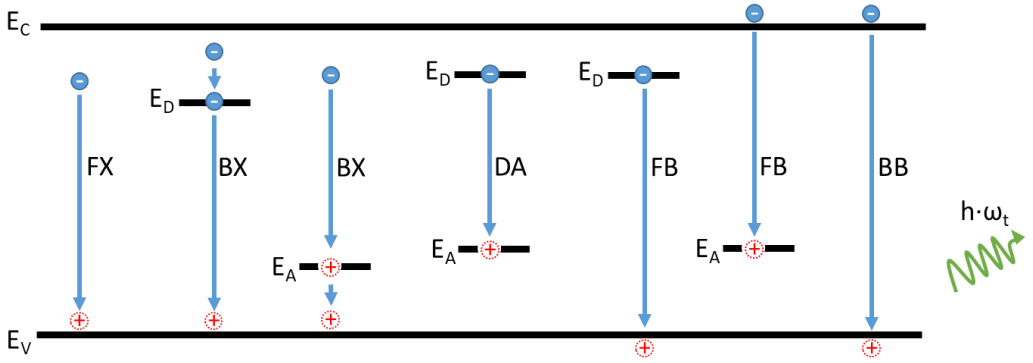

Figure 11. *Radiative transitions observable in photoluminescence measurements: free exciton transition (FX), bound exciton transitions (BX), donor–acceptor pair transition (DA), free-to-bound transitions (FB), and band–band transition (BB). Blue-filled circles represent electrons, while red-dashed circles represent holes. E_C and E_V are the energy values of the conduction band minimum and the valence band maximum, respectively; E_D and E_A are the energy values of donor and acceptor states, respectively. h is the Planck constant and ω_t is the frequency of the photon resulting from the previous transition.*

1.3.2.3. Transmittance and reflectance spectroscopy

Transmittance and reflectance spectroscopies consist in measuring the ratio of light transmitted and reflected by the sample, respectively, with respect to the incident light. As shown in Figure 12, transmission and reflection can be specular, when the light is transmitted or reflected in just one direction, or diffuse, when the light is transmitted or reflected in different directions. In the specular case, the angle of the transmitted beam (θ_t) is determined by the Snell's law of refraction, while the angle of the reflected light is $\theta_r = -\theta_i$, being θ_i the angle of the incident beam (all the angles are determined with respect to an axis perpendicular to the sample surface).[113] In the diffuse case, ideally, there exists a spherical angular distribution of the reflected and transmitted light; in consequence, integrating sphere methods are required for capturing uniformly all the light.[113] Finally, there can exist retroreflection, which is produced when a portion of the incident light is returned to its source ($\theta_r = \theta_i$).[113]

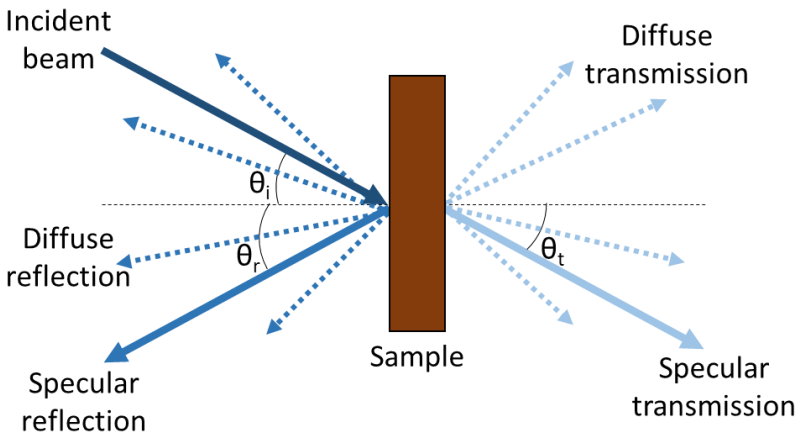

Figure 12. *Schematic representation of the reflection and transmission of light by a sample. Solid lines represent specular reflection and transmission, while dashed lines represent diffuse reflection and transmission. θ_i, θ_r, and θ_t are the angles of the incident, specular reflected, and specular transmitted beams, respectively, with respect to an axis perpendicular to the sample surface.*

Knowing the degree of optical transparency of a solar cell, or of its constituent layers, is useful for different applications such as semi-transparent devices and systems for BIPV. In these cases, the transparency is typically evaluated by means of the average visible transmittance (AVT), which is expressed as:[114]

$$AVT = \frac{\int_{\lambda_1}^{\lambda_2} T_{opt} \cdot PR \cdot S \cdot d\lambda}{\int_{\lambda_1}^{\lambda_2} PR \cdot S \cdot d\lambda} \quad (17)$$

where λ is the wavelength, T_{opt} is the transmission spectrum of the sample, PR is the photonic response of the human eye, S is the solar photon flux, and (λ_1, λ_2) is the integration range. All the previous parameters depend on the wavelength λ. The integration has to be performed over a wavelength range to completely encompass PR.[114]

1.3.2.4. X-ray fluorescence spectroscopy

XRF spectroscopy consists in irradiating the sample with high-energy X-rays and measuring the energy of the resulting emitted X-rays, which is correlated with the atomic number Z of each element. The determination of the emitted X-rays energy allows a qualitative analysis of elemental identification, while the determination of the number of emitted X-rays allows a quantitative analysis of elemental concentration.[115] Generally, K_α or L_α-lines are used for chemical analysis, because they are the most intense lines in the spectra.[116] The penetration depth of the incident X-rays is some micrometers for light elements and some hundreds of micrometers for heavy elements;[115] in consequence, for

thin film solar cells, XRF provides global information of the sample that allows a simultaneous analysis of the different layers of the device, although it implies a poor depth resolution. The lateral resolution of XRF is also relatively poor and is limited by the sample holder opening, which is usually of the order of some millimeters. However, there is a dependency between the intensity of the XRF lines and the layer thickness that is almost linear for thin films, so XRF can be employed for determining the thickness of the solar cell.[116]

1.3.2.5. Impedance and capacitance spectroscopy

Impedance and capacitance measurements allow to study bulk and interface properties of the absorber layers in the thin film solar cells, since these techniques are sensitive to carrier capture and emission from trap states. They provide information about the electronic structure of the sample such as the doping profile, the built-in voltage, electronic trap profiles in the absence of mobile charge, the absorber dielectric constant, and carrier mobility values.[117]

Impedance spectroscopy consists in applying a small alternating voltage (typically 10 – 50 mV) to the sample and measuring the current response. This alternating current (AC) is superimposed onto a much larger direct voltage (DC) in the order of hundreds of mV or even some V. Then, from impedance measurements, it is possible to derive the capacitance of the sample as follows:[117,118]

$$C_p = \frac{B}{\omega_{AC}} = \frac{-X}{(R^2 + X^2) \cdot 2 \cdot \pi \cdot f_{AC}} \tag{18}$$

$$C_s = \frac{-1}{X \cdot 2 \cdot \pi \cdot f_{AC}} \tag{19}$$

where C_p and C_s and are the capacitance for a parallel and series circuit, respectively. B is the susceptance, ω_{AC} and f_{AC} are the angular and ordinary frequency of the applied AC, R is the resistance (real part of the impedance), and X is the reactance (imaginary part of the impedance). For solar cells, a simple parallel circuit model is usually assumed consisting of a series resistor with resistance R_s, a parallel resistor with resistance R_p, and a parallel capacitor with capacitance C_p. In this case, it is necessary that $\omega_{AC} \cdot R_s \cdot C_p << 1$ and that $R_s << R_p$; otherwise, the series resistance and capacitance form a low-pass filter and Equation 18 is not valid.[118]

Capacitance spectroscopy is applied to solar cells using the depletion approximation, which assumes that the SCR is precisely defined, ends abruptly, and is fully depleted of free carriers. In consequence, as long as the free carrier relaxation time is short compared with f_{AC}, the capacitance response originates from the depletion edge, so the width of the SCR can be obtained from:[118]

$$W_{SCR} = \frac{\varepsilon_s \cdot \varepsilon_0 \cdot A}{C} \tag{20}$$

where ε_s is the semiconductor dielectric constant, ε_0 is the vacuum permittivity, A is the area of the solar cell, and C is the capacitance of the sample.

Then, the apparent doping density can be estimated from $C(V)$ data according to:[118]

$$N_{CV} = \frac{-2}{q_e \cdot \varepsilon_s \cdot \varepsilon_0 \cdot A^2} \cdot \left[\frac{1}{\frac{d\left(\frac{1}{C^2}\right)}{dV_{DC}}} \right] \tag{21}$$

where V_{DC} is the applied DC voltage. Equation 21 is only true if the doping concentration on one side of the p–n junction is much larger than that of the other side. For example, in order to know the doping concentration in p-type absorbers such as chalcopyrite and kesterite, it is necessary that $N_D >> N_A$, which results in $N_{CV} \approx N_A$, being N_D the donor doping concentration of the n-type buffer layer and N_A the acceptor doping concentration of the p-type absorber.

Finally, by combining Equation 20 and Equation 21, it is possible to obtain the doping profile of the majority carriers inside the solar cell absorber, which is represented in a $N_{CV}(W_{SCR})$ plot.

1.3.2.6. Electron microscopy

Electron microscopy consists in obtaining images of the sample with high lateral resolution by irradiating the sample with an electron beam. There are two main types of electron microscopy, which are SEM, where the image is obtained from electrons reflected by the sample, and TEM, where the image is obtained from electrons transmitted through the sample.[119] In both cases, the incident electrons beam can be generated by thermionic electron guns, such as W or LaB_6 cathodes, or by field-emission guns. Typical accelerating voltage in SEM is lower than 20 kV, and the typical accelerating voltage in

TEM ranges between 80 and 1200 kV.[119] Then, SEM can achieve lateral resolutions down to below 1 nm and TEM can achieve resolutions down to the angstroms range.[119]

Both SEM and TEM can be coupled with a tool allowing to perform EDX measurements. When an incident electron collides with the sample, it may scatter with an inner-shell electron of an atom, so the sample can emit X-rays. The energy positions of X-ray lines depend on the energy differences between the states of inner-shell electrons, which are characteristic for each element. Therefore, recording the X-rays emitted by the sample allows to analyze its chemical composition. Additionally, TEM can be coupled with electron energy-loss spectroscopy (EELS), which is based on the loss of kinetic energy of the incident electrons due to the interaction with the sample. EELS provides higher spatial and energy resolutions than EDX, and better count rates and detection limits, but it suffers from a higher background and its analysis is more complex. Generally, EELS is the optimal technique for detecting and quantifying light elements, while EDX can be advantageous for heavy elements.[119]

1.4. Objectives of the thesis

The main objective of this thesis is to identify the main physicochemical mechanisms that occur at the interfaces (back and front) of the chalcogenide absorber layers used in high efficiency chalcopyrite and emerging kesterite thin film solar cells and that have a relevant impact on the device performance, and to define methodologies suitable for the comprehensive analysis of the interfaces. This goal was proposed taking into account the main technological issues that were found in the thin film technology in general, and in the kesterite and chalcopyrite based solar cells in particularly, also considering the importance of the specific analysis of the interfaces in the thin film devices, as it is described in details in the above sections. In order to achieve this global objective, the following partial objectives are defined:

- To perform an in-depth characterization of thin film solar cell devices including the analysis of the bulk and interface properties of the absorber layers by using various advanced characterization techniques (article entitled *Insights into interface and bulk defects in a high efficiency kesterite-based device*).
- To develop methodologies allowing to make an advanced and complete deep resolved characterization of the absorbers in thin film solar cells

(articles entitled *Defect depth-profiling in kesterite absorber by means of chemical etching and surface analysis*, *Rear interface engineering of kesterite $Cu_2ZnSnSe_4$ solar cells by adding $CuGaSe_2$ thin layers*, and *Controlling the Anionic Ratio and Gradient in Kesterite Technology*).

- To perform an advanced analysis of the solar cells based on different materials and with different technological solutions by selected techniques in order to understand the physicochemical processes taking place at both front and back absorber interfaces (articles entitled *Rear interface engineering of kesterite $Cu_2ZnSnSe_4$ solar cells by adding $CuGaSe_2$ thin layers*, *Insights into the Effects of RbF-Post-Deposition Treatments on the Absorber Surface of High Efficiency $Cu(In,Ga)Se_2$ Solar Cells and Development of Analytical and Machine Learning Process Monitoring Methodologies Based on Combinatorial Analysis*, and *Characterization of the Stability of Indium Tin Oxide and Functional Layers for Semitransparent Back-Contact Applications on $Cu(In,Ga)Se_2$ Solar Cells*).
- To develop new methodologies based on optical techniques for non-destructive characterization of functional devices compatible with their implementation as quality control tools for in-line industrial process monitoring (article entitled *Insights into the Effects of RbF-Post-Deposition Treatments on the Absorber Surface of High Efficiency $Cu(In,Ga)Se_2$ Solar Cells and Development of Analytical and Machine Learning Process Monitoring Methodologies Based on Combinatorial Analysis*).

Chapter 2: Methodology

This chapter describes the general technical aspects of the methodology employed in this thesis, which is presented as an article compendium. In consequence, each study included in this work has its own particularities, but all of them have in common the synthesis of the samples and, afterwards, the analysis of such samples by different characterization techniques. The synthesis of the characterized samples is outside the scope of this work, so no precise explanation of the solar cells fabrication is included in this chapter, although a brief description is provided. Then, since this work is focused on the samples characterization, the details of the characterization techniques selected for the study are presented individually. However, the articles included in this thesis employ more characterization techniques (such as AES, ML or XPS, among others) than the ones discussed in this chapter; the reason for this is that the corresponding measurements and analysis were provided by colleagues and partners who are not the author of this thesis and, in consequence, such techniques are considered to be outside the scope of this work. Nevertheless, their results were used to complete the final picture that describes the complex systems analyzed in the present thesis. In Chapter 3, detailed explanations of the synthesis processes and of all the used characterization techniques can be found in the *Experimental Section* (or *Materials and methods* section) of each article that constitutes this thesis.

2.1. Solar cells fabrication

Kesterite solar cells analyzed in the thesis have been synthesized according to the kesterite baseline process defined at IREC. In this process the absorbers are synthesized following a sequential process that involves i) deposition of metallic precursors on Mo-coated SLG substrates by DC magnetron sputtering (Alliance Concept Ac540), and ii) reactive recrystallization under chalcogen atmosphere in a tubular furnace (Hobersal). In the case of chalcopyrite absorbers, however, they are deposited by co-evaporation processes that have been developed either at the semi-industrial pilot line available at ZSW (Stuttgart, Germany, in the frame of the In4CIS SolarEra.Net collaborative project) or at the Martin Luther University (Halle, Germany, in the frame of the MasterPV Solar-Era.Net collaborative project). . Depending on the study, there may exist deposition of additional layers (Ge, $CuGaSe_2$, RbF) or alternative back contacts (based on ITO). After

the absorber synthesis, devices are completed by depositing the CdS buffer layer by CBD and the window layer (ZnO/ITO or ZnO/AZO) by pulsed DC magnetron sputtering (Alliance Concept CT100 for kesterite cells manufactured at IREC). Finally, individual cells are mechanically scribed using a manual microdiamond scriber (OEG MR200). Variations regarding the completion of the devices may exist depending on the study and details about this can be found in the *Experimental Section* of each article in the *Chapter 3*.

2.2. *J–V* characteristics

The *J–V* characteristics of the solar cells were obtained under simulated AM1.5 illumination (1000 $W \cdot m^{-2}$) at room temperature using a solar simulator in four-point geometry and calibrated with a Si reference solar cell. Depending on the study, the solar simulator was an Abet Technologies Sun 3000 Class AAA or a WACOM. For electrical probing and sensing, a Keithley 2400 source meter was utilized.

2.3. Raman spectroscopy

The Raman spectroscopy system employed at IREC is schematically shown in Figure 13a. A He-Cd gas laser (λ_{exc} = 325 nm) and different solid state lasers (λ_{exc} = 532, 638 and 785 nm) were employed as light source. The reason for employing lasers is that they offer a light which is monochromatic, coherent, collimated, and with a stable spectrum; in addition, they allow to control their power and the light path. An unpolarized laser beam was used to minimize the impact of the crystalline orientation in the Raman spectra. Then, the selection of the excitation wavelengths depended on the penetration depth inside the sample, the possibility to reach resonant or close to resonant conditions, the suitability for detecting different phases, and the possibility to avoid undesired fluorescent and luminescent signals.

The monochromatic and parallel beam of the laser was coupled with an optical probe manufactured in IREC by means of an optical fiber. Inside the probe, as shown in Figure 13b, first of all, the laser light was "cleaned" by passing through an interferential narrow-band filter that removes the parasitic light contribution coming from the different components of the system. Then, a long-wave (low-energy) pass edge filter was used as an achromatic beam splitter to direct the parallel laser beam towards the objective, which focuses the light on the sample. Laser power densities below 150 $W \cdot cm^{-2}$ were used to prevent thermal effects on the samples and the diameter of the laser macro-spot was

around 70 µm. Additionally, micro-Raman spectroscopy was performed using an Olympus metallographic microscope which concentrated the measurement spot down to 1 µm diameter; in this case, the laser power did not exceed 1 mW. Measurement mappings were performed by means of a high precision XY-stage. To optimize the signal, a backscattering configuration was employed, which means that the propagation of the incident and scattered lights forms an angle of 180º. Thus, after the interaction with the sample, the elastic and inelastic scattered light was collected using the same objective. The Rayleigh scattered component (elastically scattered photons) is ~10^6 times higher than the Raman signal and, in addition, they are spectrally close (<0.1 eV), so the former could hide the latter. In consequence, a long-wave pass edge filter was also used to separate the low-energy inelastic light contribution (Stokes scattering) from the elastic one, which is blocked. Finally, the remaining Raman scattered light passed into the monochromator using an optical fiber.

The employed monochromators were FHR-640 or iHR-320 Horiba Jobin Yvon monochromators, which incorporate a diffraction grating where constructive and destructive interference is used to spatially separate the polychromatic light that is incident on the grating into its constituent wavelengths. The rotation of the grating allows to change the wavelength that aligns with and passes through the exit slit. Different gratings for dispersing the light were used to optimize the spectral resolution. Then, the monochromators were coupled to a CCD detector cooled down either to −70 ºC or −130 ºC.

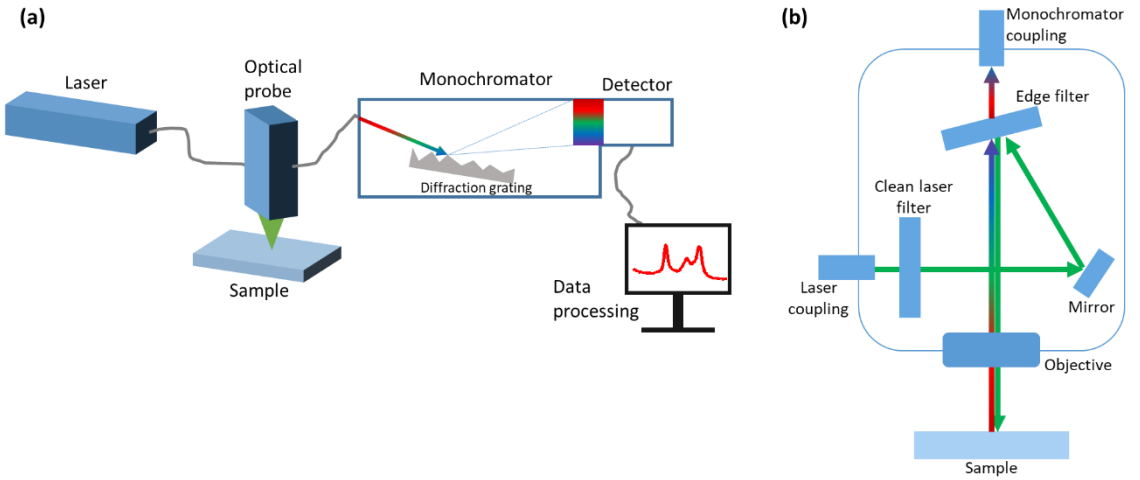

Figure 13. *(a) Schematic diagram of the setup of the Raman spectroscopy system at IREC. (b) Schematic diagram of an optical probe manufactured at IREC for Raman spectroscopy measurements.*

Finally, the data from the measured Raman spectra was recorded by a PC. However, this data has to be processed to properly analyze it, as seen in Figure 14. First of all, the spectra were calibrated by imposing the shift of the main peak of a Si single crystal reference at 520 cm^{-1}. Then, a reference spectrum measured without any sample was subtracted from the samples spectra to remove the contributions from the air and system components. After this, the baseline generated by different origins, such as the tail of the laser or the luminescence, was removed. Finally, the spectra were normalized to some reference peak of the spectrum itself.

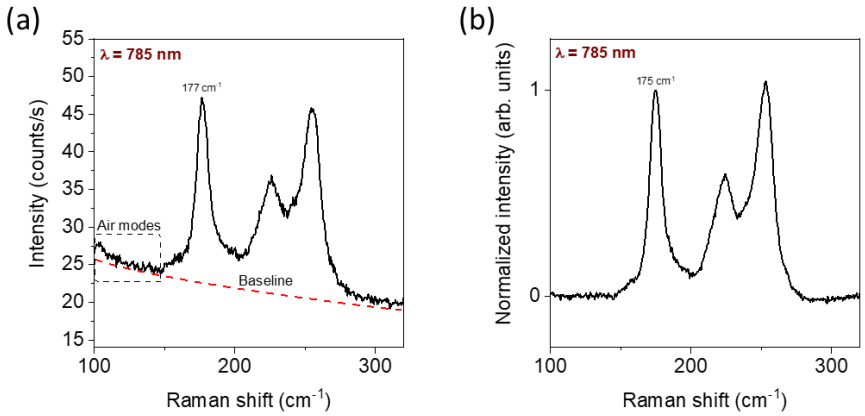

Figure 14. *Example of a Raman spectrum from a $CuIn_{1-x}Ga_xSe_2$ sample (a) before and (b) after the data processing.*

Regarding the sample preparation, no special preparation was needed to analyze the front absorber/buffer interface of the different solar cells by Raman spectroscopy. This was possible thanks to the high penetration depth of the used excitation wavelengths through the wide band gap top layers of the solar cells, which allowed performing the measurements through the front window layers. However, for the characterization of the back interface, the typical Mo back contact prevented to perform direct measurements through the glass substrate, so a previous sample preparation was required. In this case, the absorber was detached from the substrate through a mechanical lift-off process consisting in bonding the front surface of the devices to a steel or a glass substrate with an adhesive epoxy and, then, removing them mechanically. The interface between the back contact and the absorber in thin film chalcogenides is highly stressed due to the presence of the $MoSe_2$ layer formed during the absorber synthesis, which has a layered structure and renders this interface very weak, easing the separation. In the cases of samples with semi-transparent ITO-based back contacts, the back interface was also

analyzed by direct measurements through the glass substrate and through the semi-transparent back contact.

2.4. PL spectroscopy

PL spectroscopy measurements were performed with a special optical probe developed at IREC that allowed to measure the Raman scattering and the PL spectra at the same point quasi-simultaneously using a large area spot around 70 μm. For the PL measurements, the probe was coupled to a Sol 1.7 spectrometer from B&WTek with a built-in InGaAs detector cooled down at −5 ºC in near-backscattering configuration. Solid state lasers of 638 and 785 nm excitation wavelength were employed with power densities lower than 150 $W \cdot cm^{-2}$ to prevent any thermal effect on the samples. It was worth noticing that the specific conditions of the measurements and the applied system did not allow to directly measure the absolute quantum yield (QY) of the emission band, but they allowed to define the relative QY, which showed the relative changes from one measured point/sample to another.

2.5. Transmittance and reflectance spectroscopy

Transmittance measurements were performed using a light-emitting diode table and an iHR-320 spectrometer from Horiba Jobin Yvon coupled with a CCD detector cooled down to −70 ºC. The measurement spot size had a diameter of ~1 mm. Transmittance was measured by illuminating the samples from the bottom side and the transmitted light was collected at the top side of the samples. The obtained transmittance spectra allowed to calculate the AVT as defined in Equation 17.

Reflectance measurements were performed using a Lambda 950 UV/VIS spectrometer from PerkinElmer coupled with a 150 mm integrating sphere from the same company. Average reflectance was calculated in the 380 – 780 nm spectral range as the arithmetic mean of the reflectance values measured at each wavelength.

2.6. XRF spectroscopy

XRF spectroscopy was performed to determine the chemical composition and to estimate the films thickness by means of a Fisherscope XDV-SDD system calibrated by inductively coupled plasma mass spectrometry. For each sample, different points were measured and the average of the obtained data was performed. The measurements were

done using a 50 kV accelerating voltage, a Ni10 filter to reduce background signal, and an integration time per measuring point of 45 s.

2.7. Impedance and capacitance spectroscopy

Impedance spectroscopy was performed using a Keysight E4990A Impedance Analyzer at room temperature and in dark conditions. The applied AC voltage was 50 mV with different AC frequency steps from 20 Hz to 10 MHz, while the applied DC voltage varied from −1.5 V to 0.5 V. The frequency range was established in accordance to the limitations of the system, while the voltage range was determined by the V_{OC} of the device and signal-to-noise ratio criteria. The number of frequency and voltage steps was selected to allow a proper calculation of the first derivatives of capacitances $C(f_{AC})$ and $C(V)$.

2.8. Electron microscopy

Cross-sectional SEM images were obtained with a ZEISS Series Auriga microscope applying 5 kV as the accelerating voltage and at working distances of 3−5 mm to study the morphology of the absorbers.

High-resolution TEM (HRTEM) planar-view images were acquired in a JEOL-2100 with a LaB_6 filament at 200 keV. The HRTEM and low magnification dark field (DF)-bright field (BF) cross-sectional images were acquired in a JEOL-2010F with a field emission gun at 200 keV. The high resolution high-angle annular DF (HAADF) images by scanning TEM (STEM) and the EELS spectrum images were acquired in a JEOLARM-F with field emission gun at 200 keV and C_s aberration correction in the condenser lens system. The obtained images were analyzed through a combination of Gatan Digital Micrograph proprietary software and Hyperspy Python-based free software. CaRIne Crystallography and TEM-UCA EJE-Z[120] were also used to identify the crystalline structures.[121]

For the cross-sectional TEM sample preparation, focused ion beam (FIB) was used. A platinum nanolayer was deposited onto the sample to protect it. For the planar-view TEM sample preparation, the ITO, i-ZnO, and CdS layers were removed by chemical etching in HCl (5% v/v). Then, the etched sample was cut with a filament diamond saw into 3 mm thick (including the SLG substrate) 2.5 × 2.5 mm^2 pieces. These pieces were polished from the substrate side to preserve the front interface surface by means of a series of diamond abrasive films with decreasing grain sizes (30, 15, 6, 1 and 0.5 μm) until the samples were thinned down to 30 – 70 μm. Then, a final thinning (down to a thickness

around 50 nm) was performed by ion milling tripod polisher kit (model 590, South Bay Technologies) and a 1200 metallographic manual polisher (NANO 1200T, Pace Technologies) using a Fischione 1010 Precision Ion Polishing System with the upper source working at 5.0 kV and 5.0 mA.

Chapter 3: Publications

This thesis is presented as a compendium of six scientific articles, which are collected in this section. The articles have been published in high impact factor journals placed in the first quartile (Q1) of the categories directly corresponding to the main topic of the present thesis (Materials Science, Multidisciplinary and/or Energy & Fuels)[122] under the titles:

- Insights into interface and bulk defects in a high efficiency kesterite-based device. **Energy Environ. Sci.**, vol. 14, no. 1, p. 507, January 2021, DOI: 10.1039/D0EE02004D. **IMPACT FACTOR (IF): 39.714 (Q1)**.
- Defect depth-profiling in kesterite absorber by means of chemical etching and surface analysis. **Appl. Surf. Sci.**, vol. 540, no. 2, p. 148342, February 2021, DOI: 10.1016/j.apsusc.2020.148342. **IMPACT FACTOR (IF): 7.392 (Q1)**.
- Rear interface engineering of kesterite $Cu_2ZnSnSe_4$ solar cells by adding $CuGaSe_2$ thin layers. **Prog Photovolt Res Appl.**, vol. 29, no. 3, p. 334, March 2021, DOI: 10.1002/pip.3366. **IMPACT FACTOR (IF): 8.490 (Q1)**.
- Controlling the Anionic Ratio and Gradient in Kesterite Technology. **ACS Appl. Mater. Interfaces**, vol. 14, no. 1, p. 1177, January 2022, DOI: 10.1021/acsami.1c21507. **IMPACT FACTOR (IF): 10.383 (Q1)**.
- Insights into the Effects of RbF-Post-Deposition Treatments on the Absorber Surface of High Efficiency $Cu(In,Ga)Se_2$ Solar Cells and Development of Analytical and Machine Learning Process Monitoring Methodologies Based on Combinatorial Analysis. **Adv. Energy Mater.**, vol. 12, no. 8, p. 2103163, February 2022, DOI: 10.1002/aenm.202103163. **IMPACT FACTOR (IF): 29.698 (Q1)**.
- Characterization of the Stability of Indium Tin Oxide and Functional Layers for Semitransparent Back-Contact Applications on $Cu(In,Ga)Se_2$ Solar Cells. **Sol. RRL**, vol. 6, no. 7, p. 2101071, July 2022, DOI: 10.1002/solr.202101071. **IMPACT FACTOR (IF): 9.173 (Q1)**.

It has to be underlined that instead of being classified by topics, the articles are ordered chronologically by publication date of the corresponding volume and issue of the journal. This is due to the fact that each publication covers different topics that are interrelated with the other publications. The schematic diagram in Figure 15 shows the different topics covered by the different articles. In terms of the type of absorber material, four articles cover kesterite absorbers and two articles cover chalcopyrite absorbers. In terms of the focus on specific absorber region, four articles study the front interface between the absorber and the buffer layer, two articles study the absorber bulk, and five articles study the back interface between the absorber and the back contact. Finally, all six articles are focused on the advanced characterization of the devices for fundamental research, while one of them also proposes a process monitoring methodology which is based on the performed advanced characterization, showing the possibility of application of the proposed non-destructive optical methodologies as quality control tools in PV industrial processes.

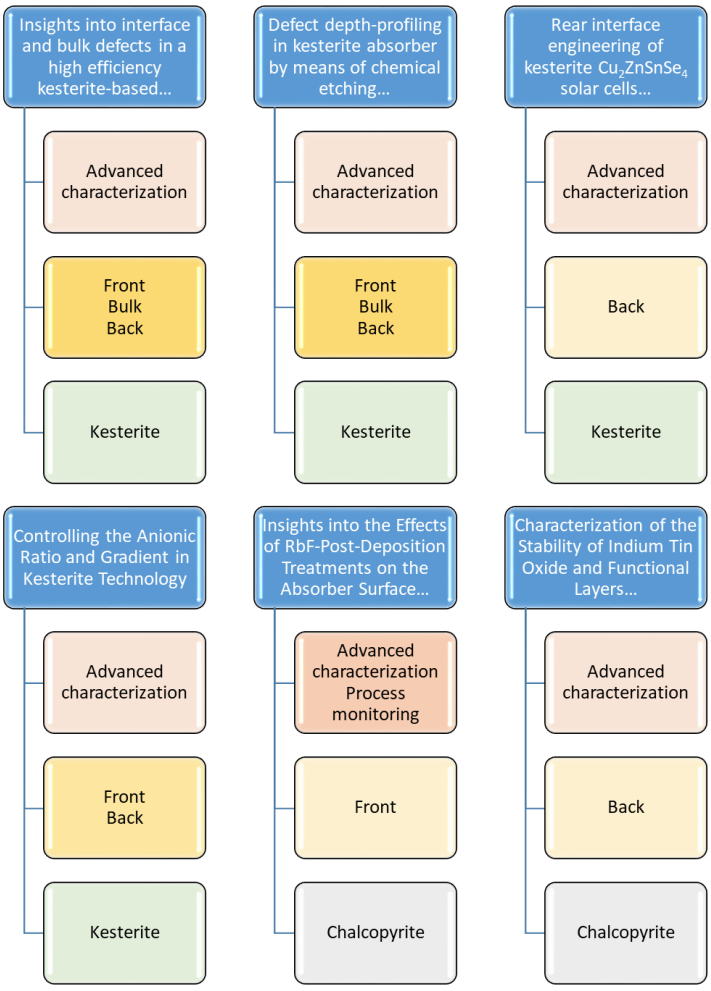

Figure 15. *Diagram indicating the topics covered by each article.*

3.1. Introduction to publications, summary of the results, and general discussion

Chalcopyrite-based solar cells have achieved the highest energy conversion efficiency among thin film chalcogenide solar cells (23.35%)[24], while kesterite-based ones offer a promising alternative composed of non-toxic and earth-abundant materials.[64] The advantages of thin film PV with respect to the traditional crystalline Si technology are a reduction of the material consumption and an increase of the possible applications such as BIPV, VIPV, wearables, or Internet of things, among others, based on their higher technological flexibility. However, both chalcopyrite and kesterite technologies present an efficiency that is lower than the one achieved by crystalline Si, mainly at module level.[22,23] In consequence, this thesis characterizes chalcopyrite and kesterite-based solar cells with the focus to deepen in the knowledge of the impact of the absorber interfaces on the device efficiency. This is strongly required for a further optimization of these technologies.

The main limitation of kesterite absorbers is considered to be the V_{OC} deficit, that has been attributed to several issues taking place at different parts of the device.[123] For example, at the front interface, it has been attributed to non-optimum band alignment with the CdS buffer layer, Fermi level pinning due to Cu_{Zn} antisite point defects, incomplete CdS coverage, high density of interface defects, as well as ZnSe and SeO_2/$Sn(O,Se)_x$ secondary phase formation.[35–44] In the bulk, it has been explained by Cu–Zn disordering leading to bandgap and electrostatic potential fluctuations, by formation of secondary phases that can lead to compositional fluctuations and induce the formation of defects, by non-passivated grain boundaries, and by short minority carrier lifetime.[57,124–126] Finally, at the back interface, it has been attributed to defective coupling with the back contact and chemical instability, as well as an excessive $MoSe_2$ formation that may alter the back band alignment unfavorably.[47–53] Possible solutions to the previous problems can be found in the literature, such as doping the absorber with light alkaline elements, cationic substitution, or band gap engineering.[63,64] However, most of the reported studies typically focused on only one part of the device, while the most likely explanation for the high V_{OC} deficit was a combination of several issues taking place simultaneously in different parts of the device.[64,123] In order to build up a full picture of the main limitations of kesterite-based devices, a high efficiency (η = 9.2%) CZTSe-based solar cell was characterized by different techniques, including HRTEM, Raman spectroscopy, impedance spectroscopy,

and *J–V* characteristics, among others. This study resulted in the first article of this thesis, entitled *Insights into interface and bulk defects in a high efficiency kesterite-based device*. This article presents a good practice in comprehensive analysis of absorber bulk together with the detailed analysis of the front and back interfaces combining very high resolution electron microscopy techniques with Raman spectroscopy, XRF and AES measurements at the macro, micro and nano scales. The analysis compares the influence of the defects that are present in the bulk of the absorber with the ones at the absorber interface, and as one of the results the importance of the interfaces quality to the final device efficiency is explicitly shown. An alternative methodology for studying the bulk and interface properties of the absorber layers at both front and back interfaces is proposed in the second article of the thesis, entitled *Defect depth-profiling in kesterite absorber by means of chemical etching and surface analysis*. Here, the analysis was made by applying mainly Raman spectroscopy, which was capable to assess the absorber at different depths thanks to the application of a chemical etching controlled procedure with a bromine solution. This approach allowed studying the redistribution of the defects and of the secondary phases along the absorber depth. The two articles allowed to make a comparative study of the possible influence of the bulk of the absorber and its interfaces on the performance of a thin film solar cell, and additionally emphasized the possibility to use mainly Raman spectroscopy for making a comprehensive analysis of the absorber.

After performing a complex investigation of the different regions of CZTSe-based solar cells and selecting the main techniques for this investigation, the band gap engineering of kesterite absorbers was studied by applying different strategies. On the one hand, small amounts of Ga were added at the back region of CZTSe absorbers to promote the formation of a back-surface field that shifts the CB minimum to higher energies and improves the collection of the charge carriers generated deeper in the absorber.[127] This experiment resulted in the third article of this thesis, whose title is *Rear interface engineering of kesterite $Cu_2ZnSnSe_4$ solar cells by adding $CuGaSe_2$ thin layers*. Here, the combination of a mechanical lift-off and Raman measurements allowed to confirm the formation of CGS at the back interface, thus confirming the formation of a phase with a wider band gap than CZTSe and, in consequence, the formation of the desired back-surface field, which improved the device performance. On the other hand, an anionic (Se−S) gradient was investigated in CZTSSe and $Cu_2ZnGe(S_{1-x}Se_x)_4$ absorbers; compositional grading is valuable at the device interfaces for an optimum band

alignment, for the control of interface defects and recombination, and for the optimization of carrier-selective contacts.[128,129] The preparation of solid solution kesterite phases in the literature reported that a reproducible control on the anionic ratio was difficult to achieve or that complicated setups were required.[130,131] The proposal of an innovative approach for accurately controlling the anionic ratio in kesterite absorbers led to the publication of the fourth article of this thesis, entitled *Controlling the Anionic Ratio and Gradient in Kesterite Technology*. Here, applying multiwavelength Raman spectroscopy allowed to assess the chemical composition at the absorber surface and subsurface regions; additionally, the performed mechanical lift-off allowed applying this approach to the back side of the absorber. The results of the Raman analysis showed different chemical compositions at the different regions, which confirmed the possibility to control the anionic ratio by the employed simple technique; in addition, it also showed fundamental differences between the formation paths of Sn-based and Ge-based kesterite compounds.

Regarding the chalcopyrite-based technology, it presents a more mature stage of development than the kesterite-based technology, but there is still a room for improvement. For example, recent efficiency improvements in this technology were achieved thanks to heavy alkali PDTs. While the results reported in the literature suggested that the main effect of such PDTs was produced on the V_{OC}, the reasons for the positive impact of these treatments remained under discussion, and the main disputes are whether the changes at the front interface are important or only the improvement of the bulk of the absorber leads to the observed positive effect of the PDT.[132–134] In order to shed the light on the influence of RbF-PDT on the absorber surface in high efficiency CIGSe-based devices, 620 solar cells were characterized by Raman and PL spectroscopies, and by optoelectronic characterization, which resulted in publication of the fifth article of this thesis, entitled *Insights into the Effects of RbF-Post-Deposition Treatments on the Absorber Surface of High Efficiency Cu(In,Ga)Se_2 Solar Cells and Development of Analytical and Machine Learning Process Monitoring Methodologies Based on Combinatorial Analysis*. The high statistics employed in this study allowed detecting very small variations in the Raman spectra of the CIGSe absorbers, providing a clear evidence of the correlation of the spectral changes detected at the front absorber interface with the improved device performance. The changes at the absorber surface consisted in a decrease of the ordered vacancy compound (OVC), an increase of a defective chalcopyrite phase, and a higher apparent hole concentration. The correlation

between the observed variations and the device performance was also proposed as a possible base for establishing a methodology for controlling the quality of the PDT process when scaled up to module level within an industrial environment.

Finally, the sixth and last article of this thesis, entitled *Characterization of the Stability of Indium Tin Oxide and Functional Layers for Semitransparent Back-Contact Applications on Cu(In,Ga)Se_2 Solar Cells*, studies the stability of ITO-based back-contact configurations under the co-evaporation processes that are developed for the synthesis of high-efficiency CIGSe solar cells. Semitransparent back contacts offer different applications such as bifacial devices, semitransparent BIPV, and tandem solar cells.[135–137] The literature reported the replacement of standard Mo back contact by different TCOs such as ITO, FTO, and AZO; while high efficiencies were achieved with a bare ITO back contact for a co-evaporation process temperature of 520ºC, higher process temperatures required the application of nanometric functional layers such as Mo or $MoSe_2$.[137,138] Despite these reported results, the impact of the absorber fabrication process on the back contact and its optical properties had not been deeply studied before, which motivated the development of this study focused on the back interface between the CIGSe absorber and the semi-transparent back contact. The combined analysis by Raman, transmittance, and reflectance spectroscopies revealed that bare ITO layers can be used as back contacts for CIGSe co-evaporation deposition process temperatures of 480ºC, but higher temperatures lead to the formation of an amorphous In–Se phase at the ITO surface that reduces drastically both the transparency of the contacts and the efficiency of solar cells. Inclusion of a Mo functional layer on the ITO surface led to the formation of $MoSe_2$ interfacial phase that improves significantly the efficiency of the cells and the contact optical transparency up to 50% in the visible region. Additionally, a relevant decrease in back reflectivity in the CIGSe devices was observed when applying ITO-based back contacts.

As a general discussion of the results obtained for kesterite absorbers, the work developed in the thesis shows that at the present state of development issues related to the front/back absorber interfaces have a potential higher impact on limiting the device performance that the bulk properties of the layers. In the case of the back interfaces, synthesis strategies ensuring a good element intermixing and avoiding the formation of volatile phases could minimize the appearance of large voids at the back absorber region. In the case of the front interfaces, research on alternative buffer materials and deposition techniques is relevant to improve the band and structural alignment with the CZTSe

absorber. For both interfaces, etching or passivation strategies, such as the application of Ga at the back interface, and band gap engineering, which is achieved by controlling the composition at the different interfaces, could reduce the formation of interfacial defects.

Regarding the chalcopyrite absorber, which is already in a commercial stage of development, the obtained results indicate that RbF-PDT promotes a redistribution of defects between the OVC and chalcopyrite phases at the absorber surface that improves the V_{OC} of the solar cells. The correlation observed between the Raman spectral features and the device performance has allowed the development of a process monitoring methodology for the in-line quality control of the upscale of the PDT processes at module level. On the other hand, the systematic application of the Raman scattering methodologies developed in the thesis have also allowed to deepen in the knowledge of the impact of the CIGSe deposition processes on the optical and electrical quality of ITO based semi-transparent bac contact, which is strongly relevant for BIPV, tandem and bifacial device applications. As shown in the study, the stability of ITO-based contacts at high process temperatures can be improved by applying functional nanometric layers such as $MoSe_2$.

Finally, regardless the material absorber, the results obtained during the development of this thesis show that a rigorous characterization of the absorber interfaces by combining different techniques provides critical information about the solar cell properties that can be employed to optimize its performance and to increase its possible applications, which, consequently, facilitates its scaling from the research level to the industrial level.

The next six articles that constitute the main body of the thesis are reprinted with permission as described herein: *Insights into interface and bulk defects in a high efficiency kesterite-based device* is reproduced from Ref. 139 with permission from the Royal Society of Chemistry according to the right as an author of the article of using it in submissions of academic requirements such as theses or dissertations. *Defect depth-profiling in kesterite absorber by means of chemical etching and surface analysis* is reproduced from Ref. 140 according to the right as the author of this Elsevier article to include it in a thesis or dissertation, provided it is not published commercially. *Rear interface engineering of kesterite $Cu_2ZnSnSe_4$ solar cells by adding $CuGaSe_2$ thin layers* is reproduced from Ref. 141 according to the right as the author of the published Wiley article to reuse the full text of the published article as part of my thesis or dissertation.

Controlling the Anionic Ratio and Gradient in Kesterite Technology is reproduced from Ref. 142 using a Creative Commons license. *Insights into the Effects of RbF-Post-Deposition Treatments on the Absorber Surface of High Efficiency Cu(In,Ga)Se_2 Solar Cells and Development of Analytical and Machine Learning Process Monitoring Methodologies Based on Combinatorial Analysis* is reproduced from Ref. 143 according to the right as the author of the published Wiley article to reuse the full text of the published article as part of my thesis or dissertation. *Characterization of the Stability of Indium Tin Oxide and Functional Layers for Semitransparent Back-Contact Applications on Cu(In,Ga)Se_2 Solar Cells* is reproduced from Ref. 144 according to the right as the author of the published Wiley article to reuse the full text of the published article as part of my thesis or dissertation.

3.2. Article 1: Insights into interface and bulk defects in a high efficiency kesterite-based device

Energy & Environmental Science

ROYAL SOCIETY OF CHEMISTRY

PAPER

View Article Online
View Journal | View Issue

Cite this: *Energy Environ. Sci.*, 2021, **14**, 507

Insights into interface and bulk defects in a high efficiency kesterite-based device†

Robert Fonoll-Rubio,[a] Jacob Andrade-Arvizu,[a] Javier Blanco-Portals,[bc] Ignacio Becerril-Romero,[a] Maxim Guc,*[a] Edgardo Saucedo,[ad] Francesca Peiró,[bc] Lorenzo Calvo-Barrio,[ef] Maurizio Ritzer,[g] Claudia S. Schnohr,[gh] Marcel Placidi,[ad] Sònia Estradé,[bc] Victor Izquierdo-Roca*[a] and Alejandro Pérez-Rodríguez[af]

This work provides a detailed analysis of a high efficiency $Cu_2ZnSnSe_4$ device using a combination of advanced electron microscopy and spectroscopy techniques. In particular, a full picture of the different defects present at the interfaces of the device and in the bulk of the absorber is achieved through the combination of high resolution electron microscopy techniques with Raman, X-ray fluorescence and Auger spectroscopy measurements at the macro, micro and nano scales. The simultaneous investigation of the bulk and the interfaces allows assessing the impact of the defects found in each part of the device on its performance. Despite a good crystalline quality and homogeneous composition in the bulk, this work reports, for the first time, direct evidence of twinning defects in the bulk, of micro and nano-voids at the back interface and of grain-to-grain non-uniformities and dislocation defects at the front interface. These, together with other issues observed such as strong absorber thickness variations and a bilayer structure with small grains at the bottom, are shown to be the main factors limiting the performance of CZTSe devices. These results open the way to the identification of new solutions to further developing the kesterite technology and pushing it towards higher performances. Moreover, this study provides an example of how the advanced characterization of emergent multilayer-based devices can be employed to elucidate their main limitations.

Received 23rd June 2020,
Accepted 24th December 2020

DOI: 10.1039/d0ee02004d

rsc.li/ees

Broader context

Current cutting-edge environmentally-friendly energy generation devices usually present multi-component and multi-layer complex structures. One example of this type of devices are the new earth abundant generations of chalcogenide-based thin film solar cell concepts like kesterites. Although this technology has already shown a high potential for the fabrication of sustainable solar cell devices, it still suffers from the several limitations that strongly impact device performance and do not allow reaching the commercial state. The complex nature of these devices makes necessary an advanced characterization of the main properties at the macro-, micro- and nano scales for a deep understanding of these limitations. This work represents a reliable demonstration of a combinatorial analysis for compositional and structural study of kesterite solar cells that provides a full picture of the main factors limiting their performance including compositional inhomogeneities, structural defects, and degradation in the interfaces. As such, the results presented in this work open the way to the identification of new solutions that will aid to further develop the kesterite technology and push it towards higher performances contributing in the clean, responsible, and sustainable energy production necessary for a greener future.

[a] *Catalonia Institute for Energy Research – IREC, Sant Adrià de Besòs, 08930, Barcelona, Spain. E-mail: vizquierdo@irec.cat, mguc@irec.cat*
[b] *LENS-MIND, Departament d'Enginyeria Electrònica i Biomèdica, Universitat de Barcelona, 08028, Barcelona, Spain*
[c] *Institute of Nanoscience and Nanotechnology (IN²UB), Universitat de Barcelona, 08028, Barcelona, Spain*
[d] *Photovoltaic Group, Electronic Engineering Department, Universitat Politècnica de Catalunya (UPC), 08034, Barcelona, Spain*
[e] *Centres Científics i Tecnològics (CCiTUB), Universitat de Barcelona, C/Lluis Solé i Sabaris, 08028 Barcelona, Spain*
[f] *Departament d'Enginyeria Electrònica i Biomèdica, INUB, Universitat de Barcelona, C/Martí i Franqués 1, 08028 Barcelona, Spain*
[g] *Institut für Festkörperphysik, Friedrich-Schiller-Universität Jena, Max-Wien-Platz 1, 07743 Jena, Germany*
[h] *Felix-Bloch-Institut für Festkörperphysik, Universität Leipzig, Linnéstraße 5, 04103 Leipzig, Germany*

† Electronic supplementary information (ESI) available. See DOI: 10.1039/d0ee02004d

View Article Online
Paper Energy & Environmental Science

Introduction

Thin film photovoltaic (PV) technologies based on CdTe and $Cu(In,Ga)Se_2$ (CIGS), have reached an advanced degree of maturity with proven efficiencies at the laboratory scale beyond 22%.[1,2] These efficiency values combined with the inherent advantages of thin film PV such as low material usage, fabrication versatility or their easy integration (*e.g.* building integrated photovoltaics, wearables, internet of things, *etc.*) open the way to the democratization and ubiquity of PV through mass production of cheap and efficient solar cell devices. However, the dependence of these technologies on scarce elements like Te, In and Ga inevitably sets a limit to their future production yield restraining their mass deployment below the TW/year scale.[3–5] In this context, $Cu_2ZnSn(S_xSe_{1-x})_4$ (CZTSSe) and related compounds, also known as kesterites, represent a promising Earth-abundant alternative for thin film PV with higher potential for a future low cost mass production of PV devices. However, despite the great similarities in composition and crystal structure of CZTSSe and CIGS, the best efficiency achieved for a kesterite-based device at laboratory scale has been stagnated at 12.6% for more than 6 years.[6,7] In the case of pure selenide kesterites (CZTSe), on which this work is focused, the best device reported so far exhibits a slightly lower efficiency, just below 12%.[8]

In order to understand the origin of such a large performance gap between CIGS and CZTSSe, it is useful to take a look at the characteristics of comparable devices fabricated with both technologies. The first four rows of Table 1 show the main optoelectronic parameters of the two highest efficiency $CuInSe_2$ (CISe) and CZTSe devices reported in the literature.[8–11] Taking a look at the record CZTSe device,[8] it can be observed that the main differences with CISe are found in the short-circuit current (J_{sc}) and open-circuit voltage (V_{oc}) while the fill factor (FF) is similar for both technologies. However, the differences in the J_{sc} cannot be considered critical since this parameter can be greatly enhanced by optimizing the optical configuration of the solar cell for better light collection (*e.g.* texturing, choice of window layers, anti-reflective coatings, *etc.*) as in the case of the second best CZTSe device[11] which shows a J_{sc} value similar to that of CISe. This is not the case for the V_{oc}, which is more intimately related to the intrinsic limitations of the technology. These limitations can be clearly observed by looking at the V_{oc} deficit (defined as $E_g/q - V_{oc}$) values reported in Table 1. Compared to the highest efficiency CISe device,[9] the V_{oc} deficit of the CZTSe devices is around 250 mV higher. Nevertheless, this comparison is not entirely fair since this CISe device was fabricated with a Ga-enriched back interface and a RbF post-deposition treatment at the front interface. A more adequate comparison can be made with the second best CISe device which does not include these additional features.[10] The V_{oc} deficit of the CZTSe devices, in this case, is still around 130 mV higher. As such, it is evident that the main limitations of the CZTSe technology arise from this parameter. The origin of such a high V_{oc} deficit in kesterites has been attributed to several issues taking place at different parts of the device. To mention some:

I. At the front interface: non-optimum band alignment with the CdS buffer layer,[12–15] Fermi level pinning due to Cu_{Zn} antisite point defects,[16] incomplete CdS coverage,[17,18] high density of interface defects,[19,20] as well as ZnSe[21] and SeO_2/$Sn(O,Se)_x$[22] secondary phase formation.

II. In the bulk: Cu–Zn disordering leading to bandgap and electrostatic potential fluctuations,[23–29] formation of secondary phases that can lead to compositional fluctuations and induce the formation of defects,[21,30–32] non-passivated grain boundaries[33] and short minority carrier lifetime.[27,34]

III. At the back interface: defective coupling with the back contact and chemical instability[12,13,35–37] as well as an excessive $MoSe_2$ formation that may alter the back band alignment unfavorably.[38]

Possible solutions of the listed above problems were proposed by several authors. For instance, the use Cu-poor Zn-rich compositions allows minimizing the formation of Cu_{Zn} antisite point defects at the front interface.[23] Although these compositional regime may lead to a more likely formation of ZnSe, selective etchings have been proposed to effectively remove this and other secondary phases from the surface of the kesterite absorber after synthesis.[21,30] Front interface recombination can also be reduced through surface passivation treatments[11,39] or the use of passivating nanolayers.[17,20,40,41] Regarding the back interface, the use of a thin ZnO layer on the Mo back contact has been demonstrated to reduce chemical instability[36] and the thickness of the $MoSe_2$ layer can be controlled through multilayer Mo configurations and the use of selenization barriers.[37] Finally, in the bulk of the absorber, partial substitution of Cu by Ag or of Zn by Cd has been proposed to reduce Cu–Zn disordering[15,16] and Na-doping is commonly regarded as a means of grain boundary passivation.[42]

Nevertheless, most of the studies of kesterite-based devices typically focus on only one part of the device, *i.e.* in the bulk or in one of the interfaces, while the most likely explanation for the high V_{oc} deficit of kesterites is a combination of several issues taking place simultaneously in different parts of the device.[43,44] In this context, this work aims at providing a complete analysis of a high efficiency CZTSe device using a combination of advanced microscopy and spectroscopy

Table 1 Main optoelectronic parameters of the two highest efficiency CISe and CZTSe devices reported in the literature as well as of the device analysed in this work. The values in brackets were calculated by correcting the reflection losses of the device (see Fig. 1)

Technology	V_{oc} (mV)	J_{sc} (mA cm^{-2})	FF (%)	Efficiency (%)	E_g (eV)	$E_g/q - V_{oc}$ (mV)	Ref.
CISe[a]	609	42.3	74.6	19.2	1.00	391	9
CISe	491	40.6	75.2	15.0	1.00	509	10
CZTSe	432	36.3	76.2	11.9	1.07	638	8
CZTSe	423	41.7	66.6	11.7	1.07	647	11
CZTSe	434	33.8 (36.8)	63.0	9.2 (10.0)	1.04	606	This work

[a] With a Ga-enriched back interface and a RbF post-deposition treatment at the front interface.

View Article Online
Energy & Environmental Science Paper

techniques. In particular, the combination of high resolution electron microscopy techniques with Raman, X-ray fluorescence and Auger spectroscopy measurements at the macro, micro and nano scales allows us building a full picture of the different defects present at the front and back interfaces as well as in the bulk of the absorber and of how they affect the optoelectronic characteristics of the device with a focus on the V_{oc}. We are able to show, for the first time, direct proof of the formation of twinning defects in the bulk of the absorber, nano and micro-voids at the back interface as well as grain-to-grain non-uniformity and point and line defects at the front interface within the same high efficiency CZTSe device. The observations made and the results obtained in this work represent an important insight in the complete understanding of the main limitations of CZTSe based devices. Moreover, the present work represents an example of an advanced characterization study of a complex system (thin film solar cell) that may serve as an instructive handbook to help building up the full picture of multilayer-based devices for a broad spectrum of readers and researchers.

Results

Optoelectronic characterization

Using the preparation process described in the Experimental section, a sample with 20 individual solar cells (3×3 mm^2) was fabricated (Fig. 1c). The illuminated and dark J–V curves as well as the main optoelectronic parameters of the best solar cell obtained in the sample are shown in Fig. 1a. In addition, Fig. 1b shows the external quantum efficiency (EQE), internal quantum efficiency (IQE), and reflectance of the record device. A 9.2% record efficiency device with a 1.04 eV bandgap (calculated from the EQE using the derivative method, see bottom of Fig. 1b) was achieved. Both the V_{oc} (434 mV) and V_{oc} deficit (606 mV) of this device are very close to those reported for the best CZTSe devices shown in Table 1. However, the difference between the EQE and IQE curves indicates that the device presents important reflectance losses, especially in the 500–750 nm region. By correcting these reflectance losses, the gain in J_{sc} (value in brackets in Table 1 and Fig. 1a) could potentially increase the efficiency of this device up to 10%. In addition, the device was fabricated following the procedure employed for our in-house champion CZTSe solar cell (11.0%)[45] but without an optimized structure (*i.e.* without anti-reflecting coating, metallic grid, *etc.*). Thus, it is safe to assume that the device studied in this work can be considered inside the state-of-the-art and that the limitations of the V_{oc} identified throughout this work are universal and, thus, relevant for other high efficiency CZTSe devices. On the other hand, the slightly lower efficiency of the device fabricated in this work can be attributed to its lower J_{sc} and FF. Regarding the former, besides reflectance losses, the main limitation of the J_{sc} seems to arise from a low collection at the near infrared (NIR) of long wavelength (>750 nm) photons. This could be indicating that the device suffers from either light absorption issues, recombination issues or a combination of both. As for the low FF, it can be directly linked to the high series resistance (R_s) found in the device (2–5 times higher than previously reported values).[8,11] However, if long wavelength collection is limited by recombination issues, these would further contribute in lowering the FF of the device. All these issues together with the possible limitations of the V_{oc} of CZTSe solar cells will be explored throughout the upcoming analysis.

Bulk characterization

The overall morphology of the 9.2% CZTSe device fabricated in this work was studied by means of scanning electron microscopy (SEM) and scanning transmission electron microscopy (STEM) in cross section configuration. Fig. 2 shows a collage of a series of cross-sectional SEM and bright field (BF) STEM images of the full device where the different layers (including the Pt layer added during focused ion beam (FIB) sample preparation) are indicated. The comparison between both techniques allows discarding the presence of artefacts in the STEM image generated during lamella preparation. An irregular CZTSe

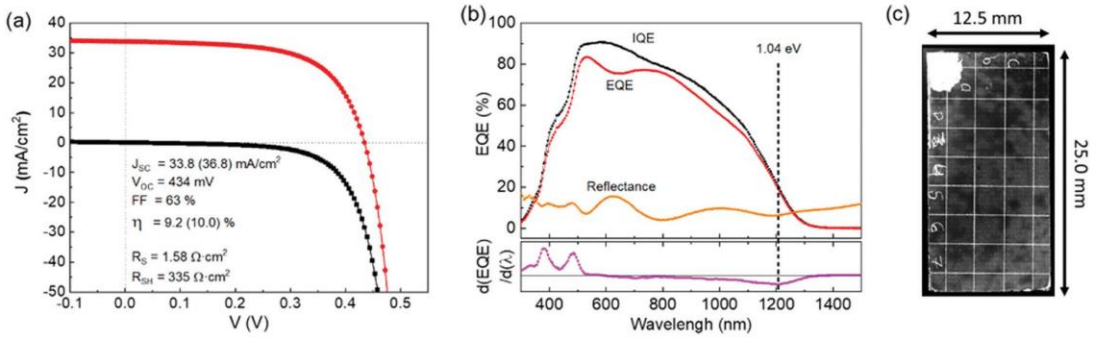

Fig. 1 (a) Illuminated (red) and dark (black) J–V curves together with the main optoelectronic parameters of the best CZTSe solar cell fabricated in this work. The values in brackets were calculated by correcting the reflection losses. (b) EQE, IQE and reflectance curves of the same device. The bottom part shows the first derivative of the EQE curve employed to estimate the bandgap of the absorber. (c) Optical image of the CZTSe sample with the individual 3×3 mm^2 solar cells.

View Article Online
Paper Energy & Environmental Science

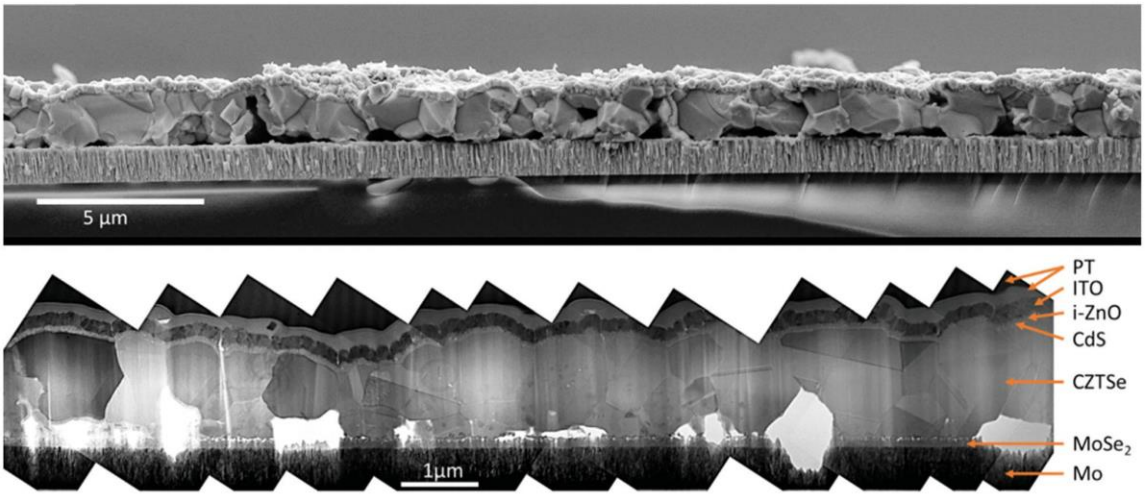

Fig. 2 Collage image of a series of cross-sectional SEM (top) and STEM (bottom) images of a CZTSe-based solar cell in bright field configurations. The different observed layers of the device are indicated in the STEM image, including the platinum layer added during FIB sample preparation.

absorber morphology with thickness variations in the 0.9–1.3 µm range is detected, which generates undulating buffer and window layers and, thus, a rough surface. Besides surface roughness, the varying absorber thickness also influences the thickness of the upper layers (In_2O_3–SnO_2 (ITO) thickness – 100 to 170 nm, i-ZnO thickness – 40 to 130 nm, and CdS thickness – 40 to 90 nm). Another interesting feature that can be spotted in Fig. 2 is the presence of very bright areas that indicate the existence of multiple voids at the back interface. These can also be observed as dark areas in the dark field (DF) image presented in Fig. S1 (ESI†). The origin of these voids and their possible effects on device performance will be studied in more detail later on.

Besides the void-related bright areas, subtler contrast differences can be also detected in Fig. 2 within the CZTSe absorber layer. These can be attributed to two main different effects. First, the different crystalline orientation of the different grains of the absorber results in different contrasts in the image. This contrast difference enables to study the grain boundaries present in the CZTSe absorber in detail. Several columnar grains that extend throughout the whole thickness of the absorber and are formed by vertical grain boundaries with the regular shape can be observed both in SEM and STEM images (Fig. 2). However, a closer look reveals that there exist specific absorber regions with a bilayer structure (Fig. 3a) in which large micron-sized grains (1–2 μm^2) occupy the top part of the absorber layer, and smaller submicron grains ($\sim 0.3\ \mu m^2$) form the bottom part. This can be better observed in Fig. 3a.2 where the grain boundaries are highlighted in red. In order to study the possible distortion of the CZTSe crystal structure around the grain boundaries, a high-resolution high angle annular dark field (HAADF) image of a grain boundary was acquired (Fig. 3b). Fast Fourier transformations (FFTs) were made on the HAADF image at a region completely inside a grain and at a region extending from the grain boundary limit to 5 nm inside the grain (Fig. 3b). The similarity between both FFTs indicates that the grain boundary does not distort the crystal structure noticeably.

The second effect influencing the contrast in the STEM images, is related to twinning defects inside the grains (highlighted in orange in Fig. 3a.2). These were studied in detail through high-resolution transmission electron microscopy (HRTEM) images and are presented in Fig. 3c. Although at first glance, the HRTEM image seems to correspond to a triple grain boundary, a careful analysis of the atomic planes and the boundaries shows that it is a twinning defective region. FFT analyses were made on the three regions tagged as dashed squares in Fig. 3c and labelled as 1, 2 and 3. The patterns obtained indicate that the three regions analysed are oriented very close to the [021] zone axis (ZA). However, by further magnifying the spotty patterns of the HRTEM image (Fig. 3d), it can be observed that while the crystalline planes are well resolved for region 3, a slightly worse resolution and contrast of the atomic planes is detected in regions 1 and 2. This points out that regions 1 and 2 are slightly deviated from the [021] ZA. Furthermore, the angles of the crystalline planes shown in Fig. 3d indicate that region 3 is rotated with respect to regions 1 and 2 around the axis of observation. This is a usual feature of twinning defects. Nonetheless, the clear and defined spotty patterns indicate that, despite twinning, the grains in the bulk region of the absorber display a good crystalline quality. Although evidences of the formation of twin boundaries in CZTSe have been recently reported,[46] to the best of our knowledge, this is the first time that twinning defects are directly observed for this material.

A more detailed analysis of the crystal structure inside a grain of the bulk of the CZTSe absorber was made through a HAADF image and is shown in Fig. 4. The image on the left is a denoised version of the original image, and was obtained by

View Article Online
Energy & Environmental Science Paper

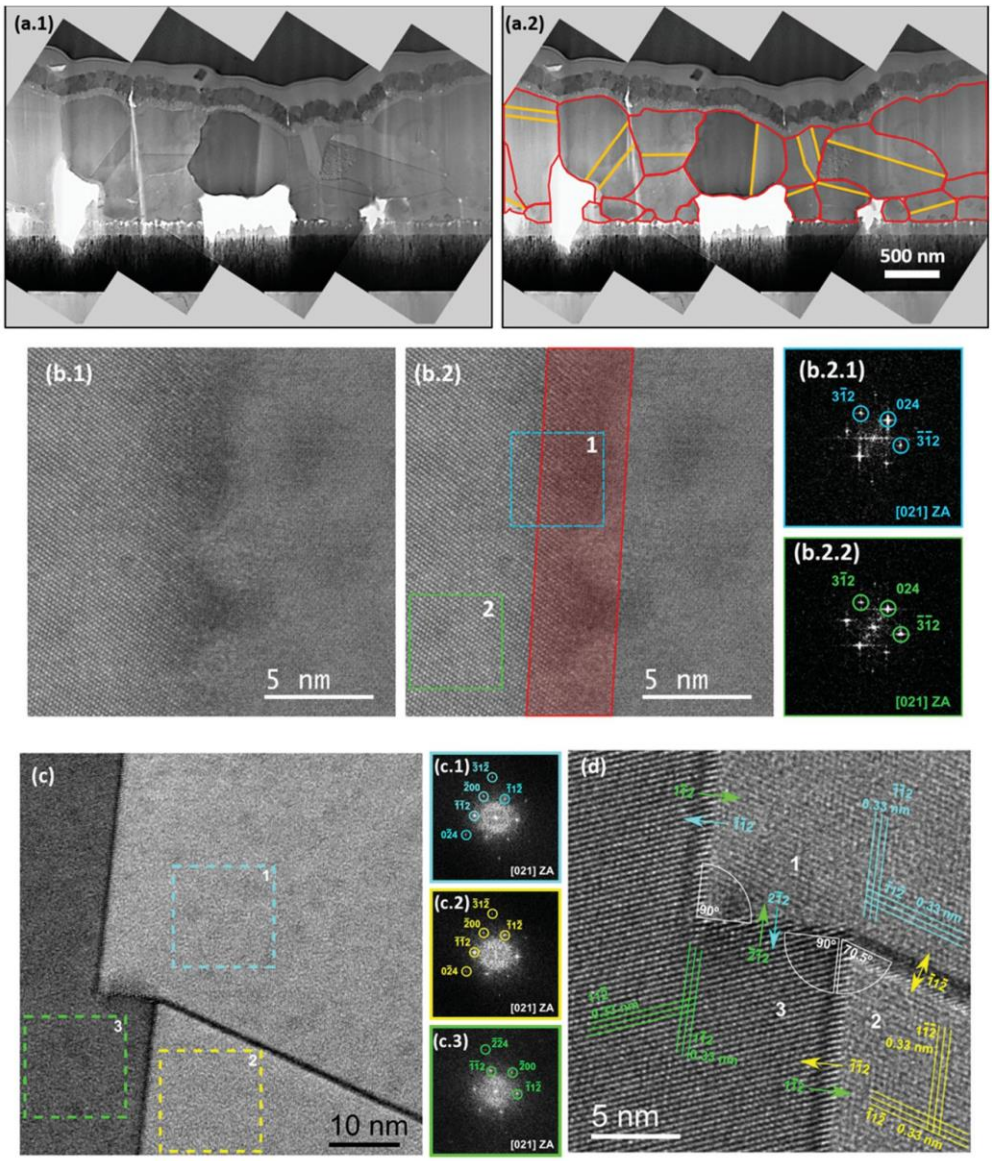

Fig. 3 (a) Cross-sectional STEM images of a CZTSe-based solar cell in bright field configuration with indication of different grains (red lines) and twinning (orange lines) in the right image. (b) Cross-sectional HAADF of two different grains and their grain boundary with (b.2.1.–b.2.2) FFTs of corresponding regions indicated by the dashed rectangles. The region in red, indicates the grain boundary. (c) Cross-sectional HRTEM image of the bulk of the CZTSe absorber at a region with twinning defects and (c.1–c.3) FFT of the corresponding regions indicated by dashed rectangles. (d) Magnified spotty patterns of the HRTEM image of the triple junction area shown in in (c). Visual guidelines are included for some of the families of atomic planes resolved in the FFTs. The directions of the families of planes forming the twinning defects and angles between them are also included.

applying a mask to the FFT (red inset in Fig. 4, left) and then carrying out an inverse-FFT (iFFT). The original image can be consulted in Fig. S2 (ESI†). The zoomed region highlighted in green shows that the lateral resolution enables the identification of the dumbbell structure (Fig. 4, right-top). The structure observed is in good agreement with the proposed atomic model for the kesterite type structure (space group $I\bar{4}$ and space number 82),[47] when observed from the [021] ZA (see Fig. 4, right top and bottom). The slight differences that may be observed in the image with respect to the kesterite structure may arise from tiny tilting deviations from the exact [021] ZA during the observation. Finally, some interplanar distances were measured in Fig. 4 and the results obtained are in good agreement with the crystalline structure of kesterite CZTSe (PDF #04-010-6295).

View Article Online
Paper Energy & Environmental Science

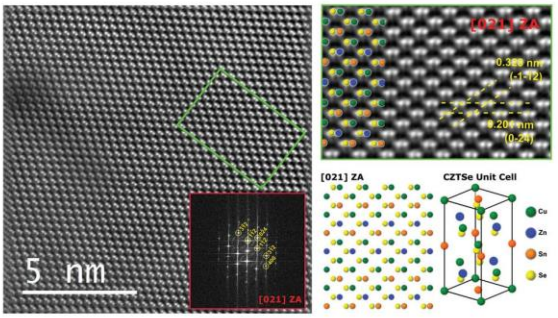

Fig. 4 On the left, iFFT of a HAADF filtered image of a CZTSe grain. Red inset: FFT of the whole area of the image. The area in green is zoomed on the right, where an overlay of the atomic structure and the HAADF image is shown at the top with some of the atomic planes resolved in yellow. In the right-bottom image, the atomic structure of the kesterite in [021] ZA is displayed.

In order to complete the study of the bulk of the CZTSe absorber, its chemical composition was analysed by means of a nano-X-ray fluorescence (XRF) mapping performed on a thin cross-section lamella sample (see Fig. 5). The composition of each measuring point was averaged over the whole thickness of the lamella (260 nm) and the region analysed included at least 6 different grains. Despite the strong thickness variation and the presence of relatively large voids at the back interface, the cation ratio deviation maps (Fig. 5d) show a quite homogeneous composition with no noticeable intra-grain or inter-grain differences or variations at the grain boundaries. Note that despite the size of the beam spot of roughly 50 nm, nanoXRF is well capable of resolving compositional variations of nanosized features like grain boundaries as demonstrated for both CZTSe[46] and CIGS.[48] In order to go in depth into the homogeneity analysis in the nanoXRF mappings, several scanning lines parallel and perpendicular to the absorber surface were selected. The parallel scanning lines show an overall homogeneous composition. Only in some specific points (*e.g.* at around 4 μm from the left side of the absorber) a decrease of the Zn content is observed. However, the perpendicular scanning lines (in-depth analysis) show a slight increase of the Cu content towards the back region of the absorber (see lines 2 and 3 in Fig. 5d, Δ([Cu]/([Zn] + [Sn])) from −0.04 to +0.04).

Back interface characterization

The CZTSe/back contact interface is characterized by small CZTSe grains (as discussed in the Bulk characterization section), a ∼100 nm $MoSe_2$ layer (resulting from the partial selenization of the Mo back contact during annealing) and the presence of voids.

The voids observed at the back interface of the CZTSe absorber in Fig. 2 and Fig. 5, were studied in more detail using cross-sectional STEM and planar view SEM images (Fig. 6). Two different types of voids can be distinguished in Fig. 6: large micrometric voids (orange rectangles) and small nanometric voids (red rectangles). The micrometric voids observed in cross-section SEM and STEM collage images can achieve sizes up to 0.5 μm^2 (Fig. 2). This represents around 8% of the cross-section area of the CZTSe absorber layer and 37% of the contact interface length between CZTSe and Mo/$MoSe_2$. A different perspective of the micrometric voids can be obtained from the planar view SEM image of the back interface of the absorber (obtained after mechanical lift-off) presented in Fig. 6b. This figure shows that the presence of large voids spreads over the whole back surface of the CZTSe absorber decreasing the contact area with the back contact. In particular, Fig. 6b shows that the contact area between CZTSe and Mo/$MoSe_2$ back contact is around 40% of the total area of the image (in agreement with the cross-sectional

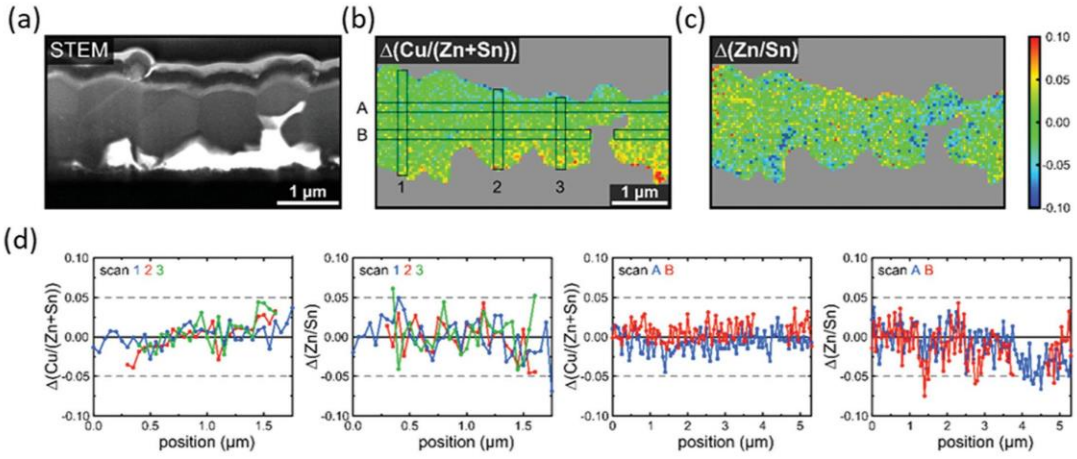

Fig. 5 BF-STEM image (a) and mappings of the deviation of the [Cu]/([Zn] + [Sn]) (b) and [Zn]/[Sn] (c) cation ratios (calculated by subtracting the mean value obtained for the whole sample from the value obtained in each individual pixel). The grey regions (b) and (c) mark the areas where no absorber was present. The graphs at the bottom (d) show the cation ratio deviations (averaged over 3 pixels, 150 nm) along the vertical scans 1, 2, 3, and horizontal scans A, B, as indicated in the top middle panel. Scan B is interrupted in the region where the void is present.

View Article Online
Energy & Environmental Science Paper

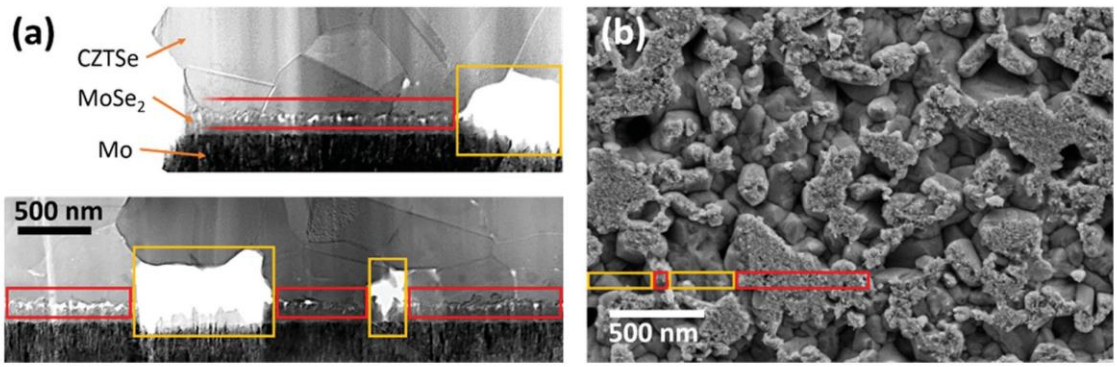

Fig. 6 (a) Collage image of a series of cross-sectional STEM images of the CZTSe device. The CZTSe, $MoSe_2$ and Mo layers in the back interface are indicated. (b) Planar view SEM image of the CZTSe back interface after being detached from the substrate by mechanical lift-off. Red squares indicate regions with nano-voids, and orange squares indicate micro-voids.

analysis). In the case of the small nanometric voids, the cross-sectional STEM image shown in Fig. 6a allows estimating their size to a radius of some tens of nanometres. The presence of these small voids is also confirmed by the rough texture of the CZTSe grains observed in the planar SEM image of the back interface (Fig. 6b). These nanometric voids can create weak points that enable an easy and clean mechanical exfoliation process of the CZTSe absorber from the back contact layer.

In order to evaluate the CZTSe crystal quality, confirm the $MoSe_2$ formation, and evaluate the possible formation of residual secondary phases at the back interface region, a detailed analysis of the Raman scattering spectra measured under 532 nm and 325 nm excitation wavelengths was performed on the back interface of the lifted-off CZTSe absorber, and on the substrate from which the absorber was detached. The use of 532 nm excitation wavelength enables the detection and analysis of the CZTSe phase together with possible formation of Cu–Sn–S and Sn–Se secondary phases.[49] On the other hand, the 325 nm excitation wavelength shows a high sensitivity to the presence of the $SnSe_2$ secondary phase which has been proven to be detrimental for the V_{oc} of CZTSe devices.[31] Likewise, the 325 nm excitation wavelength can also be used for analysing defect types and concentration in the CZTSe phase, which have strong impact on the optoelectronics properties of the device.[49–52] The Raman spectra obtained under 532 and 325 nm excitation wavelengths are presented in Fig. 7a and b, respectively. Both spectra show mainly the CZTSe phase with some peaks of the $MoSe_2$ phase on the back interface of the lifted-off absorber, while only $MoSe_2$ peaks can be observed in the spectra obtained from the substrate. No additional peaks related to any secondary phases were observed in the spectra. The presence of $MoSe_2$ peaks in the back side of the lifted-off absorber arises from the not perfect exfoliation process in which some $MoSe_2$ remains attached to the

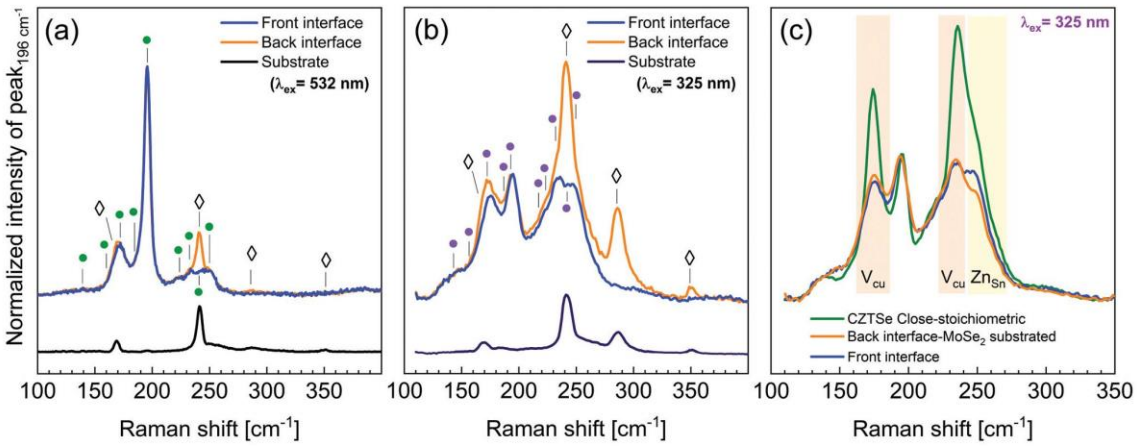

Fig. 7 Raman spectra measured at CZTSe surface and back interface from CZTSe and $MoSe_2$ sides under green (a) and UV (b) excitation wavelength. The dots (●) and diamonds (◊) indicates the position of the CZTSe[47] and $MoSe_2$[50] peaks, respectively. (c) Raman spectra of the close to stoichiometric CZTSe, measured on the absorber surface, and obtained from the back interface of the CZTSe after the $MoSe_2$ subtraction. The shadow areas indicate the spectral regions related to V_{Cu} and Zn_{Sn} punctual defects in the CZTSe.[47]

View Article Online
Paper Energy & Environmental Science

absorber. These $MoSe_2$ peaks are more intense under UV excitation due to its lower penetration depth (it does not typically exceed 10 nm in the case of CZTSe) which results in an analysed volume with a high proportion of $MoSe_2$. This, in turn, results in a high overlapping of the CZTSe and $MoSe_2$ peaks. In order to perform an analysis of the defects present in the CZTSe phase, the spectrum acquired from the substrate (pure $MoSe_2$ phase) was mathematically subtracted from the spectrum acquired from the back side of the absorber for the 325 nm excitation wavelength. The different relative intensity of the $MoSe_2$ peaks in the spectra acquired at back side of absorber and at the substrate indicates a different preferential structural orientation of $MoSe_2$ on substrate and the absorber sides.[53] Taking this into account, the Raman spectrum measured on the back side of the CZTSe absorber was corrected by recalculating the intensities in accordance to the texture[53] (more details in Fig. S3 (ESI†)). The resulting spectrum was compared to a spectrum of a close-to-stoichiometric CZTSe absorber measured under the same excitation conditions (Fig. 7c). A clear variation in the peaks related to V_{Cu} and Zn_{Sn} were observed.[50] These differences indicate that the CZTSe back region is Cu-poor (with higher concentration of the of the V_{Cu} point defect) and Zn-rich (with higher concentration of the Zn_{Sn} point defect).

Front interface characterization

The front interface of the record CZTSe device was analysed after chemically removing the CdS/i-ZnO/ITO top layer. Fig. 7a and b include the Raman spectra acquired at the front interface of the CZTSe absorber with 532 and 325 excitation wavelengths, respectively. Both spectra indicate that the main phase is the CZTSe kesterite type compound and no presence of the secondary phases can be detected. Similarly to the case of the back interface, the spectrum measured under UV excitation wavelength was employed to analyse defect formation in the CZTSe surface by comparing it to a reference stoichiometric CZTSe spectrum (Fig. 7c). The spectrum of the front interface shows a reduced relative intensity of the peaks at 175 and 250 cm^{-1} in comparison to the reference spectrum as in the case of the back interface. This is associated to the formation of the V_{Cu} and Zn_{Sn} point defects expected for the Cu-poor and Zn-rich composition of the absorber.[50] However, a detailed comparison between the spectra of the CZTSe front and back interfaces reveals a different intensity of the V_{Cu} and Zn_{Sn} associated peaks. These differences are related to a slightly reduced V_{Cu} defect concentration and slightly increased Zn_{Sn} defect concentration at the CZTSe back interface region. These variations are in agreement with the small increase of the Cu content at the back interface observed by nanoXRF.

In order to delve into the inhomogeneities in defect formation at the front interface of the absorber, that can have strong influence on the J_{sc} and V_{oc} of the solar cell, a 20×20 μm^2 micro-Raman mapping was performed (Fig. 8a). In the previous Raman measurements, a 70 μm spot was used and information was gathered from several grains in one measurement. Here, micro-Raman measurements, with a spot size <1 μm, allow analysing single grains of the absorber, thus providing information about phase and defect distribution along different grains. The micro-Raman mappings presented in Fig. 8a show a clear difference in the relative intensity of the peaks at 175 and 250 cm^{-1} measured under UV excitation wavelength. As mentioned above, the changes in the relative intensity of these peaks can be directly correlated to the

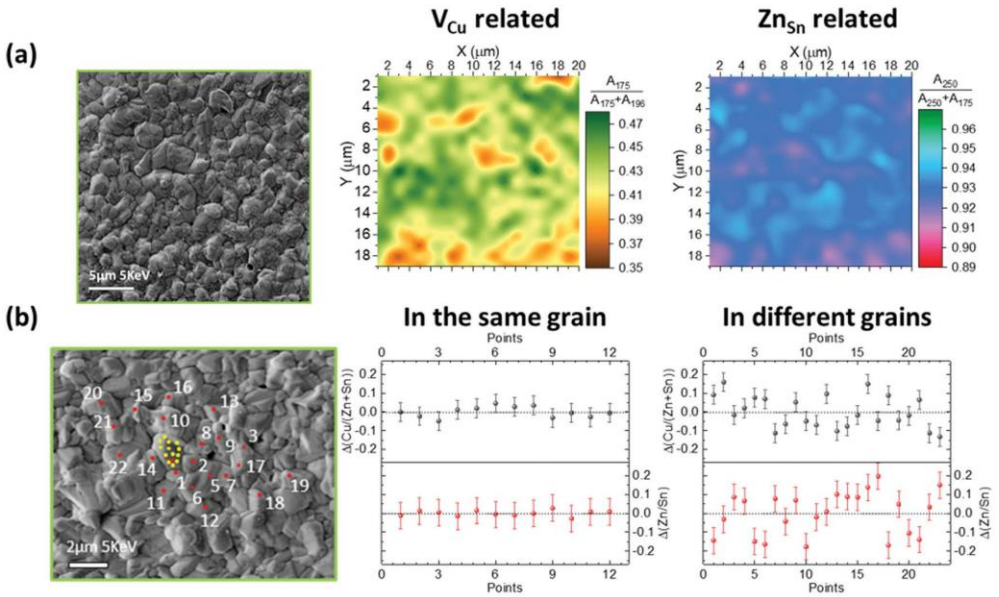

Fig. 8 (a) Micro-Raman mappings of the defects distributions and (b) cations ratios estimated by AES in the CZTSe surface. SEM images of the absorber surface where micro-Raman and AES were carried out are presented on the left side.

View Article Online
Energy & Environmental Science Paper

changes in concentration of V_{Cu} and Zn_{Sn} point defects. The micro-Raman mappings were compared with AES compositional measurements carried out in a similar area of the absorber (Fig. 8b). The AES measurements show similar inhomogeneities in the [Cu]/([Zn] + [Sn]) and [Zn]/[Sn] cationic ratios between the different grains in agreement with the micro-Raman mappings while intragrain variations did not exceed the measurement error. AES is a highly sensitive technique for chemical composition measurements that provides information about the first 1–3 nm of the layer. Taking into account the relative penetration depth of the 325 nm laser used for the Raman analysis, the inhomogeneities detected in the distribution of defects can be directly associated to the compositional inhomogeneities detected by AES in line with reported results.[49,50,54] On the other hand, both Raman and AES suggest a preferential composition in most grains analysed with just slightly different compositions in small regions of the grains. This is in agreement with the nanoXRF results, where only one of the six analysed grains showed small difference in the [Zn]/[Sn] ratio.

In order to exclude possible interlayer diffusion of elements, a compositional characterization of the interfaces between the window and buffer layers, and between the buffer and absorber layers was performed by EELS (Fig. 9). No interlayer diffusion is observed from the elemental maps shown in the figure. It should be noted that although the energy windows were carefully selected for the analysis, the influence of the preceding edge produces artefacts on the elemental maps in some cases, like the O signal detected in the CZTSe region or the Sn signal in i-ZnO region. Moreover, no residual signal of Ge has been detected at the front interface of the analysed device in agreement with ref. 46.

The front interface of the CZTSe device was further investigated by HRTEM images in cross-sectional and planar view configuration. Fig. 10a shows a cross-sectional image of the front interface between the CdS buffer layer and the CZTSe absorber in which both layers can be distinguished by the differences in contrast. FFTs (Fig. 10a.1–a.4) were performed to study the crystallinity of the sample on four different regions tagged as dashed squares in Fig. 10a: the CdS buffer layer, the CZTSe absorber, the CdS/CZTSe interface and the CdS/CZTSe

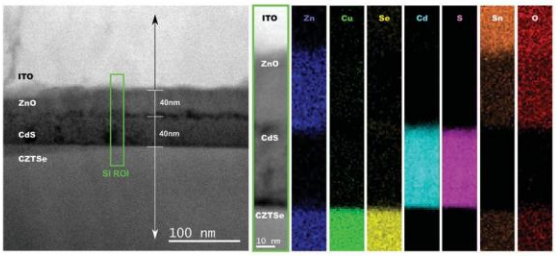

Fig. 9 HAADF image of the front ITO/i-ZnO/CdS/CZTSe interfaces. Green box: region of the EELS scanning image. First stripe on the right: HAADF image of the area in the green box. Rest of stripes: elemental maps extracted from the EELS edges displayed in the top images.

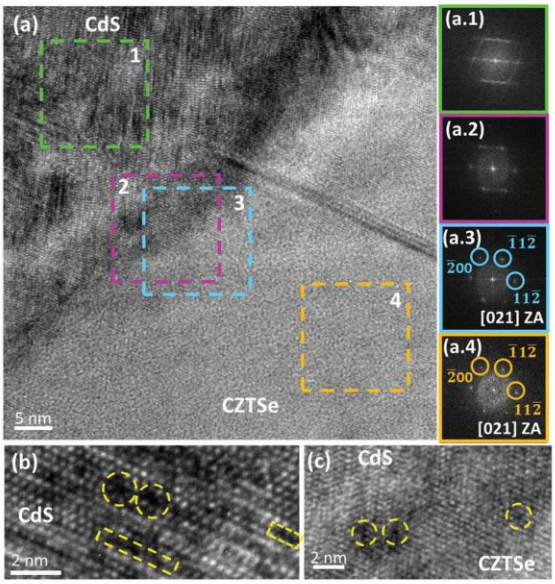

Fig. 10 (a) Cross-sectional HRTEM image of the front interface between the CdS buffer layer and the CZTSe absorber. (a.1)–(a.4) FFT of the corresponding regions indicated by dashed rectangles in (a). ZA and three atomic planes are indicated in FFT with well-defined patterns. (b) Magnified cross-sectional HRTEM image of the CdS layer with highlighted point (dashed circles) and line defects (dashed rectangles). (c) Magnified cross-sectional HRTEM image of front interface between CdS and CZTSe with highlighted point defects.

interface area but displaced a few nanometres towards the CZTSe absorber. The distorted FFT pattern obtained for the CdS region is indicative of a very defective structure (Fig. 10a.1), expectable from a CBD-deposited thin film. The distortion spans down to the interface between the CdS and the CZTSe (Fig. 10a.2), which points out the presence of structural defects in this region as well. By displacing the area of the FFT analysis towards the absorber layer a few nanometres, a well-defined pattern arises in the [021] ZA (Fig. 10a.3). This pattern is almost identical to the one of the bulk of the absorber (Fig. 10a.4). The magnification of the HRTEM images covering the CdS/CZTSe interface reveals the existence of structural point and line defects both in the buffer layer and within the first nanometres of the front interface towards the CZTSe absorber (Fig. 10b and c).

Planar view HRTEM images of the surface of the front interface of CZTSe absorber were acquired after removing the ITO/i-ZnO window layer and the CdS buffer layer by HCl etching and are shown in Fig. 11. Under high enough magnification, the images present multiple short narrow white lines distributed periodically over the surface. They can be attributed to line defects (one-dimensional defect). The periodicity of these defects indicates that they are not a by-product of sample preparation. Similar FFT patterns of areas containing these line defects and areas free of defects (Fig. 11a.1 and a.2) suggest that the line defects do not affect the crystal structure of the surrounding area. In addition, both patterns present the [021] ZA of the CZTSe

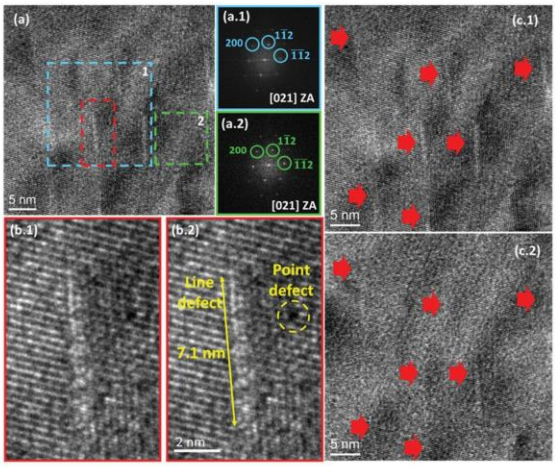

Fig. 11 (a) Planar view HRTEM image of the front interface of the CZTSe device. A lower magnification image with the analysed area highlighted with a dashed rectangle can be found in Fig. S5 (ESI†). (a.1) and (a.2) FFT of the regions indicated by dashed rectangles in (a). The ZA and three atomic planes are indicated. (b) Magnified HRTEM image of the region indicated by a red dashed rectangle in (a), with (b.2) indication of dimensions of a line defect and highlighted point defect. (c) Planar view HRTEM images of the same area of the front interface obtained at different focus. The red arrows indicate dislocation defects.

structure, which means that the observed surface corresponds to CZTSe and, thus, that the ITO, i-ZnO and CdS layers were effectively removed. It can also be observed that the preferred orientation of the observed line defects is parallel to the $(\bar{1}\bar{1}2)$ atomic plane. Magnified planar view HRTEM images of one line defect (Fig. 11b) reveal that the average length of all the observed line defects is about 9 nm. The orientation of the clearly resolved atomic planes does not change before and after the defect, in agreement with the similarity of the FFT patterns. However, some point defects can be observed in the area surrounding the line defect (marked with the dashed circle in Fig. 11b.2). These observations confirm the high density of defects at the front interface between CdS buffer layer and CZTSe absorber observed before in cross-sectional configuration. Fig. 11c shows planar view HRTEM images of the same area but obtained with different focus. The line defects almost disappear as the focus is changed towards the interior of absorber in depth so it can be concluded that these line defects are mainly concentrated at the surface (the remaining traces of the lines are probably related to the artefacts during the measurements). All these observations represent the first direct evidence of defect formation at the front interface of the absorber of kesterite-based PV devices measured in planar view configuration.

Finally, to complete the above presented analysis of the front interface of the absorber, impedance measurements were performed to estimate the carrier distribution throughout the space charge region (SCR). The measurements were performed in the solar cell with the highest efficiency and the data were treated by applying the equivalent circuit model consisting of a series resistor, a parallel resistor and a parallel capacitor[55–57]

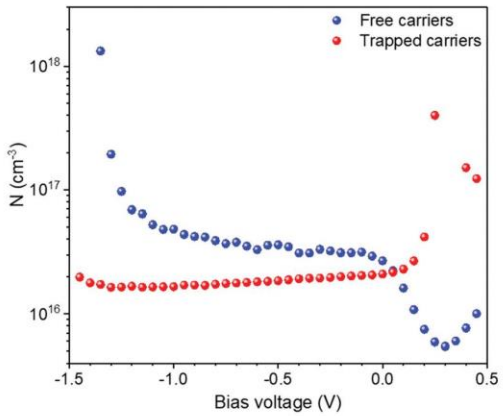

Fig. 12 Dependencies of free and trapped carriers' concentrations from the bias voltage.

(details on the capacitance derived from the impedance data analysis are presented in Fig. S4 (ESI†)). As a result, the dependence of the density of trapped and free carriers with the applied bias voltage was estimated (Fig. 12). It should be noted that an increase of the bias voltage results in a decrease of the width of the SCR. In these conditions, and considering that the SCR mainly lies in the absorber region of the solar cell, it is possible to assume that, at bias voltages >0 V, the carrier concentration will be more strongly influenced by the carriers present at the CdS/CZTSe interface. In these conditions, the drop of the density of free carriers and the increase of the density of trapped carriers at the bias voltage >0 V suggest the there is a higher density of trapping centres at the interface than in the bulk of the absorber. This finding is in accordance with the Raman and HRTEM observations, where a greater concentration of point and line structural defects was detected at the CdS/CZTSe interface.

Discussion

In this section, the main results obtained in the different regions of the CZTSe device are discussed and employed to construct a full picture of possible factors that influence the performance of high efficiency kesterite devices with a focus on their V_{oc}.

The analysis of the CZTSe device has revealed that there is a considerable amount of voids, both micrometric and nanometric, at the back interface. Regarding the nanometric voids, they are not expected to have a noticeable influence on the performance of kesterite devices as their small size ($<$ 50 nm) is significantly lower than the expected diffusion length of minority and majority carriers ($>$500 nm according to reported values).[58,59] Oppositely, the large micrometric holes have been shown to decrease the contact area between the CZTSe absorber and the back contact by $\sim$40%. Consequently, the low diffusion length in CZTSe combined with these large voids undoubtedly hinders charge extraction at the back interface and lies at the

View Article Online
Energy & Environmental Science Paper

origin of the large series resistance observed in the CZTSe device analysed in this work (see Fig. 2a). Although the large series resistance results in a low J_{sc} and FF in the analysed device,[60] which is discussed in the Optoelectronic characterization section, it is not expected to have a significant influence in the V_{oc}. However, besides affecting the back interface, the presence of holes has also been observed to lead to inhomogeneities in the thickness of the CZTSe absorber layer. Additionally, the thickness homogeneity of the active layer, and as result of the upper layers, is suffering from the relatively high roughness of the surface. A high surface roughness can increase the J_{sc} in PV devices since it increases the effective SCR of the device and, thus, increases light absorption and carrier generation.[61] However, in this case, any possible benefit of an increased roughness is shadowed by the strong thickness variation of the absorber layer that results in a low effective thickness impeding an efficient absorption of NIR photons. This effect is in agreement with the observed low IQE of the device at the NIR region (Fig. 1b) and contributes, in addition to the series resistance, to its low J_{sc}. Similar effects in the J_{sc} and the IQE have been reported in absorber thinning studies in CIGS devices.[62–65] In addition, the combination of large voids and thickness variations can produce fluctuations of the SCR width up to appearance of shunt paths that would limit the V_{oc} of the device. The presence of areas with thickness below the width of the SCR can be clearly observed in the SEM image presented in Fig. 2. Finally, in the case of wider band gap kesterite absorbers, the variation in thickness and increased roughness can result in a higher front interface area that may aggravate CdS/CZTSe alignment-related interface recombination issues lowering the V_{oc} and FF of the device.[66] However, this should not affect the device analysed in this work since a favourable spike-like band alignment is expected between CZTSe and CdS.[67]

Regarding the origin of such large holes and thickness inhomogeneities, different possibilities can be considered. The first one is related to the well-known volatility of SnSe that, if formed at the back, would left voids behind after evaporation at the high temperatures employed for the synthesis of CZTSe.[68] Another possibility would be that the voids originate upon the reaction of CZTSe with Mo as previously reported.[36] However, the cross sectional images presented in this work suggest that the formation of voids may be somehow related to the observed bilayer absorber structure with small grains towards the back interface (see Fig. 2 and 3a). More specifically, it seems that some of the voids observed at the back interface arise from the absence of small grains at the bottom (Fig. 3a). This implies that the origin of the voids could be more fundamentally linked to the crystallization process and formation pathway of the CZTSe phase itself than to an ''external cause''.

The combination of different transmission electron microscopy techniques for the analysis of bulk of the absorber has revealed that the analysed CZTSe device has a good crystalline quality, with kesterite type structure, very regular and well defined grain boundaries and without element interdiffusion. These observations hint that the crystalline structure of the absorber bulk region is not the main origin of the V_{oc} deficit in high efficiency CZTSe devices. However, despite the good crystal quality, both small grains in some back interface regions (as explained above) and twinning defects have been observed in the bulk of the absorber (see Fig. 3). Although the grain boundaries are generally considered as benign in CZTSe,[69,70] a large density of horizontal grain boundaries and twinning defects could act as barriers that shorten the diffusion length of carriers and increase recombination in the bulk of the absorber. This would be reflected in the device as an increased series resistance, impacting the FF and J_{sc}.

The presence of voids and small grains at the back interface is not usually discussed or reported for high efficiency CZTSe devices.[7,8,45,71,72] However, it seems that they are universal features of the kesterite technology since they can be observed even in kesterite devices with efficiencies beyond 12%.[6,73] As such, it is difficult to come to a solid conclusion about and their real limiting effect on the optoelectronic properties of kesterite solar cells.

All the compositional measurements performed in this work point towards an overall Cu-poor Zn-rich homogeneous absorber composition. Nevertheless, the use of advanced spectroscopy techniques at the micro- and nanoscale has revealed slight inter-grain compositional variations. In particular, these were observed in cross-sectional configuration nanoXRF analysis and at the top interface of the absorber from AES and micro-Raman studies. All these slight compositional variations translate into changes in the intrinsic defect concentration and the preferential point defects in the CZTSe[49,54] which, in turn, may cause grain-to-grain non-uniformity of the electrical and optical properties of the absorber. These changes may cause finally inhomogeneity in the performance of each individual grain and band fluctuation effects resulting in overall decrease of mainly V_{oc} that is directly related to the intrinsic properties of the absorber. In addition, a slight inhomogeneity was observed in-depth by nanoXRF and UV-Raman. This indicates an increase of the Cu content in the bottom region and a reduction of the V_{Cu} defects. This gradient affects charge carrier mobility and recombination at the back interface. On the other hand, it should be noted that no evidence of secondary phases (except for $MoSe_2$ at the back interface) has been found throughout the device so the compositional variations observed can be attributed solely to the kesterite phase. Finally, the inclusion of a Ge nanolayer in our standard process is a particularity of the present device (it is not the general procedure for the state of the art devices). Although the presence of residual Ge in the bulk of the absorber grains, mainly aggregated in the form of GeO_2, has been proposed to contribute to recombination mechanisms,[46] the reduced Ge layer thickness employed in our process results in a negligible effect in device performance. Furthermore, analyses of the influence of the Ge nanolayer on the bulk of the absorber concluded that it mainly affects the kesterite formation pathway leading to an improved crystalline properties and no effect in the interfaces has been observed.[45,46,74] As such, the effect of the Ge nanolayer was mostly excluded from the evaluation and discussions presented in this work.

View Article Online
Paper Energy & Environmental Science

The formation of $MoSe_2$ at the back interface has been confirmed by Raman and STEM. The latter has shown that the thickness of this layer is around 100 nm which can be considered to be in the optimum range and not have a detrimental effect on the device.[38] However, Raman spectroscopy has revealed a difference in the relative intensity of the peaks of this layer in the absorber and substrate sides of the lifted-off samples. This is an indication of a different preferential structural orientation of $MoSe_2$ on each side,[53] and implies that this layer is really formed by two staked $MoSe_2$ layers with different textures: one close to the back region of the absorber and the other one close to the Mo contact. Changes in the orientation of the *c*-axis (perpendicular or parallel to the substrate) of $MoSe_2$ have been reported to have a relevant impact on the electrical and electronic properties of the back interface both for $CuIn(S,Se)_2$[75] and CZTSe[37] devices having a profound impact in the FF and V_{oc}. Therefore, the double texture observed in the device analysed in this work is likely to be causing a strong anisotropy of the electrical and electronic properties of the back interface and, consequently, influencing the FF and V_{oc} of the device.

The study of the front interface by HRTEM has revealed that there is a transitional region at the front interface of about 6 nm which is not so defective as the CdS buffer layer, but that has a worse crystalline quality than the bulk of the CZTSe absorber with a high density of line and point defects. These defects cover the full surface of the absorber and their appearance is in a great accordance with the presented Raman scattering results, which also showed a higher concentration of V_{Cu} and Zn_{Sn} point defects at the front interface of the absorber, and with the reduced concentration of free charge carriers observed by admittance spectroscopy. The line defects have been found to have a periodicity and a preferred orientation which implies that they are dislocations generated by stress relaxation. This means that there is an important stress at the front interface that is not present in the bulk of the absorber, which generates dislocations of the atomic planes that can act as recombination centres and affect the V_{oc} of the device. The clear presence and higher density of defects encountered at the front interface suggests that this interface may be the main limitation for the V_{oc} of the analysed device. The use of passivation layers at the front interface, or an etching technique to remove superficially these defects, could mitigate this issue. This has already been suggested in previous reports by applying a passivation Al_2O_3 layer,[20,40,41] sulfurizing the CZTSe surface,[39] and performing a surface oxygen plasma treatment.[11]

Finally, Cu–Zn disordering, usually pointed out as the main cause of the V_{oc} deficit in kesterites[27,76,77] was not described in the present study. Unfortunately, the EELS measurements carried out in this work did not allow an atomic-resolved analysis. Thus, it was not possible to determine which specific element corresponds to each atom resolved in the HAADF images (Fig. 4). As such, Cu–Zn disordering is likely to have a significant influence in the V_{oc} deficit of the device analysed in this work although no concluding proof of this can be provided.

Based on the presented findings and their possible influence on kesterite devices, it is possible to point out several issues that could be addressed as a general roadmap to overcome the existing efficiency limitations of the kesterite technology. Firstly, the development of a strict fabrication process focused on a high reproducibility would minimize some of the well-known and widely discussed problems typically found in kesterite absorbers such as secondary phases, low crystalline quality and compositional inhomogeneities as well as those observed in this work such as the twining defects, and double layer structure of the grains. However, at the current level of development of the technology, the appearance of inhomogeneity problems is mostly unavoidable and seems a fundamental property of kesterites due to their high compositional flexibility that allows a high degree of stoichiometric and structural fluctuations.[49] Nevertheless, we strongly believe that slight compositional and structural inhomogeneities may just have a residual effect on device performance at the current level of development of the technology in comparison to the problems located at the interfaces. Regarding the back interface, the development of strategies that ensure a good element intermixing and favor a formation pathway that avoids the formation of volatile phases (see ref. 42, 74 and 78) could minimize the appearance of large voids. As for the front interface, the distorted region with increased amount of point and line defects found in this work could be eliminated employing specific passivation or etching strategies (see ref. 17 and 40) as well as by researching on alternative materials and deposition techniques for the buffer layer that have better band and structural alignment with the kesterite absorber.

Conclusions

The combination of advanced electron microscopy and spectroscopy techniques at the macro, micro and nanoscale has enabled to carry out a deep analysis of defect formation in a high efficiency CZTSe device. The work has tackled the simultaneous investigation of the bulk and the front and back interfaces to assess the impact on the performance of the defects found in each part of the device. Table 2 summarizes the main findings identified in this work as potential issues, their location within the device, the technique employed to detect them and their possible influence on device performance. The study of the bulk has revealed large absorber thickness variations that reduce NIR photon absorption and increase the probability of shunting. On the other hand, a good crystalline quality, homogeneous composition and well-defined grain boundaries have been observed in the bulk of the absorber. However, the analysis has also revealed the formation of a bilayer structure with small grains at the bottom and of twinning defects that could act as barriers leading to recombination. Voids have been observed at the back interface decreasing the contact area between CZTSe and Mo and leading to a high series resistance in the device. Finally, a high density of defects and grain-to-grain non-uniformities have been observed at the

View Article Online
Energy & Environmental Science Paper

Table 2 Summary of the main findings identified by different advanced techniques in bulk and interfaces of CZTSe absorber layer and their possible impact in the device performance

Device layer	Findings	Technique	Main possible influence on device performance
CZTSe/CdS front interface	V_{Cu} and Zn_{Sn} point defects	Macro-Raman spectroscopy	Control P-type doping, act as recombination centres and affect V_{oc} device
	Grain-to-grain non-uniformity[a]	Micro-Raman spectroscopy, AES	Contribution in band fluctuations impacting in the V_{oc}
	~6 nm depth distorted region[a], point and line structural defects[a]	Cross-sectional & planar view HRTEM	Recombination in the space charge region, reduction of V_{oc}
	Decrease of the density of free charge carriers	Admittance spectroscopy	Reduction of J_{sc}
CZTSe bulk	Good crystalline quality grains & well defined grain boundaries	Cross-sectional HRTEM	Good carrier mobility
	Twinning defects[a]	Cross-sectional HRTEM	Bulk recombination centres affecting FF and J_{sc}
	Thickness inhomogeneity	Cross-sectional HRTEM and SEM	Space charge region fluctuation, shunting, decrease J_{sc} due to reduce absorption of NIR photons
	Bilayer structure (small grains in the bottom)	Cross-sectional HRTEM and SEM	Bulk recombination centres affecting FF and J_{sc}
	Slightly in-depth compositional inhomogeneity	nanoXRF	Impact in the mobility and recombination of charge carriers
Mo/$MoSe_2$/CZTSe back interface	~100 nm $MoSe_2$ thickness	Cross-sectional TEM	Favourable thickness for ohmic back contact
	Bilayer structure of $MoSe_2$ layer[a]	Raman spectroscopy	Influences in electrical properties in the back contact, FF and V_{oc}
	Voids	Planar view SEM & cross-sectional TEM	Shunting, decrease back contact area, reduction of FF and J_{sc}, reduction of the NIR photon absorption, decrease J_{sc}

[a] Issues of the kesterite absorbers found or clearly observed for the first time.

front interface. The defective area covers the full surface of the absorber and extends from the CdS/CZTSe interface towards the first 6 nm of the absorber with a high presence of line and point defects. These results point towards the front interface being the main source of V_{oc} deficit of the device. Nevertheless, the issues observed in the bulk and back interface also represent important and comparable drawbacks for device performance. This work has provided, for the first time, direct evidence of twinning defects in the bulk, micro and nano-voids at the back interface and of the widely-suspected high density of defects at the front interface. This represents a step forward in the comprehension of the main limitations of the kesterite solar cells and opens the way to the identification of new solutions to further developing this technology and pushing it towards higher performances.

Experimental

The high-efficiency CZTSe solar cell device analysed in this work was fabricated through a sequential process. First, a Cu/Sn/Cu/Zn metallic stack precursor was deposited by DC magnetron sputtering (Alliance Concept Ac540) onto a Mo coated soda lime glass (SLG) substrate. The thickness of the different layers of the stack was selected to obtain a Cu-poor Zn-rich composition with [Cu]/([Zn] + [Sn]) = 0.73 and [Zn]/[Sn] = 1.11 as measured macroscopically by XRF (Fisherscope XDV-SDD). A 10 nm Ge nanolayer was evaporated (Oerlikon Univex 250) on top of the precursor mainly to control the formation pathway as previously described in ref. 45 and 74. The metallic precursor was then reactively annealed under a Se + Sn atmosphere to form the CZTSe absorber, and several chemical etching treatments were applied to remove selectively secondary phases and to passivate the surface as reported elsewhere.[74] The solar cell was completed with a CdS buffer layer deposited by chemical bath deposition with reduced layer growth kinetics based on the use of cadmium nitrate precursor salts as described elsewhere.[67] The deposition of the buffer layer was followed by pulsed DC magnetron sputtering (Alliance Concept CT100) deposition of i-ZnO and In_2O_3–SnO_2 (ITO) window layers. The different layers composing the complete device are depicted in Fig. 13 (left). Individual 3 × 3 mm^2 solar cells were mechanical scribed employing a manual microdiamond scriber (OEG MR200).

The *J*–*V* characteristics of the devices were obtained under simulated AM1.5 illumination using a pre-calibrated Sun 3000 Class AAA solar simulator (Abet Technologies). The EQE, IQE and reflectance of the solar cells were measured using a spectral response system (Bentham PVE300) calibrated with Si and Ge photodiodes. The electronic properties of the solar cells were characterized by impedance spectroscopy using a Keysight E4990A Impedance Analyzer. Impedance measurements were carried out at room temperature in dark conditions with a 50 mV alternating current (AC) signal over 40 AC frequency steps (from 20 Hz to 10 MHz), and 41 bias voltage steps (from −1.5 V to 0.5 V). The frequency range was stablished in accordance to the limitations of the system, while the voltage range was determined by the V_{oc} of the device and signal-to-noise ratio criteria. The number of steps was selected to allow a proper calculation of the first derivatives of capacitances $C(\omega)$ and $C(V)$.

View Article Online
Paper Energy & Environmental Science

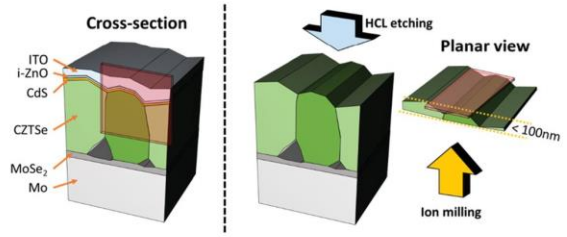

Fig. 13 Schematic representation of the sample preparation for cross-section (left) and planar (right) view STEM geometries. The observation planes are highlighted with red rectangles. For planar view geometry, the direction of HCl etching to remove CdS, i-ZnO and ITO layers, and of the ion milling to thin down the CZTSe absorber are indicated with a blue and yellow arrow, respectively.

The morphology at the micro and nanoscales was investigated by SEM, and several configurations of TEM: STEM, HRTEM and HAADF. The use of different electron microscopy techniques and imaging modes allows focusing on different characteristics of the absorber at different scales. In this way, SEM and STEM images were mainly used for an overall view of the device at a microlevel, for investigation absorber grains and voids, and for selecting interesting regions for further deeper analysis. Subsequently, HRTEM and HAADF provided results about the structural and compositional properties of the absorber and the interfaces at the nanoscale. All these techniques were used both in cross-sectional and planar view configuration as presented in Fig. 13. Regarding the cross-sectional sample preparation for TEM, FIB was used. A platinum nanolayer was deposited onto the sample to protect its surface from the aggressive FIB etching process. On the other hand, the planar view required a carefully adjusted sample preparation (see Fig. S6 (ESI†)) that, to the best of our knowledge, has not been previously reported for kesterite based devices. This preparation started with the removal of the ITO, i-ZnO and CdS layers by submitting the sample to a chemical etching in HCl (5% v/v). Then, the etched sample was cut with a filament diamond saw into 3 mm thick (including the SLG substrate) 2.5 × 2.5 mm^2 pieces. These pieces were then polished from the substrate side to preserve the front interface surface (see Fig. 13, right). A first polishing was carried out with a series of diamond abrasive films with decreasing grain sizes (30, 15, 6, 1 and 0.5 μm), a until the samples were thinned down to 30–70 μm. Then, a final thinning (down to a thickness < 50 nm) was performed by ion milling tripod polisher kit (model 590, South Bay Technologies) and a 12″ metallographic manual polisher (NANO 1200T, Pace Technologies) using a Fischione 1010 Precision Ion Polishing System with the upper source working at 5.0 kV and 5.0 mA. Although the mechanical polishing approach was successfully implemented for the planar view preparation, some difficulties are worth mentioning. For instance, the CZTSe multilayer overall thickness complicated the thinning process down to the electron transparency range. Furthermore, the observable area was small since, being a granular sample, the CZTSe thin foil resulted extremely brittle and some sections were easily damaged when handling, but without affecting the remaining electro-transparent regions.

SEM images were obtained with a ZEISS Series Auriga microscope using 5 kV accelerating voltage. The HRTEM planar view images were acquired in a JEOL-2100 with a LaB_6 filament at 200 keV. The HRTEM and low magnification DF-BF cross-sectional images were acquired in a JEOL-2010F with a field emission gun at 200 keV. The high resolution HAADF (STEM) images and EELS spectrum images were acquired in a JEOL-ARM-F with field emission gun at 200 keV (FEG electron source and C_s aberration correction in the condenser lens system). The obtained images were analysed through a combination of Gatan Digital Micrograph proprietary software and Hyperspy (Python-based) free software. CaRIne Crystallography and TEM-UCA EJE-Z[79] were also used to identify the crystalline structures.[80]

Raman spectroscopy was employed to analyse the presence of secondary phases and point defects in the macro scale at the front (after a chemical removing the top layers with an etching in 5% v/v HCl) and back (after detaching the absorber from the substrate through a mechanical lift-off process, see Fig. S7 (ESI†)) interfaces. A FHR640 Horiba Jobin Yvon spectrometer coupled to a Raman probe developed at IREC and a CCD detector cooled to −70 °C was used. Laser excitation wavelengths of 325 and 532 nm were employed in backscattering configuration. A laser power density of about 50 W cm^{-2} was used to prevent thermal effects on the samples and the diameter of the laser macro-spot was around 70 μm. The Raman shift was calibrated using a monocrystalline Si reference by imposing the position of its main peak to be at 520 cm^{-1}. An unpolarised laser beam was used to minimize the impact of the crystalline orientation in the Raman spectra.

Mappings of the defect distribution at the microscale were performed at the front interface of the absorber by micro-Raman spectroscopy using a LabRam spectrometer (Horiba Jobin Yvon) coupled with a CCD. The measurements were performed in a backscattering configuration under a 532 nm excitation wavelength. An Olympus metallographic microscope was used to allow the concentration of the measurement spot down to 1 μm. The laser power did not exceed 1 mW. A high precision *XY*-stage was used to manipulate the sample and enable mapping a 20 × 20 μm^2 area. Auger electron spectroscopy (AES) was performed at the front interface of the absorber in similar area to study the compositional homogeneity at the nanoscale using a PHI 670 Scanning Auger Microscope from Physical Electronics. The Auger spectra were acquired using a FE electron source working at 10 keV and 10 nA. The mappings were performed in UHV (below 10^{-10} Torr) and measurements were done using a point spot (diameter around 50 nm) with an estimated penetration depth in the range of 1 to 3 nm. To remove the signal corresponding to adventitious carbon and native surface oxidation that occurs on a surface exposed to air, a 3.5 keV light Ar^+ ion surface sputtering of ∼2 nm was performed previously to the measurements. Multipak version 9.9.08 software from ULVAC-PHI was used for data treatment of the signal for the different cations.

The composition throughout the bulk of the absorber was analyzed by nanoXRF on a cross-sectional lamella prepared

View Article Online
Energy & Environmental Science Paper

using a FIB. The nanoXRF measurements were performed in spot analysis and mapping mode at the nano-analysis beamline ID16B of the European Synchrotron Radiation Facility (ESRF) in Grenoble, France.[81] The X-ray energy was set to 29.6 keV in "pink-beam" mode with a focal spot size of 54×52 nm^2 and an average flux of 2.5×10^{10} photons per s. The lamella was raster scanned through the nano-beam with a step size of 50 nm in the vertical and horizontal directions. Detecting the emitted X-ray fluorescence radiation for each position by two 3-element silicon drift detectors, and fitting the respective spectra, provides compositional information for each individual spot.[46] Finally, electron energy-loss spectroscopy (EELS) (GIF Quantum EF spectrometer attached to JEOL-ARM-F) was used to study interlayer element diffusion at the front interface.

Conflicts of interest

There are no conflicts to declare.

Acknowledgements

The authors acknowledge the ESRF for provision of synchrotron radiation (experiment: MA-3564). This research was partially supported by the H2020 Programme under the project INFINITE-CELL (H2020-MSCA-RISE-2017-777968), by the In4CIS project from the SOLAR-ERA.NET International program (subproject ref. PCIN-2018-48), and by the Spanish Ministry of Science, Innovation and Universities under the FOTOSENS project (RTC-2017-5857-3). Part of this work was financially supported by the German Federal Ministry of Education and Research under the nano@work project (contract number: 05K16SJ1) and by the Deutsche Forschungsgemeinschaft (DFG, German Research Foundation) under the project number SCHN 1283/2-1. Authors from IREC and the University of Barcelona belong to the SEMS (Solar Energy Materials and Systems) Consolidated Research Group of the "Generalitat de Catalunya" (Ref. 2017 SGR 862), and acknowledge the support of the European Regional Development Funds (ERDF, FEDER Programa Competitivitat de Catalunya 2007–2013). Other UB authors belong to the Consolidated Research Group of the "Generalitat de Catalunya" MIND (Micro-nanotechnology and nanoscopies for electronic and photonic devices) (Ref. 2017 SGR 776) and acknowledge funding from the Spanish Ministery through the research project MAT2017-79455-P and research network RED2018-102609-T. M. P. and M. G. thanks the Government of Spain for the Ramon y Cajal (RYC-2017-23758) and Juan de la Cierva (IJC2018-038199-I) Fellowships, respectively.

References

1 First Solar, First Solar Achieves Yet Another Cell Conversion Efficiency World Record, http://www.pes.eu.com/renewable-news/first-solar-achieves-yet-another-cell-conversion-efficiency-world-record/, accessed June 2020.
2 Solar Frontier, Solar Frontier Achieves World Record Thin-Film Solar Cell Efficiency of 23.35%, http://www.solar-frontier.com/eng/news/2019/0117_press.html, accessed June 2020.
3 C. Candelise, M. Winskel and R. Gross, *Prog. Photovoltaics*, 2012, **20**, 816–831.
4 A. Feltrin and A. Freundlich, *Renewable Energy*, 2008, **33**, 180–185.
5 G. Phipps, C. Mikolajczak and T. Guckes, Indium and Gallium: long-term supply, http://www.renewableenergyfocus.com/view/3322/indium-and-gallium-long-term-supply/, accessed June 2020.
6 W. Wang, M. T. Winkler, O. Gunawan, T. Gokmen, T. K. Todorov, Y. Zhu and D. B. Mitzi, *Adv. Energy Mater.*, 2014, **4**, 1301465.
7 Z. Su, G. Liang, P. Fan, J. Luo, Z. Zheng, Z. Xie, W. Wang, S. Chen, J. Hu, Y. Wei, C. Yan, J. Huang, X. Hao and F. Liu, *Adv. Mater.*, 2020, **32**, 2000121.
8 X. Li, D. Zhuang, N. Zhang, M. Zhao, X. Yu, P. Liu, Y. Wei and G. Ren, *J. Mater. Chem. A*, 2019, **7**, 9948–9957.
9 T. Feurer, R. Carron, G. Torres Sevilla, F. Fu, S. Pisoni, Y. E. Romanyuk, S. Buecheler and A. N. Tiwari, *Adv. Energy Mater.*, 2019, **9**, 1901428.
10 J. AbuShama, R. Noufi, S. Johnston, S. Ward and X. Wu, in Conference Record of the Thirty-first IEEE Photovoltaic Specialists Conference, 2005, IEEE, pp. 299–302.
11 H. Tampo, S. Kim, T. Nagai, H. Shibata and S. Niki, *ACS Appl. Mater. Interfaces*, 2019, **11**, 13319–13325.
12 O. Gunawan, T. K. Todorov and D. B. Mitzi, *Appl. Phys. Lett.*, 2010, **97**, 233506.
13 D. A. R. Barkhouse, O. Gunawan, T. Gokmen, T. K. Todorov and D. B. Mitzi, *Prog. Photovoltaics*, 2012, **20**, 6–11.
14 J. J. Scragg, T. Ericson, X. Fontané, V. Izquierdo-Roca, A. Pérez-Rodríguez, T. Kubart, M. Edoff and C. Platzer-Björkman, *Prog. Photovoltaics*, 2014, **22**, 10–17.
15 Y. Zhao, X. Han, B. Xu, W. Li, J. Li, J. Li, M. Wang, C. Dong, P. Ju and J. Li, *IEEE J. Photovolt.*, 2017, **7**, 874–881.
16 Z.-K. Yuan, S. Chen, H. Xiang, X.-G. Gong, A. Walsh, J.-S. Park, I. Repins and S.-H. Wei, *Adv. Funct. Mater.*, 2015, **25**, 6733–6743.
17 H. Xie, Y. Sáncheza, P. Tang, M. Espíndola-Rodríguez, M. Guc, L. Calvo-Barrio, S. López-Marino, Y. Liu, J. R. Morante, A. Cabot, V. Izquierdo-Roca, J. Arbiol, A. Pérez-Rodríguez and E. Saucedo, *Sol. RRL*, 2019, **3**, 1800279.
18 Y. Sánchez, M. Espíndola-Rodríguez, H. Xie, S. López-Marino, M. Neuschitzer, S. Giraldo, M. Dimitrievska, M. Placidi, V. Izquierdo-Roca, F. A. Pulgarín-Agudelo, O. Vigil-Galán and E. Saucedo, *Sol. Energy Mater. Sol. Cells*, 2016, **158**, 138–146.
19 L. Yin, G. Cheng, Y. Feng, Z. Li, C. Yang and X. Xiao, *RSC Adv.*, 2015, **5**, 40369–40374.
20 M. E. Erkan, V. Chawla and M. A. Scarpulla, *J. Appl. Phys.*, 2016, **119**, 194504.
21 S. López-Marino, Y. Sánchez, M. Placidi, A. Fairbrother, M. Espindola-Rodríguez, X. Fontané, V. Izquierdo-Roca, J. López-García, L. Calvo-Barrio, A. Pérez-Rodríguez and E. Saucedo, *Chem. – Eur. J.*, 2013, **19**, 14814–14822.

22 Y. Zhao, X. Han, L. Chang, J. Li, C. Dong, Y. Fang and J. Li, *Sol. Energy Mater. Sol. Cells*, 2018, **179**, 427–434.
23 S. Chen, A. Walsh, X.-G. Gong and S.-H. Wei, *Adv. Mater.*, 2013, **25**, 1522–1539.
24 S. Schorr, *Sol. Energy Mater. Sol. Cells*, 2011, **95**, 1482–1488.
25 M. Paris, L. Choubrac, A. Lafond, C. Guillot-Deudon and S. Jobic, *Inorg. Chem.*, 2014, **53**, 8646–8653.
26 G. Rey, G. Larramona, S. Bourdais, C. Choné, B. Delatouche, A. Jacob, G. Dennler and S. Siebentritt, *Sol. Energy Mater. Sol. Cells*, 2018, **179**, 142–151.
27 T. Gokmen, O. Gunawan, T. K. Todorov and D. B. Mitzi, *Appl. Phys. Lett.*, 2013, **103**, 103506.
28 M. Neuschitzer, Y. Sanchez, T. Olar, T. Thersleff, S. Lopez-Marino, F. Oliva, M. Espindola-Rodriguez, H. Xie, M. Placidi, V. Izquierdo-Roca, I. Lauermann, K. Leifer, A. Pérez-Rodriguez and E. Saucedo, *Chem. Mater.*, 2015, **27**, 5279–5287.
29 G. Rey, A. Redinger, J. Sendler, T. P. Weiss, M. Thevenin, M. Guennou, B. El Adib and S. Siebentritt, *Appl. Phys. Lett.*, 2014, **105**, 112106.
30 H. Xie, Y. Sánchez, S. López-Marino, M. Espíndola-Rodríguez, M. Neuschitzer, D. Sylla, A. Fairbrother, V. Izquierdo-Roca, A. Pérez-Rodríguez and E. Saucedo, *ACS Appl. Mater. Interfaces*, 2014, **6**, 12744–12751.
31 I. Becerril-Romero, L. Acebo, F. Oliva, V. Izquierdo-Roca, S. López-Marino, M. Espíndola-Rodríguez, M. Neuschitzer, Y. Sánchez, M. Placidi, A. Pérez-Rodríguez, E. Saucedo and P. Pistor, *Prog. Photovoltaics*, 2018, **26**, 55–68.
32 T. Schwarz, O. Cojocaru-Mirédin, P. Choi, M. Mousel, A. Redinger, S. Siebentritt and D. Raabe, *J. Appl. Phys.*, 2015, **118**, 095302.
33 K. Sardashti, R. Haight, T. Gokmen, W. Wang, L.-Y. Chang, D. B. Mitzi and A. C. Kummel, *Adv. Energy Mater.*, 2015, **5**, 1402180.
34 I. L. Repins, H. Moutinho, S. G. Choi, A. Kanevce, D. Kuciauskas, P. Dippo, C. L. Beall, J. Carapella, C. DeHart, B. Huang and S. H. Wei, *J. Appl. Phys.*, 2013, **114**, 084507.
35 J. J. Scragg, J. T. Wätjen, M. Edoff, T. Ericson, T. Kubart and C. Platzer-Björkman, *J. Am. Chem. Soc.*, 2012, **134**, 19330–19333.
36 S. López-Marino, M. Placidi, A. Pérez-Tomás, J. Llobet, V. Izquierdo-Roca, X. Fontané, A. Fairbrother, M. Espíndola-Rodríguez, D. Sylla, A. Pérez-Rodríguez and E. Saucedo, *J. Mater. Chem. A*, 2013, **1**, 8338–8343.
37 S. Lopez-Marino, M. Espíndola-Rodríguez, Y. Sánchez, X. Alcobé, F. Oliva, H. Xie, M. Neuschitzer, S. Giraldo, M. Placidi, R. Caballero, V. Izquierdo-Roca, A. Pérez-Rodríguez and E. Saucedo, *Nano Energy*, 2016, **26**, 708–721.
38 B. Shin, Y. Zhu, N. A. Bojarczuk, S. Jay Chey and S. Guha, *Appl. Phys. Lett.*, 2012, **101**, 053903.
39 S. Wang, S. Gao, D. Wang, Z. Jiang, J. Ao, Z. Zhou, S. Liu, Y. Sun and Y. Zhang, *Sol. RRL*, 2019, **3**, 1800236.
40 E. Ojeda-Durán, K. Monfil-Leyva, J. Andrade-Arvizu, I. Becerril-Romero, Y. Sánchez, R. Fonoll-Rubio, M. Guc, Z. Jehl, J. A. Luna-López, A. L. Muñoz-Zurita, J. A. D. Hernández-de la Luz, V. Izquierdo-Roca, M. Placidi and E. Saucedo, *Sol. Energy*, 2020, **198**, 696–703.
41 J. Kim, S. Park, S. Ryu, J. Oh and B. Shin, *Prog. Photovoltaics*, 2017, **25**, 308–317.
42 T. Gershon, B. Shin, N. Bojarczuk, M. Hopstaken, D. B. Mitzi and S. Guha, *Adv. Energy Mater.*, 2015, **5**, 1400849.
43 L. Grenet, M. A. A. Suzon, F. Emieux and F. Roux, *ACS Appl. Energy Mater.*, 2018, **1**, 2103–2113.
44 S. Giraldo, Z. Jehl, M. Placidi, V. Izquierdo-Roca, A. Pérez-Rodríguez and E. Saucedo, *Adv. Mater.*, 2019, **31**, 1806692.
45 S. Giraldo, E. Saucedo, M. Neuschitzer, F. Oliva, M. Placidi, X. Alcobé, V. Izquierdo-Roca, S. Kim, H. Tampo, H. Shibata, A. Pérez-Rodríguez and P. Pistor, *Energy Environ. Sci.*, 2018, **11**, 582–593.
46 M. Ritzer, S. Schönherr, P. Schöppe, W. Wisniewski, S. Giraldo, G. Gurieva, A. Johannes, C. T. Plass, K. Ritter, G. Martínez-Criado, S. Schorr, E. Saucedo, C. Ronning and C. S. Schnohr, *ACS Appl. Energy Mater.*, 2020, **3**, 558–564.
47 S. Chen, X. G. Gong, A. Walsh and S.-H. Wei, *Appl. Phys. Lett.*, 2009, **94**, 041903.
48 P. Schöppe, S. Schönherr, P. Jackson, R. Wuerz, W. Wisniewski, M. Ritzer, M. Zapf, A. Johannes, C. S. Schnohr and C. Ronning, *ACS Appl. Mater. Interfaces*, 2018, **10**, 40592–40598.
49 S. Schorr, G. Gurieva, M. Guc, M. Dimitrievska, A. Pérez-Rodríguez, V. Izquierdo-Roca, C. S. Schnohr, J. Kim, W. Jo and J. M. Merino, *J. Phys. Energy*, 2020, **2**, 012002.
50 M. Dimitrievska, F. Oliva, M. Guc, S. Giraldo, E. Saucedo, A. Pérez-Rodríguez and V. Izquierdo-Roca, *J. Mater. Chem. A*, 2019, **7**, 13293–13304.
51 M. Dimitrievska, S. Giraldo, P. Pistor, E. Saucedo, A. Pérez-Rodríguez and V. Izquierdo-Roca, *Sol. Energy Mater. Sol. Cells*, 2016, **157**, 462–467.
52 M. Dimitrievska, A. Fairbrother, E. Saucedo, A. Pérez-Rodríguez and V. Izquierdo-Roca, *Sol. Energy Mater. Sol. Cells*, 2016, **149**, 304–309.
53 T. Sekine, M. Izumi, T. Nakashizu, K. Uchinokura and E. Matsuura, *J. Phys. Soc. Jpn.*, 1980, **49**, 1069–1077.
54 L. E. Valle Rios, K. Neldner, G. Gurieva and S. Schorr, *J. Alloys Compd.*, 2016, **657**, 408–413.
55 H.-S. Kim, D. B. Patel, H. Kim, M. Patel, K. R. Chauhan, W. Park and J. Kim, *Sol. Energy Mater. Sol. Cells*, 2017, **164**, 7–12.
56 R. Bodeux, J. Rousset, F. Tsin, F. Mollica, E. Leite and S. Delbos, *Appl. Phys. A: Mater. Sci. Process.*, 2018, **124**, 22.
57 J. T. Heath, J. D. Cohen and W. N. Shafarman, *J. Appl. Phys.*, 2004, **95**, 1000–1010.
58 H. Hempel, A. Redinger, I. Repins, C. Moisan, G. Larramona, G. Dennler, M. Handwerg, S. F. Fischer, R. Eichberger and T. Unold, *J. Appl. Phys.*, 2016, **120**, 175302.
59 C. J. Hages, A. Redinger, S. Levcenko, H. Hempel, M. J. Koeper, R. Agrawal, D. Greiner, C. A. Kaufmann and T. Unold, *Adv. Energy Mater.*, 2017, **7**, 1700167.
60 V. Karade, A. Lokhande, P. Babar, M. G. Gang, M. Suryawanshi, P. Patil and J. H. Kim, *Sol. Energy Mater. Sol. Cells*, 2019, **200**, 109911.

61 Z. Jehl, M. Bouttemy, D. Lincot, J. F. Guillemoles, I. Gerard, A. Etcheberry, G. Voorwinden, M. Powalla and N. Naghavi, *J. Appl. Phys.*, 2012, **111**, 114509.

62 E. Leonard, L. Arzel, M. Tomassini, P. Zabierowski, D. Fuertes Marrón and N. Barreau, *J. Appl. Phys.*, 2014, **116**, 074512.

63 Z. Jehl, F. Erfurth, N. Naghavi, L. Lombez, I. Gerard, M. Bouttemy, P. Tran-Van, A. Etcheberry, G. Voorwinden, B. Dimmler, W. Wischmann, M. Powalla, J. F. Guillemoles and D. Lincot, *Thin Solid Films*, 2011, **519**, 7212–7215.

64 H. Heriche, Z. Rouabah and N. Bouarissa, *Int. J. Hydrogen Energy*, 2017, **42**, 9524–9532.

65 L. Grenet, F. Emieux, O. Dellea, A. Gerthoffer, G. Lorin, F. Roux and S. Perraud, *Thin Solid Films*, 2017, **621**, 188–194.

66 K. Beom Cheon, S. K. Hwang, S. W. Seo, J.-H. Park, M.-A. Park and J. Y. Kim, *ACS Appl. Mater. Interfaces*, 2019, **11**, 24088–24095.

67 M. Neuschitzer, Y. Sanchez, S. López-Marino, H. Xie, A. Fairbrother, M. Placidi, S. Haass, V. Izquierdo-Roca, A. Perez-Rodriguez and E. Saucedo, *Prog. Photovoltaics*, 2015, **23**, 1660–1667.

68 J. J. Scragg, P. J. Dale, D. Colombara and L. M. Peter, *ChemPhysChem*, 2012, **13**, 3035–3046.

69 J. B. Li, V. Chawla and B. M. Clemens, *Adv. Mater.*, 2012, **24**, 720–723.

70 G. Y. Kim, A. R. Jeong, J. R. Kim, W. Jo, D.-H. Son, D.-H. Kim and J.-K. Kang, *Sol. Energy Mater. Sol. Cells*, 2014, **127**, 129–135.

71 T. Taskesen, J. Neerken, J. Schoneberg, D. Pareek, V. Steininger, J. Parisi and L. Gütay, *Adv. Energy Mater.*, 2018, **8**, 1703295.

72 Y. S. Lee, T. Gershon, O. Gunawan, T. K. Todorov, T. Gokmen, Y. Virgus and S. Guha, *Adv. Energy Mater.*, 2015, **5**, 1401372.

73 S.-Y. Kim, S.-H. Kim, S. Hong, D.-H. Son, Y.-I. Kim, S. Kim, K. Ahn, K.-J. Yang, D.-H. Kim and J.-K. Kang, *ACS Appl. Mater. Interfaces*, 2019, **11**, 23160–23167.

74 S. Giraldo, M. Neuschitzer, T. Thersleff, S. López-Marino, Y. Sánchez, H. Xie, M. Colina, M. Placidi, P. Pistor, V. Izquierdo-Roca, K. Leifer, A. Pérez-Rodríguez and E. Saucedo, *Adv. Energy Mater.*, 2015, **5**, 1501070.

75 C. M. Ruiz, A. Pérez-Rodríguez, J. Arbiol, J. R. Morante and V. Bermúdez, *Phys. Status Solidi*, 2015, **212**, 61–66.

76 J. J. S. Scragg, J. K. Larsen, M. Kumar, C. Persson, J. Sendler, S. Siebentritt and C. Platzer Björkman, *Phys. Status Solidi*, 2016, **253**, 247–254.

77 S. Bourdais, C. Choné, B. Delatouche, A. Jacob, G. Larramona, C. Moisan, A. Lafond, F. Donatini, G. Rey, S. Siebentritt, A. Walsh and G. Dennler, *Adv. Energy Mater.*, 2016, **6**, 1502276.

78 A. Hernández-Martínez, M. Placidi, L. Arqués, S. Giraldo, Y. Sánchez, V. Izquierdo-Roca, P. Pistor, M. Valentini, C. Malerba and E. Saucedo, *ACS Appl. Energy Mater.*, 2018, **1**, 1981–1989.

79 TEM-UCA, EJE-Z – TEM-UCA development software for Electron Microscopy, http://www2.uca.es/dept/cmat_qinor/catalisis/tem-uca-server.htm, accessed June 2020.

80 S. Bernal, F. Botana, J. Calvino, C. López-Cartes, J. Pérez-Omil and J. Rodríguez-Izquierdo, *Ultramicroscopy*, 1998, **72**, 135–164.

81 G. Martínez-Criado, J. Villanova, R. Tucoulou, D. Salomon, J.-P. Suuronen, S. Labouré, C. Guilloud, V. Valls, R. Barrett, E. Gagliardini, Y. Dabin, R. Baker, S. Bohic, C. Cohen and J. Morse, *J. Synchrotron Radiat.*, 2016, **23**, 344–352.

Electronic Supplementary Material (ESI) for Energy & Environmental Science.

Supplementary Information

Insights into interface and bulk defects in a high efficiency kesterite-based device

Robert Fonoll-Rubio,[a] Jacob Andrade-Arvizu,[a] Javier Blanco-Portals,[b,c] Ignacio Becerril-Romero,[a] Maxim Guc,*[a] Edgardo Saucedo,[a,d] Francesca Peiró,[b,c] Lorenzo Calvo-Barrio,[e,f] Maurizio Ritzer,[g] Claudia S. Schnohr,[g,h] Marcel Placidi,[a,d] Sònia Estradé,[b,c] Víctor Izquierdo-Roca*[a] and Alejandro Pérez-Rodríguez[a,f]

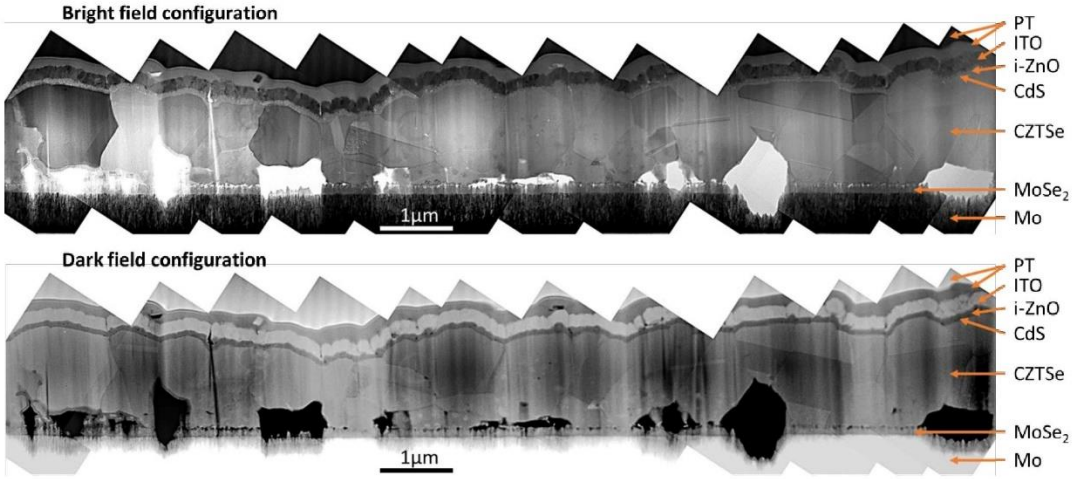

Fig. S1 Collage image of a series of cross-sectional STEM images of a CZTSe-based solar cell in both bright field and dark field configurations. Each image is acquired as de-magnified as possible. The different observed layers of the device are indicated, including the platinum layers added during FIB sample preparation.

[a] *Catalonia Institute for Energy Research – IREC, 08930, Sant Adrià de Besòs, Barcelona, Spain. E-mail: vizquierdo@irec.cat and mguc@irec.cat*
[b] *LENS-MIND, Departament d'Enginyeria Electrònica i Biomèdica, Universitat de Barcelona, 08028, Barcelona, Spain*
[c] *cInstitute of Nanoscience and Nanotechnology (IN2UB), Universitat de Barcelona, 08028, Barcelona, Spain*
[d] *Photovoltaic Group, Electronic Engineering Department, Universitat Polytècnica de Catalunya (UPC), 08034, Barcelona, Spain*
[e] *Centres Científics i Tecnològics (CCiTUB), Universitat de Barcelona, C/ Lluis Solé i Sabaris, 08028 Barcelona, Spain*
[f] *Departament d'Enginyeria Electrònica i Biomèdica, IN2UB, Universitat de Barcelona, C/ Martí i Franqués 1, 08028 Barcelona, Spain*
[g] *Institut für Festkörperphysik, Friedrich-Schiller-Universität Jena, Max-Wien-Platz 1, 07743 Jena, Germany*
[h] *Felix-Bloch-Institut für Festkörperphysik, Universität Leipzig, Linnéstraße 5, 04103 Leipzig, Germany*
* *Corresponding authors: vizquierdo@irec.cat (V.I.-R.) and mguc@irec.cat (M.G.)*

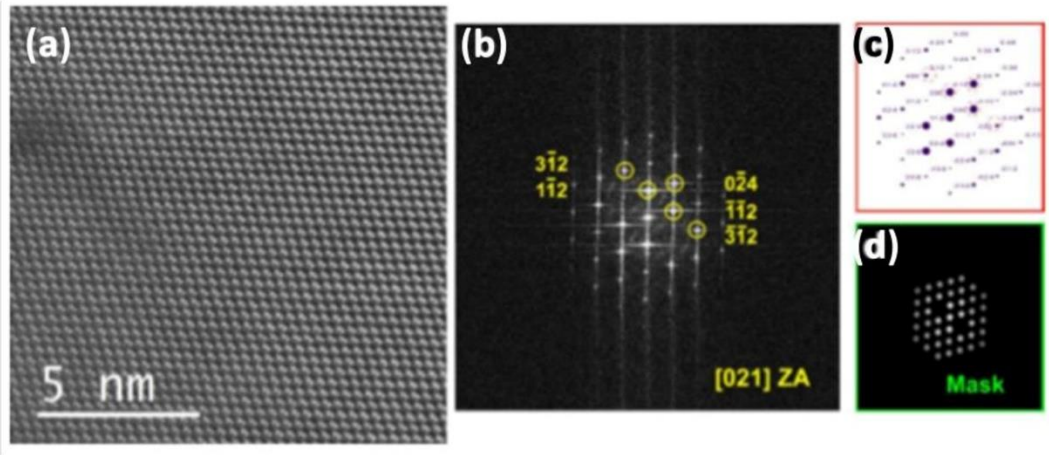

Fig. S2 (a) H-Res HAADF image of a CZTSe grain. (b) FFT for the whole image in (a). [021] ZA is clearly resolved. (c) Theoretical computation for the reciprocal space of the modeled kesterite atomic cell (TEM-UCA software, University of Cádiz). (d) Mask generated to filter the noise in the HAADF image in (a).

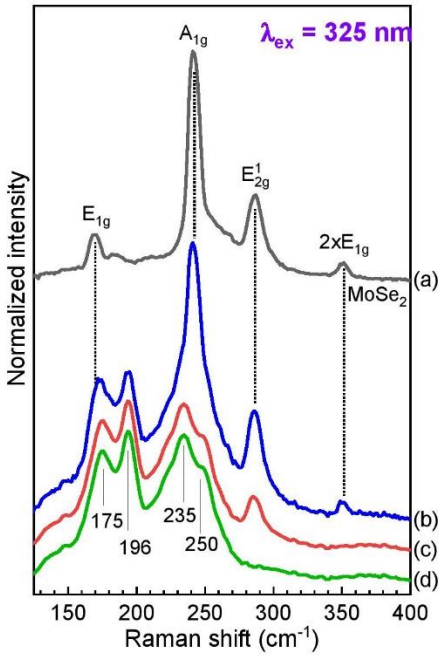

Fig. S3 Raman spectra measured under 325 nm excitation wavelength at the back interface from the (a) back contact side and (b) CZTSe side. Here (c) is CZTSe spectrum at back interface region obtained after subtracting the $MoSe_2$ spectrum (a); and (d) is CZTSe spectrum at back interface region obtained after subtracting the $MoSe_2$ peaks taking into account the different crystal texture.

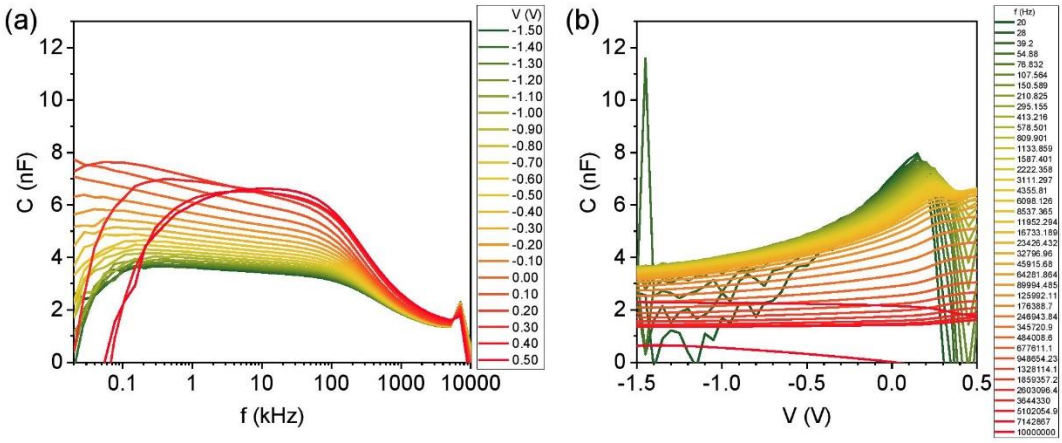

Fig. S4 (a) Measured capacitance of a CZTSe-based device in function of the AC frequency for different applied bias voltages. (b) Measured capacitance of a CZTSe-based device in function of the applied bias voltages for different AC frequencies. Capacitance values tending to zero are due to parasitic effects produced by the series resistance and the inductance which dominate at the corresponding AC frequencies and applied DC voltages.

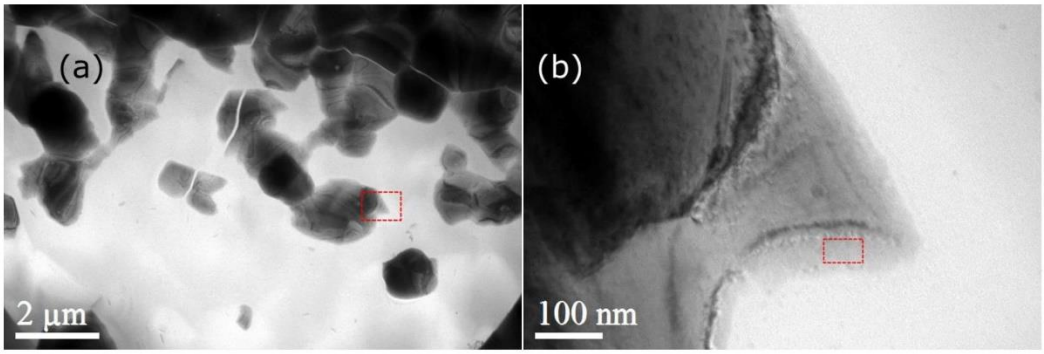

Figure S5. (a) Planar view TEM image of the front interface of a CZTSe absorber after removing the ITO/i-ZnO window layer and CdS buffer layer by HCl etching. Some grains delimited by bright boundaries can be distinguished. The grain boundaries are regular and narrow, so they should have a low impact on V_{oc} deficit. The large brighter areas correspond to empty regions that are produced during the ion milling, so they are not an intrinsic characteristic of the material (b) TEM image of the region indicated by a dashed rectangle in (a) with increased magnification. The dashed rectangle in this image indicates the region shown in Fig. 10a. Contrast differences are produced by thickness differences due to the low control of the ion milling by PIPS and rounded boundaries are also produced by material removing during ion milling.

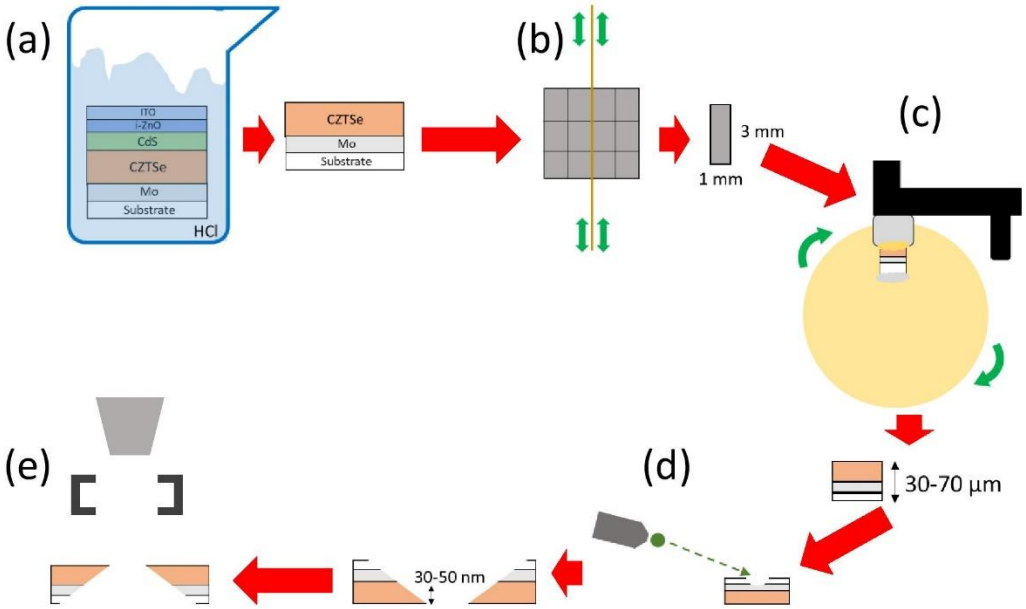

Fig. S6 Diagram of the sample preparation for planar view TEM study. (a) Removal of the ITO/i-ZnO window layer and the CdS buffer layer by HCl etching. (b) Etched sample cutting to obtain a piece with a CZTSe area of 2.5 × 2.5 mm^2 (with ~3mm thickness) (c) Polishing from the substrate side with a series of consecutively finer grain abrasive diamond films to obtain a sample thickness between 30 and 70 µm. (d) Final thinning by ion milling using a Precision Ion Polishing System (PIPS) to obtain a CZTSe region with thickness between 30 and 50 nm. (e) Planar view study of CZTSe absorber surface by TEM.

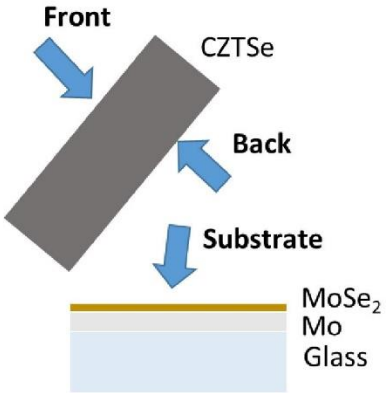

Fig. S7 Scheme representation about the mechanical lift-off for the interface Raman characterization.

3.3. Article 2: Defect depth-profiling in kesterite absorber by means of chemical etching and surface analysis

Applied Surface Science 540 (2021) 148342

Contents lists available at ScienceDirect

Applied Surface Science

journal homepage: www.elsevier.com/locate/apsusc

Defect depth-profiling in kesterite absorber by means of chemical etching and surface analysis

Kunal J. Tiwari [a], Robert Fonoll Rubio [a], Sergio Giraldo [a], Lorenzo Calvo-Barrio [b,c], Victor Izquierdo-Roca [a], Marcel Placidi [a,d], Yudania Sanchez [a], Alejandro Pérez-Rodríguez [a,c], Edgardo Saucedo [a,d], Zacharie Jehl Li-Kao [a,d,*]

[a] Institut de Recerca en Energia de Catalunya (IREC), 1,2apl. Jardins de les Dones de Negre, 08930 Sant Adria de Besos, Barcelona, Spain
[b] Centres Científics i Tecnològics (CCiTUB), Universitat de Barcelona, C/Lluis Solé i Sabaris 1-3, 08028 Barcelona, Spain
[c] IN2UB, Departament d'Enginyeria Electrònica i Biomèdica, Universitat de Barcelona, C/Martí i Franquès, 1, 08028 Barcelona, Spain
[d] Electronic Engineering Department, Polytechnic University of Catalonia (UPC), c/Jordi Girona 1, 08034 Barcelona, Spain

ARTICLE INFO

Keywords:
Chemical etching
Defect
Kesterite
Raman Spectroscopy
XPS

ABSTRACT

A method to probe the depth morphology, defect profile and possible secondary phases in a thin film semiconductor is presented, taking a standard Kesterite film as an example. Using a top-down approach based on a previously reported controlled Methanol-Br_2 chemical etching, well-defined slabs of a state of the art Kesterite absorber are fabricated. The analysis of their morphology both by Scanning Electron Microscopy and 3D optical Profilometry reveals the extent of a previously reported poor film morphology toward the back interface, and we are able to determine that more than 50% of a standard absorber is disconnected from the substrate. More importantly, these etched films are subsequently analyzed by surface sensitive techniques such as X-ray Photoelectron Spectroscopy and UV-Raman analysis. An accurate composition profile is established, and for the first time, a direct observation of the defects' nature and their depth profiling in Kesterite is made possible. While V_{Cu} are found with a constant amount throughout the absorber, indicating a homogenous carrier concentration, a prevalence of the Zn_{Sn} defect is observed with a steep gradient toward the back interface, associated with an increase in the $SnSe_2$ secondary phase. With bulk defects being often pointed out as the intrinsic limitation of this material, this result highlights what possibly is the main impediment of Kesterite solar cells, and a critical point to address in the design of future devices. Beyond the case of Kesterite absorbers, the method presented here offers a combination of simplicity, tunability and versatility making a straightforward transfer to other emerging thin film absorbers feasible, and it could possibly be an important tool in their future performance assessment and comparison.

1. Introduction

With several technologies reaching their industrial maturity, thin film solar cells are now credible players in the photovoltaic landscape, reinforced by the need for new applications in fields like Building Integrated Photovoltaics (BIPV) [1], the Internet of Things (IoT) along with the emerging indoor photovoltaics systems [2]. Throughout the development of thin film solar cells, spanning more than 4 decades, material scarcity and toxicity has been an ongoing research axis [3] and the level to which it could hamper the growth of these technologies remains debatable among the photovoltaic community [4,5].

In that context, Kesterite absorbers being free of toxic and critical raw materials were seen (and to some extent still are) as a potential low-cost answer [6]; disappointingly however, the conversion efficiency of the PV devices has been stalling throughout most of the last decade [7–9], and fundamental limitations challenge further progresses of this technology [10]. Namely, a strong voltage deficit has been identified as the main parameter constraining the performance of Kesterite-based devices [8]. A recent landmark study [11] even concluded to an upper limit in the efficiency of those imperfect crystals around 20%, mostly ascribed to the presence of native defects in the absorber. The presence of such defects has been long suspected in the community, but their direct observation remains challenging and one has to rely on indirect approaches such as admittance spectroscopy to identify the energy position of defects and infer their nature [12]; hence the need for a novel approach to this problem. In semiconductor materials for energy

* Corresponding author.

https://doi.org/10.1016/j.apsusc.2020.148342
Received 20 July 2020; Received in revised form 28 September 2020; Accepted 30 October 2020
Available online 6 November 2020
0169-4332/

application, the lack of easy characterization methodologies compatible with an extensive application in different synthesis conditions is a critical limitation to the understanding of the defects' role, and their engineering would allow for a pathway to device optimization [13].

The chemical etching of thin film absorbers using a bromine solution has been a valuable top-down method used in the past to investigate on the possible improvement of the p-n junction [14] as well as the fabrication of proof-of-concept ultrathin absorbers in CIGSe [15,16], and similar solutions have proven applicable to Kesterite absorbers as well [17,18]. In this work, we aim at building upon these past investigations to propose an original yet simple method in the thorough characterization of the defects existing in reference CZTSe Kesterite absorbers. Unlike previous studies, our approach allows for a direct defect observation throughout the whole absorber thickness, by dividing the film into slabs with a bromine etching on reference samples, and using surface sensitive characterizations to build a complete composition and defect profile of the absorber. Chemically etched films will be analyzed by confocal optical 3D Profilometry (3D-P), Scanning Electron Microscopy (SEM), Raman Spectroscopy and X-ray Photoelectron Spectroscopy (XPS), and the morphology of the back side of the absorber will be revealed as a major limiting factor, with a poor crystallinity, several voids, and the presence of various secondary phases; such problems have long been ascribed to poor performances in Kesterite-based solar cells [19,20], and the progressive chemical etching of our absorbers reveals that more than 50% of the surface area of the film is disconnected from the Mo back contact. The analysis of etched absorbers by XPS allows for an accurate composition profiling of the films, revealing features that were not observable in a standard profiling using sputtering. From UV-Raman observations [21], a strong prevalence of the Zn_{Sn} deep donor defect is demonstrated, and discussed in regard to previous calculations made on this material [11]; it is to the best of our knowledge the first time that such experimental depth-resolved defect profile is established in Kesterite absorbers, and our method allows to directly identify what fundamental limitations to the performance of the resulting PV devices. This work uses a combination of well controlled experimental techniques to provide direct experimental insights on critical aspects of CZTSe Kesterite solar cells which were so far either indirectly inferred or deduced from numerical modelling.

Beyond the issues related to Kesterite solar cells, our method is, to some extent, material agnostic and it can potentially be applied to a wide array of other thin films; it could prove particularly valuable in the study of emerging materials, as a mean to devise improvement strategies based on their defect profile and the presence of secondary phases in the bulk.

2. Materials and methods

2.1. Samples preparation

Kesterite $Cu_2ZnSnSe_4$ (CZTSe) films are prepared following the standard process in our laboratory on Soda Lime Glass (SLG) coated by an 800 nm layer of molybdenum (Mo). A Cu, Zn and Sn metallic precursor with the elemental layer stack order Cu/Sn/Cu/Zn is first deposited by sequential DC sputtering (Alliance concept AC450), and the semiconductor film is realized by a 2-steps thermal annealing in a tubular furnace (Hobersal) in the presence of the chalcogen element Se. In a first step, the sample was heated to 400 °C for 30 min under a constant Ar flow of 1.5 mbar; in a second step, the temperature was ramped up to 550 °C and a static Ar pressure of 950 mbar was maintained, for a total of 15 min. The as-selenized film was 3 μm thick for this work, thicker than our usual absorbers. This is the only variation with the standard process, and it was deemed useful in the context of a top-down approach to use thicker films. While beyond the scope of this study, a complete solar cell using the as-deposited 3 μm absorber was fabricated, with a conversion efficiency on par with the expectation of a reference sample. Additionally, the etching of thinner standard absorbers was also performed and a more limited analysis of these samples brought similar observations to what is discussed in this study, confirming that using thicker absorbers should not change our conclusion. Hence, we make the choice to discuss our experiments on 3 μm thick CZTSe films, providing here a more exhaustive analysis. No additional treatment is done prior to the etching of the films.

2.2. Bromine etching process

Bromine etching is a previously reported method [14] to effectively reduce the thickness of metallic and semiconductor thin films without altering their properties, and the demonstration of its effectiveness was previously made on CIGS [15,22]. While the most widely reported method involves H_2O and HBr along with Br_2, we chose a to use a Methanol-Br2 solution for practical reasons [17], which yields equivalent results. The Br_2 concentration was 0.02 M, and the etching was carried out with a controlled temperature close to $0^{\circ}C$ by maintaining the etching vessel in an ice bath 10 min before dipping the samples in the solution, as well as during the etching process. Unless specified otherwise, no additional treatment to the samples was done after etching. The samples were kept in a vacuum environment and characterized less than 12 h following the etching process. A series of 9 samples was fabricated (including a reference non-etched sample), with etching durations for 8 samples ranging from 30sec up to 13 min, the latter corresponding to an etched thickness > 2 μm, though we will later see that determining an etched thickness is not straightforward when approaching the back contact. The etched samples are numbered from 1 to 9, with #4 being deliberately excluded from the series. A special emphasis was put on short etches, for reasons detailed later in the manuscript.

2.3. Samples characterization

The characterization process of as deposited and etched samples in this study is fully contactless. The films are characterized by Zeiss series Auriga scanning electron microscope (SEM) with accelerating voltage of 5 kV and X-ray fluorescence (XRF, *FISCHERSCOPE XDV*) to allow determining their thickness, and having a direct observation of their morphology change from the bromine etching. 3D Optical Profilometry (3D-P) is used to obtain numerical values related to the surface smoothing post Br_2 etching, and the film composition for different etching durations is monitored by XRF. All XRF data reported are the average values obtained on 9 different positions on the samples.

UV-Raman analysis is performed on as-deposited and etched samples using a 325 nm excitation wavelength and an in-lab developed Raman system with an extremely low power density (<60 W/cm^{-2}) to avoid thermal effects and alterations, and a large laser diameter spot (70 μm) covering a representative area of the sample. This latter point is also critical in our opinion, as the observations reported here are thus more representative than what a local analysis would provide. Working under UV conditions allows for a light penetration depth below 10 nm while non-bandgap resonance Raman conditions enhance the detection of peaks sensitive to V_{Cu} and Zn_{Sn} type defects [21]. The samples were stored in vacuum conditions and analyzed by Raman less than 24 h after the chemical etching.

X-ray Photoelectron Spectroscopy (XPS) experiments are performed in a PHI 5500 Multitechnique System from Physical Electronics, using a monochromatic X-ray source Al Kα line of 1486.6 eV energy and 350 W power, placed perpendicular to the analyzer axis and calibrated by the $3d_{5/2}$ line of Ag with a full width at half maximum (FWHM) of 0.8 eV. The analyzed area is a circle of about 0.8 mm diameter. The selected resolution for the survey spectra (from 0 to 1100 eV of binding energy) is 187.5 eV of Pass Energy (PE) and 0.8 eV/step. For the high-resolution spectra 23.5 eV of PE and 0.1 eV/step are chosen to measure the main orbitals of Kesterite's elements (Cu2p, $Zn2p_{3/2}$, Sn3d and Se3d), Molybdenum (Mo3d), Carbon (C1s) and Oxygen (O1s). Due to this large number of existing elements, overlaps will appear between some of the signals that must be considered to avoid confusion (more explained in

Supporting Information).

Besides, in-depth measurements (profiles) are obtained in the reference sample by sputtering it with an Ar^+ ion source (3.5 keV). One profile following only Mo3d signal is run to know the sputter ratio, and a second profile for all CZTSe elements, Mo and O main orbitals with the same parameters of high-resolution spectra is done to compare with the obtained data on the bromine etching samples.

The analysis and fitting of the XPS spectra are done with Multipak Version 9.9.08 program

from ULVAC-PHI. Measurements are referenced to the C1s signal, which binding energy is equal to 284.8 eV in adventitious Carbon (from atmospheric contamination). For quantification purposes, the corrected relative sensitivity factors provided by the same program are used. These factors consider both the specific analyzer parameters and the geometry of the experimental system. No charge compensation is used in any of these measurements that are made in an ultra-high vacuum (UHV) chamber, with pressures between $1x10^{-9}$ and 2×10^{-8} torr.

3. Results and discussion

3.1. Samples' morphology and interplay with the etching process

The effect of bromine etching on the morphology of CIGSe absorbers has been widely reported [14,15,22], and a strong smoothing effect with RMS values below 50 nm was observed in previous studies from Atomic Force Microscopy (AFM) analysis. A similar statement was anecdotally made on CZTSe [17] but the morphology of the films was beyond the scope of this aforementioned study. We deem necessary to confront and confirm those results, and this work starts by investigating the evolution of the surface roughness of CZTSe films and its interplay with the etching kinetics. Optical Profilometry (3D-P) is preferred to AFM in our case, as we aim at analyzing a surface area as representative as possible of the sample; however, one may keep in mind that this approach has the drawback of a comparatively lower resolution (in our case of the order of 10–20 nm). Moreover, a higher RMS value is expected when using 3D-P as compared to AFM (as done in previous studies), as a larger area is being analyzed; hence, a direct 1:1 comparison with the previous AFM work on CIGSe is not advisable, and only trends should be considered.

Fig. 1a–c show the surface profile of 3 selected CZTSe samples with different etching durations; the evolution of the surface RMS and etching rate are shown in the supplementary information of this manuscript, as those would not qualify as new results since similar trends have been observed on CIGSe [22]. The reported thickness (remaining sample thickness) was measured by XRF analysis; due to the textured nature of the samples, which makes the concept of thickness somehow inaccurate, this value should rather be seen as indicative of the quantity of material being removed from the sample. A clear decrease in the surface roughness is observed, starting from ≈300 nm for the reference non-etched sample Fig. 1a down to a minimum of 160 nm for three consecutive samples etched for 240 s, 360 s and 540 s (corresponding to a remaining thickness of 2.27 μm, 2.07 μm and 1.73 μm respectively as shown Fig. 1b). For longer etching durations, a strong increase in the RMS value is observed; concurrently, large and very flat areas (in light blue in Fig. 1c) appear on the 3D-P images (Fig. 1c). These areas correspond to the bare Mo surface, and are thus indicative of very large voids existing at the back side of the films. An image analysis shows that up to 50% of the Mo surface is disconnected from the CZTSe film, which is a severe limitation to the performance of solar cell devices. Similar observations

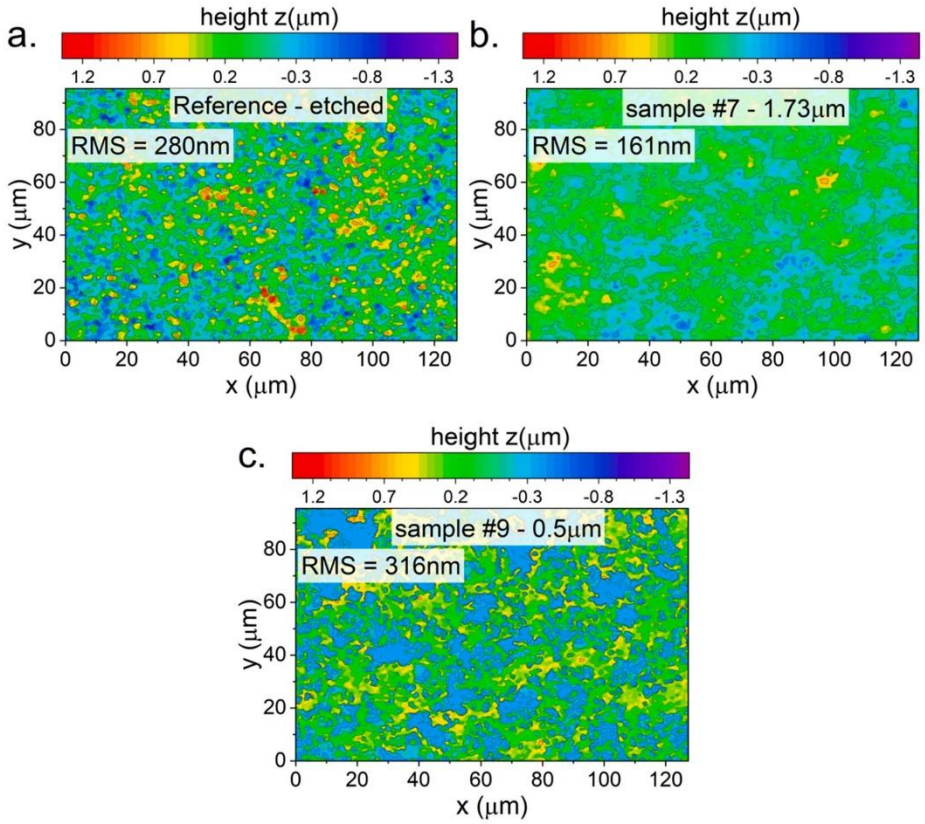

Fig. 1. Surface profile of the reference non-etched CZTSe film (a) and differently etched samples (b and c), representative of the evolution of the surface roughness.

have been made in the recent years and were recently attributed to a wettability mismatch at the back interface [23]. The images presented Fig. 1 provide here a direct observation of the extent to which this issue affects Kesterite absorbers, and it is the main novelty of the morphological analysis permitted through chemical etching. In the future, a similar analysis of samples fabricated with strategies addressing this specific issue (see reference [20]) could prove valuable in assessing possible improvements at the back interface. Though beyond the scope of this work, a mechanical lift-off was performed on a different series of CZTSe samples revealing similar features as those observed here; this specific point will be thoroughly addressed in a future study.

The etching rate is calculated from the XRF analysis of the samples, and is presented Figure SI 1. Two seemingly linear rates coexist; a fast etching rate for the first 500 nm, followed by an approximately 30% slower rate. As the etching rate should remain constant in terms of quantity of etched material, the limiting parameter is the exposed film total area; such behavior is therefore consistent with a rapid smoothing of the film's surface, and expected as similar results were reported on CIGS [15]. Consistently with the presence of voids at the back side, a "3D" surface is quickly formed for deeper etchings, increasing the exposed film area and thus accelerating the apparent etching rate; it is also possible that the presence of secondary phases will influence the etching kinetics, though only few experimental points are available here. This specific aspect will need a more thorough analysis in the future before any conclusion can be made. While the chemistry of the etching was discussed elsewhere [14,17] and is out of the scope of this study, this simple process combined with a surface profiling gives a direct visual and quantitative representation of a major limitation of standard Kesterite absorbers.

The observation of the layers by cross-sectional SEM (Fig. 2, comparing the reference sample with an etched one) reveals consistent information with the previously discussed points; though they do not allow to assess the full extent of the back contact issue, voids and a poor morphology are observed at the back interface between CZTSe and Mo. The smoothing effect from the chemical etching is also visible, though again, a full assessment is only possible through the 3D-P analysis. No apparent damage from the chemical etching are observed on the SEM images.

The etching process of Kesterite films resembles that of chalcopyrite, and in that context, we believe that it could also be used to fabricate complete solar cell devices with a new degree in tailoring the front interface's morphology and render it more specular. In this study however, our main focus remains the composition and defect profiling of a standard CZTSe film, and a point which will be addressed in the following main part of this work.

3.2. *Composition and defects' profiling*

The investigation of these samples by XPS is not straightforward, and to justify an appropriate approach, three different methods are considered: direct characterization of as-deposited samples (raw), after surface cleaning using ethanol and N_2 dry-off (ethanol cleaned), and after a light sputtering of the surface (sputtered) using Ar^+ ions inside the Ultra High Vacuum chamber for half a minute, leading to an erosion below 10 nm.

Survey and high-resolution results (figures for raw and sputtered samples are presented in the Supporting Information) show that no real differences can be appreciated between raw and ethanol cleaned measurements, as similar quantities of carbon (C1s) and oxygen (O1s) and no apparent differences in the rest of the Kesterite elements are found. The sputtered measurements show the total disappearance of C1s signals, which is consistent with an adventitious carbon contamination from the air exposure of the samples. The O1s signal however did not fully disappear after sputtering, even though it would have been expected in the case of an atmospheric contamination; it is thus likely that O exists in some form in the film, while C does not. Fig. 3 shows the evolution O1s peaks and its relative amount for the different etched samples after sputtering; here, the samples will be referred to by their ascribed number rather for clarity reasons. This amount of oxygen is probably oxidizing a metal, being Sn and Mo the best candidates as it would be shown later. Moreover, Kesterite individual elements for sputtered samples show the expected signal incremental evolution with respect to the raw spectra from the elimination of the surface

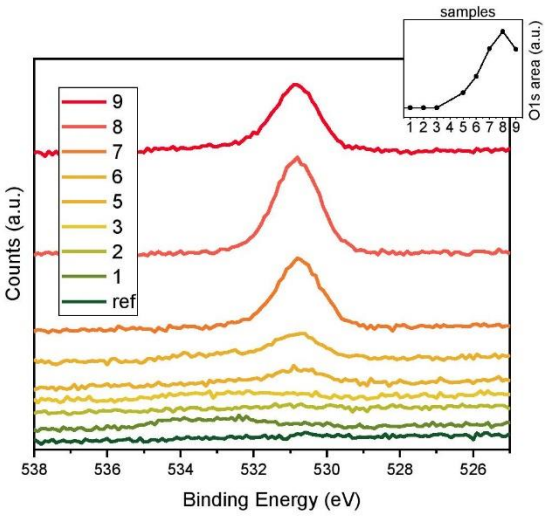

Fig. 3. Evolution of the O1s orbital measured by XPS in the complete sample series.

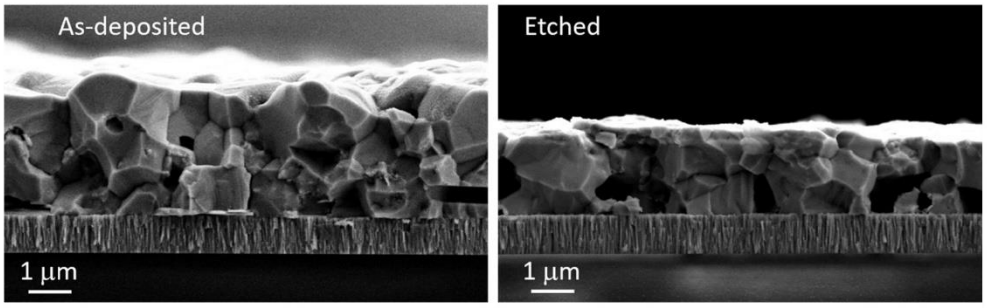

Fig. 2. Scanning Electron Microscopy images of the cross sections for the reference non-etched sample (top) and sample #6 (bottom, 360 s etching duration). Both images are taken at 30 k magnification.

contamination. Measurements performed on sputtered samples were, for that reason, chosen for quantification purpose.

On the other hand, the high-resolution Kesterite spectra of sputtered samples show notable changes in shape, FWHM and binding energy with respect to the raw samples. This effect is clearly visible in Fig. 4 where Se3d orbital for raw (a) and sputtered (b) measurements together with their detailed fit are shown for sample #7 as an example (a similar conclusion was made on other samples). There exist 5 different bonds (each being a doublet) on the raw sample, among which 3 disappear after the sputtering. The disappearing bonds at about 59, 63 and 68 eV can be matched to the different types of oxidation states + 2, +4 and + 6 respectively, and are routinely observed on surfaces including elemental Se [24]. The remaining bonds at about 55 and 54 eV are related to 0 (elemental) and −2 (as in Kesterite) states. However, the ratio between these 2 remaining bonds changes clearly after the sputtering and the amount of 0 state notably decreases, showing a significant alteration (reduction), of the chemical bonding from sputtering. Hence, it is conversely preferred to refer to the raw measurements for the analysis, fit, and subsequent study of the possible changes in chemical bonding occurring between the differently etched samples.

From the analysis of the area of the peaks corresponding to the different CZTSe elements on all the sputtered samples, and using the corresponding corrected relative sensitivity factors, the atomic concentration profile for CZTSe elements and Mo of Fig. 5a is created. In this figure, the expected composition of a stoichiometric Kesterite is obtained for the reference non-etched sample, but as the etching progresses, the Sn profile begins to increase and reaches a maximum at about 1 μm in remaining thickness, decaying at 0.5 μm. This tin enrichment matches well with the appearance of $SnSe_2$ peaks on the Raman spectra, as will be later discussed. The molybdenum unsurprisingly appears for the deepest etching, while the Sn content decreases as less material remains scattered on the surface (see Fig. 1c). The decrease in both Se and Sn as Mo appears in the profile is consistent with a previously made hypothesis that the voids at the back interface are the result of the evaporation of Sn-Se phases [20]. This profile should be compared to the in-depth profile obtained directly from the reference sample using a more standard sputtering etching (Figure SI 5 shown in the Supporting Information). In that case, every element displays a more stable and homogenous behaviour until the appearance of molybdenum and no depth tin enrichment is observed. Specifically, the Zn/Sn ratio appears constant in Figure SI 5, while the composition analysis obtained from the chemically etched samples Fig. 5a highlighted a strong Sn

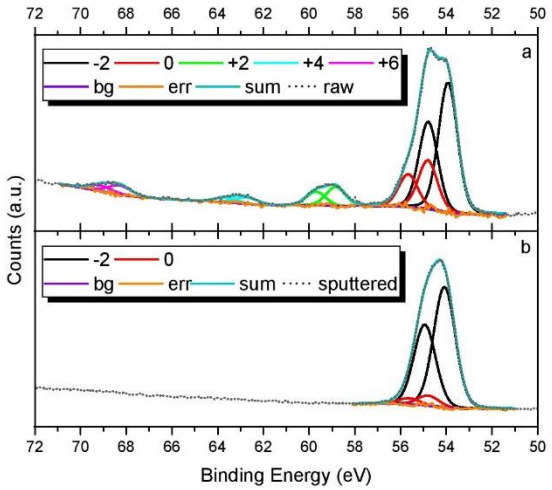

Fig. 4. a: XPS Se3d orbital analysis and fit for raw sample #7. b: similar analysis with sputtered sample #7.

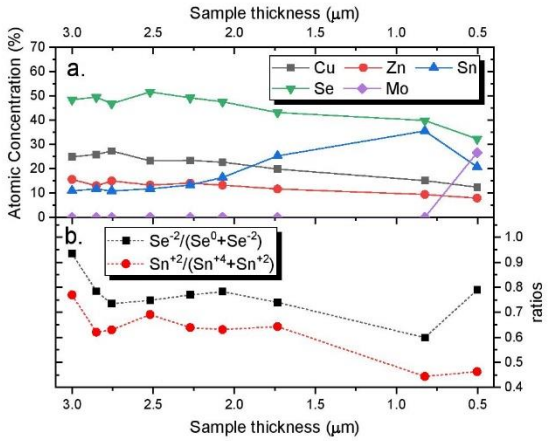

Fig. 5. a: Composition profile obtained from XPS analysis of chemically etched samples after a light Ar^+ sputtering (sputtered). b: Sn and Se chemical state ratio evolution on chemically etched samples (raw).

enrichment from the surface to the Mo back interface, and thus a decrease of the Zn/Sn atomic ratio. We believe that the difference observed when using a standard sputtering etching stems from the confluence of a very long sputter time (continuous damage in bulk by the Ar^+ ions) and a relatively big area of measurement (the data could be disrupted by the walls of the created crater), usually giving as a result similar homogeneous profiles and losing finer information in deeper layers. The approach chosen in our study, using a soft chemical etching of the surface over a large area, presents apparently a superior element resolution when it comes to depth composition profiling, and allows a more accurate identification of possible grading such as Sn in this specific case. An overview over a larger number of samples would however be necessary to fully confirm this hypothesis.

For the analysis of the Kesterite elements' bounds on the etched samples, high-resolution spectra of the raw samples have been analyzed. No significant differences are found on $Cu2p_{3/2}$ and $Zn2p_{3/2}$ orbitals for deeper etchings. Both orbitals can be fitted with peaks at about 932.0 eV and 1021.8 eV. On the other hand, Se3d and $Sn3d_{5/2}$ orbitals need to be fitted with different chemical species to reach an acceptable agreement. $Sn3d_{5/2}$ can be fitted with peaks at about 486.7 and 487.4 eV, matching the + 2 and + 4 chemical species respectively [25]. While five doublets are used for the fitting of Se3d, only two of them, corresponding to 0 and −2, are not related with oxidized states typical of a surface atmospheric contamination. Fig. 5b shows the ratio between the aforementioned different chemical species for Sn and Se elements for all the etched samples. In the case of selenium, the curve shows that the major bound is always −2, as expected in Kesterite, with a ratio close to 1 at the vicinity of the as-deposited surface. As the etching progresses toward the middle of the layer, a steady regime is reached with a quarter of the selenium appearing elemental. This elemental selenium could have been created around secondary phases present in the sample or around oxidized areas in contact with the voids shown in Fig. 1c. When molybdenum appears in the composition profile, we observe an increase in the −2 bond, which can thus easily be ascribed to the presence of $MoSe_2$. The tin ratio between the + 2 and + 4 species follows a similar pattern. While +4 is the stoichiometric state for Kesterite and $SnSe_2$ secondary phase, +2 also appears in non-stoichiometric samples, and could be an indirect way to identify the appearance of $SnSe_x$, SnO_x secondary phases or the evidence of defects in the structure [26].

While the approach to combine Br_2 etching with XPS for composition profiling brings valuable information, the investigation of the defects throughout the material is of utmost importance when it comes to assess the current limitations of Kesterite solar cells. A UV-Raman method was

recently developed by our group to analyze the surface defects in CZTSe solar cells [21], using a non-bandgap resonant effect observed under 325 nm excitation conditions. This non-destructive approach allows for an accurate determination of the surface defects, and combined with a systematic chemical etching, it should permit to establish a semi-quantitative defect profile of the material throughout the entire film thickness.

Fig. 6 shows the 325 nm Raman spectra of all measured samples (a) and the area ratio of different peaks evaluated from the fitting of the spectra with a lorentzian curve (b). The deconvolution for all samples is shown in the supplementary information Figure SI 6. A clear change of the Raman spectrum is visible with the increased etching duration, previously ascribed to defect concentration variations within the Kesterite structure [21] and to the presence of secondary phases [27]. The analysis of the Raman spectra with the increase of the etching time shows:

- No evidence of changes in the intensity of the peak at 174–176 cm^{-1}, previously ascribed to the formation of the V_{Cu} point defect linked with the formation of the A-type defect cluster [$Zn_{Cu} + V_{Cu}$] [21]. As Cu vacancies are often ascribed to the carrier concentration in the material, this tends to indicate a homogeneous distribution in that regard.
- An increase of the area of the 245–250 cm^{-1} peak toward the back interface, previously associated to an increase of the Zn_{Sn} point defect (formation of the B-type defect cluster [$2Cu_{Zn} + Zn_{Sn}$]) [21]. This observation is consistent with the low crystalline quality observed in this region by SEM; it also correlates with a prevalence of the $SnSe_2$ secondary phase, thus reducing the amount of Sn in the Kesterite film.
- A strong accumulation of $SnSe_2$ phase at the absorber/Mo interface, along with a slight presence at the front surface. In the bulk, the contribution observed is related to tails of the CZTSe peaks suggesting an absence or low concertation of this phase. This observation is also consistent with the SEM observations, XPS analysis and with previous studies on that specific issue [20]. It also aligns well with a lower incorporation of Sn in the matrix leading to the formation of the Zn_{Sn} point defect.
- A simultaneous detection of a strong signal of the $MoSe_2$ phase and CZTSe phase in the samples with higher etching time, again consistent with the pinholes observed at the absorber/Mo interface. For those samples, it is evident that part of the signal comes directly from the exposed Mo/$MoSe_2$ substrate. It should be noted that this $MoSe_2$ signal is only recorded for the 3 samples with the longer etching durations, and while a logical increase is observed, more experimental points would be necessary to discuss about a trend in that context. Fig. 6b illustrates the depth profile of each defect and secondary phase previously discussed. This is to the best of our knowledge the first direct in-depth characterization and

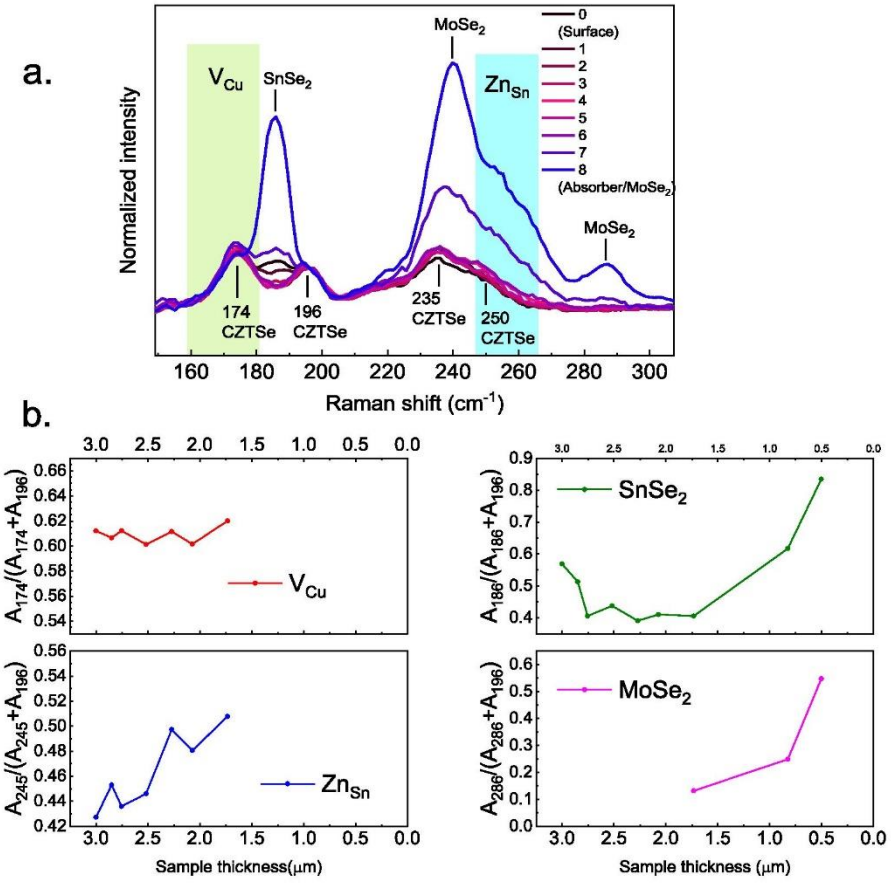

Fig. 6. a. Raman spectra using 325 nm excitation wavelength for etched samples. b. Evolution of the integrated area under the peaks associated with the point defects V_{cu}, Zn_{Sn}, and the secondary phases $SnSe_2$ and $MoSe_2$.

experimental semi-quantitative profiling in Kesterite absorbers of such structural imperfections, and it constitutes the highlight of this work.

A. Discussion, limitations and improvement pathways

The novelty of this work lies in the determination of an accurate defect and composition profile using only surface sensitive methods combined with chemical etching. As we investigate Kesterite films produced with the standard process from our laboratory, one should keep in mind that the results obtained are possibly specific to our fabrication method. There is also a possibility that some of the observed defects are either created or affected by the chemical etching; there are however several arguments which tend to demonstrate otherwise. Firstly, the creation of surface defects following a Br_2 etching of chalcogenide films has never been reported, and reference [14] specifically states that etched surfaces are well defined. Similarly, the fabrication of solar cells on etched absorbers [16,22] does not indicate the creation of surface defects. The results from the UV Raman analysis compared with the literature yield very consistent conclusions. In a study from 2013 [28], Chen et al. predicted the prevalence of Sn and Zn related defects, though Sn_{Zn} in cluster with (2) Cu_{Zn} was reported at that time; while we report instead the Zn_{Sn} point defect, it was demonstrated in reference [21] that such defect naturally occurs in a slightly Sn poor Kesterite structure. The prevalence of Sn-related secondary phases tends to confirm that less Sn is incorporated in the absorber. Therefore, it is very unlikely that the defect profile observed in this study results from the Br_2 etching process. Similar defects have recently been identified as directly responsible for the poor carrier lifetime in Kesterite solar cells [11] and are in all likelihood the main reason for the high V_{oc} deficit observed in solar cells. Our analysis allows for a direct experimental demonstration of this limitation and a quantitative defect profiling could even be feasible when combined with other characterizations such as admittance spectroscopy, or through the numerical modeling of complete solar cells. Several solutions have been proposed to offset this limitation such as alkali doping or substitution of Cu by Ag, which could potentially help significantly decreasing the concentration of Sn/Zn related defects; this is however beyond the scope of this study, though the method proposed here is fully applicable to the characterization of such films.

The smoothing effect of the chemical etching on chalcogenide films is not a new result; our method allows however to analyze the morphology of the back side of the layer, which is arguably the second most important limitation of Kesterite absorbers. It is however not trivial to assess the extent to which it will degrade the performances. The presence of defects and secondary phases can potentially pin the fermi level below the bandgap and severely hinder the voltage of the solar cells. Back contact recombination may also be an issue despite the high absorption coefficient of the material. Considering the thickness of standard absorbers however (1.5 μm), back contact recombination has regularly been observed in quantum efficiency curves. Strategies are currently being developed in our laboratory with a significant improvement of the back interface morphology [Giraldo et al., *in preparation*, 2020]. Among the methods used to assess those samples, Br_2 etching of the films is a valuable asset in that regard.

The current study lacks data to investigate on the possible interplay between the films' morphology and the surface composition. As shown Figure SI 1, three regimes seem to co-exist when etching a Kesterite film, related to the surface roughness of the layer. A link could possibly exist with the surface composition of the films in the case of selective etching; specifically, if a different etching kinetic exists between the Kesterite and the secondary phases, as illustrated Fig. 5b. At this stage, we do not believe however that such interplay exists, as it was not reported in previous studies and the smoothing effect of the etching tends to indicate a homogeneous reaction; this point is specifically addressed in reference [29], albeit on CIGSe films rather than Kesterite. Also on CIGSe, Canava et al. showed that an ultrathin layer of elemental Se can be detected at the sample's surface following the etching, though a KCN treatment prior to the buffer layer deposition allows to fully eliminate this layer [14]. Additional experiments would be needed before drawing a conclusion in that regard.

The approach proposed in this work was successfully applied to both CIGSe and CZTSe, and preliminary results from our laboratory suggest that Br_2 etching could possibly be used on emerging PV absorbers such Sb_2Se_3. While this reinforces our hypothesis that our method is to an extent material agnostic, it may still be too early to qualify it as such and we hope that the community will contribute in the future with assessing other materials in a similar approach.

Nevertheless, the use of chemical etching combined with surface sensitive characterization methods sheds light on what we believe to be the two main limitations in state of the art CZTSe absorbers, namely a poor back interface morphology, and the prevalence of the Zn_{Sn} point defect, allowing for a direct observation of both.

4. Conclusion

A method for in-depth analysis of thin film photovoltaic absorbers is proposed and applied to CZTSe Kesterite films. A well-known Br_2 based chemical etching is used and the morphology of etched samples is assessed by surface profiling revealing a smoothing effect similar to previous reports on CIGSe. More importantly, deeper etchings illustrate the extent of the poor back interface morphology of standard CZTSe films, with numerous voids and up to 50% of the Mo surface not directly contacted by the absorber.

A depth-composition analysis of the films by successive chemical etchings and XPS reveals finer details in the elemental profile of the layer, and a specific Sn enrichment toward the back interface is observed; such important feature was not visible when following the standard profiling method in reference sample with a long sputter time, which leads to conclude to a much better accuracy of our approach in that context. The bonds analysis of the Se and Sn elements reveals an increasing occurrence of Se^0 consistent with a decline in film quality at the back interface, and the presence of both Sn^{+4} and Sn^{+2} could be an indirect way to identify the appearance of secondary phases and defects in the Kesterite structure.

The UV-Raman analysis of etched samples reveals the prevalence of the Zn_{Sn} defect throughout the absorber thickness, ascribed to the limited carrier lifetime and high V_{oc} deficit typically observed in Kesterite solar cells; on the other hand, V_{Cu} is found mostly unchanged throughout the bulk of the film, indicating a homogenous carrier concentration profile. Finally, tin-related secondary phase $SnSe_2$ is found increasingly prevalent toward the back interface of the film, which aligns well with the poor morphology observed both by electronic microscopy and confocal surface analysis, as well as the depth-composition profile established using XPS.

The results presented here, obtained on large sample areas, are the first direct observation of the nature and relative profile of defects in CZTSe absorber, highlighting several limitations of this material when fabricated in standard conditions, and providing a valuable insight for the design of future improvement strategies. This approach also holds implications for the entire field of thin films, and it possibly paves the way to both an exhaustive and simple assessment of emerging photovoltaic absorbers, for which the intrinsic limitations remain debatable.

CRediT authorship contribution statement

Kunal J. Tiwari: Methodology, Investigation. **Robert Fonoll Rubio:** Investigation, Data curation, Visualization. **Sergio Giraldo:** Investigation, Validation. **Lorenzo Calvo-Barrio:** Investigation, Data curation, Visualization. **Victor Izquierdo-Roca:** Investigation. **Marcel Placidi:** Writing - review & editing. **Yudania Sanchez:** Resources. **Alejandro Pérez-Rodríguez:** Funding acquisition, Supervision. **Edgardo Saucedo:** Funding acquisition, Supervision. **Zacharie Jehl Li-Kao:** Conceptualization, Methodology, Investigation, Data curation,

Visualization, Supervision, Writing - original draft.

Declaration of Competing Interest

The authors declare that they have no known competing financial interests or personal relationships that could have appeared to influence the work reported in this paper.

Acknowledgements

This work is possible thanks to the funding from the Ministry of Science and Innovation of Spain under IGNITE project (ENE2017-87671-C3-1-R), the European Regional Development Funds (ERDF, FEDER Programa Competitivitat de Catalunya 2007–2013) and CERCA Programme / Generalitat de Catalunya. Authors from IREC belong to the SEMS (Solar Energy Materials and Systems) Consolidated Research Group of the "Generalitat de Catalunya" (Ref. 2017 SGR 862).

Dr. Z. Jehl Li-Kao acknowledges the TecnioSpring Plus program (TECSPR17-1-0052) and the Marie Sklodowska Curie actions for their financial support.

M.Placidi thanks the Government of Spain for the Ramon y Cajal Fellowship (RYC-2017-23758).

Appendix A. Supplementary material

Supplementary data to this article can be found online at https://doi.org/10.1016/j.apsusc.2020.148342.

References

[1] M. Pagliaro, R. Ciriminna, G. Palmisano, BIPV: merging the photovoltaic with the construction industry: Merging photovoltaic with the construction industry, Prog. Photovolt. Res. Appl. 18 (1) (2010) 61–72.
[2] I. Mathews, S.N. Kantareddy, T. Buonassisi, I.M. Peters, Technology and Market Perspective for Indoor Photovoltaic Cells, Joule (2019).
[3] V. Fthenakis, Sustainability of photovoltaics: The case for thin-film solar cells, Renew. Sustain. Energy Rev. 13 (9) (2009) 2746–2750, https://doi.org/10.1016/j.rser.2009.05.001.
[4] C. Candelise, M. Winskel, R. Gross, Implications for CdTe and CIGS technologies production costs of indium and tellurium scarcity: Effects of indium and tellurium scarcity, Prog. Photovolt. Res. Appl. 20 (6) (2012) 816–831.
[5] H. Duan, J. Wang, L. Liu, Q. Huang, J. Li, Rethinking China's strategic mineral policy on indium: implication for the flat screens and photovoltaic industries: Rethinking China's strategic mineral policy on indium, Prog. Photovolt: Res. Appl. 24 (1) (2016) 83–93.
[6] S. Delbos, Kësterite Thin Films for Photovoltaics : A Review, EPJ. Photovolt. 3 (2012) 35004, https://doi.org/10.1051/epjpv/2012008.
[7] S.K. Wallace, D.B. Mitzi, A. Walsh, The Steady Rise of Kesterite Solar Cells, ACS Energy Lett. 2 (4) (2017) 776–779.
[8] S. Giraldo, Z. Jehl, M. Placidi, V. Izquierdo-Roca, A. Pérez-Rodríguez, E. Saucedo, Progress and Perspectives of Thin Film Kesterite Photovoltaic Technology: A Critical Review, Adv. Mater. 31 (16) (2019) 1806692, https://doi.org/10.1002/adma.v31.1610.1002/adma.201806692.
[9] Wong, L. H.; Zakutayev, A.; Major, J. D.; Hao, X.; Walsh, A.; Todorov, T. K.; Saucedo, E. Emerging Inorganic Solar Cell Efficiency Tables (Version 1). J. Phys. Energy 2019, 1 (3), 032001. https://doi.org/10.1088/2515-7655/ab2338.
[10] S. Siebentritt, Why are kesterite solar cells not 20% efficient? Thin Solid Films 535 (2013) 1–4, https://doi.org/10.1016/j.tsf.2012.12.089.
[11] S. Kim, J.A. Márquez, T. Unold, A. Walsh, Upper limit to the photovoltaic efficiency of imperfect crystals from first principles, Energy Environ. Sci. 13 (5) (2020) 1481–1491, https://doi.org/10.1039/D0EE00291G.
[12] E. Kask, M. Grossberg, R. Josepson, P. Salu, K. Timmo, J. Krustok, Defect studies in Cu2ZnSnSe4 and Cu2ZnSn(Se0.75S0.25)4 by admittance and photoluminescence spectroscopy, Mater. Sci. Semicond. Process. 16 (3) (2013) 992–996, https://doi.org/10.1016/j.mssp.2013.02.009.
[13] G. Li, G.R. Blake, T.T.M. Palstra, Vacancies in functional materials for clean energy storage and harvesting: the perfect imperfection, Chem. Soc. Rev. 46 (6) (2017) 1693–1706.
[14] Canava, B.; Guillemoles, J. F.; Vigneron, J.; Lincot, D.; Etcheberry, A. Chemical Elaboration of Well Defined Cu(In,Ga)Se2 Surfaces after Aqueous Oxidation Etching. Journal of Physics and Chemistry of Solids 2003, 64 (9–10), 1791–1796. https://doi.org/16/S0022-3697(03)00201-4.
[15] M. Bouttemy, P. Tran-Van, I. Gerard, T. Hildebrandt, A. Causier, J.L. Pelouard, G. Dagher, Z. Jehl, N. Naghavi, G. Voorwinden, B. Dimmler, M. Powalla, J. F. Guillemoles, D. Lincot, A. Etcheberry, Thinning of CIGS solar cells: Part I: Chemical processing in acidic bromine solutions, Thin Solid Films 519 (21) (2011) 7207–7211, https://doi.org/10.1016/j.tsf.2010.12.219.
[16] Z. Jehl Li-Kao, N. Naghavi, F. Erfurth, J.F. Guillemoles, I. Gérard, A. Etcheberry, J. L. Pelouard, S. Collin, G. Voorwinden, D. Lincot, Towards Ultrathin Copper Indium Gallium Diselenide Solar Cells: Proof of Concept Study by Chemical Etching and Gold Back Contact Engineering, Prog. Photovolt. Res. Appl. 20 (5) (2012) 582–587, https://doi.org/10.1002/pip.2162.
[17] M. Mousel, A. Redinger, R. Djemour, M. Arasimowicz, N. Valle, P. Dale, S. Siebentritt, HCl and Br2-MeOH etching of Cu2ZnSnSe4 polycrystalline absorbers, Thin Solid Films 535 (2013) 83–87, https://doi.org/10.1016/j.tsf.2012.12.095.
[18] H. Miyazaki, M. Aono, H. Kishimura, H. Katagiri, Surface Etching of CZTS Absorber Layer by Br-Related Solution, Physica Status Solidi C 12 (6) (2015) 741–744, https://doi.org/10.1002/pssc.201400274.
[19] C. Yan, K. Sun, F. Liu, J. Huang, F. Zhou, X. Hao, Boost Voc of pure sulfide kesterite solar cell via a double CZTS layer stacks, Solar Energy Mater. Solar Cells 160 (2017) 7–11, https://doi.org/10.1016/j.solmat.2016.09.027.
[20] S. Giraldo, E. Saucedo, M. Neuschitzer, F. Oliva, M. Placidi, X. Alcobé, V. Izquierdo-Roca, S. Kim, H. Tampo, H. Shibata, A. Pérez-Rodríguez, P. Pistor, How small amounts of Ge modify the formation pathways and crystallization of kesterites, Energy Environ. Sci. 11 (3) (2018) 582–593, https://doi.org/10.1039/C7EE02318A.
[21] M. Dimitrievska, F. Oliva, M. Guc, S. Giraldo, E. Saucedo, A. Pérez-Rodríguez, V. Izquierdo-Roca, Defect characterisation in Cu 2 ZnSnSe 4 kesterites via resonance Raman spectroscopy and the impact on optoelectronic solar cell properties, J. Mater. Chem. A 7 (21) (2019) 13293–13304, https://doi.org/10.1039/C9TA03625C.
[22] Z. Jehl, F. Erfurth, N. Naghavi, L. Lombez, I. Gerard, M. Bouttemy, P. Tran-Van, A. Etcheberry, G. Voorwinden, B. Dimmler, W. Wischmann, M. Powalla, J. F. Guillemoles, D. Lincot, Thinning of CIGS solar cells: Part II: Cell characterizations, Thin Solid Films 519 (21) (2011) 7212–7215, https://doi.org/10.1016/j.tsf.2010.12.224.
[23] S.-Y. Kim, S.-H. Kim, S. Hong, D.-H. Son, Y.-I. Kim, S. Kim, K. Ahn, K.-J. Yang, D.-H. Kim, J.-K. Kang, Secondary Phase Formation Mechanism in the Mo-Back Contact Region during Sulfo-Selenization Using a Metal Precursor: Effect of Wettability between a Liquid Metal and Substrate on Secondary Phase Formation, ACS Appl. Mater. Interf. 11 (26) (2019) 23160–23167.
[24] S. López-Marino, Y. Sánchez, M. Placidi, A. Fairbrother, M. Espindola-Rodríguez, X. Fontané, V. Izquierdo-Roca, J. López-García, L. Calvo-Barrio, A. Pérez-Rodríguez, E. Saucedo, ZnSe Etching of Zn-Rich Cu 2 ZnSnSe 4 : An Oxidation Route for Improved Solar-Cell Efficiency, Chem. Eur. J. 19 (44) (2013) 14814–14822.
[25] Wagner, C.; Riggs, W.; Davis, L.; Moulder, J.; Muilenberg, G. Handbook of X-Ray Photoelectron Spectroscopy. 1979. Eden, MN Perkin-Elmer Corp., Physical Electronics Division.
[26] Sunghyun Kim, Ji-Sang Park, Aron Walsh, Identification of Killer Defects in Kesterite Thin-Film Solar Cells, ACS Energy Lett. 3 (2) (2018) 496–500.
[27] Ignacio Becerril-Romero, Laura Acebo, Florian Oliva, Víctor Izquierdo-Roca, Simón López-Marino, Moisés Espíndola-Rodríguez, Markus Neuschitzer, Yudania Sánchez, Marcel Placidi, Alejandro Pérez-Rodríguez, Edgardo Saucedo, Paul Pistor, CZTSe solar cells developed on polymer substrates: Effects of low-temperature processing, Prog. Photovolt. Res. Appl. 26 (1) (2018) 55–68.
[28] Chen, S.; Wang, L.-W.; Walsh, A.; Gong, X. G.; Wei, S.-H. Abundance of CuZn + SnZn and 2CuZn + SnZn Defect Clusters in Kesterite Solar Cells. Appl. Phys. Lett. 2012, 101 (22), 223901. https://doi.org/10.1063/1.4768215.
[29] Jehl, Z.; Bouttemy, M.; Lincot, D.; Guillemoles, J. F.; Gerard, I.; Etcheberry, A.; Voorwinden, G.; Powalla, M.; Naghavi, N. Insights on the Influence of Surface Roughness on Photovoltaic Properties of State of the Art Copper Indium Gallium Diselenide Thin Films Solar Cells. Journal of Applied Physics 2012, 111 (11), 114509. https://doi.org/10.1063/1.4721648.

Supporting Information

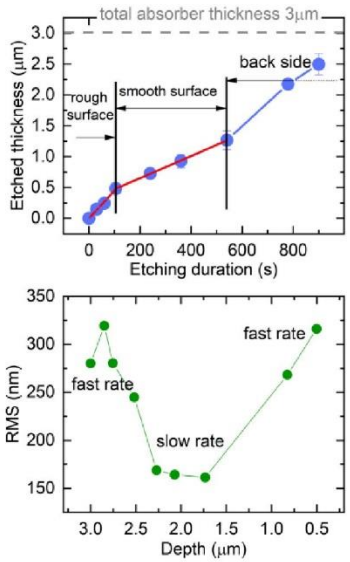

Figure SI 1 Etching rate (top) and surface RMS (bottom) of etched kesterite films.

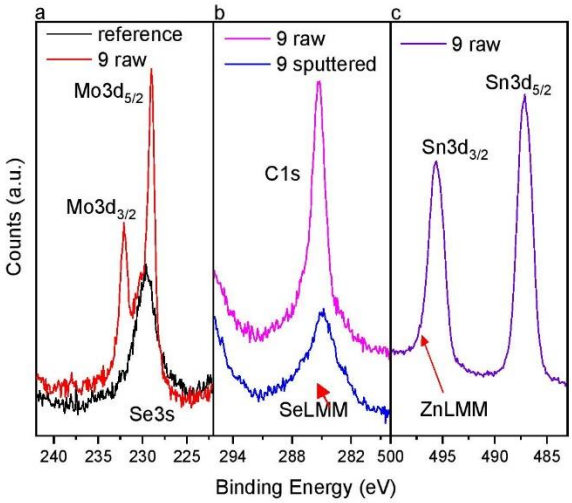

Figure SI 2 XPS Signals from orbitals and auger lines of different elements present in the samples that can overlap when analysing by X-ray source Al Kα line: Mo3d with Se3s, C1s with SeLMM and Sn3d3/2 with ZnLMM in a, b and c respectively, in sample raw and sputtered and the reference sample as example.

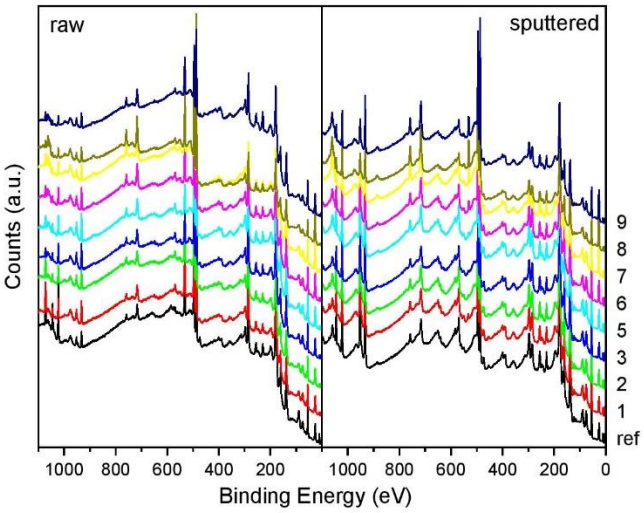

Figure SI 3 Survey XPS spectra for all the set of etched samples as presented (raw) and sputtered.

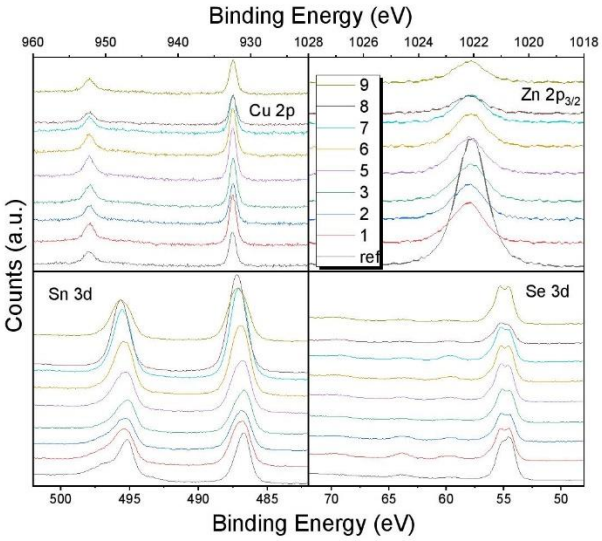

Figure SI 4 High-resolution XPS spectra for the main orbitals of the CZTSe elements in all the set samples as presented (raw).

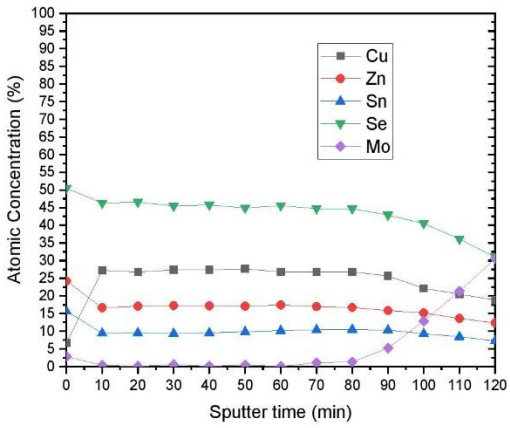

Figure SI 5 Atomic concentration profile obtained by XPS for the reference sample.

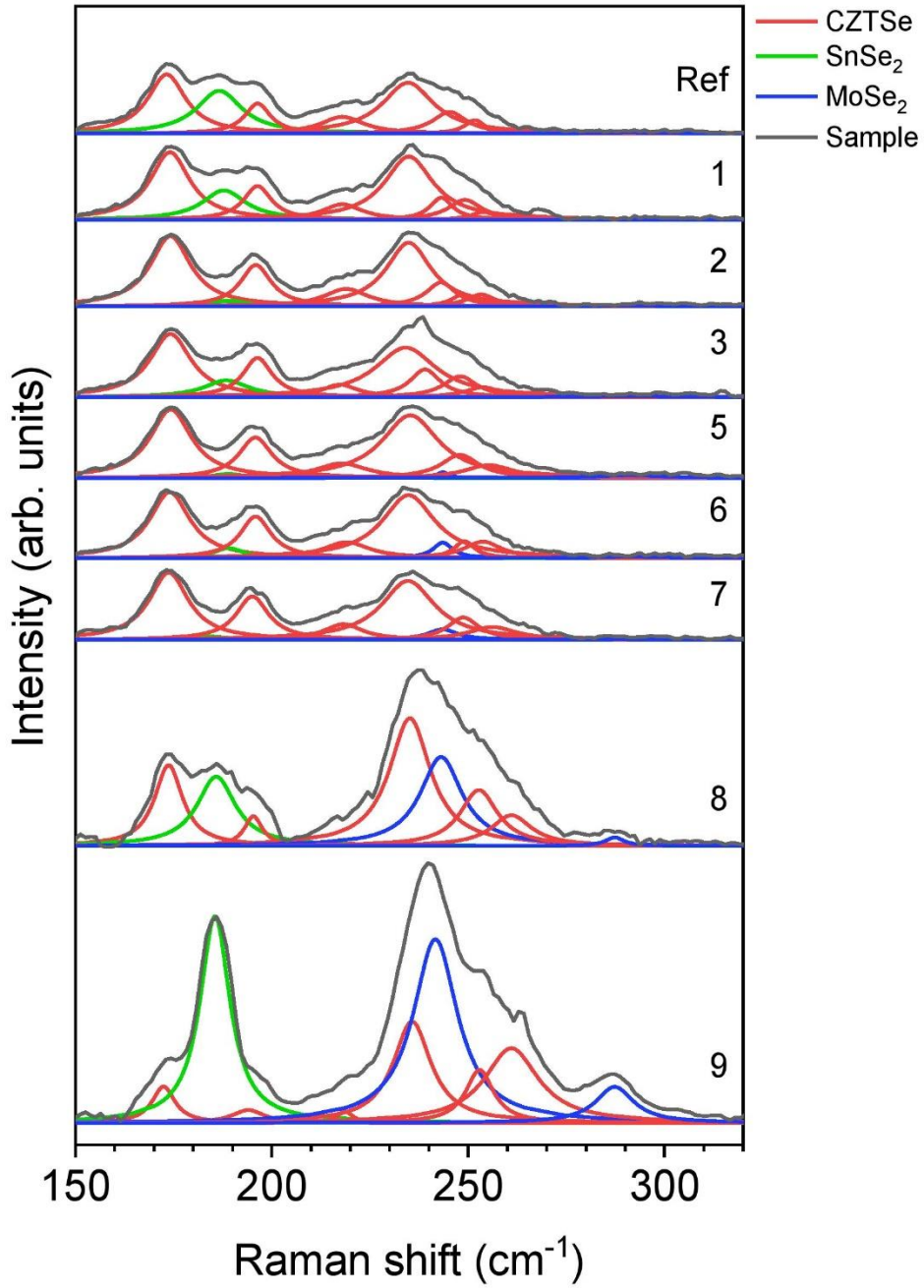

Figure SI 6 Raman spectra fitting deconvolution using Lorentzian curves of the spectra acquired under 325 nm excitation wavelength for the different etching times samples.

3.4. Article 3: Rear interface engineering of kesterite $Cu_2ZnSnSe_4$ solar cells by adding $CuGaSe_2$ thin layers

Received: 19 June 2020 | Revised: 1 October 2020 | Accepted: 22 October 2020

DOI: 10.1002/pip.3366

RESEARCH ARTICLE

PROGRESS IN PHOTOVOLTAICS WILEY

Rear interface engineering of kesterite $Cu_2ZnSnSe_4$ solar cells by adding $CuGaSe_2$ thin layers

Sergio Giraldo[1] | **Robert Fonoll-Rubio**[1] | **Zacharie Jehl Li-Kao**[1] | **Yudania Sánchez**[1] | **Lorenzo Calvo-Barrio**[2,3] | **Victor Izquierdo-Roca**[1] | **Alejandro Pérez-Rodríguez**[1,3] | **Edgardo Saucedo**[1]

[1]Catalonia Institute for Energy Research (IREC), Jardins de les Dones de Negre 1, Sant Adrià de Besòs, Barcelona, 08930, Spain

[2]Centres Científics i Tecnològics de la Universitat de Barcelona (CCiTUB), Lluís Solé i Sabarís 1-3, Barcelona, 08028, Spain

[3]IN2UB, Departament d'Enginyeria Electrònica i Biomèdica, Universitat de Barcelona, Martí i Franquès 1, Barcelona, 08028, Spain

Correspondence
Sergio Giraldo, Catalonia Institute for Energy Research (IREC), Jardins de les Dones de Negre 1, Sant Adrià de Besòs, 08930 Barcelona, Spain.
Email: sgiraldo@irec.cat

Funding information
H2020 Programme under the project INFINITE-CELL, Grant/Award Number: H2020-MSCA-RISE-2017-777968; Ministry of Science and Innovation of Spain under IGNITE project:, Grant/Award Number: ENE2017-87671-C3-1-R; SEMS (Solar Energy Materials and Systems) Consolidated Research Group of the "Generalitat de Catalunya", Grant/Award Number: 2017 SGR 862; European Regional Development Funds (ERDF, FEDER Programa Competitivitat de Catalunya 2007–2013); CERCA Programme/Generalitat de Catalunya

Abstract

Kesterite $Cu_2ZnSn(S,Se)_4$ thin film technology has been thoroughly investigated during the last decade as a promising solution in the field of low-cost, sustainable, and environmental-friendly photovoltaic technologies. However, despite efforts to boost kesterite solar cells performance by numerous strategies, the efficiencies remain stagnant around 13%. Some commonly observed issues in this technology refer to recombination events due to the likely presence of defects and, largely in line with the latest, the presence of voids and poor morphologies at the rear interface. This work, partly inspired by the copper indium gallium selenide (CIGS) technology and the use of wide-bandgap Ga-rich region as back surface field (BSF), focuses on an innovative approach using ultrathin CuGa layers at the rear interface to promote the formation of wide-bandgap $CuGaSe_2$, acting as an efficient electron reflector or BSF, and to function as an effective interlayer improving the kesterite crystallinity at the back interface. Kesterite $Cu_2ZnSnSe_4$ devices fabricated with added CuGa layers show a general increase in photovoltaic parameters and a significantly enhanced collection efficiency compared with reference devices without CuGa. This strategy proves to be successful, for not only passivating but also for improving the Mo/kesterite interface morphology, preventing to a large extent the presence of voids at the back region of the absorber.

KEYWORDS

back surface field (BSF), $Cu_2ZnSnSe_4$ (CZTSe), interface engineering, kesterite, thin film PV

1 | INTRODUCTION

Kesterite $Cu_2ZnSn(S,Se)_4$ (CZTSSe) is nowadays still considered one of the most promising inorganic thin film photovoltaic (PV) absorbers with a good prognostic for a large number of applications in the future, from custom-made modules with appealing features, such as flexible or colorful devices, being an ideal candidate for building-integrated PV (BIPV), to smaller modules capable of powering many types of sensors, including the wide and recent field of Internet of Things (IoT) applications.[1] In addition, kesterite holds a great number of advantages that makes it an ideal PV semiconductor, including its environment- and sustainability-friendly features because it is synthesized from earth-abundant and low-toxicity elements, it has excellent optical absorption properties ($\alpha > 10^4$ cm^{-1}), naturally p-type conductivity, and a direct bandgap that can be easily tuned from 1.0 to 1.5 eV by simply varying the S/Se ratio,[2] and even reach higher values when cationic substitution strategies are used.[3,4]

Despite an intensive research effort in this family of semiconductor materials, the efficiency of kesterite solar cells remains stagnant at values around 13%.[5,6] Especially, comparing the certified record

device efficiency of kesterite CZTSSe (12.6%) with its more mature close cousin Cu (In,Ga)Se_2 (23.35%),[7] it is clear that a large improvement margin remains. It is in that context a logical approach to take inspiration from proven strategies used in copper indium gallium selenide (CIGS), specifically the rear interface engineering and the formation of a controlled cationic grading. The presence of Ga-rich CIGS at the rear interface induces a higher bandgap by mainly increasing the conduction band, thus contributing to a better collection of the charge carriers generated deeper in the absorber, which are normally associated to long-wavelength light absorption, impacting positively on the devices efficiency by increasing the current density and decreasing recombination events.[8] This concept, known as electron reflector or back surface field (BSF), has been widely exploited in many other mature PV technologies through different approaches.[9,10]

On this topic, several examples can be found in the literature for different PV materials, leading to a similar improvement of the devices performance. First, in the case of silicon solar cells, the formation of a heavily doped p-type region by using different dopant elements, like Al or B, has demonstrated an efficient BSF effect leading to a better long-wavelengths collection.[11,12] Other examples include the use of a ZnTe layer in CdTe solar cells, which can create a barrier in the conduction band due to the bandgap difference between both materials, reflecting minority carriers away from the back surface.[13] As previously mentioned, the CIGS technology relies on a Ga grading, thus forming a bandgap grading towards the back contact, and again improving the carrier collection and decreasing surface recombination at the back contact.[14] In theory, a similar approach could be applicable in the case of kesterite; however, these compositional gradients have shown to be more challenging so far.

The need of a BSF becomes relevant especially when the back surface recombination velocity begins to strongly influence solar cells performance, which is a possibility when the minority-carrier diffusion length approaches or exceeds film thickness. Moreover, the absorption coefficient of the PV material plays an important role in the aforementioned matter, as it determines the depth at which charge carriers are generated within the absorber layer. If low energy photons can create charge carriers able to diffuse towards the rear interface, an electron reflector could have a significant beneficial impact on the carriers' collection. In the case of kesterite CZTSe, although the absorption coefficient is high and the photon penetration depth is expected to remain lower than 200 nm even for low energy photons,[15,16] its diffusion length ranging from 500 nm to 2 μm[17–19] along with the typical absorber thicknesses used around 1.5 μm makes the implementation of a BSF layer a promising approach to reduce back contact recombination also in this technology.

Regarding rear interface passivation in kesterite, some strategies have been studied with relatively successful outcome. Lee et al[20] reported an effective interface passivation approach by implementing nanometer-scale Al_2O_3 thin films grown by ALD in CZTS solar cells, resulting in enhanced power conversion efficiencies by improving the V_{OC}, FF, long-wavelength collection efficiency, and the short-circuit current density (J_{SC}). Similarly, Kim et al[21] achieved remarkable V_{OC} deficit improvements, suppressing nonradiative recombination via interface passivation through patterned thin Al_2O_3 layers, applied to both front and rear interfaces. Other investigated strategies include the use of high work function MoO_3 layers, in which Ranjbar et al[22] demonstrated an improved minority-carrier lifetime and open-circuit voltage by introducing 10 nm of MoO_3 between Mo rear contact and CZTSe, showing a reduced interface recombination. Similarly, Antunez et al[23] presented a method to increase V_{OC}, decreasing electron–hole recombination, by using a combination of MoO_3 with an original Au back contact. This approach proved very useful especially for thin absorbers where the BSF effect becomes critical. On the other hand, the influence of SnS compound at the interfaces was studied by Ren et al,[24] showing promising beneficial effects for the J_{SC} of the solar cells when it is located at the rear interface, likely attributable to a passivation effect.

In the same vein, the rear interface in kesterite CZTSSe has shown recurrently issues related to the presence of voids along the Mo/kesterite interface, in some cases attributed to the diffusion of the different elements during the reactive annealing and/or the formation of volatile compounds such as $Sn(S,Se)_2$.[25,26] More recently, Kim et al[27] attributed the formation of voids and secondary phases to the wettability behavior between the substrate and metal precursor, presenting promising strategies through the implementation of intermediate layers to prevent these phenomena. Besides this, there is a wide consensus on the detrimental decomposition reaction that occurs at the Mo/kesterite interface resulting in decomposition of the CZTS layer into Cu_2S, ZnS and SnS_2 and growth of MoS_2 (same for the selenide compound CZTSe).[28] In this regard, the implementation of several interlayers has been investigated using a variety of materials with the aim of avoiding absorber decomposition and improving the back interface morphology. López-Marino et al[29] reported a process based on the use of an ultrathin ZnO intermediate layer, inhibiting the decomposition reaction, thus leading to improved morphologies and achieving significant device performance improvements. Later on, this same strategy was further improved by applying a rapid thermal annealing (RTA) treatment on glass/Mo/ZnO substrates, where Placidi et al[30] showed greatly improved CZTSe device performance, through the increase of the shunt resistance and decreased series resistance, related to the reduction of defects induced such as voids at the back interface and cracks in the window layer. Interestingly, Schnabel et al[31] investigated on the use of TiN as interlayer, showing that direct contact between CZTSSe and Mo is necessary to form a large-grain layer near the back contact, and stating that the decomposition of the kesterite phase and formation of $Mo(S,Se)_2$ might be needed for forming large grains, although it seemed that only the presence of $Mo(S,Se)_2$ is required for achieving good performing devices. A different approach was reported by Cui et al,[32] who introduced a thin Ag intermediate layer, showing a reduction of secondary phases as well as the amount of voids, leading to better carrier collection efficiencies and lower series resistance, improving the overall performance of CZTS solar cells. In connection with the latter, recent first principle calculations showed that introducing Ag in kesterite is a promising strategy to stabilize the defect formation in the films, lowering significantly nonradiative

recombination.[33] Furthermore, the use of Al_2O_3 by the team of X. Hao was shown to be an effective method to avoid phase segregation and voids at the back contact region, achieving longer minority lifetime and reduced back contact recombination, ultimately leading to boosted CZTS solar cells efficiency.[34] On the other hand, Meng et al[35] demonstrated a carbon-doping strategy to enhance the back contact adhesion, significantly eliminating the voids with good repeatability and improved long-term stability.

In this work, partly inspired by the CIGS technology and the formation of the wide-bandgap Ga-rich rear region acting as BSF, we study the effect of adding small amounts of Ga at the back region of kesterite $Cu_2ZnSnSe_4$ (CZTSe) absorbers. The aim of this strategy is, on one hand, to promote the formation of wider bandgap $CuGaSe_2$ (CGSe) compound at the rear interface to create a BSF and, on the other hand, to investigate its impact on the interface morphology as a possible approach to prevent voids formation and improve adhesion. It is important to note that although Ga is considered a critical raw material, the quantities used in this approach are minimal; therefore, the sustainability of the presented technology would not be compromised. The method described here represents a simple yet effective strategy to address some critical limitations in kesterite CZTSe solar cells, such as the poor morphology and the presence of highly defective interfaces, increasing the likelihood of recombination events. In this context, the approach presented here shows a significant positive impact on the absorber's morphology, greatly improving the quality of the CZTSe especially at back side. The latter along with the demonstration of a BSF effect through the formation of CGSe phases, address one key issue in CZTSe technology, ultimately leading to remarkable cell performance improvements. Additional SCAPS-1D simulations are presented to study the impact of thin BSF layers as a function of the absorber thickness and discussed in regard to the experimental results.

2 | EXPERIMENTAL SECTION

Samples were prepared on Mo-coated (DC magnetron sputtering, Alliance AC450) soda-lime glass substrates. Ga addition was studied through the deposition of various thicknesses of CuGa (0, 5, 10, and 25 nm) on the Mo back contact, prior to the CZT metallic stack precursor. CuGa layers were sputtered and subsequently subjected to different preselenization treatments (samples without preselenization treatment also included). These thermal treatments were performed at temperatures ranging from 400°C to 500°C for 10 min at 1.5-mbar Ar pressure, under Se atmosphere. Then, the standard Sn/Cu/Zn metallic stack was completed on top, using optimum Cu-poor and Zn-rich composition (Cu/(Zn + Sn) ∼ 0.75; Zn/Sn ∼ 1.10, determined with calibrated X-ray fluorescence (XRF) (Fischerscope XVD), and subjected to reactive annealing under Se + Sn atmosphere in order to synthesize the final CZTSe absorber. The full absorber thickness was estimated at ∼1.5 μm, measured by XRF and scanning electron microscopy (SEM). Ultimately, solar cell devices were fabricated by depositing 50 nm CdS by chemical bath deposition (CBD), followed by 50-nm i-ZnO and 200-nm ITO by DC-pulsed sputtering (Alliance CT100). To perform the optoelectronic characterization, 3 × 3 mm^2 cells were mechanically scribed using a manual microdiamond scriber (OEG Optical Metrology MR200). Further detailed experimental steps for the fabrication of CZTSe solar cell devices have been reported in previous works.[30,36]

J-V characteristics were acquired using a calibrated class AAA solar simulator (Abet Technologies). Measurements were performed at 25°C, under AM1.5G 1-sun illumination conditions (uniform illumination area of 15 × 15 cm^2). Spectral response measurements were carried out using a Bentham PVE300 system calibrated with Si and Ge photodiodes, to obtain the EQE of the solar cells under different bias voltage conditions. SEM was performed at 5 kV accelerating voltage using a ZEISS Series Auriga microscope. Auger spectroscopy characterization was performed in a PHI 670 Scanning Auger Nanoprobe from Physical Electronics, using a field emission electron gun working at 10 keV and 10 nA as excitation source, and scanning a surface of 15 × 15 μm to avoid inhomogeneities. In-depth chemical composition profiles were obtained with alternate sputtering of Ar^+ ion source (4 keV). The estimated sputter ratio was about 75 nm/min. These measurements were performed in an ultrahigh vacuum (UHV) chamber with pressures between 5×10^{-10} and 9×10^{-9} Torr in order to prevent the reabsorption of the sputtered material. The data analysis of the spectra was done with Multipak Version 9.9.08 program from ULVAC-PHI. For quantification purposes, due to very important matrix effects of the Auger measurements, sensitivity factors provided by the same program were adapted to fit actual measurements of own standard samples used as references. Raman characterization was carried out using an FHR640 and an iHR320 spectrometers (Horiba Jobin-Yvon) optimized for the 532- and 785-nm excitation wavelengths, respectively. The different penetration length in the absorber of both excitations (50-nm penetration for the 532-nm excitation, and 150-nm penetration for the 785-nm one) allowed to obtain information from points at different depth. Each spectrometer was coupled to a CCD detector cooled down to −75°C. The measurements were performed in the backscattering configuration through an Olympus objective coupled to an IREC-designed probe. Both excitations were performed using solid-state lasers. The laser power densities were kept below 220 W/cm^2 in order to prevent thermal effects. The Raman shift was calibrated by imposing the shift for the main silicon band of a Si monocrystal reference at 520 cm^{-1}. The study of the back interface was achieved by means of a mechanical lift-off, detaching the absorber from the Mo substrate. Solar cell modeling was performed using SCAPS-1D ver. 3.3.07,[37] and the model parameters were taken from various literature sources.[38,39] The model was kept as simple as possible to keep the focus on the influence of the back contact when varying the absorber thickness; the complete set of modeling parameters can be found in the supporting information.

3 | RESULTS AND DISCUSSION

As mentioned in Section 1, a consensus regarding the issues of a badly crystallized kesterite absorber in the back region exists in the

community. Usually, this includes the presence of smaller crystals, voids, in some cases segregated secondary phases, but in general, a more degraded morphology and poorer adhesion between the Mo back contact and the kesterite absorber. Figure 1 illustrates pretty well the presence of voids at the rear interface, despite the well-crystallized top layer, in a standard CZTSe reference cell (Figure 1A). Nevertheless, the implementation of a thin layer of CuGa, followed by a preselenization treatment as described in the Section 2, demonstrates a significant improvement in the rear interface morphology with a denser and well-compacted structure, showing a greatly improved adhesion between the layers. In particular, Figure 1 shows a clear improvement of the rear morphology when 25 nm of CuGa (preselenized at 400°C) are introduced before the metallic stack precursor deposition (Figure 1B). In fact, substantial improvements in the morphology are observed even for thinner layers of CuGa. Figure S1 shows the effect of only 10-nm CuGa, with and without preselenization treatment. As can be seen, when no selenization treatment is applied to the CuGa layer, although slightly bigger crystals might form, the presence of voids is not prevented. In this case, the thin CuGa layer is likely totally decomposed during the reactive annealing forming the CZTSe, leading to a slightly higher Cu amount during the annealing, which could explain the observed enlarged crystals, and to the presence of some Ga impurities in the kesterite matrix. Even though high Cu concentrations in CZTSe have been found to be detrimental for the solar cell performance, Cu-rich growth conditions are able to assist the grain growth.[40] Nonetheless, when the CuGa layer is preselenized, the morphology quality improvement is much more noticeable. In such a case, a stable thin $CuGaSe_2$ layer is expected to form, thus creating a seed layer for the kesterite growth avoiding the direct contact between the CZTSe and the Mo, and preventing its decomposition and the subsequent formation of voids. As can be noticed in Figure 1B, the half bottom part of the absorber is formed by smaller grains, especially near the rear interface. Indeed, this is due to the formation of the thin $CuGaSe_2$ layer during the preselenization step; however, the fact of being smaller crystals should not be an issue for the device performance provided the grain boundaries are well passivated and this layer provides a good contact.

To evaluate the impact of the back CuGa layers on the devices performance, a complete set of CZTSe absorbers synthesized on different thicknesses of CuGa with and without Se treatments was made into solar cells. Figure 2 shows a comparison of the different PV parameters of the devices included in this study. As may be seen, samples with no preselenization treatment present the lowest efficiencies, especially with increasing CuGa thickness. In this regard, Kondrotas et al[41] studied previously the system Cu (In,Ga)Se_2-ZnSe and demonstrated the formation of Cu-Zn-Ga-Se phases, which might be responsible for the solubility of the thin CuGa layers without any treatment in the presence of Zn and Se during the reactive annealing, thus preventing the formation of a $CuGaSe_2$ layer at the back interface. In this case, the additional Cu amount together with Ga impurities throughout the absorber could explain the performance decrease. Nevertheless, when these thin CuGa layers are thermally treated under Se atmosphere, all of them lead to a general efficiency improvement regardless of the temperature used for the treatment. Surprisingly, thicknesses as low as 5 nm of CuGa (and up to 25-nm CuGa), previously preselenized, are already sufficient to achieve remarkable improvements in terms of device performance (+2% absolute increase in efficiency), showing a general improvement of V_{OC}, J_{SC}, and FF. In particular, the beneficial effect on the current density together with the V_{OC} improvement could be an indication that this CuGa layer is forming the $CuGaSe_2$ compound at the back region acting as back electron reflector. Furthermore, the positive effect on the FF would correlate well with the previously shown improved morphology at the interface, leading to a decreased series resistance in the devices. In the same way, the better morphology of the back side could also explain to a large extent the V_{OC} improvement, as the presence of defects and recombination centers would be notably reduced, therefore preventing a detrimental pinning of the quasi Fermi level and the consequent limitation on the cell voltage.

Figure 3 shows additional external quantum efficiency (EQE) measurements for selected devices without and with 25-nm CuGa. First, we can notice an enhanced charge carriers' collection with increasing the CuGa thickness, especially in the long-wavelengths region correlating well with the J_{SC} improvement. The complete set of measured EQEs of the different devices is displayed in Figure S2, showing the gradual collection efficiency improvement. This specific behavior is recurrently reported when BSF layers are used regardless of the PV technology, such as in silicon solar cells by introducing boron-based BSF,[11] in CIGS with the Ga-gradient,[14] or even in kesterite theoretical studies have shown how the introduction of a p-Si layer would efficiently act as BSF.[42] Intriguingly, also in Figure 3, the EQE measured under reverse bias voltage (−1 V) confirms a remarkable improvement in collection efficiency, likely related to lower recombination at the rear interface for the CuGa containing sample, which could be directly

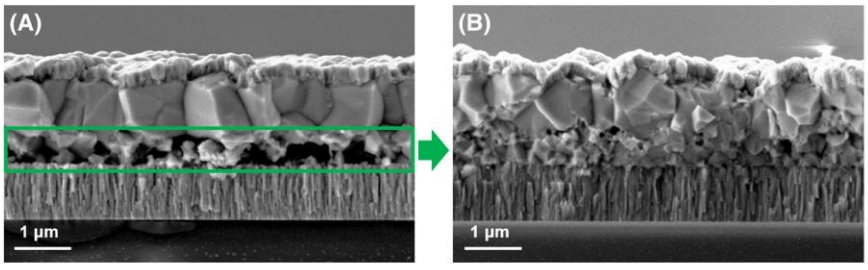

FIGURE 1 Cross-sectional scanning electron microscopy (SEM) images of a reference CZTSe cell (without CuGa) (A), and a CZTSe cell fabricated with 25-nm CuGa (preselenized) at the rear interface (B) [Colour figure can be viewed at wileyonlinelibrary.com]

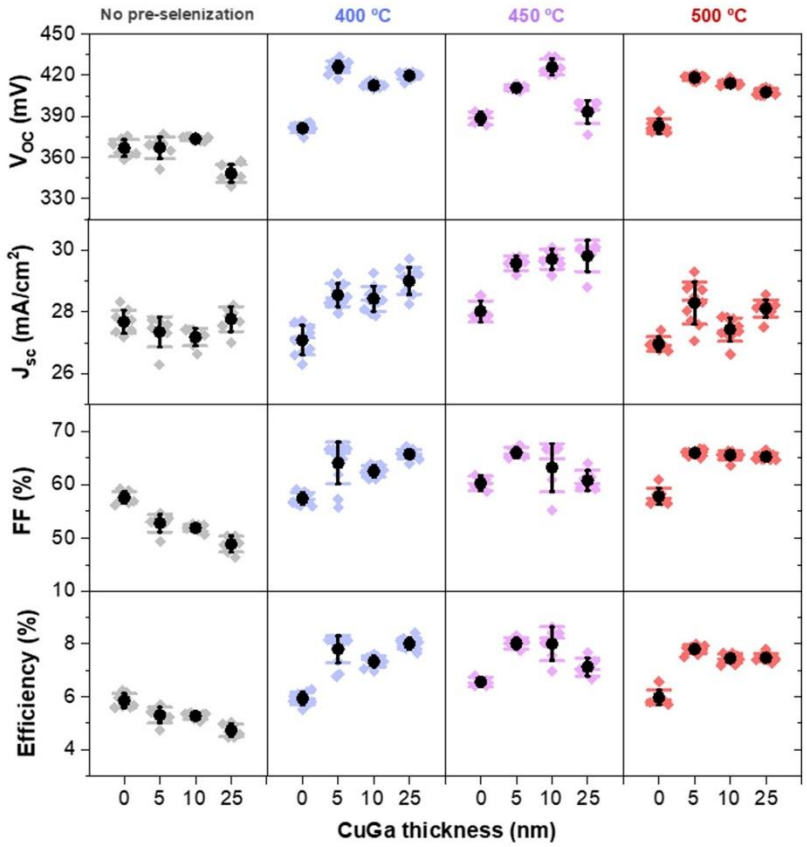

FIGURE 2 Photovoltaic parameters of CZTSe solar cell devices fabricated with different CuGa thicknesses added on the Mo back contact, subjected to four different treatments: no preselenization (grey), preselenization at 400°C (blue), preselenization at 450°C (purple), and preselenization at 500°C (red) [Colour figure can be viewed at wileyonlinelibrary.com]

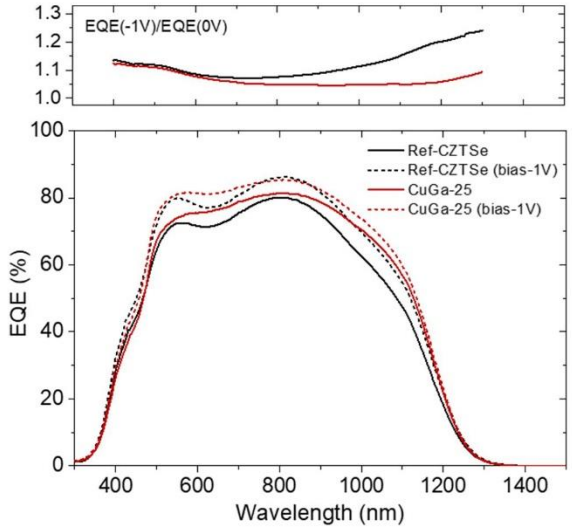

FIGURE 3 EQE spectra of a reference CZTSe solar cell device and a device fabricated with preselenized 25-nm CuGa at 400°C, measured under 0 V (solid lines) and −1 V bias voltage (dashed lines). In the upper part, the ratio EQE(−1 V)/EQE(0 V) is displayed. EQE, external quantum efficiency [Colour figure can be viewed at wileyonlinelibrary.com]

associated with the observed morphology improvement as well as the fact of having a passivating layer at the back side. This is especially noted in the plot of the ratio EQE(−1 V)/EQE(0 V), displayed in the upper part of the figure.

The question of the existence of a separate $CuGSe_2$ phase however remains at this point. To have a clear answer, a combination of in-depth compositional analysis by Auger spectroscopy and detailed structural and phase analysis by Raman spectroscopy was performed on the different samples. Figure 4 shows the Auger in-depth profiling of a device fabricated with 25 nm of CuGa (preselenized) at the back side. As can be seen, especially in the zoomed view corresponding to the interface between the CZTSe and the Mo back contact, the Ga mostly accumulates at the rear interface (in the region from 12 to 20 min, sputter time). This could be a clear indication that CuGa layers, after being preselenized, are resilient enough to remain at the back interface forming most likely $CuGaSe_2$ phases. In fact, the literature about $CuGaSe_2$ thin films shows synthesis conditions very similar to the ones utilized in this work, with synthesis temperatures in the range of 530°C–550°C, which might support its stability during further cell processing.[43,44] Regarding the rest of the elements, an expected even distribution and constant flat profiles are observed, without traces of Ga in any other region of the CZTSe absorber. Additionally, Figure S3 shows a clear evolution of the Ga accumulation at

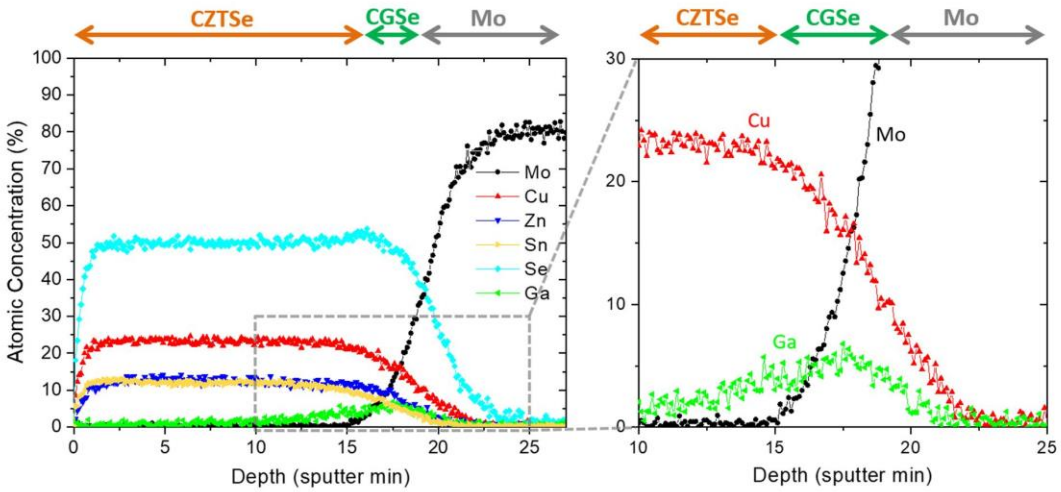

FIGURE 4 Auger spectroscopy in-depth compositional analysis of a CZTSe absorber fabricated with 25-nm CuGa (preselenized at 400°C) at the Mo/CZTSe rear interface [Colour figure can be viewed at wileyonlinelibrary.com]

the back region with the increasing CuGa thickness (0, 5, 10, and 25 nm of CuGa).

Following with the same question, a deep Raman analysis with two different excitation wavelengths (532 and 785 nm) was performed on the back surface of the CZTSe absorbers, accessible through previous mechanical lift-off. Both front and back surfaces of the absorber were analyzed, as well as the remaining material on the substrate side (not shown). Figure 5 shows the Raman spectra of the back surface of the absorbers obtained for a reference CZTSe sample (without CuGa layer) and a CZTSe absorber fabricated with a 25-nm CuGa layer (CuGa-25), along with a $CuGaSe_2$ (CGSe) sample grown in the same preselenization conditions as reference. The characteristic Raman peaks of CZTSe are observed in the reference and the CuGa-25 samples for both excitations.[45] In addition, $MoSe_2$ vibrational modes, which are enhanced with the 785-nm excitation due to resonant effects, are observed in both samples too.[46] Thus, confirming the proper formation of CZTSe at the back side, along with an expected partial selenization of the Mo back contact. It should be noted that the intensity of the peaks related to $MoSe_2$ phases can vary from one sample to another due to the nature of the mechanical lift-off process, as these phases can remain in both sides after the lift-off. In any case, the formation of thin $MoSe_2$ layers at the rear interface in

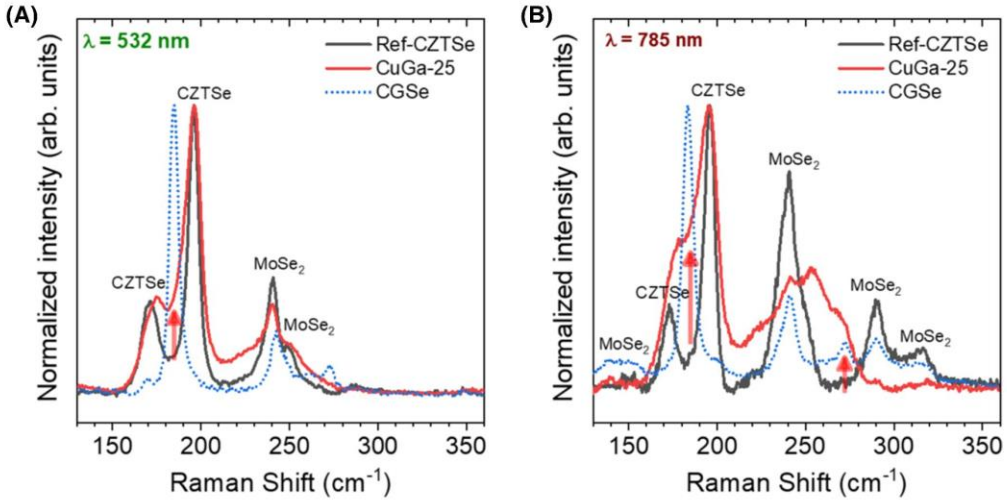

FIGURE 5 Raman analysis performed with 532- (A) and 785-nm (B) excitation wavelengths on the back surface of a reference CZTSe sample (without CuGa), a CuGa-25 sample (with 25 nm of CuGa preselenized), and a $CuGaSe_2$ sample as reference [Colour figure can be viewed at wileyonlinelibrary.com]

chalcogenide solar cells has been proven to be beneficial to achieve a good ohmic contact positively affecting the device performance.[47,48] As can be noticed in the same figure, the CGSe presents a characteristic peak at 185 cm^{-1} leading to a clear contribution in the CuGa-25 spectra (measured with both excitation wavelengths). However, this is not the case in the reference CZTSe spectra, where there is only evidence of kesterite CZTSe and $MoSe_2$. An additional CGSe characteristic peak at 270 cm^{-1} leads to a clear shouldering in the CuGa-25 spectra, whereas such feature is again absent from the reference CZTSe. Regarding the front surface analysis, Figure S4 shows no significant differences between the Raman spectra of the studied samples, demonstrating the presence of the CZTSe phase, whereas no effect of the CuGa addition is observed in any absorber at the front side. These results therefore confirm the presence of resilient CGSe phases exclusively at the rear interface.

To support the experimental results presented and to discriminate between the BSF effect and the improved morphology in terms of PV performance, SCAPS-1D simulations were performed. In such model, mostly based on the Anderson approach of clear separation between layers,[49] simulating the back side morphology improvement is near impossible; implementing a BSF is however trivial. Three different scenarios were studied using three different CZTSe absorber thicknesses: (i) 1.2-μm CZTSe as the standard case (considering the size of the voids in the actual layers, this is deemed a more realistic value for the effective absorber thickness); (ii) 1.8-μm CZTSe as a thicker absorber; and (iii) 600-nm CZTSe as a thinner absorber. In all three cases, the thickness of the bottom $CuGaSe_2$ was kept constant. Figure 6 shows the effect on the PV performance for all three scenarios (Figures S5 and S6 show the SCAPS parameters used for the CZTSe and the $CuGaSe_2$ layer, respectively). As can be observed, for thick absorbers, the use of a BSF is largely irrelevant. In this case, considering the relatively low diffusion length and lifetime together with the high absorption coefficient, the absorber layer is thick enough so the vast majority of charge carriers generated (mainly within the first hundreds of nm of the CZTSe) never reach the back region; therefore, the effect of the added BSF layer proves to be negligible. However, for our standard thickness kesterite, a significant impact is observed. Here, the 1.2-μm CZTSe absorber has an optimal thickness to allow the charge carriers to diffuse toward the back interface and to be efficiently reflected by the BSF (enhancing collection) and while the absorber

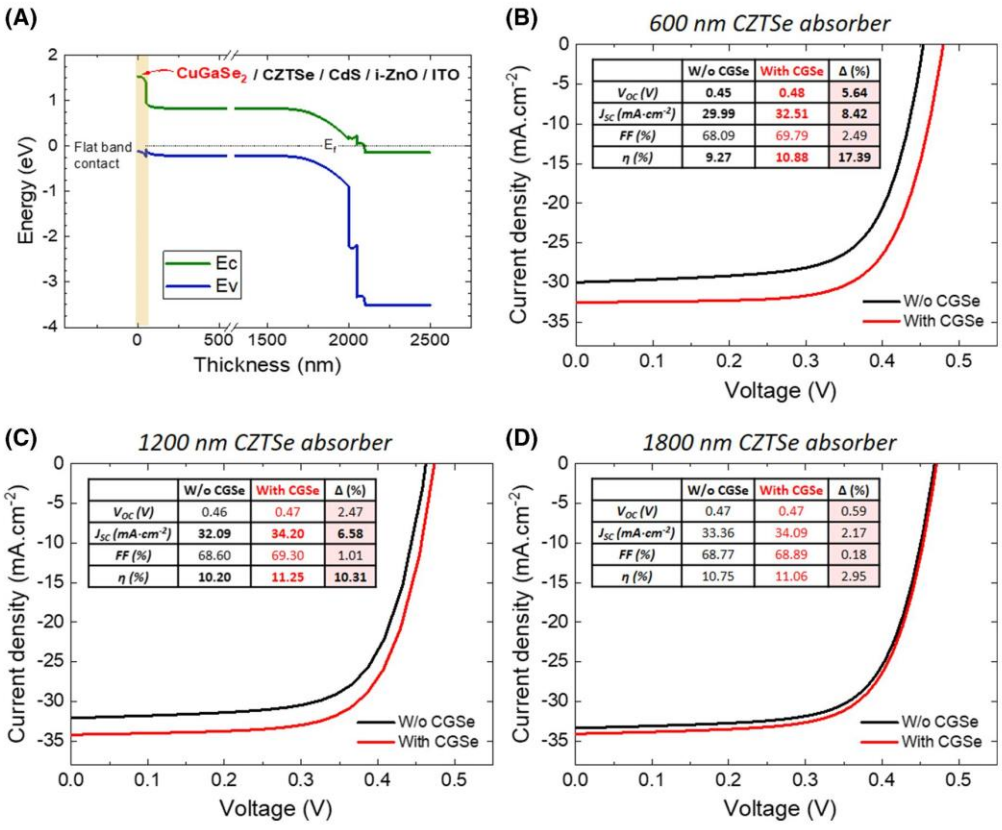

FIGURE 6 Energy band diagram of the simulated solar cell structure with $CuGaSe_2$ (A); J-V characteristics and photovoltaic parameters obtained with SCAPS-1D simulations for CZTSe solar cells with and without $CuGaSe_2$ (CGSe) at the rear interface, using different absorber thicknesses: a thinner absorber of 600 nm (B); a standard absorber of 1,200 nm (C); and a thicker absorber of 1,800 nm (D) [Colour figure can be viewed at wileyonlinelibrary.com]

remains at the same time thick enough to allow for a complete photon absorption. As expected, the most remarkable improvement is the J_{SC} increase, correlating well with the previously presented experimental results. The V_{OC} also shows an improvement coming from the reduced recombination, especially when dealing with thinner absorbers, but it remains more limited than the J_{SC}. As for the FF, the improvement is only marginal regardless of the absorber thickness. It thus confirms that the FF improvement observed in the experimental part is most likely related to the better morphology of the layer and the interface than the BSF effect. Finally, taking the thinnest absorber case (600-nm CZTSe), when the absorber thickness becomes comparable with that of the carrier diffusion length (460 nm using state of the art modeling parameters), and considering photon penetration depth, the $CuGaSe_2$ layer clearly preserves the PV performances by blocking back contact recombination (particularly noticeable in the J_{SC} improvement). Thus, the BSF allows for devices much more resilient to an absorber thickness reduction.

4 | CONCLUSIONS

In summary, we studied the addition of thin CuGa layers at the rear interface of kesterite CZTSe solar cells, leading to several beneficial effects. Solar cells including a CuGa precursor with thicknesses in the range of 5–25 nm show a remarkable improvement in their PV performance, provided that the CuGa is preselenized to form resilient $CuGaSe_2$ phases. Additional positive effects have been identified in the charge carrier collection especially for long wavelengths, revealing an effective passivation/BSF effect. Furthermore, this approach has been proven extremely useful to prevent the formation of voids at the back side and improve significantly the interface morphology, the $CuGaSe_2$ film acting as a seed layer for the growth of higher quality absorbers. Finally, the presence of $CuGaSe_2$ phases exclusively at the interface has been demonstrated by means of Raman spectroscopy supported by Auger depth profiles. A solar cell model using SCAPS-1D supports the experimental results presented, allowing to relate the different improvements observed to either the morphology or the BSF effect, respectively. Ultimately, this work presents an innovative strategy for facing some relevant issues in kesterite solar cells, such as the poor rear interface morphology and the lack of new promising approaches to overcome the current relatively low device efficiencies.

ACKNOWLEDGEMENTS

This research was supported by the H2020 Programme under the project INFINITE-CELL (H2020-MSCA-RISE-2017-777968), by the Ministry of Science and Innovation of Spain under IGNITE project (ENE2017-87671-C3-1-R), by the European Regional Development Funds (ERDF, FEDER Programa Competitivitat de Catalunya 2007–2013) and CERCA Programme/Generalitat de Catalunya. Authors from IREC belong to the SEMS (Solar Energy Materials and Systems) Consolidated Research Group of the "Generalitat de Catalunya" (Ref. 2017 SGR 862). Dr Z. Jehl Li-Kao acknowledges the TecnioSpring Plus program and the Marie Sklodowska Curie actions for their financial support.

ORCID

Sergio Giraldo https://orcid.org/0000-0003-4881-5041
Robert Fonoll-Rubio https://orcid.org/0000-0002-6292-6648
Zacharie Jehl Li-Kao https://orcid.org/0000-0002-2610-5973
Yudania Sánchez https://orcid.org/0000-0002-5740-1150
Lorenzo Calvo-Barrio https://orcid.org/0000-0002-6993-1482
Victor Izquierdo-Roca https://orcid.org/0000-0002-5502-3133
Alejandro Pérez-Rodríguez https://orcid.org/0000-0002-3525-1497
Edgardo Saucedo https://orcid.org/0000-0003-2123-6162

REFERENCES

1. Larramona G, Choné C, Meissner D, et al. Stability, reliability, upscaling and possible technological applications of kesterite solar cells. *J Phys Energy*. 2020;2(2):024009. https://doi.org/10.1088/2515-7655/ab7cee
2. Mitzi DB, Gunawan O, Todorov TK, Wang K, Guha S. The path towards a high-performance solution-processed kesterite solar cell. *Sol Energy Mater sol Cells*. 2011;95(6):1421-1436. https://doi.org/10.1016/j.solmat.2010.11.028
3. Romanyuk YE, Haass SG, Giraldo S, et al. Doping and alloying of kesterites. *J Phys Energy*. 2019;1(4):044004. https://doi.org/10.1088/2515-7655/ab23bc
4. Giraldo S, Jehl Z, Placidi M, Izquierdo-Roca V, Pérez-Rodríguez A, Saucedo E. Progress and perspectives of thin film kesterite photovoltaic technology: a critical review. *Adv Mater*. 2019;31(16):1806692. https://doi.org/10.1002/adma.201806692
5. Wong LH, Zakutayev A, Major JD, et al. Emerging inorganic solar cell efficiency tables (version 1). *J Phys Energy*. 2019;1(3):032001. https://doi.org/10.1088/2515-7655/ab2338
6. Wang W, Winkler MT, Gunawan O, et al. Device characteristics of CZTSSe thin-film solar cells with 12.6% efficiency. *Adv Energy Mater*. 2014;4(7):1301465. https://doi.org/10.1002/aenm.201301465
7. Green MA, Dunlop ED, Hohl-Ebinger J, Yoshita M, Kopidakis N, Ho-Baillie AWY. Solar cell efficiency tables (version 55). *Prog Photovoltaics Res Appl*. 2020;28(1):3-15. https://doi.org/10.1002/pip.3228
8. Lundberg O, Edoff M, Stolt L. The effect of Ga-grading in CIGS thin film solar cells. *Thin Solid Films*. 2005;480–481:520-525. https://doi.org/10.1016/j.tsf.2004.11.080
9. Hsiao KJ, Sites JR. Electron reflector to enhance photovoltaic efficiency: application to thin-film CdTe solar cells. *Prog Photovoltaics Res Appl*. 2012;20(4):486-489. https://doi.org/10.1002/pip.1143
10. Sharbati S, Gharibshahian I, Orouji AA. Proposed suitable electron reflector layer materials for thin-film CuIn1−xGaxSe2 solar cells. *Opt Mater (Amst)*. 2018;75:216-223. https://doi.org/10.1016/j.optmat.2017.09.032
11. Singh G, Verma A, Jeyakumar R. Fabrication of c-Si solar cells using boric acid as a spin-on dopant for back surface field. *RSC Adv*. 2014;4(9):4225-4229. https://doi.org/10.1039/C3RA45746J
12. Kaminski A, Vandelle B, Fave A, et al. Aluminium BSF in silicon solar cells. In: *Solar Energy Materials and Solar Cells*. Vol.72 North-Holland; 2002:373-379. https://doi.org/10.1016/S0927-0248(01)00185-4
13. Khosroabadi S, Keshmiri SH. Design of a high efficiency ultrathin CdS/CdTe solar cell using back surface field and backside distributed Bragg reflector. *Opt Express*. 2014;22(S3):A921-A929. https://doi.org/10.1364/oe.22.00a921
14. Ramanujam J, Singh UP. Copper indium gallium selenide based solar cells—a review. *Energ Environ Sci*. 2017;10(6):1306-1319. https://doi.org/10.1039/C7EE00826K

15. Buffière M, Brammertz G, Oueslati S, et al. Spectral current–voltage analysis of kesterite solar cells. *J Phys D Appl Phys*. 2014;47(17):175101. https://doi.org/10.1088/0022-3727/47/17/175101
16. Henry J, Mohanraj K, Sivakumar G. Electrical and optical properties of CZTS thin films prepared by SILAR method. *J Asian Ceramic Soc*. 2016;4(1):81-84. https://doi.org/10.1016/j.jascer.2015.12.003
17. Lee YS, Gershon T, Gunawan O, et al. $Cu_2ZnSnSe_4$ thin-film solar cells by thermal co-evaporation with 11.6% efficiency and improved minority carrier diffusion length. *Adv Energy Mater*. 2015;5(7):1401372. https://doi.org/10.1002/aenm.201401372
18. Repins IL, Moutinho H, Choi SG, et al. Indications of short minority-carrier lifetime in kesterite solar cells. *J Appl Phys*. 2013;114(8):084507. https://doi.org/10.1063/1.4819849
19. Gunawan O, Pae SR, Bishop DM, et al. Carrier-resolved photo hall measurement in world-record-quality perovskite and kesterite solar absorbers. February 2018. http://arxiv.org/abs/1802.07910
20. Lee YS, Gershon T, Todorov TK, et al. Atomic layer deposited aluminum oxide for interface passivation of $Cu_2ZnSn(S,Se)_4$ thin-film solar cells. *Adv Energy Mater*. 2016;6(12):1600198. https://doi.org/10.1002/aenm.201600198
21. Kim J, Park S, Ryu S, Oh J, Shin B. Improving the open-circuit voltage of $Cu_2ZnSnSe_4$ thin film solar cells via interface passivation. *Prog Photovoltaics Res Appl*. 2017;25(4):308-317. https://doi.org/10.1002/pip.2864
22. Ranjbar S, Brammertz G, Vermang B, et al. Improvement of kesterite solar cell performance by solution synthesized MoO_3 interfacial layer. *Phys Status Solidi Appl Mater Sci*. 2017;214(1):1600534. https://doi.org/10.1002/pssa.201600534
23. Antunez PD, Bishop DM, Lee YS, et al. Back contact engineering for increased performance in kesterite solar cells. *Adv Energy Mater*. 2017;7(15). https://doi.org/10.1002/aenm.201602585
24. Ren Y, Richter M, Keller J, et al. Investigation of the SnS/Cu_2ZnSnS_4 interfaces in kesterite thin-film solar cells. *ACS Energy Lett*. 2017;2(5):976-981. https://doi.org/10.1021/acsenergylett.7b00151
25. Giraldo S, Saucedo E, Neuschitzer M, et al. How small amounts of Ge modify the formation pathways and crystallization of kesterites. *Energ Environ Sci*. 2018;11(3):582-593. https://doi.org/10.1039/c7ee02318a
26. Yan C, Sun K, Liu F, Huang J, Zhou F, Hao X. Boost Voc of pure sulfide kesterite solar cell via a double CZTS layer stacks. *Sol Energy Mater sol Cells*. 2017;160(August 2016):7-11. https://doi.org/10.1016/j.solmat.2016.09.027
27. Kim SY, Kim SH, Hong S, et al. Secondary phase formation mechanism in the Mo-back contact region during sulfo-selenization using a metal precursor: effect of wettability between a liquid metal and substrate on secondary phase formation. *ACS Appl Mater Interfaces*. 2019;11(26):23160-23167. https://doi.org/10.1021/acsami.9b03969
28. Scragg JJ, Wätjen JT, Edoff M, Ericson T, Kubart T, Platzer-Björkman C. A detrimental reaction at the molybdenum back contact in $Cu_2ZnSn(S,Se)_4$ thin-film solar cells. *J am Chem Soc*. 2012;134(47):19330-19333. https://doi.org/10.1021/ja308862n
29. López-Marino S, Placidi M, Pérez-Tomás A, et al. Inhibiting the absorber/Mo-back contact decomposition reaction in $Cu_2ZnSnSe_4$ solar cells: the role of a ZnO intermediate nanolayer. *J Mater Chem A*. 2013;1(29):8338-8343. https://doi.org/10.1039/c3ta11419h
30. Placidi M, Espindola-Rodriguez M, Lopez-Marino S, et al. Effect of rapid thermal annealing on the Mo back contact properties for $Cu_2ZnSnSe_4$ solar cells. *J Alloys Compd*. 2016;675:158-162. https://doi.org/10.1016/j.jallcom.2016.03.043
31. Schnabel T, Ahlswede E. On the interface between kesterite absorber and Mo back contact and its impact on solution-processed thin-film solar cells. *Sol Energy Mater sol Cells*. 2017;159:290-295. https://doi.org/10.1016/j.solmat.2016.09.029
32. Cui H, Liu X, Liu F, Hao X, Song N, Yan C. Boosting Cu_2ZnSnS_4 solar cells efficiency by a thin Ag intermediate layer between absorber and back contact. *Appl Phys Lett*. 2014;104(4):041115. https://doi.org/10.1063/1.4863951
33. Kim S, Márquez JA, Unold T, Walsh A. Upper limit to the photovoltaic efficiency of imperfect crystals from first principles. *Energ Environ Sci*. 2020;13(5):1481-1491. https://doi.org/10.1039/d0ee00291g
34. Liu F, Huang J, Sun K, et al. Beyond 8% ultrathin kesterite Cu_2ZnSnS_4 solar cells by interface reaction route controlling and self-organized nanopattern at the back contact. *NPG Asia Mater*. 2017;9(7):e401-e401. https://doi.org/10.1038/am.2017.103
35. Meng L, Yao B, Li Y, et al. Significantly enhancing back contact adhesion and improving stability of $Cu_2(Zn,Cd)Sn(S,Se)_4$ solar cell by a rational carbon doping strategy. *J Alloys Compd*. 2017;710:403-408. https://doi.org/10.1016/j.jallcom.2017.03.281
36. Giraldo S, Thersleff T, Larramona G, et al. $Cu_2ZnSnSe_4$ solar cells with 10.6% efficiency through innovative absorber engineering with Ge superficial nanolayer. *Prog Photovoltaics Res Appl*. 2016;24(10):1359-1367. https://doi.org/10.1002/pip.2797
37. Burgelman M, Nollet P, Degrave S. Modelling polycrystalline semiconductor solar cells. *Thin Solid Films*. 2000;361:527-532. https://doi.org/10.1016/S0040-6090(99)00825-1
38. Adachi S. *Earth-Abundant Materials for Solar Cells: Cu_2-II-IV-VI4 Semiconductors*. Chichester, UK: wiley; 2015 https://doi.org/10.1002/9781119052814
39. Hanna G, Jasenek A, Rau U, Schock HW. Influence of the Ga-content on the bulk defect densities of Cu (In,Ga)Se_2. *Thin Solid Films*. 2001;387(1–2):71-73. https://doi.org/10.1016/S0040-6090(00)01710-7
40. Hsu W-CC, Repins I, Beall C, et al. Growth mechanisms of co-evaporated kesterite: a comparison of Cu-rich and Zn-rich composition paths. *Prog Photovoltaics Res Appl*. 2014;22(1):35-43. https://doi.org/10.1002/pip.2296
41. Kondrotas R, Oliva F, Alcobe X, et al. Double band gap gradients in sequentially processed photovoltaic absorbers from the Cu (In,Ga)Se_2-ZnSe pseudobinary system. *Prog Photovoltaics Res Appl*. 2018;26(2):135-144. https://doi.org/10.1002/pip.2958
42. Minbashi M, Omrani MK, Memarian N, Kim D-H. Comparison of theoretical and experimental results for band-gap-graded CZTSSe solar cell. *Curr Appl Phys*. 2017;17(10):1238-1243. https://doi.org/10.1016/j.cap.2017.06.003
43. Jeong AR, Shin RH, Jo W, Song M, Yoon S. Synthesis and physical properties of Cu (In,Ga)Se_2 nanoparticles and $CuGaSe_2$ thin-films for tandem cell photovoltaic applications. In: *Conf Rec IEEE Phot Spec Conf IEEE*; 2010:3432–3434. https://doi.org/10.1109/PVSC.2010.5614600
44. Steichen M, Larsen J, Gütay L, Siebentritt S, Dale PJ. Preparation of $CuGaSe_2$ absorber layers for thin film solar cells by annealing of efficiently electrodeposited Cu-Ga precursor layers from ionic liquids. *Thin Solid Films*. 2011;519(21):7254-7258. https://doi.org/10.1016/j.tsf.2011.01.135
45. Guc M, Levcenko S, Izquierdo-Roca V, Fontané X, Arushanov E, Pérez-Rodríguez A. Polarized Raman scattering analysis of $Cu_2ZnSnSe_4$ and $Cu_2ZnGeSe_4$ single crystals. *J Appl Phys*. 2013;114(19):193514. https://doi.org/10.1063/1.4830028
46. Nam D, Lee JU, Cheong H. Excitation energy dependent Raman spectrum of $MoSe_2$. *Sci Rep*. 2015;5(1):1-6. https://doi.org/10.1038/srep17113
47. Pang JB, Cai YA, He Q, et al. Preparation and characteristics of $MoSe_2$ interlayer in bifacial Cu (In,Ga)Se_2 solar cells. *Physics Procedia*. 2012;32:372-378. https://doi.org/10.1016/j.phpro.2012.03.571
48. Lopez-Marino S, Espíndola-Rodríguez M, Sánchez Y, et al. The importance of back contact modification in $Cu_2ZnSnSe_4$ solar cells: the role of a thin MoO_2 layer. *Nano Energy*. 2016;26:708-721. https://doi.org/10.1016/j.nanoen.2016.06.034

49. Anderson RL. Germanium-gallium arsenide heterojunctions [letter to the editor]. *IBM J Res Dev*. 2010;4(3):283-287. https://doi.org/10.1147/rd.43.0283

SUPPORTING INFORMATION

Additional supporting information may be found online in the Supporting Information section at the end of this article.

How to cite this article: Giraldo S, Fonoll-Rubio R, Jehl Li-Kao Z, et al. Rear interface engineering of kesterite $Cu_2ZnSnSe_4$ solar cells by adding $CuGaSe_2$ thin layers. *Prog Photovolt Res Appl*. 2021;29:334–343. https://doi.org/10.1002/pip.3366

SUPPORTING INFORMATION

Rear interface engineering of kesterite $Cu_2ZnSnSe_4$ solar cells by adding $CuGaSe_2$ thin layers

Sergio Giraldo[1], Robert Fonoll[1], Zacharie Jehl Li-Kao[1], Yudania Sánchez[1], Lorenzo Calvo-Barrio[2,3], Victor Izquierdo-Roca[1], Alejandro Pérez-Rodríguez[1,3], Edgardo Saucedo[1]*

[1] Catalonia Institute for Energy Research (IREC), Jardins de les Dones de Negre 1, 08930 Sant Adrià de Besòs, Barcelona, Spain.

[2] Centres Científics i Tecnològics de la Universitat de Barcelona (CCiTUB), Lluís Solé i Sabarís 1-3, 08028 Barcelona, Spain.

[3] IN2UB, Departament d'Enginyeria Electrònica i Biomèdica, Universitat de Barcelona, Martí i Franquès 1, 08028 Barcelona, Spain

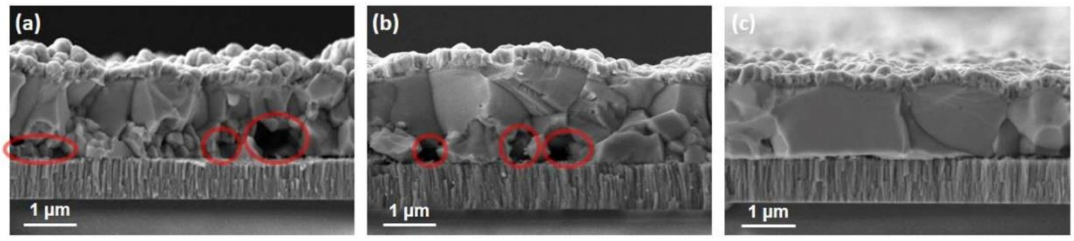

Figure S1. Cross-sectional SEM images of a reference device without CuGa (a), a device fabricated with 10 nm CuGa at the back region without pre-selenization treatment (b), and a device fabricated with 10 nm CuGa pre-selenized (c).

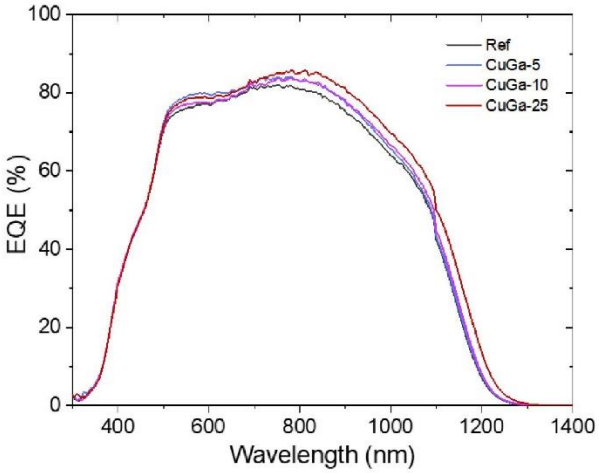

Figure S2. External quantum efficiency (EQE) spectra of solar cell devices fabricated with increasing CuGa thickness at the rear interface (0 nm, 5 nm, 10 nm, and 25 nm CuGa).

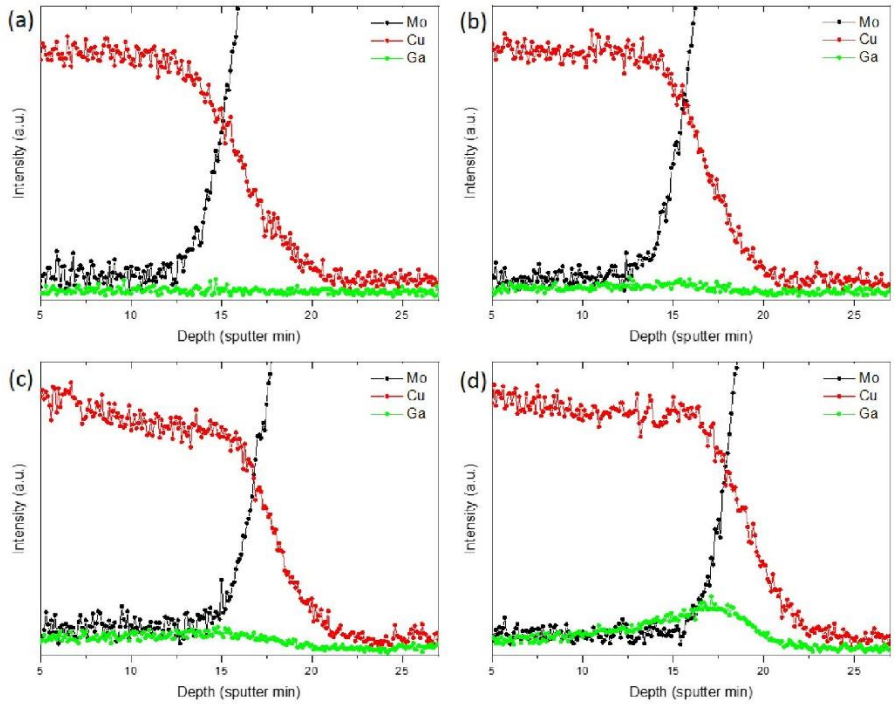

Figure S3. Auger in-depth compositional analysis of the Mo/CZTSe rear interface of the samples: Ref CZTSe-without CuGa (a), CuGa-5 (b), CuGa-10 (c), and CuGa-25 (d), fabricated with 0 nm, 5 nm, 10 nm and 25 nm of CuGa respectively.

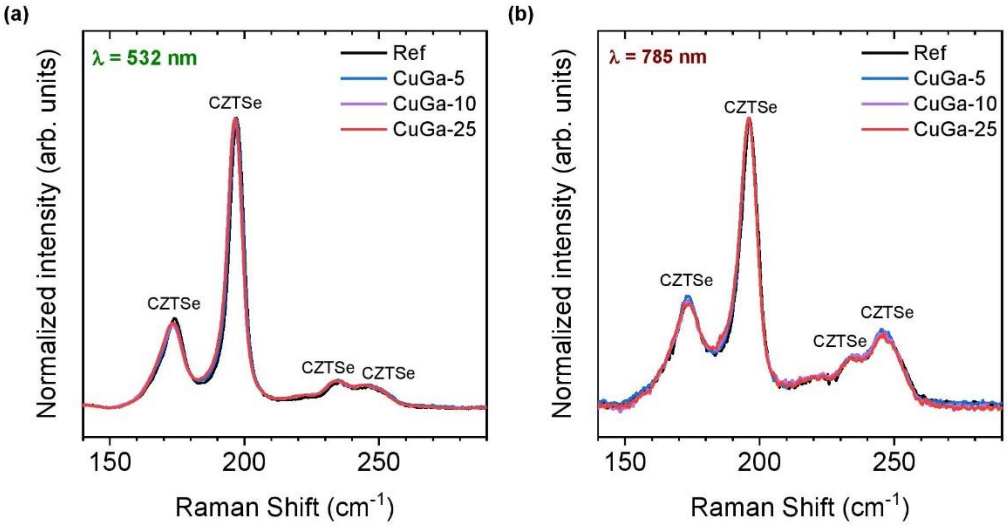

Figure S4. Raman spectra obtained using 532 nm (a) and 785 nm (b) excitation wavelengths of the front interface of CZTSe samples fabricated with 0 nm, 5 nm, 10 nm and 25 nm of CuGa.

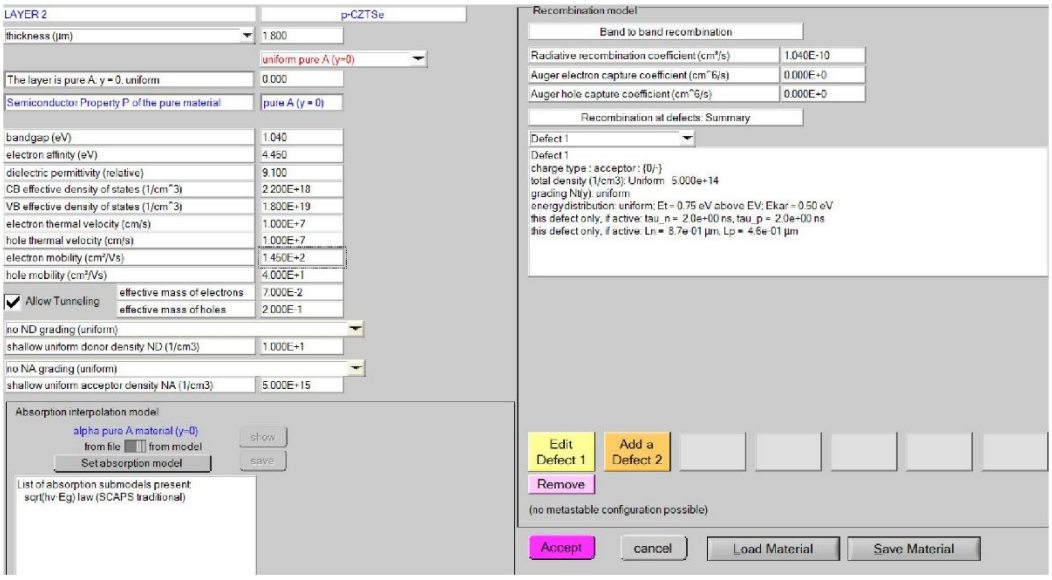

Figure S5. SCAPS parameters for the CZTSe layer.

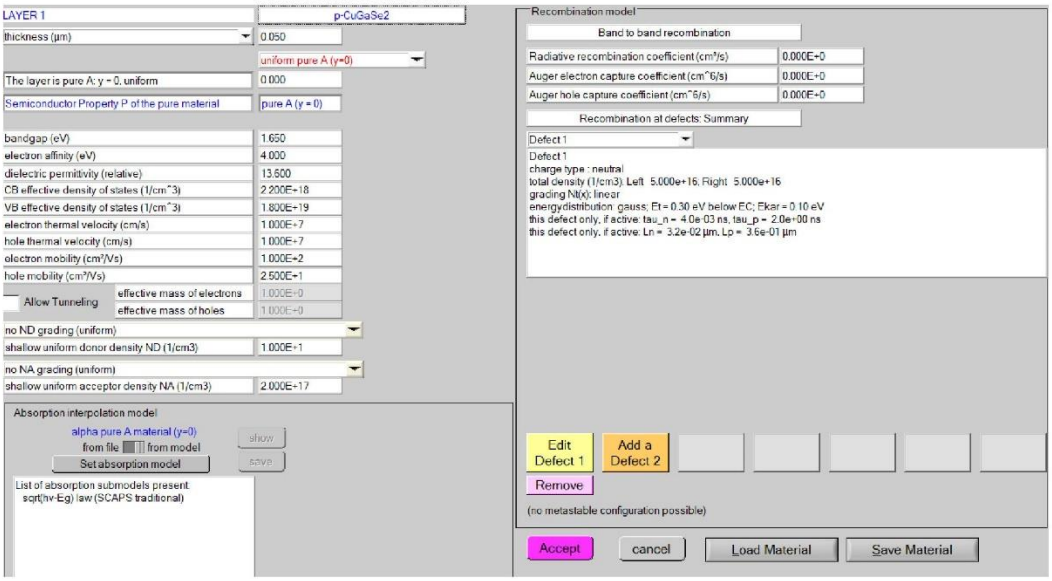

Figure S6. SCAPS parameters for the $CuGaSe_2$ layer.

3.5. Article 4: Controlling the Anionic Ratio and Gradient in Kesterite Technology

ACS APPLIED MATERIALS & INTERFACES

www.acsami.org Research Article

Controlling the Anionic Ratio and Gradient in Kesterite Technology

Jacob Andrade-Arvizu, Robert Fonoll Rubio, Victor Izquierdo-Roca, Ignacio Becerril-Romero, Diouldé Sylla, Pedro Vidal-Fuentes, Zacharie Jehl Li-Kao, Angélica Thomere, Sergio Giraldo, Kunal Tiwari, Shahaboddin Resalati, Maxim Guc,* and Marcel Placidi*

Cite This: *ACS Appl. Mater. Interfaces* 2022, 14, 1177−1186 Read Online

ACCESS | Metrics & More | Article Recommendations | Supporting Information

ABSTRACT: Accurate anionic control during the formation of chalcogenide solid solutions is fundamental for tuning the physicochemical properties of this class of materials. Compositional grading is the key aspect of band gap engineering and is especially valuable at the device interfaces for an optimum band alignment, for controlling interface defects and recombination and for optimizing the formation of carrier-selective contacts. However, a simple and reliable technique that allows standardizing anionic compositional profiles is currently missing for kesterites and the feasibility of achieving a compositional gradient remains a challenging task. This work aims at addressing these issues by a simple and innovative technique. It basically consists of first preparing a pure sulfide absorber with a specific thickness followed by the synthesis of a pure selenide part of complementary thickness on top of it. Specifically, the technique is applied to the synthesis of $Cu_2ZnSn(S,Se)_4$ and $Cu_2ZnGe(S,Se)_4$ kesterite absorbers, and a series of characterizations are performed to understand the anionic redistribution within the absorbers. For identical processing conditions, different Se incorporation dynamics is identified for Sn- and Ge-based kesterites, leading to a homogeneous or graded composition in depth. It is first demonstrated that for Sn-based kesterite the anionic composition can be perfectly controlled through the thicknesses ratio of the sulfide and selenide absorber parts. Then, it is demonstrated that for Ge-based kesterite an anionic (Se−S) gradient is obtained and that by adjusting the processing conditions the composition at the back side can be finely tuned. This technique represents an innovative approach that will help to improve the compositional reproducibility and determine a band gap grading strategy pathway for kesterites. Furthermore, due to its simplicity and reliability, the proposed methodology could be extended to other chalcogenide materials.

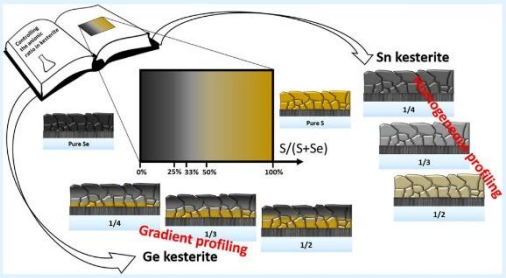

KEYWORDS: *kesterite, $Cu_2ZnSn(S,Se)_4$, $Cu_2ZnGe(S,Se)_4$, anionic control, band gap grading*

1. INTRODUCTION

Thin-film techniques based on different chalcogenide materials are widely explored owing to their versatility, tailorable properties, and relatively low-cost manufacturing processes, offering a high potential for optoelectronic device application. Frequently, accurate anionic and/or cationic control for the formation of chalcogenide solid solutions is fundamental to the tuning of the physicochemical properties of the compounds and is one of the main issues in the field. A kesterite $Cu_2ZnSn(S,Se)_4$ (CZTSSe)-based thin film is one of the chalcogenide family members that have been more intensively investigated in the last decade owing to its potential to make flexible, light-weight, and low-cost photovoltaic (PV) devices based on earth-abundant materials.[1] Several groups have demonstrated efficiencies higher than 10%,[2−7] often with different compositional ratios. However, no consensus exists on reliable processes and reproducible efficiencies, which remain extremely challenging despite ongoing efforts at the different levels of the device. This relates not only to the difficult control of the synthesis process of the material but also to the various layers and interfaces involved in the full solar cell devices. Interfaces within the absorber itself, i.e., defects at the grain boundaries or even in-grain defects, can seriously alter the performance of the devices.[8−10]

Defect formation can be restrained to some extent through fine tuning of the compositional anionic ratio and/or cationic ratio. However, achieving such accurate control is not straightforward, especially if the anions are introduced during the thermal synthesis of the absorbers. A particularly relevant application of precise compositional mastery is the achievement of a graded composition in the absorber. Compositional

Received: November 6, 2021
Accepted: December 23, 2021
Published: January 3, 2022

https://doi.org/10.1021/acsami.1c21507
ACS Appl. Mater. Interfaces 2022, 14, 1177−1186

grading is the key aspect of band engineering and is especially valuable at the device interfaces for an optimum band alignment while also finding application in the control of interface defects and recombination; it is additionally necessary for the optimization of carrier-selective contacts.[11−19] The preparation of solid solution kesterite phases typically involves mainly either (1) a chemical or physical route already containing a precursor with sulfur or selenium (often in the form of Zn or Sn chalcogenides), which is submitted to a reactive annealing process under an atmosphere containing an alternate chalcogen (i.e., sulfur for selenide precursors and selenium for sulfide precursors),[20,21] or (2) a direct route with a reactive annealing atmosphere containing both chalcogens.[20−22] However, in all of these cases, crystallizing the desired compositional phase in a repeatable way is a laborious task and, often, requires tens of processes to properly adjust the S/Se weight ratio of the reaction.

Moreover, the high volatility of S and Se species during the thermal processes renders reproducible control on the ratio of these elements difficult to achieve.[23] In the same way, and while few reports exist on kesterite absorbers with compositional anionic gradients, similar strategies to the ones reported above were implemented, i.e., including S and Se mixtures during thermal annealing.

Sequential S and Se thermal treatments were used, with sulfide or selenide binaries in the precursor material, and then submitted to reactive annealing introducing the alternate chalcogen, resulting in complicated setups.[12,20] The straightforward formation of a compositional gradient in a foolproof way remains a challenging task that this work aims to address.

The difficulty of controlling the anionic composition in kesterite compounds is mainly related to the small difference in the formation enthalpies of the end members of the solid solutions (e.g., the difference between Cu_2ZnSnS_4/$Cu_2ZnSnSe_4$ or Cu_2ZnGeS_4/$Cu_2ZnGeSe_4$ is 1.08 and 0.68 eV, respectively).[24]

As such, directing the S−Se behavior becomes challenging and necessarily implies complex multistep processes rather than a single step in which control is almost impossible to achieve.

In this context, developing a methodology that allows controlling the anionic composition and/or creating anionic compositional grading in a simple, precise, and reproducible way represents a step forward in the development of kesterite-based photovoltaic (PV) technology.

In this work, an innovative approach is proposed for accurately controlling the anionic (sulfur−selenium) compositional ratio in kesterite absorbers that consists of first preparing a pure sulfide absorber with a specific thickness followed by the synthesis of a pure selenide part of complementary thickness on top of it.

We employ this methodology for the synthesis of $Cu_2ZnSn(S,Se)_4$ (CZTSSe) and $Cu_2ZnGe(S,Se)_4$ (CZGSSe) kesterite absorbers, and, through the use of several characterization techniques, we show that Se presents a different incorporation dynamics in each of them, leading to a homogeneous or graded in-depth composition. In this way, we demonstrate that for Sn-based kesterite, the anionic composition can be perfectly regulated through the thicknesses ratio of the sulfide and selenide absorber parts and that for the Ge-based kesterite an anionic (Se−S) gradient is obtained and can be finely tuned by adjusting the processing conditions. While slightly beyond the scope of this work, the leading hypothesis explaining the Se−S dynamics is discussed at the end of this work in regard to the literature.

2. EXPERIMENTAL SECTION

2.1. Absorber Synthesis and Device Fabrication. The synthesis process began with the deposition (Alliance AC450 DC-sputtering system) of the first metallic precursor with a thickness $1/X$ of the total one (see Figure 1a) on a Mo layer on soda-lime glass. Cu/Sn/Cu/Zn and Cu/Zn/Cu/Ge structures were used for the Sn- and Ge-based kesterite, respectively.[7,25] In all of the cases, the metallic precursors were adjusted to give Cu-poor and Zn-rich composition ratios ([Cu]/([Zn] + [Sn]) ∼ 0.77 and [Zn]/[Sn] ∼ 1.15 for Sn precursors and [Cu]/([Zn] + [Ge]) ∼ 0.67 and [Zn]/[Ge] ∼ 1.07 for Ge precursors), as measured by X-ray fluorescence (XRF).

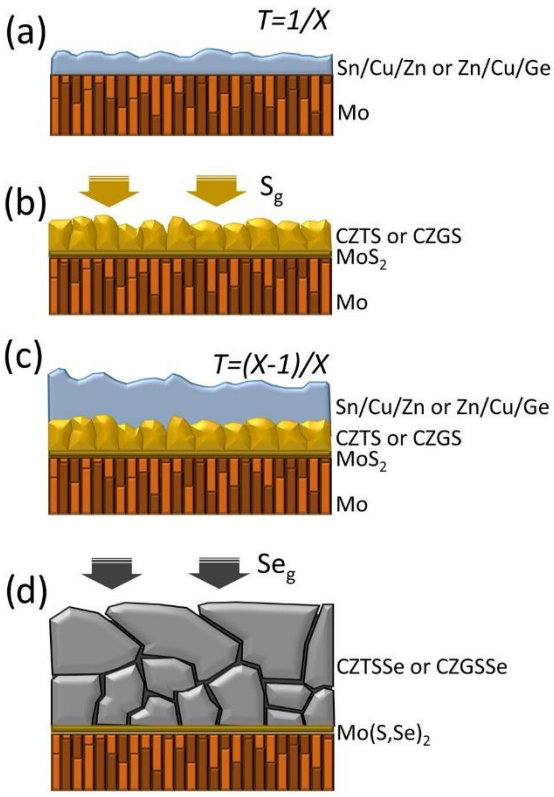

Figure 1. Followed strategy for the preparation of the solid solution samples of the study. (a) Deposition of $1/X$ of the total metallic stack thickness. (b) Sulfurization of the first metallic stack. (c) Second deposition of $(X - 1)/X$ of the total metallic stack. (d) Final selenization of all of the layers.

The first precursor is submitted to sulfurization (see Figure 1b) in a tubular furnace (Hobersal) with a semiclosed graphite box containing 50 mg of sulfur and using a thermal profile consisting of the first step at 200 °C during 5 min (under 1 mbar Ar flow) and the second step at 550 °C during 5 min (at 1 bar). Then, the second metallic stack precursor was deposited on the sulfide absorber (Figure 1c) with a thickness of $(X - 1)/X$ of the total one, and the samples were selenized in a tubular furnace with a graphite box containing 50 mg of selenium and using a thermal profile consisting of the first step at 400 °C during 30 min (under 1 mbar Ar flow) and the second step at 550 °C during 15 min (at 1 bar), forming the solid solution (CZTSSe or CZGSSe) absorber (Figure 1d). In the case of Ge kesterite, the

https://doi.org/10.1021/acsami.1c21507
ACS Appl. Mater. Interfaces 2022, 14, 1177−1186

ACS Applied Materials & Interfaces www.acsami.org Research Article

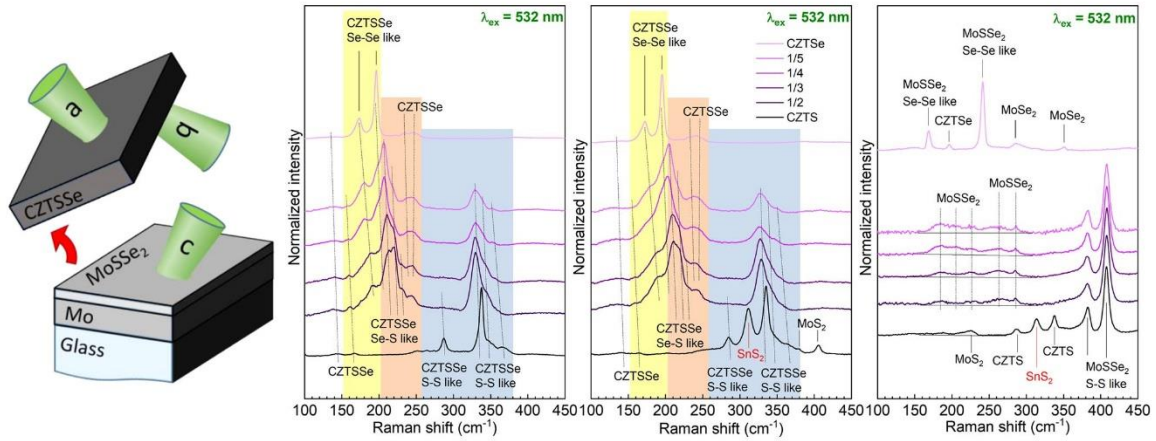

Figure 2. Lift-off procedure scheme (left) revealing the different a, b, and c measured interfaces corresponding to the front surface region, the CZTSSe back contact region, and the Mo back contact region. Raman spectra of (a) front surface, (b) back, and (c) substrate side interfaces of the CZTSSe and pure CZTS and CZTSe compounds measured under 532 nm excitation wavelength.

second batch of samples was prepared using a lower selenization temperature process, defined by a thermal profile consisting of the first step at 330 °C during 30 min (under 1 mbar Ar flow) and the second step at 480 °C during 15 min (at 1 bar). In all of the absorbers, the thicknesses of the bottom and top metallic precursors were adjusted to have a total absorber thickness of around 1.5 μm. Prior to the thermal processes, the employed graphite boxes were cleaned and submitted to high-temperature (750 °C) annealing in vacuum for 2 h to remove any possible contaminations.

Devices were finally fabricated for both Sn- and Ge-based kesterite by depositing an n-type CdS buffer layer (50 nm) by chemical bath deposition at 80 °C and a window layer formed by an i-ZnO (50 nm) and an indium tin oxide (ITO) (150 nm) layer deposited by DC-pulsed magnetron sputtering (Alliance Concept CT100) at 200 °C. Individual cells (3 × 3 mm^2) were then insulated using a mechanical scriber (OEG MR200). In both cases, the experimental results are compared and interpreted with the help of a numerical model.

2.2. Characterization. Raman spectroscopy measurements were performed using FHR-640 and iHR320 Horiba-Jobin Yvon spectrometers coupled to Raman probes developed at IREC and charge-coupled device (CCD) detectors. A lift-off procedure allowed to reveal the back side of the absorber and the substrate side, and Raman measurements were thus performed at different interfaces. Lift-off was performed by bonding the samples from the front side to a steel substrate with an adhesive epoxy and then removing them mechanically. The back contact−absorber interface in thin-film chalcogenides is generally highly stressed, and the presence of a Mo chalcogenide layer there (formed during the absorber synthesis), which has a layered structure, renders this interface very weak, easing separation. The Raman measurements were performed in back-scattering configuration, and different excitation wavelengths (532 and 785 nm) were employed. Due to the difference in the band gap of the different analyzed layers, the penetration depth of the used excitation wavelength was different, enabling an in-depth compositional analysis of the very top surface (with 532 nm excitation) and subsurface (with 785 nm excitation) regions of the absorbers at front and back faces, as well as of the top surface of the substrate. The analysis also included the detection of possible secondary phases at these interfaces. To inhibit thermal effects on the samples, the excitation power density was about 100−150 W/cm^2. A calibration was performed using a monocrystalline Si reference to correct the Raman shift to the main Si band at 520 cm^{-1}. The in-depth chemical composition of the CZTSe absorbers was investigated by means of Auger electron spectroscopy (AES) using a Phi 670 scanning Auger nanoprobe. Cross-sectional scanning electron microscopy (SEM) images were obtained with a ZEISS Series Auriga microscope applying 5 kV as the accelerating voltage and at working distances of 3−5 mm to study the morphology of the absorbers.

The crystallographic features of the CZTSe absorbers were characterized by X-ray diffraction (XRD) using a Bruker D8 Advance system with Cu Kα radiation. The overall composition of the absorber layers was measured with an X-ray fluorescence (XRF) system (FISCHERSCOPE XVD) calibrated by inductively coupled plasma mass spectrometry (ICP-MS).

Current−voltage measurements were performed under AM1.5G illumination (1000 W/m^2) using a solar simulator (Abet Technologies Sun 3000 Class AAA) at room temperature and calibrated with a Si reference solar cell.

3. CHARACTERIZATION RESULTS

3.1. Sn Kesterite. Raman analysis was performed for all of the CZTSSe absorbers, which allowed us to estimate the anionic composition of the surface. Pure CZTSe has its main Raman peak at 196 cm^{-1} (A symmetry mode), a weaker contribution at 174 cm^{-1} (overlap of the A and B symmetry modes), and a broad band in the 220−250 cm^{-1} region (overlapping of E and B symmetry modes).[26] Pure CZTS has a similar fingerprint but with well-defined contributions at 337 cm^{-1} (main peak) and 287 cm^{-1} (weaker one) for the A mode and at 310−380 cm^{-1} for E and B modes.[27] For both pure compounds, the A symmetry modes are related to the pure anion vibrations, while E and B symmetry modes include different combinations of vibrations of cations and anions.[28] In the case of the CZTSSe solid solution, a more complex situation is observed with three different spectral regions wherein no S (between 150 and 200 cm^{-1}) and no Se (250−380 cm^{-1}) vibrational modes are present and wherein a combination of vibrations of both anions (200−250 cm^{-1}) can be seen.[29] Depending on the intensity ratio of the different spectral regions, the anionic composition of the CZTSSe solid solution layer can be estimated.[12,30] In the first step, a multiwavelength (using laser excitations at 532−785 nm) Raman analysis was performed on the front surface (see Figures 2 and S1), taking advantage of the different penetration laser depths. This preliminary result indicated that the anionic composition [S]/([S] + [Se]) of the surface was varying from sample to sample (from approximatively 45−20%) but

https://doi.org/10.1021/acsami.1c21507
ACS Appl. Mater. Interfaces 2022, 14, 1177−1186

ACS Applied Materials & Interfaces www.acsami.org Research Article

Table 1. Anion Composition [S]/([S] + [Se]) Calculated from Different Techniques, XRF and XRD, Applying Vegard's Law, Raman Spectra Obtained at the Front and Back of the Samples,[30] and from Auger Measurements

	XRF				XRD		Raman		AES		
	bulk				bulk		surface (<100 nm)	back (<100 nm)	surface (<100 nm)	bulk	back (<200 nm)[b]
sample	[Cu]/M[a]	[Cu]/[Sn]	[Zn]/[Sn]	[S]/([S] + [Se]) [%]	[S]/([S] + [Se]) [%]	(112) FWHM [°]	[S]/([S] + [Se]) [%]	[S]/([S] + [Se]) [%]	[S]/([S] + [Se]) [%]	[S]/([S] + [Se]) [%]	[S]/([S] + [Se]) [%]
	(±0.3)	(±0.04)	(±0.03)	(±3)	(±1)	(±0.01)	(±3)	(±3)	(±2)	(±2)	(±4)
CZTSe	44.5	1.72	1.14	0	0	0.05	0	0			
1/5	44.7	1.66	1.05	23	21	0.11	18	16	18	19	23
1/4	45.0	1.71	1.09	23	23	0.11	20	17	21	21	25
1/3	45.0	1.72	1.11	36	36	0.11	34	33	36	35	38
1/2	44.4	1.70	1.13	44	42	0.12	43	35	40	41	45
CZTS	44.7	1.69	1.09	100	100	0.07	100	100			

[a]M = [Cu] + [Zn] + [Sn]. [b]Sulfur overestimation due to the overlapping of the S and Mo AES signals and the contribution of the S-rich $MoSSe_2$ layer.

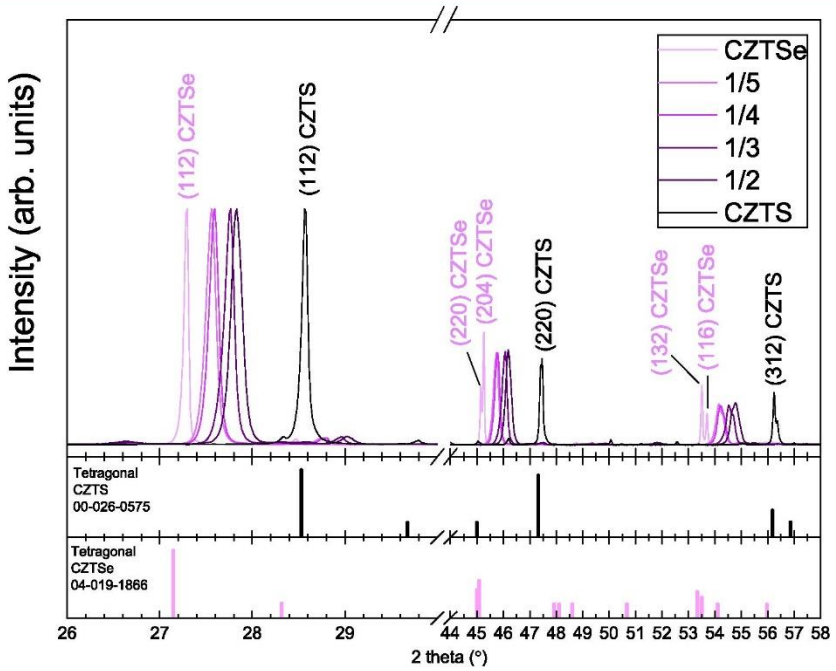

Figure 3. Difractograms of the CZTSSe absorbers and the CZTS and CZTSe reference samples.

showing similar values for the surface (using 532 nm) and subsurface (using 785 nm) of each absorber. This anionic composition of the front surface was clearly indicating a mixture of anions in the final CZTSSe absorbers, and it was then decided to perform a complete structural and compositional characterization to detect the presence of an anionic gradient at the back side and/or eventual secondary phases. To complete Raman analysis, the measurements were performed at the back sides of the absorbers and at the Mo back contact side (revealed by a mechanical lift-off procedure) (see Figure 2). Reference spectra of pure CZTSe and CZTS were also added, allowing a better distinguishing of the solid solution compounds. The calculated values for the anionic compositions for the different CZTSSe absorbers are reported in Table 1 and were found to be almost similar for the front and back sides of the absorbers, with only minor changes in some cases, which indicates a homogeneous composition within the thickness of the absorber. Efficient penetration of Se through the whole layer was also confirmed by the formation of the $Mo(S,Se)_2$ phase found at the substrate side of the samples. Moreover, a clear change in the anion ratio of the $Mo(S,Se)_2$ phase can be deduced from the measured Raman spectra (see Figure 2c), which follows the change in the relative thickness of S and Se precursors.

To confirm the homogeneous in-depth distribution of the anions in the CZTSSe layers, X-ray diffraction (XRD) measurements and depth-resolved AES analysis were performed. The measured diffractograms, shown in Figure 3, clearly revealed the CZTSSe structure in all of the absorbers, without the presence of separated CZTSe and CZTS phases

https://doi.org/10.1021/acsami.1c21507
ACS Appl. Mater. Interfaces 2022, 14, 1177−1186

and also without any evidence of secondary phases, suggesting the formation of the CZTSSe solid solution phase with good anionic compositional homogeneity through all of the thickness of the film without any anionic gradient. Moreover, the systematic shift of the Bragg reflections toward higher diffraction angles as the thickness of the CZTSe/CZTS ratio increases correlates well with the replacement of smaller S atoms with bigger Se atoms. Applying the Vegard law, the anionic compositions [S]/([S] + [Se]) of the bulk CZTSSe thin films were calculated together with the full width at half-maximum (FWHM) values of the (112) reflection for the different CZTSSe absorbers (see Table 1). The results suggest comparable crystalline quality of the synthesized CZTSSe layers compared with that of the pure CZTS and CZTSe reference samples. The AES measurements are presented in Figure 4, and the profiles are almost linear for all of the

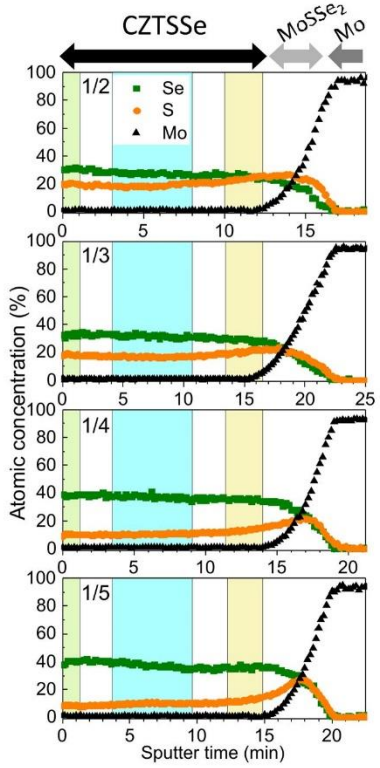

Figure 4. Auger spectroscopy (AES) depth profiles of the CZTSSe samples. The colored region indicates the sample depth used for the evaluation of the composition of the surface (green), bulk (blue), and back (yellow).

absorbers, confirming a very high in-depth compositional homogeneity from the surface toward the back interface, where $Mo(S,Se)_2$ is formed and an increase of the S content is detected. However, in this region, S was overestimated due to the strong overlapping of the main Mo and S AES emission peaks. For this reason, the composition was evaluated in three distinct regions, front surface, bulk, and back interface, and the values obtained are shown in Table 1. For comparison, the composition values estimated by XRF are also included in Table 1. It can be observed that the different characterization techniques show very similar values of the anionic ratio.

The thickness and morphology of the CZTSSe absorbers were observed by SEM cross-sectional study and compared with those of reference pure selenide CZTSe kesterite. Figure S2 shows that in all the cases, with the introduction of sulfur, a similar morphology with a compact layer is created with thicknesses comprised between 1.6 and 1.7 μm. However, in most of the cases, larger grain sizes in the top region and lower sizes at the bottom were also seen, which was previously mentioned as frequently detected in the kesterite-based absorber layers' culprit that limits the device performance.[10,12,30] In our case, this apparent bilayer morphology is however found unrelated to compositional segregation and is thus more likely to be inherent to the surface state of the substrate and its subsequent influence on the film's growth as previously reported.[31] Comparing with the CZTSe reference sample, the sequential annealing process proposed here leads to CZTSSe layers with similar bilayer morphology structures but with slightly smaller grains. It is interesting to point out that the $Mo(S,Se)_2$ formed at the back contact presents a similar thickness (<200 nm) in all of the cases.

We want also to point out that the processes were reproduced twice for the Sn kesterite with a total of two operators, and in both cases, the results (i.e., the anionic compositional ratios, see Table S1) were almost identical, with very good reproducibility.

3.2. Ge Kesterite. The first set of CZGSSe samples (labeled as batch 1) was processed using the same processing conditions as those employed for CZTSSe. In this case, and similarly to CZTSSe, the anionic composition of the absorbers was first studied using multiwavelength Raman analysis at the front, i.e., at the surface (532 nm) and subsurface (785 nm), taking advantage of the different penetration depths of the different excitations employed. Similar to the observations made for the CZTSSe solid solution samples, Se−Se-, Se−S-, and S−S-like vibrational modes can be also differentiated in the spectra obtained for the CZGSSe samples. The spectral areas corresponding mainly to these different types of vibrations are highlighted in Figure 5 (in yellow, red, and blue, respectively).

The Raman spectra measured at the front side of the different CZGSSe absorbers are shown in Figure 5a,b, respectively, for 532 and 785 nm excitation wavelengths. Additionally, the Raman spectra of reference samples, corresponding to pure CZGS (initial bottom part of the absorber) and pure CZGSe (added top part of absorber), are also shown in Figure 5 for comparison. The CZGSe reference sample shows small contamination with S, which could come either from the back side of the 1/2, 1/3, and 1/4 samples or is related to accumulated S in the graphite box employed for annealing. The latter is less probable since the box was cleaned prior to annealing; thus, it is believed that S loss is occurring during selenization of the samples. Under 532 nm, all of the CZGSSe samples clearly showed an almost pure CZGSe composition on the surface, similar to the CZGSe reference sample. The [S]/([S] + [Se]) ratio was found to slightly vary from sample to sample but without any correlation with the thickness ratio of precursors. Under 785 nm excitation, the intensity of the E/B-like symmetry peaks was observed to increase significantly. This is explained by the resonance effect of the excitation wavelength employed with the analyzed compound, and this reveals that in the subsurface region, the

https://doi.org/10.1021/acsami.1c21507
ACS Appl. Mater. Interfaces 2022, 14, 1177−1186

ACS Applied Materials & Interfaces www.acsami.org Research Article

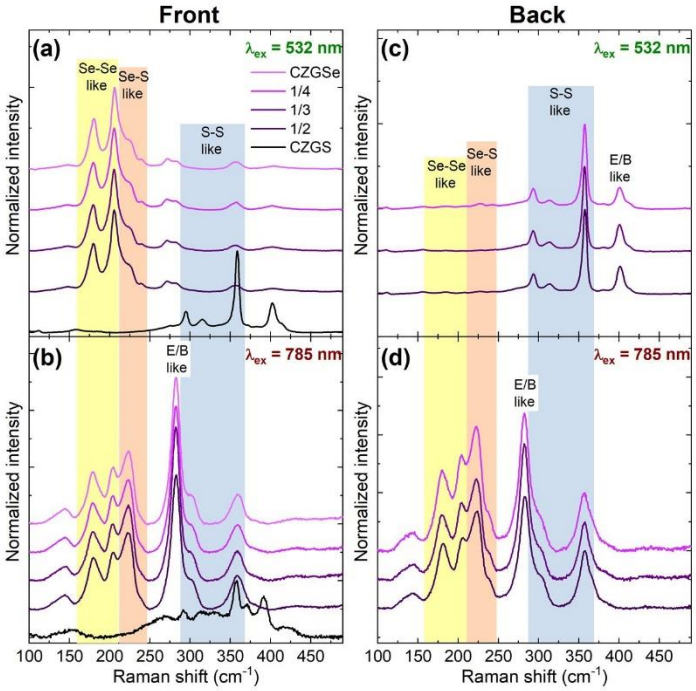

Figure 5. Raman spectra measured at the front of the samples using (a) 532 nm and (b) 785 nm excitation wavelengths for surface and subsurface analysis, respectively, for the different CZGSSe absorbers prepared. Raman spectra of pure CZGSe and CZGS used as references during selenization and sulfurization steps are also shown. Raman spectra measured at the back of the samples (after lift-off) using (c) 532 nm and (d) 785 nm excitation wavelengths, for surface and subsurface analysis, respectively, for the different CZGSSe absorbers prepared.

anionic composition is rather Se-rich. Nevertheless, the slight increase of the S−S-like peaks also observed in these spectra suggests that the S content is higher in the subsurface region than on the very surface (Figure 5a). The [S]/([S] + [Se]) ratio slightly changes from sample to sample but without correlating with the thicknesses ratio of precursors. Combining the measurements performed, it is possible to confirm that all CZGSSe samples present a Se-rich composition on the front surface.

The same analysis was applied to the back side of the layers (after lift-off, see Section 2), and the measured Raman spectra are shown in Figure 5c,d, respectively, for 532 and 785 nm excitation wavelengths. Under 532 nm, the spectra of all of the CZGSSe samples present a high S-rich composition, with an insignificant amount of Se. On the contrary, the spectra measured under 785 nm show a clear resonance effect (also confirmed by the high intensity of the E/B-like peaks), indicating that the laser penetration depth is high enough to pass through the entire S-rich region, which is supposed to be close to half of the film depth (at least for the sample 1/2 and is expected to be less for the sample 1/4).

As a result of Raman scattering analysis, it can be concluded a high Se content at the front and high S content at the back side of the CZGSSe thin films, confirming the presence of an in-depth compositional gradient profile. Note that no inhomogeneity from point-to-point measurements in the samples was observed, and no apparent secondary phases were detected using the 532 and 785 nm lasers. Using the Raman scattering spectra discussed above and supposing a linear change of the areas of peaks related to S−S and Se−Se vibrations, a very rough estimation of the [S]/([S] + [Se]) profile was performed (top panel of Figure 6). Although AES would be more reliable to have precise anionic profiling along the absorber thickness, the method here reported is completely valid to identify unambiguously a grading profile and has the

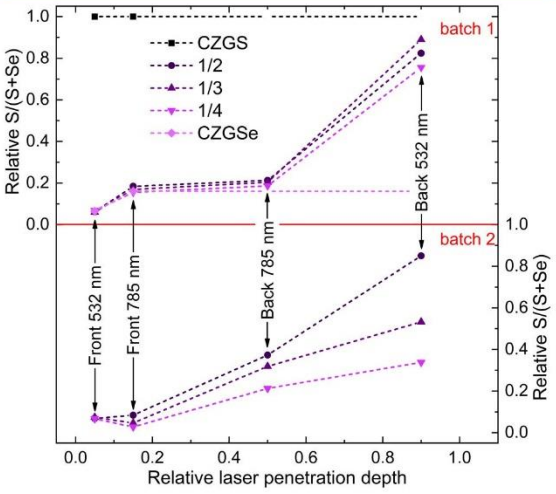

Figure 6. Rough estimation of the relative [S]/([S] + [Se]) ratio as a function of relative laser penetration depth for the CZGSSe absorbers prepared in batch 1 (top) and batch 2 (bottom).

https://doi.org/10.1021/acsami.1c21507
ACS Appl. Mater. Interfaces 2022, 14, 1177−1186

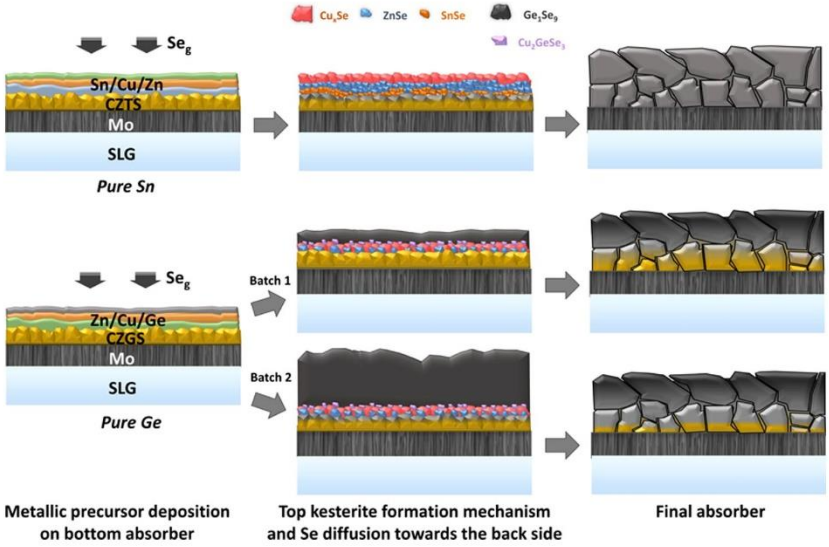

Figure 7. Schematic sketches of different intermediate steps and top kesterite reaction mechanism and Se diffusion involved in the formation of the solid solution absorbers prepared in this work.

main advantage of being faster. However, this could be a limitation for further future optimization of the grading profiles.

Previous investigations on pure CZGSe compounds revealed that slightly different processing conditions (mainly lower selenization temperature) compared to pure CZTSe compounds were needed to get better CZGSe-based devices.[13,25,32] Taking this into account, the second set of CZGSSe samples (labeled as batch 2) was prepared by lowering the annealing temperatures during selenization (see Section 2).

The same Raman multiwavelength characterization using the lift-off procedure was employed, and the resulting relative [S]/([S] + [Se]) ratio as a function of the relative laser penetration depth is shown in the bottom panel of Figure 6. Similar to the previous batch, at the front side, all of the samples exhibited a Se-rich composition, with insignificant change in the subsurface spectra excited with a 785 nm laser. In contrast to this, spectra measured at the back side of the sample clearly show an enrichment of the Se content with the thickness of the top precursor. As a result, a less abrupt gradient of the anion ratio can be observed for all samples. This indicates the possibility of more precise control of the in-depth gradient by changing the thicknesses ratio of the precursors under optimal selenization temperatures.

All of the results for the fabricated device characterization are shown in the Supporting Information (Figures S3 and S4), and unfortunately, the PV performance was not improved without additional optimizations. Demonstrating that the proposed method will allow improving the PV performance would imply optimizing not only the absorber band gap profile but also the different interfaces in contact with the absorber, which is beyond the scope of the proposed work. Nevertheless, a discussion supported with simulation results is also included to explain the observed device behavior.

4. DISCUSSION

Following a similar experimental process between samples, it has been shown that a homogeneous anionic composition is achieved for CZTSSe, while a graded anionic composition is obtained with CZGSSe. The anionic composition for CZTSSe is perfectly controlled with the thickness ratio of the sulfide and selenide absorber parts, varying from approximatively 45 to 20%. For CZGSSe, the composition varies from an almost pure selenide part (approximatively 10% of the relative value) at the front to an almost sulfide part (approximatively 80% of the relative value) at the back for certain processing conditions (batch 1) and with an increased intermixing (comprising approximatively between 40 and 80% of the relative values, depending on the sulfide part thickness) by adjusting the processing parameters (batch 2). This result shows the potential of the technique and that the anionic composition can be finely tuned in a homogeneous or graded form within the absorber thickness. The elemental interplay responsible for the different S−Se dynamics between compounds is not yet completely understood and is beyond the scope of this study, which aims at reporting the end result and potential of the method. Nevertheless, several possible hypotheses can be made. During selenization, two reactions are involved sequentially or at the same time: (1) selenization of the top metallic precursors and (2) anion substitution. Regarding reaction (1), a difference in the formation mechanism of Ge and Sn kesterite has already been reported elsewhere.[7,25] In the case of the formation of CZGSe, the presence of a Se-rich Ge−Se liquid phase during the initial moment of annealing acts as a Se reservoir and is key to controlling Se incorporation. During the formation of the CZGSe phase, Se diffusion occurs via this thick eutectic liquid phase formed on the surface,[25] while for CZTSe, Se diffusion is mainly controlled from a thin compact Cu_xSe phase layer on the surface.[7] At 400 °C, this Ge−Se liquid phase has probably been largely reduced in thickness (i.e., Se being evaporated) and thus less Se is available to diffuse. This explains why for batch 1, a low amount of Se is

https://doi.org/10.1021/acsami.1c21507
ACS Appl. Mater. Interfaces 2022, 14, 1177−1186

available for substitution of S (reaction 2) in the bottom CZGS part of the absorber, inducing, thus, a strong anionic gradient. By reducing the temperature to 380 °C in batch 2 for the formation of CZGSe, a thicker liquid phase remains on the surface and thus more Se is available to diffuse and substitute S (reaction 2 is promoted) in the CZGS bottom laye, inducing less abrupt gradient. However, for the case of CZTSSe, reaction 2 is promoted, leading to the formation of a homogeneous composition within the thickness. Other mechanisms could be involved to explain this observation and especially a possible degradation of the bottom sulfide part into binary phases. This could result in an intermixing of different sulfide and selenide phases, leading to the formation of a kesterite layer with a fix solid solution composition. It could even be hypothesized that this degradation could be higher for the bottom Sn sulfide part than the Ge one, as degradation of the CZTS/Mo interface is a well-known problem.[33] The metal in contact with the sulfide part (i.e., Sn in the case of CZTSe and Zn in the case of CZGSe) has maybe also some role to play. For example, Sn could be reacting with the bottom part, creating volatile $Sn_x(S,Se)_y$ phases that react with the top and bottom parts, leading faster to homogeneity. In any case, these differences obtained between Ge and Sn kesterite clearly reveal a different Se incorporation dynamics, which seems to be highly dependent on the involved cations and also probably on the stacking order of the metal precursor. In a similar way, it was recently reported that depending on the stacking order, the formation mechanism of Ge-based kesterite proceeds at different speeds, and putting Ge on top delays the formation reaction.[34] Finally, Figure 7 depicts the schematic representation summarizing the proposed mechanisms involved in the formation of Ge- and Sn-based kesterite in this work.

5. CONCLUSIONS

In this paper, an innovative method for the formation of kesterite absorbers with very well controlled anionic compositions is reported. A simple technique consisting of first preparing a pure sulfide absorber at the bottom and completing it with a metallic precursor to be selenized on the top allows us to obtain fixed (constant) or graded compositions in Sn- and Ge-containing kesterites. It is shown that this depends mainly on the different kesterite formation mechanisms, imposed by the top metallic stacking order, and on the processing parameters used for selenization, as a way of regulating the Se incorporation and diffusion toward the bottom pure sulfide part and avoiding/promoting substitution. These results demonstrate the potential of this simple technique and could pave the way to define and standardize anionic compositional profiles not only for kesterite but also for other chalcogenide-related technologies.

■ ASSOCIATED CONTENT

Supporting Information

The Supporting Information is available free of charge at https://pubs.acs.org/doi/10.1021/acsami.1c21507.

Raman spectra of CZTSSe absorbers on the surface and cross-sectional SEM images of CZTSe reference samples (PDF)

■ AUTHOR INFORMATION

Corresponding Authors

Maxim Guc − *Solar Energy Materials and Systems (SEMS), Institut de Recerca en Energia de Catalunya (IREC), Sant Adrià de Besòs, Barcelona 08930, Spain;* orcid.org/0000-0002-2072-9566; Email: mguc@irec.cat

Marcel Placidi − *Solar Energy Materials and Systems (SEMS), Institut de Recerca en Energia de Catalunya (IREC), Sant Adrià de Besòs, Barcelona 08930, Spain; Departament d'Enginyeria Electrònica, Universitat Politècnica de Catalunya, Barcelona 08034, Spain;* orcid.org/0000-0001-5684-9669; Email: marcel.placidi@upc.edu

Authors

Jacob Andrade-Arvizu − *Solar Energy Materials and Systems (SEMS), Institut de Recerca en Energia de Catalunya (IREC), Sant Adrià de Besòs, Barcelona 08930, Spain;* orcid.org/0000-0001-6643-7270

Robert Fonoll Rubio − *Solar Energy Materials and Systems (SEMS), Institut de Recerca en Energia de Catalunya (IREC), Sant Adrià de Besòs, Barcelona 08930, Spain;* orcid.org/0000-0002-6292-6648

Victor Izquierdo-Roca − *Solar Energy Materials and Systems (SEMS), Institut de Recerca en Energia de Catalunya (IREC), Sant Adrià de Besòs, Barcelona 08930, Spain*

Ignacio Becerril-Romero − *Solar Energy Materials and Systems (SEMS), Institut de Recerca en Energia de Catalunya (IREC), Sant Adrià de Besòs, Barcelona 08930, Spain;* orcid.org/0000-0002-7087-6097

Diouldé Sylla − *Solar Energy Materials and Systems (SEMS), Institut de Recerca en Energia de Catalunya (IREC), Sant Adrià de Besòs, Barcelona 08930, Spain*

Pedro Vidal-Fuentes − *Solar Energy Materials and Systems (SEMS), Institut de Recerca en Energia de Catalunya (IREC), Sant Adrià de Besòs, Barcelona 08930, Spain;* orcid.org/0000-0001-5776-9986

Zacharie Jehl Li-Kao − *Departament d'Enginyeria Electrònica, Universitat Politècnica de Catalunya, Barcelona 08034, Spain;* orcid.org/0000-0002-2610-5973

Angélica Thomere − *Solar Energy Materials and Systems (SEMS), Institut de Recerca en Energia de Catalunya (IREC), Sant Adrià de Besòs, Barcelona 08930, Spain*

Sergio Giraldo − *Solar Energy Materials and Systems (SEMS), Institut de Recerca en Energia de Catalunya (IREC), Sant Adrià de Besòs, Barcelona 08930, Spain;* orcid.org/0000-0003-4881-5041

Kunal Tiwari − *Solar Energy Materials and Systems (SEMS), Institut de Recerca en Energia de Catalunya (IREC), Sant Adrià de Besòs, Barcelona 08930, Spain*

Shahaboddin Resalati − *Architectural Engineering Research Group, Oxford Brookes University, Oxford OX3 0BP, United Kingdom*

Complete contact information is available at: https://pubs.acs.org/10.1021/acsami.1c21507

Author Contributions

J.A.-A. and R.F.R. contributed equally to this work. The manuscript was written through the contributions of all authors. All authors have given approval to the final version of the manuscript.

https://doi.org/10.1021/acsami.1c21507
ACS Appl. Mater. Interfaces 2022, 14, 1177−1186

Notes

The authors declare no competing financial interest.

■ ACKNOWLEDGMENTS

This research was partially supported by the H2020 Programme under project INFINITE-CELL (H2020-MSCA-RISE-2017-777968) and by the Spanish Ministry of Science, Innovation and Universities under WINCOST (ENE2016-80788-C5-1-R) and CELL2WIN (PID2019-104372RB-C31) projects. XRD and AES measurements have been performed at CCiTUB and "Departament d'Enginyeria Electronica i Biomèdica" of Universitat de Barcelona. The authors from IREC belong to the SEMS (Solar Energy Materials and Systems) Consolidated Research Group of "Generalitat de Catalunya" (ref 2017 SGR 862) and are grateful to European Regional Development Funds (ERDF, FEDER Programa Competitivitat de Catalunya 2007−2013). M.P. and M.G. acknowledge the financial support from the Spanish Ministry of Science, Innovation and Universities within the Ramón y Cajal (RYC-2017-23758) and Juan de la Cierva (IJC2018-038199-I) programs, respectively.

■ REFERENCES

(1) Peplow, M. Kesterite Solar Cells Get Ready to Shine. *Chem. Eng. News* **2018**, *96*, 15−18.

(2) Yang, K. J.; Kim, S.; Kim, S. Y.; Ahn, K.; Son, D. H.; Kim, S. H.; Lee, S. J.; Kim, Y. I.; Park, S. N.; Sung, S. J.; Kim, D. H.; Enkhbat, T.; Kim, J. H.; Jeon, C. W.; Kang, J. K. Flexible Cu2ZnSn(S,Se)4 Solar Cells with over 10% Efficiency and Methods of Enlarging the Cell Area. *Nat. Commun.* **2019**, *10*, No. 2959.

(3) Cabas-Vidani, A.; Haass, S. G.; Andres, C.; Caballero, R.; Figi, R.; Schreiner, C.; Márquez, J. A.; Hages, C.; Unold, T.; Bleiner, D.; Tiwari, A. N.; Romanyuk, Y. E. High-Efficiency (LixCu1−x)2ZnSn-(S,Se)4 Kesterite Solar Cells with Lithium Alloying. *Adv. Energy Mater.* **2018**, *8*, No. 1801191.

(4) Yan, C.; Sun, K.; Huang, J.; Johnston, S.; Liu, F.; Veettil, B. P.; Sun, K.; Pu, A.; Zhou, F.; Stride, J. A.; Green, M. A.; Hao, X. Beyond 11% Efficient Sulfide Kesterite Cu2ZnxCd1-XSnS4 Solar Cell: Effects of Cadmium Alloying. *ACS Energy Lett.* **2017**, *2*, 930−936.

(5) Kim, S.; Kim, K. M.; Tampo, H.; Shibata, H.; Niki, S. Improvement of Voltage Deficit of Ge-Incorporated Kesterite Solar Cell with 12.3% Conversion Efficiency. *Appl. Phys. Express* **2016**, *9*, No. 102301.

(6) Wang, W.; Winkler, M. T.; Gunawan, O.; Gokmen, T.; Todorov, T. K.; Zhu, Y.; Mitzi, D. B. Device Characteristics of CZTSSe Thin-Film Solar Cells with 12.6% Efficiency. *Adv. Energy Mater.* **2014**, *4*, No. 1301465.

(7) Giraldo, S.; Saucedo, E.; Neuschitzer, M.; Oliva, F.; Placidi, M.; Alcobé, X.; Izquierdo-Roca, V.; Kim, S.; Tampo, H.; Shibata, H.; Pérez-Rodríguez, A.; Pistor, P. How Small Amounts of Ge Modify the Formation Pathways and Crystallization of Kesterites. *Energy Environ. Sci.* **2018**, *11*, 582−593.

(8) Schorr, S.; Gurieva, G.; Guc, M.; Dimitrievska, M.; Pérez-Rodríguez, A.; Izquierdo-Roca, V.; Schnohr, C. S.; Kim, J.; Jo, W.; Merino, J. M. Point Defects, Compositional Fluctuations, and Secondary Phases in Non-Stoichiometric Kesterites. *J. Phys.: Energy* **2019**, *2*, No. 012002.

(9) Yin, W. J.; Wu, Y.; Wei, S. H.; Noufi, R.; Al-Jassim, M. M.; Yan, Y. Engineering Grain Boundaries in Cu2ZnSnSe4 for Better Cell Performance: A First-Principle Study. *Adv. Energy Mater.* **2014**, *4*, No. 1300712.

(10) Fonoll-Rubio, R.; Andrade-Arvizu, J.; Blanco-Portals, J.; Becerril-Romero, I.; Guc, M.; Saucedo, E.; Peiró, F.; Calvo-Barrio, L.; Ritzer, M.; Schnohr, C. S.; Placidi, M.; Estradé, S.; Izquierdo-Roca, V.; Pérez-Rodríguez, A. Insights into Interface and Bulk Defects in a High Efficiency Kesterite-Based Device. *Energy Environ. Sci.* **2021**, *14*, 507−523.

(11) Dietrich, J.; Abou-Ras, D.; Rissom, T.; Unold, T.; Schock, H. W.; Boit, C. Compositional Gradients in Cu(In,Ga)Se 2 Thin Films for Solar Cells and Their Effects on Structural Defects. *IEEE J. Photovoltaics* **2012**, *2*, 364−370.

(12) Andrade-Arvizu, J.; Izquierdo-Roca, V.; Becerril-Romero, I.; Vidal-Fuentes, P.; Fonoll-Rubio, R.; Sánchez, Y.; Placidi, M.; Calvo-Barrio, L.; Vigil-Galán, O.; Saucedo, E. Is It Possible to Develop Complex S-Se Graded Band Gap Profiles in Kesterite-Based Solar Cells? *ACS Appl. Mater. Interfaces* **2019**, *11*, 32945−32956.

(13) Andrade-Arvizu, J.; Fonoll-Rubio, R.; Sanchez, Y.; Becerril-Romero, I.; Malerba, C.; Valentini, M.; Calvo-Barrio, L.; Izquierdo-Roca, V.; Placidi, M.; Vigil-Galán, O.; Pérez-Rodríguez, A.; Saucedo, E.; Jehl Li-Kao, Z. Rear Band Gap Grading Strategies on Sn−Ge-Alloyed Kesterite Solar Cells. *ACS Appl. Energy Mater.* **2020**, *3*, 10362−10375.

(14) Giraldo, S.; Kim, S.; Andrade-Arvizu, J. A.; Alcobé, X.; Malerba, C.; Valentini, M.; Tampo, H.; Shibata, H.; Izquierdo-Roca, V.; Pérez-Rodríguez, A.; Saucedo, E. Study and Optimization of Alternative MBE-Deposited Metallic Precursors for Highly Efficient Kesterite CZTSe:Ge Solar Cells. *Prog. Photovoltaics.: Res. Appl.* **2019**, *27*, 779−788.

(15) Izquierdo-Roca, V.; Fontañ, X.; Álvarez-Garcia, J.; Calvo-Barrio, L.; rez-Rodríguez, A.; Morante, J. R.; Ruiz, C. M.; Saucedo, E.; Bermúdez, V. Electrochemical Synthesis of CuIn (S,Se)2 Alloys with Graded Composition for High Efficiency Solar Cells. *Appl. Phys. Lett.* **2009**, *94*, No. 061915.

(16) Sohn, S. H.; Han, N. S.; Park, Y. J.; Park, S. M.; An, H. S.; Kim, D. W.; Min, B. K.; Song, J. K. Band Gap Grading and Photovoltaic Performance of Solution-Processed Cu(In, Ga)S2 Thin-Film Solar Cells. *Phys. Chem. Chem. Phys.* **2014**, *16*, 27112−27118.

(17) Kondrotas, R.; Oliva, F.; Alcobe, X.; Izquierdo-Roca, V.; Perez-Rodriguez, A.; Saucedo, E.; Pistor, P. Double Band Gap Gradients in Sequentially Processed Photovoltaic Absorbers from the Cu(In,Ga)-Se2-ZnSe Pseudobinary System. *Prog. Photovoltaics.: Res. Appl.* **2018**, *26*, 135−144.

(18) Jehl Li Kao, Z.; Kobayashi, T.; Nakada, T. Modeling of the Surface Sulfurization of CIGSe-Based Solar Cells. *Sol. Energy* **2014**, *110*, 50−55.

(19) Kobayashi, T.; Yamaguchi, H.; Jehl Li Kao, Z.; Sugimoto, H.; Kato, T.; H, H.; N, T. Impact of Surface Sulfurization on Cu(In1-XGax)Se2. *Prog. Photovolt.: Res. Appl.* **2015**, *23*, 1367−1374.

(20) Ratz, T.; Brammertz, G.; Caballero, R.; León, M.; Canulescu, S.; Schou, J.; Gütay, L.; Pareek, D.; Taskesen, T.; Kim, D.-H.; Kang, J.-K.; Malerba, C.; Redinger, A.; Saucedo, E.; Shin, B.; Tampo, H.; Timmo, K.; Nguyen, N. D.; Vermang, B. Physical Routes for the Synthesis of Kesterite. *J. Phys. Energy* **2019**, *1*, No. 042003.

(21) Todorov, T.; Hillhouse, H. W.; Aazou, S.; Sekkat, Z.; Vigil-Galán, O.; Deshmukh, S. D.; Agrawal, R.; Bourdais, S.; Valdés, M.; Arnou, P.; Mitzi, D. B.; Dale, P. J. Solution-Based Synthesis of Kesterite Thin Film Semiconductors. *J. Phys. Energy* **2020**, *2*, No. 012003.

(22) Xie, H.; Dimitrievska, M.; Fontané, X.; Sánchez, Y.; López-Marino, S.; Izquierdo-Roca, V.; Bermúdez, V.; Pérez-Rodríguez, A.; Saucedo, E. Formation and Impact of Secondary Phases in Cu-Poor Zn-Rich Cu2ZnSn(S1−ySey)4 (0≤y≤1) Based Solar Cells. *Sol. Energy Mater. Sol. Cells* **2015**, *140*, 289−298.

(23) Bag, S.; Gunawan, O.; Gokmen, T.; Zhu, Y.; Todorov, T. K.; Mitzi, D. B. Low Band Gap Liquid-Processed CZTSe Solar Cell with 10.1% Efficiency. *Energy Environ. Sci.* **2012**, *5*, 7060−7065.

(24) Sarmadian, N.; Saniz, R.; Partoens, B.; Lamoen, D. First-Principles Study of the Optoelectronic Properties and Photovoltaic Absorber Layer Efficiency of Cu-Based Chalcogenides. *J. Appl. Phys.* **2016**, *120*, No. 085707.

(25) Benhaddou, N.; Aazou, S.; Fonoll-Rubio, R.; Sánchez, Y.; Giraldo, S.; Guc, M.; Calvo-Barrio, L.; Izquierdo-Roca, V.; Abd-Lefdil, M.; Sekkat, Z.; Saucedo, E. Uncovering Details behind the Formation Mechanisms of Cu2ZnGeSe4 Photovoltaic Absorbers. *J. Mater. Chem. C* **2020**, *8*, 4003−4011.

https://doi.org/10.1021/acsami.1c21507
ACS Appl. Mater. Interfaces 2022, 14, 1177−1186

(26) Guc, M.; Levcenko, S.; Izquierdo-Roca, V.; Fontané, X.; Arushanov, E.; Pérez-Rodríguez, A. Polarized Raman Scattering Analysis of Cu2ZnSnSe4 and Cu2ZnGeSe4 Single Crystals. *J. Appl. Phys.* **2013**, *114*, No. 193514.
(27) Dimitrievska, M.; Fairbrother, A.; Fontané, X.; Jawhari, T.; Izquierdo-Roca, V.; Saucedo, E.; Pérez-Rodríguez, A. Multiwavelength Excitation Raman Scattering Study of Polycrystalline Kesterite Cu2ZnSnS4 Thin Films. *Appl. Phys. Lett.* **2014**, *104*, No. 021901.
(28) Khare, A.; Himmetoglu, B.; Johnson, M.; Norris, D. J.; Cococcioni, M.; Aydil, E. S. Calculation of the Lattice Dynamics and Raman Spectra of Copper Zinc Tin Chalcogenides and Comparison to Experiments. *J. Appl. Phys.* **2012**, *111*, No. 083707.
(29) Dimitrievska, M.; Xie, H.; Fairbrother, A.; Fontané, X.; Gurieva, G.; Saucedo, E.; Pérez-Rodríguez, A.; Schorr, S.; Izquierdo-Roca, V. Multiwavelength Excitation Raman Scattering of Cu2ZnSn(SxSe1-x)4 ($0 \leq \times \leq 1$) Polycrystalline Thin Films: Vibrational Properties of Sulfoselenide Solid Solutions. *Appl. Phys. Lett.* **2014**, *105*, No. 031913.
(30) Dimitrievska, M.; Gurieva, G.; Xie, H.; Carrete, A.; Cabot, A.; Saucedo, E.; Pérez-Rodríguez, A.; Schorr, S.; Izquierdo-Roca, V. Raman Scattering Quantitative Analysis of the Anion Chemical Composition in Kesterite Cu2ZnSn(SxSe1-x)4 Solid Solutions. *J. Alloys Compd.* **2015**, *628*, 464−470.
(31) Kim, S. Y.; Kim, S. H.; Hong, S.; Son, D. H.; Kim, Y. I.; Kim, S.; Ahn, K.; Yang, K. J.; Kim, D. H.; Kang, J. K. Secondary Phase Formation Mechanism in the Mo-Back Contact Region during Sulfo-Selenization Using a Metal Precursor: Effect of Wettability between a Liquid Metal and Substrate on Secondary Phase Formation. *ACS Appl. Mater. Interfaces* **2019**, *11*, 23160−23167.
(32) Benhaddou, N.; Aazou, S.; Sánchez, Y.; Andrade-Arvizu, J.; Becerril-Romero, I.; Guc, M.; Giraldo, S.; Izquierdo-Roca, V.; Saucedo, E.; Sekkat, Z. Investigation on Limiting Factors Affecting Cu2ZnGeSe4 Efficiency: Effect of Annealing Conditions and Surface Treatment. *Sol. Energy Mater. Sol. Cells* **2020**, *216*, No. 110701.
(33) Scragg, J. J.; Wätjen, J. T.; Edoff, M.; Ericson, T.; Kubart, T.; Platzer-Björkman, C. A Detrimental Reaction at the Molybdenum Back Contact in Cu 2ZnSn(S,Se)4 Thin-Film Solar Cells. *J. Am. Chem. Soc.* **2012**, *134*, 19330−19333.
(34) Brammertz, G.; Kohl, T.; De Wild, J.; Meuris, M.; Vermang, B.; Poortmans, J. Crystallization Properties of Cu2ZnGeSe4. *Thin Solid Films* **2019**, *670*, 76−79.

https://doi.org/10.1021/acsami.1c21507
ACS Appl. Mater. Interfaces 2022, 14, 1177−1186

Supporting Information

Controlling the anionic ratio and gradient in kesterite technology

Jacob Andrade-Arvizu,[†,‖] Robert Fonoll Rubio,[†,‖] Victor Izquierdo-Roca,[†] Ignacio Becerril-Romero,[†] Diouldé Sylla,[†] Pedro Vidal-Fuentes,[†] Zacharie Jehl Li-Kao,[‡] Angélica Thomere,[†] Sergio Giraldo,[†] Kunal Tiwari,[†] Shahaboddin Resalati,[§] Maxim Guc,[†] and Marcel Placidi*[†,‡]*

[†]Solar Energy Materials and Systems (SEMS), Institut de Recerca en Energia de Catalunya (IREC), Jardins de les Dones de Negre 1, 08930 Sant Adrià de Besòs, Barcelona, Spain
[‡]Departament d'Enginyeria Electrònica, Universitat Politècnica de Catalunya, C/ Jordi Girona 1, 08034 Barcelona, Spain
[§]Architectural Engineering Research Group, Oxford Brookes University, United Kingdom

Corresponding Authors

*mguc@irec.cat, *marcel.placidi@upc.edu

Author Contributions

The manuscript was written through contributions of all authors. All authors have given approval to the final version of the manuscript. ‖ These authors contributed equally to this work.

Raman spectra and SEM images of Sn kesterite samples

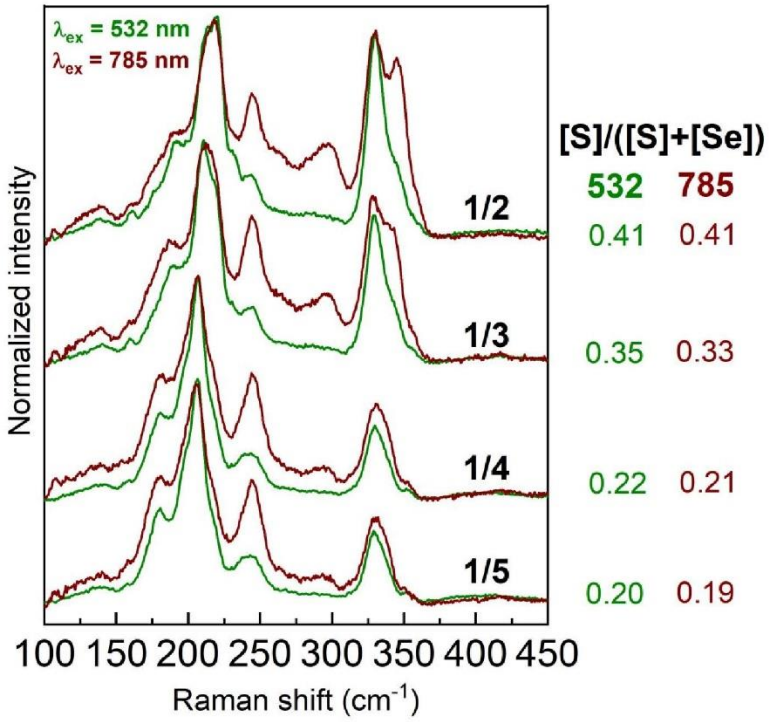

Figure S1. Raman spectra of the CZTSSe absorbers at the surface (using 532 nm excitation wavelength) and subsurface (using 785 nm excitation wavelength); in the right part, the anionic compositional ratio is indicated, for both excitation wavelengths.

Table S1. Anionic compositional ratios for different batches of CZTSSe absorbers (estimated from Raman spectra of the absorbers surface, using 532 nm excitation wavelength).

	[S]/([S]+[Se])	
Samples	**Batch 1**	**Batch 2**

1/2	0.41	0.41
1/3	0.35	0.31
1/4	0.22	0.19
1/5	0.20	0.17

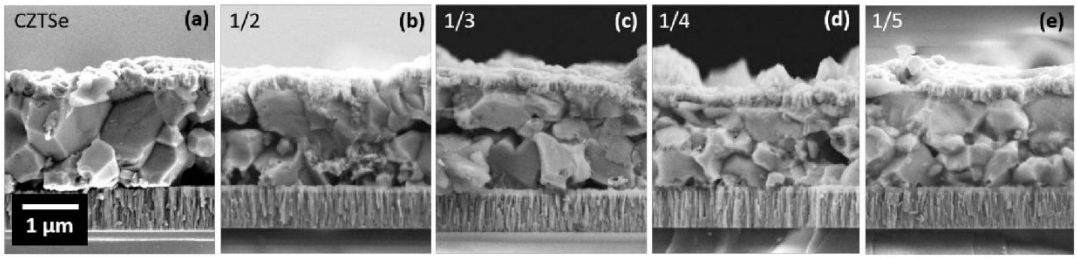

Figure S2. Cross-section SEM images of (a) a CZTSe reference samples, and (b)(c)(d)(e) the different CZTSSe prepared absorbers with different thicknesses of the bottom sulfide layer.

Devices results, simulation and discussion

The JV characteristics for the Sn kesterite solar cells with different composition ratios are shown in Fig. S3 below. In contrast to what was expected, the V_{oc} was not increasing with higher anionic composition. It has been reported, even recently, that the introduction of S in Kesterite leads to the formation of an interface defect which may limit the voltage.[1] Indeed, SCAPS modelling was performed starting from a baseline Kesterite example, and introducing a fermi level pinning from single acceptor defects at the front interface and related to the presence of S. As shown in Figure S3, the pinning of the fermi level (right side) reproduces accurately the experimental behavior of the devices. Hence, it is likely that the voltage limitation occurs due to the presence of such donor defects at the absorber/buffer interface.

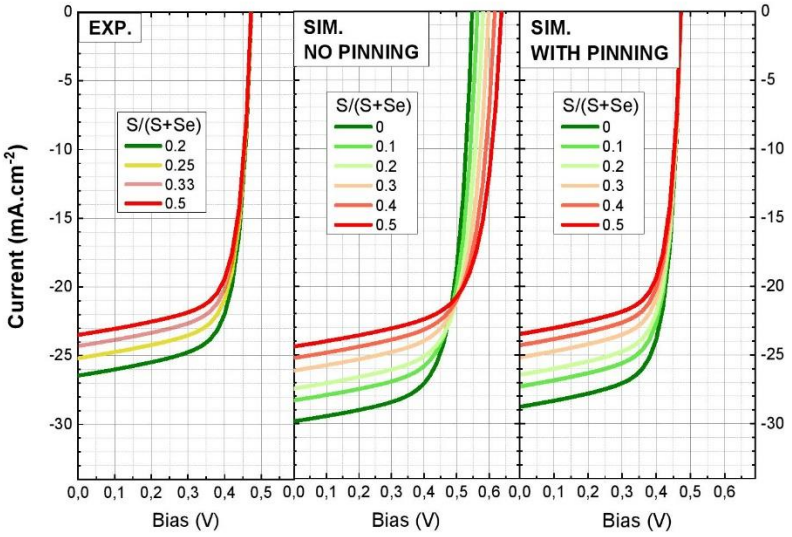

Figure S3. Current-voltage characteristics of the Sn kesterite devices made with different anionic ratios: (left) experimental results, and SCAPS simulation without (center) and with (right) fermi level pinning.

The JV characteristics of the Ge kesterite solar cells with the different compositional profiles are shown in Fig. S4. In this case, only the devices from batch 1 are represented, as the ones from batch 2 were not working. We believe the main reason is due to the higher S content towards the center of the absorber, that could result in a higher defective bulk, as the deep defect cluster Ge_{zn}+Cu_{Zn} becomes predominant and highly detrimental with a concentration exceeding the absorber's carrier concentration.[2]

Once again, SCAPS modelling considering the simultaneous presence of interfacial defects, and the existence of literature reported defect clusters shows a similar behavior akin to that of batch 1. Indeed, while the V_{oc} is marginally modified (and in ways that make us believe that different competing factors may exist), a strong variation of the current is observed. While it is easy to understand it in terms of bandgap modification, as high S content samples have expectedly a lower current, it is also worth mentioning that the introduction of S in Kesterite leads to the prevalence of a cluster defect with a higher carrier capture cross section ($\sigma_{p,n}$); indeed, while the Ge_{zn}+Cu_{Zn} cluster has a reported $\sigma_{p,n} = 10^{-14}$, it is reported as 10^{-14} for a pure S content. Such difference may also contribute to reducing the current, as the defect interact more with electrons and holes.

The SCAPS modelling including state of the art defects shown Figure S4 goes in the same direction, although those curves aren´t fully quantitative as the real bulk and interface defect density was not measured in our cells, and the data from the supplementary information of reference have been used instead.[2]

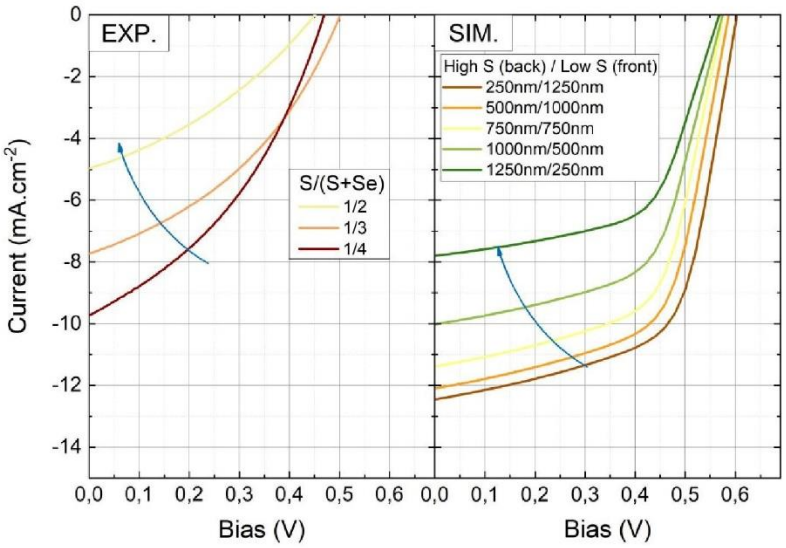

Figure S4. Current-voltage characteristics of the Ge kesterite devices made with different graded anionic profiles: (left) experimental results, and (right) SCAPS simulation including interfacial and cluster defects (here, the high S content thickness of the back side was gradually varied)

References

1. Li, J.; Huang, J.; Huang, Y.; Tampo, H.; Sakurai, T.; Chen, C.; Sun, K.; Yan, C.; Cui, X.; Mai, Y.; Hao, X., Interface Recombination of Cu2ZnSnS4 Solar Cells Leveraged by High Carrier Density and Interface Defects, Solar RRL **2021**, 5, 10, 2100418.

2. Kim, S.; Marquez, J.A.; Unold, T.; Walsh, A., Upper limit to the photovoltaic efficiency of imperfect crystals from first principles, Energy Environ. Sci. **2020**, 13, 1481-1491.

3.6. Article 5: Insights into the Effects of RbF-Post-Deposition Treatments on the Absorber Surface of High Efficiency Cu(In,Ga)Se_2 Solar Cells and Development of Analytical and Machine Learning Process Monitoring Methodologies Based on Combinatorial Analysis

Check for updates

RESEARCH ARTICLE

ADVANCED ENERGY MATERIALS

www.advenergymat.de

Insights into the Effects of RbF-Post-Deposition Treatments on the Absorber Surface of High Efficiency Cu(In,Ga)Se_2 Solar Cells and Development of Analytical and Machine Learning Process Monitoring Methodologies Based on Combinatorial Analysis

Robert Fonoll-Rubio, Stefan Paetel, Enric Grau-Luque, Ignacio Becerril-Romero, Rafael Mayer, Alejandro Pérez-Rodríguez, Maxim Guc, and Victor Izquierdo-Roca**

The latest record efficiencies of the Cu(In,Ga)Se_2 (CIGSe) photovoltaic technology are driven by heavy alkali post-deposition treatments (PDTs). Despite their positive effect, especially in the V_{oc} of the devices, their underlying mechanisms are still under discussion. This work sheds light on this topic by performing a high statistics analysis on 620 high efficiency CIGSe solar cells submitted to four different PDT processes (different RbF source temperature) employing a combinatorial approach based on Raman and photoluminescence (PL) spectroscopies. This reveals with statistical confidence subtle differences in the spectroscopic data that relate to the redistribution of defects between the ordered vacancy compound (OVC) and the chalcopyrite phases at the absorber surface. In particular, there is an intertwined decrease of the OVC phase and increase of the so-called "defective chalcopyrite phase." Additionally, two industry-compatible methodologies for the assessment of the RbF-PDT process and prediction of the V_{oc} of the final devices with a ±2% error and an efficacy of ≈95% are developed based on analytical and machine learning approaches. These results show that the combined Raman and PL spectroscopic techniques represent a powerful tool for the future development of the CIGSe technology at a research level and for more efficient industrial manufacturing.

R. Fonoll-Rubio, E. Grau-Luque, I. Becerril-Romero, R. Mayer, A. Pérez-Rodríguez, M. Guc, V. Izquierdo-Roca
Catalonia Institute for Energy Research (IREC)
Jardins de les Dones de Negre 1, Sant Adrià de Besòs-Barcelona 08930, Spain
E-mail: mguc@irec.cat; vizquierdo@irec.cat

S. Paetel
Zentrum für Sonnenenergie- und Wasserstoff-Forschung
Baden-Württemberg (ZSW)
Meitnerstr. 1, 70563 Stuttgart, Germany

A. Pérez-Rodríguez
Departament d'Enginyeria Electronica i Biomedica
IN^{2}UB
Universitat de Barcelona
C/ Marti i Franques 1, Barcelona 08028, Spain

The ORCID identification number(s) for the author(s) of this article can be found under https://doi.org/10.1002/aenm.202103163.

DOI: 10.1002/aenm.202103163

1. Introduction

Thin film photovoltaic (PV) technologies based on Cu(In,Ga)Se_2 (CIGSe) have reached an advanced degree of maturity with a record energy conversion efficiency at the laboratory scale of 23.35%.[1] These efficiency values combined with the inherent advantages of thin film PV such as low material usage, fabrication versatility, and their easy integration (e.g., building integrated photovoltaics, wearables, internet of things, etc.) open the way to the democratization and ubiquity of PV through mass production of cheap and efficient solar cell devices. In this regard, CIGSe-based thin film solar cells have been proven viable for large-scale industrial development.[2]

Recently, efficiency improvements of this type of solar cells have been achieved by applying post-deposition treatments (PDTs) based on heavy alkali elements such as K,[3–9] Rb,[5,8,10] and Cs.[5,8,11] On the one hand, this efficiency improvement is explained by the increase of the open-circuit voltage (V_{oc}) which has been reported by many authors when applying heavy alkali PDT on a wide range of CIGSe-based absorbers.[4–10,12,13] On the other hand, the short-circuit current density (J_{sc}) shows different behaviors when heavy alkali PDT is applied.[3,5,13,14] For instance, the J_{sc} has been shown to depend strongly on the characteristics of the buffer layer deposited after the PDT.[14] Finally, it has not been possible to clearly determine the impact of the PDT on the fill factor (FF).[3,5,11,15,16] Thus, the results reported in the literature suggest that the main effect of the heavy alkali PDT is produced on the V_{oc}, while the other optoelectronic parameters can be influenced by several other aspects of the technological processes.

In general, there are no doubts about the benefits of applying heavy alkali PDT on CIGSe-based devices for achieving high efficiencies, but the reasons for the positive impact of this treatment remain under discussion. Previous to the use and study of

ADVANCED SCIENCE NEWS
www.advancedsciencenews.com

ADVANCED ENERGY MATERIALS
www.advenergymat.de

heavy alkali elements, it was determined that good efficiencies cannot be achieved without the presence of the light alkali Na in the CIGSe absorber.[17–24] This was attributed to Na-induced higher net doping levels that improve the V_{oc} and the FF.[19] For light alkali metals such as Na and Li, the diffusion via copper vacancies (V_{Cu}) and the diffusion via interstitial positions in the lattice have comparable energy barriers, thus it was shown that Na can either replace vacant Cu places or occupy interstices in the crystal lattice of CIGSe.[25] However, for heavy alkali metals, such as rubidium, the energy barrier is much lower for the diffusion via V_{Cu} than for the diffusion via the interstitial positions.[25] As a consequence, under Cu-poor conditions, Rb will have a preference to occupy vacant Cu sites, in particular the ones located near the grain boundaries (GBs) or at the surface of the CIGSe absorber, since the large atomic radius of Rb prevents its deeper penetration into the CIGSe grains. In a stoichiometric CIGSe lattice, it is not probable for Rb to replace Cu due to the low availability of vacancies, and it will remain outside the CIGSe grain.[12,25] Taking this into account, it has been proposed that the positive impact of Rb on the V_{oc} for CIGSe with [Cu]/([Ga]+[In]) (CGI) ≥ 0.8 can be attributed to a Rb-Na exchange mechanism in which Rb is accumulated at the GBs and displaces Na toward the interior of the grain, thus leading to improved carrier concentrations.[26] In addition, the passivation of the GBs by Rb itself would lead to increased carrier lifetimes.[26] In the case of very Cu-poor CIGSe (CGI < 0.8), Rb could diffuse directly into the V_{Cu} of the Cu-poor material, thus forming the $RbInSe_2$ phase.[26] Since, in this case, there is no Na-Rb exchange nor GB passivation, the V_{oc} and FF of the devices would be reduced due to the formation of a $RbInSe_2$ layer that would act as a photocurrent barrier.[12,26] In addition, although the CIGSe surface is modified by RbF-PDT, it has been proposed that such surface modifications do not have an important influence on the performance improvement, but that this improvement is mainly due to a reduction of the amount of tail states, which reduces the non-radiative recombination in the bulk of the absorber.[12] On the other hand, refs. [26–28] show that the quality modifications of the absorber surface due to PDT strongly depend on the CGI ratio, which implies that they could be either positive or negative depending on the absorber composition.

From all the exposed above, it renders clear that a deeper understanding of the fundamentals behind heavy alkali PDT and its influence on device performance could be of great help for the CIGSe community providing a powerful insight that allows optimizing the fabrication process of high efficiency devices. In this regard, the main aim of the present study is to shed light on the influence of RbF-PDT on the absorber surface in high efficiency CIGSe devices. In order to provide statistically reliable results, a high number of solar cells were fabricated with four different RbF-PDT conditions (620 cells in total: 140 Rb-free cells and 160 Rb-containing for each of the three remaining PDT conditions). A combinatorial analysis was performed in all the cells by means of spectroscopic (Raman and photoluminescence (PL)) and optoelectronic characterization. The thorough analysis of the experimental data allows proposing a novel model for understanding the mechanisms that drive the positive effects of RbF-PDT that is based on the redistribution of structural defects at the absorber surface promoted by the PDT process. This model is further supported by results on charge carrier distribution in the space charge region obtained by capacitance–voltage measurements. Finally, this work also presents the development of process monitoring methodologies compatible with industrial environments that are able to predict the V_{oc} of CIGSe devices exposed to RbF-PDT at the earliest possible stage of the fabrication process. Two methodologies, one based on an analytical approach and another on machine learning (ML) algorithms, are proposed using the large set of experimental Raman and PL data obtained in this work, showing the high potential of these fast and non-destructive techniques to be used for advanced in-line process monitoring of the CIGSe solar cell production process. These non-destructive methodologies are of great relevance for the CIGSe PV industry since they allow optimizing the manufacturing process in terms of production yield and device efficiency leading to a fabrication process with lower costs and environmental impact.

2. Results and Discussion

The following results and discussions are separated into three subsections. The first subsection shows the results of the evolution of the optoelectronic properties of all the measured solar cells with the RbF source temperature. The second provides the experimental results of the Raman and PL analyses and correlates them with the electrical and optoelectronic properties allowing to propose a model that explains the influence of the RbF-PDT process on the absorber surface. Finally, the third subsection presents a possible application of the obtained results for the prediction of the V_{oc} of the solar cells based on both analytical and ML approaches, revealing the potential of Raman–PL based methodologies for the fine monitoring of the production process of CIGSe-based devices exposed to RbF-PDT.

2.1. Evolution of the Optoelectronic Properties

The evolution of the optoelectronic properties of the 620 analyzed solar cells shows that for low RbF availability (490 °C RbF source temperature), the overall device performance decreases with the PDT falling from an average (maximum) efficiency of around 16.5% (17.9%) for the Rb-free samples to 15.5% (16.9%) for the treated samples (see **Figure 1**a; Table S1, Supporting Information). As the RbF availability (source temperature) increases, the performance of the samples starts to recover with a 16.3% (17.9%) average (maximum) efficiency for the 520 °C samples, and surpasses the performance of the untreated sample for the 540 °C samples with a 17.1% (18.2%) efficiency. This evolution seems to be controlled by the FF of the devices that follows an almost exactly similar tendency than the efficiency (Figure 1d). Likewise, the V_{oc} also shows a similar trend with the average (maximum) V_{oc} decreasing from 695 mV (708 mV) in the Rb-free sample to 687 mV (697 mV) in the 490 °C sample and, then, increasing to 697 mV (706 mV) for 520 °C and to 707 mV (721 mV) for 540 °C (Figure 1b). These tendencies are analogous to a previous work by Kodalle et al. carried out in samples fabricated using a similar process but in which the amount of RbF in the samples was controlled by the

ADVANCED SCIENCE NEWS
www.advancedsciencenews.com

ADVANCED ENERGY MATERIALS
www.advenergymat.de

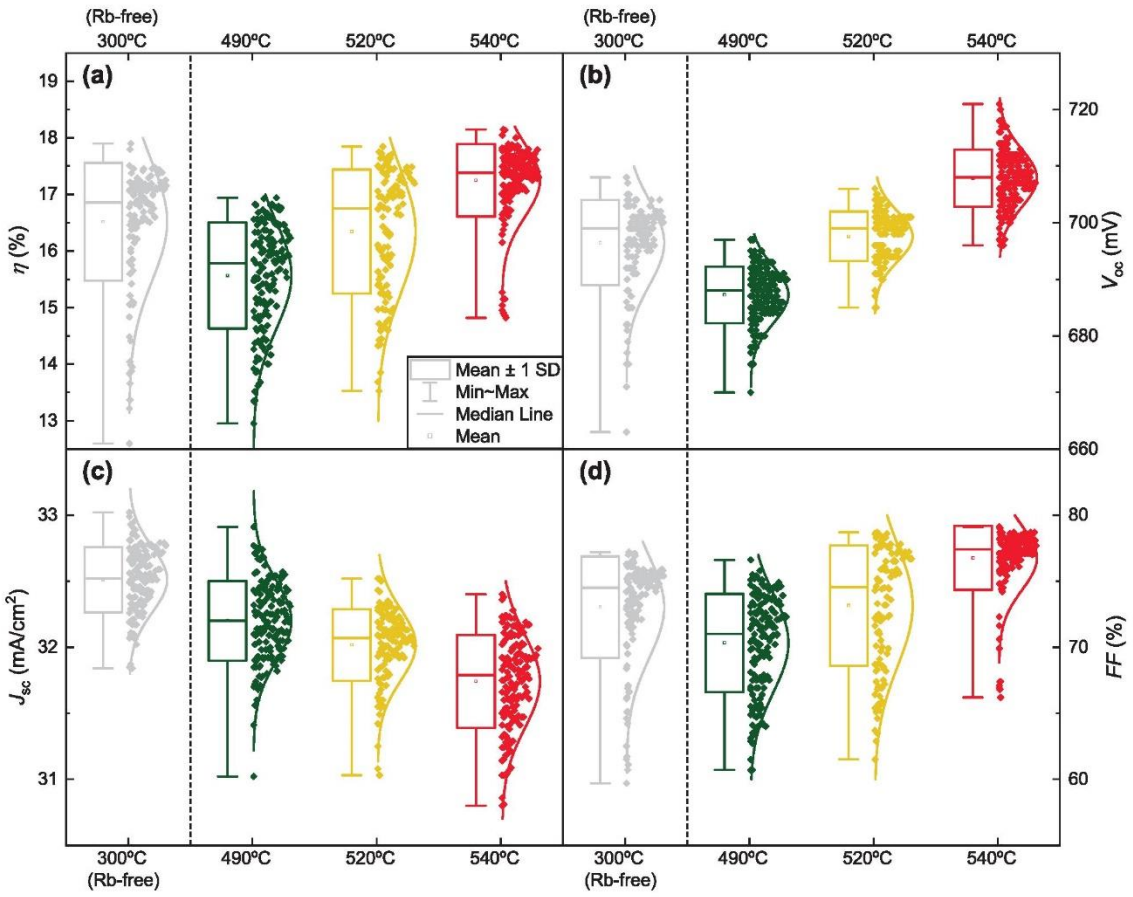

Figure 1. Evolution of the a) efficiency, b) open circuit voltage, c) short circuit current and d) fill factor of the 620 solar cells exposed to RbF-PDT with different RbF source temperature. The meaning of each element represented in the box plots is presented in the legend of panel (a). The curves attached to each box plot represent the Gaussian distribution of the displayed data points.

PDT process duration.[27] On the other hand, the J_{sc} shows a different trend in both works. While in ref. [27] no significant correlation was found, the present work shows a clearly decrease of J_{sc} with the increasing RbF source temperature (Figure 1c). This incongruence, however, can be explained by the limited number of cells analyzed in ref. [27] (15 cells per PDT condition) that may have prevented to observe a clear trend for such small variations of J_{sc}. In this regard, it is worth noticing the importance of analyzing a large number of samples in this type of studies, in which the variations of the optoelectronic properties of the solar cells are small (≈2.8% for V_{oc} and ≈1.2% for J_{sc} in the present work), and where only high statistics enable to unveil trends with statistical confidence.

In summary, the optoelectronic results obtained in this work are comparable with the state of the art devices[29,30] and prove the effectivity of the RbF-PDT that, when performed in optimum conditions, allows to increase the performance of high efficiency CIGSe devices (by more than 3.5% in average, in the present work) thanks, mainly, to an improved V_{oc} and FF.

The complex behavior of the J_{sc}, FF, and efficiency that may depend on a wide variety of parameters (e.g., CdS growth, contacts, electric probing, etc.) prevents their use for further correlations of the PDT process with the changes that occur in the CIGSe absorber layer. Thus, the main focus in the further investigations presented below will be put on the correlation of the different physicochemical properties of the CIGSe material with the V_{oc} of the final devices, as this parameter is mainly characterized by the intrinsic changes in the absorber layer and reflects any slight modifications that may occur in it.

2.2. Redistribution of Defects at the Absorber Surface

In order to correlate the optoelectronic properties of the samples with different PDT treatment with their physicochemical properties, all the cells of the different samples were evaluated by Raman spectroscopy using a 638 nm excitation (see Experimental Section for further details). Raman spectroscopy already

ADVANCED SCIENCE NEWS
www.advancedsciencenews.com

ADVANCED ENERGY MATERIALS
www.advenergymat.de

demonstrated its high potential to detect the small structural[31,32] and compositional[33–37] modifications in CIGSe compounds which, according to previous investigations of the PDT process, have been identified as critical parameters that might result in the enhancement of the final device performance.[12]

The high efficiency of the analyzed devices presupposes a good quality of the CIGSe absorber layers in terms of morphology, homogeneity, crystalline quality, and absence of any detrimental secondary phases or strong deviations from the optimal compositions. In this context, no significant changes in the Raman scattering spectra of solar cells exposed to different PDTs were expected. **Figure 2**a shows average normalized (to the intensity of the main peak of CIGSe at 177 cm^{-1}) spectra of samples that underwent PDT treatments with the RbF source at the maximum (540 °C) and minimum (490 °C, note that for 300 °C no PDT process takes place) temperatures. A typical CIGSe compound Raman spectrum is obtained independently of the PDT temperature (e.g., see refs. [32,36–39]) with extremely small deviations between them. However, the high quality of the spectra allows to detect and define through spectra subtraction (blue line in Figure 2a) the main spectral regions where the differences due to the different PDT process appear. These were mainly found in the ranges highlighted in different colors in Figure 2a, specifically in: 1) 150–165 cm^{-1}; 2) 205–233 cm^{-1}; and 3) 238–260 cm^{-1}. It is worth noticing, that the first spectral range contains mainly the A_1 symmetry peak of the ordered vacancy compound (OVC) phase at ≈160 cm^{-1}[40–42] with a slight contribution of a tail of the main A_1 symmetry peak of CIGSe at 177 cm^{-1}. The peaks in the second and third spectral ranges are assigned to E/B-like symmetry modes, that have two mode behavior in the $Cu(In,Ga)Se_2$ solid solution.[40–43] This implies that the peaks in the 205–233 cm^{-1} range are associated with the presence of In cations, while the peaks in the 238–260 cm^{-1} range relate to the presence of Ga cations. Moreover, in both ranges, the E/B-like symmetry peaks of the OVC phase are overlapped with those of the CIGSe phase,[41] resulting in a complex structure of the Raman spectra in the high wavenumber spectral ranges so the changes observed in these ranges can have different nature. Additionally, for the further upcoming analysis, all the integrated intensities of the defined ranges were normalized to the integrated intensity of the main CIGSe peak calculated in the 165–185 cm^{-1} range. The general shape of the spectral difference line between the two extreme RbF source temperatures highly resembles that of the OVC $CuIn_3Se_5$ compound Raman spectrum with a slightly increased intensity of the peaks in the high wavenumber range (>240 cm^{-1}) and shift of the peaks to higher wavenumbers due to the partial substitution of In cations by Ga.[32,40,44] This indicates that the main change occurring at the surface of the absorber due to the different RbF source temperatures is related to the change of the relative amount of the OVC phase ($Cu(In,Ga)_3Se_5$), that is usually formed at the CIGSe/CdS interface.[26,32,36,39,45,46] As mentioned above, from the three defined spectral ranges, only the first one (150–165 cm^{-1}) is mainly related with the OVC phase without a strong overlap with the Raman peaks of the chalcopyrite CIGSe phase, and with only an insignificant overlapping influence of the tail of the main chalcopyrite Raman peak at 177 cm^{-1}.[32,36–39] Taking this into account, the correlations between the integrated

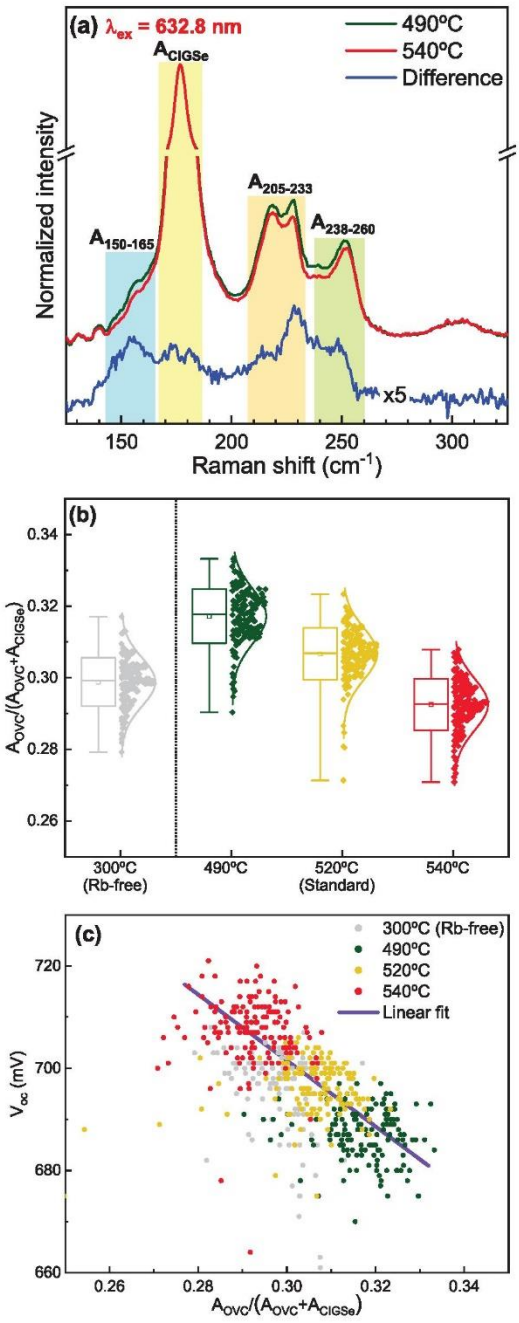

Figure 2. a) Average Raman scattering spectra of CIGSe-based devices exposed to different RbF-PDTs measured under 638 nm excitation wavelength. The spectrum obtained from subtracting the spectra is also included. The different spectral ranges selected for the analysis are highlighted in colors. b) Relative integrated intensity of the OVC-related Raman peaks in function of the source temperature of the RbF-PDT. c) Dependence of V_{oc} of CIGSe solar cells with different RbF-PDT on the relative integrated intensity of the OVC-related Raman peaks.

ADVANCED SCIENCE NEWS
www.advancedsciencenews.com

ADVANCED ENERGY MATERIALS
www.advenergymat.de

intensity of this OVC-related range and the two other spectral ranges were analyzed in order to study in more detail the variation of the different phases present at the absorber layer. The correlations obtained (see Figure S1, Supporting Information) show that the variations in the intensity of the peaks in the 205–233 cm^{-1} range correlate with the intensity change of the OVC peak, while no correlations were found in the case of the 238–260 cm^{-1} range. This suggests, that the main changes in the 205–233 cm^{-1} range are also related to the change of the OVC phase content at the absorber surface, and for the following analyses the sum of the integrated intensities of the 150–165 cm^{-1} and 205–233 cm^{-1} spectral ranges was used as an indicator of the overall change attributed to the variations in the OVC phase content, thus defining $A_{OVC} = A_{150–165} + A_{205–233}$. On the other hand, the changes in the 238–260 cm^{-1} range have a more complex nature and are related to small changes in the chalcopyrite phase that will be discussed later on.

Despite the extremely small differences between the Raman spectra of the samples exposed to the different PDTs, the high quality spectra and high statistics of the data allowed to detect clear variations with the RbF source temperature of the relative integrated intensity of the OVC and CIGSe related peaks, that is, $A_{OVC}/(A_{OVC} + A_{CIGSe})$ (Figure 2b). Moreover, a clear tendency of the V_{oc} value of the solar cells that increases with the decreasing value of A_{OVC} was found (Figure 2c). The linear fitting of these data results in an R^2 value equal to 0.40, which, however, significantly improves (up to 0.63) when only the RbF-treated samples are taken into account (i.e., excluding the Rb-free sample). This suggests a rather abrupt change between samples with and without PDT and a more marked tendency within the RbF-treated samples related to the gradual change of the PDT conditions.

The influence of the PDT processes on highly defective OVC was previously studied by several groups.[26,47,48] However, the results are quite contradictory, which is mainly related to the dissents in the question whether this phase is required or not to achieve a positive effect of the PDT. The most systematic study was performed by Kodalle et al.,[26] where the decrease of the OVC phase is explained by its "partial consume" during the PDT process, that promotes the formation of the $RbInSe_2$ phase. However, this was clearly observed only in samples with medium or high amount of OVC (CGI < 0.8), where the PDT had mainly negative effects on the overall solar cell performance.[26] On the other hand, for CGI ≥ 0.8, which is the range typically employed for high efficiency devices, the PDT treatment usually leads to an improvement of device efficiency due to an improvement of the V_{oc} (see the Introduction section for further details), which also matches with the decrease of the OVC content, in accordance with the results of this work and refs. [26,47]. All this leads to two unclear points:

i) It is commonly agreed that the PDT causes Cu-depletion at the absorber surface[3,27,28,47,49–51] which should therefore increase the OVC phase. However, this effect is not experimentally observed.
ii) What is the actual mechanism for the decrease of the OVC phase?

According to recent studies, the reduction of the OVC phase is due to the formation of Alkali-In-Se phases at the surface of the absorber ($RbInSe_2$ in ref. [26] and K-In_2Se_3 in ref. [47]) through the substitution of Cu cations and/or Cu vacancies by alkalis. Some indirect evidences of the formation of this phase have been published recently.[50,52] However, the discussions about their presence are still open.[12] Moreover, according to device simulations, the presence of high band gap n-type $RbInSe_2$ phase at the interface between the absorber and buffer layers should have none or a negative effect on the FF of the CIGSe solar cells without influencing the V_{oc} and J_{sc}.[26,53] Thus, $RbInSe_2$, even when formed, is not expected to be the main driving force behind the beneficial influence of RbF-PDT in high efficiency CIGSe-based devices with low amount of OVC.

In order to deepen into the process that leads to the observed decrease of the OVC phase content at the CIGSe absorber surface, the Raman analysis was completed by measurements under a 785 nm excitation wavelength (**Figure 3**a). This excitation wavelength results in pre-resonant conditions for both the chalcopyrite and OVC phases and allows a better detection of the changes in their relative content.[32,44] Only ten representative cells for each RbF source temperature were analyzed under these conditions (see Experimental Section). All the spectra were deconvoluted to individual Lorentzian peaks (Figure 3b shows an example of the standard fitting routine) and their relative integrated intensity was correlated with the V_{oc} of the solar cells. From all the peaks obtained in the deconvolution, only the peaks at 246 and 250 cm^{-1} showed clear correlations with the V_{oc} values of the solar cells. The peak at 246 cm^{-1} shows an inverse correlation in intensity with the increasing V_{oc} (see Figure 3c) similar to that previously found between the V_{oc} and the relative integrated intensity of the OVC peaks (Figure 2c). In typical Ga-free OVC ($CuIn_3Se_5$) spectra measured under 785 nm excitation reported in the literature, the most intense peak representative of this compound is E/B symmetry peak at 235 cm^{-1}.[32,44] The peak observed in the present work at 246 cm^{-1} can be assigned to the same E/B-like symmetry peak, but shifted to higher wavenumbers due to the incorporation of Ga atoms in the $CuIn_3Se_5$ system, that results in the contraction of the interatomic bonds and, as consequence, in the increase of the phonon energy.[41] As such, it can be directly assumed that the changes in the relative integrated intensity of the peak at 246 cm^{-1} are related to the decrease of the OVC phase discussed above.

On the other hand, the peak at 250 cm^{-1} shows a direct correlation in intensity with the increasing V_{oc} (Figure 3d). This peak can be assigned to an E/B symmetry mode of the CIGSe phase and its variations can provide more information about changes in this phase. Here, two effects can be considered. The first one is related to possible increase of the Ga content. This would increase slightly the band gap of the absorber leading to a better coupling with the 785 nm excitation wavelength and, in turn, to a more pronounced pre-resonant effect that results in an increase of the intensity of the LO component of the E symmetry modes. However, this contradicts many authors who claim a small Ga-depletion at the absorber surface after the PDT process,[27,49,50,54] and, thus, this is not expected to be the case in our samples either. Moreover, comparing the RbF-treated cells with the Rb-free one, it can be clearly observed that the intensity of the peak at 250 cm^{-1} increases without an increase (in case of 520 °C) or even a decrease (in case of 490 °C) of the V_{oc}, which also indicates that changes in the relative intensity

ADVANCED SCIENCE NEWS
www.advancedsciencenews.com

ADVANCED ENERGY MATERIALS
www.advenergymat.de

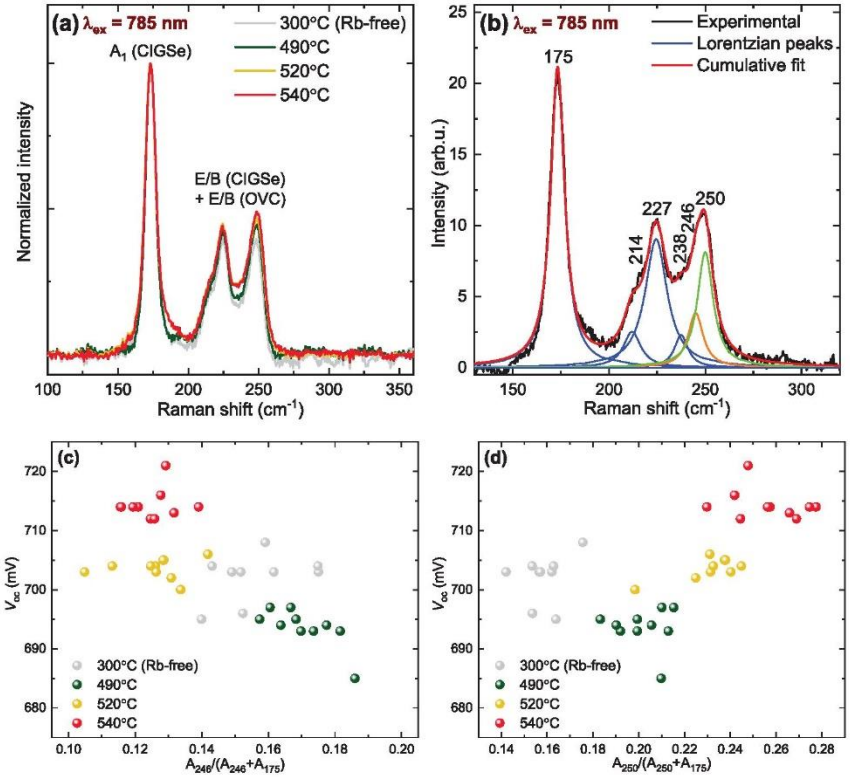

Figure 3. a) Average Raman scattering spectra of CIGSe-based devices exposed to different RbF-PDTs measured under 785 nm excitation wavelength. b) Example of standard routine for the fitting of Raman scattering spectra measured under 785 nm excitation wavelength. Dependence of V_{oc} of CIGSe solar cells exposed to different RbF-PDT on the relative integrated intensity of the peaks at c) 246 and d) 250 cm^{-1}.

of this peak cannot be directly associated to the Ga depletion at the absorber surface. The second effect that can influence the intensity of the peak at 250 cm^{-1} is related to a change in the chalcopyrite phase due to an increase of point defects. A recent publication reported the analysis of the Raman scattering spectra of the $CuInSe_2$ and CIGSe compounds under a 785 nm excitation wavelength, and showed an increase of the relative intensity of a peak in the high wavenumber range (indicated as overlapped E/B symmetry peaks of both CIGSe and OVC phases in Figure 3a of the present work).[44] This was explained by the formation of a so-called "defective chalcopyrite phase" that exists mainly under slightly Cu-poor conditions and differs from the standard stoichiometric chalcopyrite phase with a lower Cu content and higher amount of point defects (V_{Cu}, In_{Cu}, and Cu_{In}) in the chalcopyrite structure.[44] The existence of this phase also matches with recent results from the first-principle calculation of the density of state (DOS) of CIGSe absorbers with and without KF-PDT that were correlated with the experimentally derived hard X-ray photoelectron spectroscopy.[55] In the case of the PDT-free samples, the authors simply used the combination of DOS from standard stoichiometric $CuInSe_2$ and of $CuIn_5Se_8$ phases to fit the experimental results, where the latter represented the OVC at the absorber surface. However, after the KF-PDT, a more complex approach was proposed to better fit the experimental data in which a new "slightly Cu-rich $CuIn_3Se_5$" phase was combined with the $KInSe_2$ phase. Combining the results from the Raman scattering analysis[44] and the DOS fitting,[55] it can be concluded that there exists some distortion in the chalcopyrite phase due to the PDT process. This allows proposing a novel model that explains the positive effect of the RbF-PDT through the redistribution of point defects out of the OVC phase into the defective chalcopyrite phase at the absorber surface. Thus, as the OVC decreases the defective chalcopyrite phase increases. As such, the increase of the defective chalcopyrite leads to the enhancement of the V_{oc} of the solar cells. The exact mechanism of this beneficial influence is still not clear and requires a separate more detailed study, but it is clearly observed in ref. [44] and in the present study in devices fabricated following completely different technological routes which may imply that it is a universal feature of the CIGSe material. In summary, the results from the advanced Raman spectroscopy analysis show that the main effect of the RbF-PDT on the CIGSe absorbers is the intertwined decrease of the OVC phase and increase of the defective chalcopyrite phase.

The radiative properties of the CIGSe-based solar cells exposed to different PDTs were analyzed by means of PL spectroscopy. The typical PL spectra of samples exposed to the different

ADVANCED SCIENCE NEWS
www.advancedsciencenews.com

ADVANCED ENERGY MATERIALS
www.advenergymat.de

PDTs are presented in **Figure 4**a and represent a broad emission band which, in the case of Cu-poor chalcopyrite type compounds, is usually related to the close-to-fundamental radiative recombination edge: free-to-bound (with shallow acceptor level) or band-to-tail.[56–59] The increase of the PDT source temperature clearly resulted in an increase of the relative quantum yield (QY) (Figure 4b), as well as in the blue shift of the PL band maximum and in the increase of the full width at half maximum (FWHM) (see Figure S2, Supporting Information). The QY rise is explained by the increased amount of radiative recombination, which can be related to an increased concentration of beneficial point defects (the defects that contribute in radiative recombination) or to a decrease of the concentration of detrimental point defects (the defects that contribute in non-radiative recombination). Previously, the increase of the relative PL QY due to PDT was associated with the passivation of donor-like defects (V_{Se} and In_{Cu}) that contribute in the appearance of deep donor levels,[60–62] and correlates with the decrease of the concentration of detrimental defects mentioned above. However, the existence of the deep donor levels does not correlate with the high efficiency of the reference device in this work (close to 18%) which is higher than those reported in refs. [60,61]. Moreover, in these works the existence of deep donor levels was reflected in the PL spectra by the appearance of a band related to donor–acceptor recombination,[61] which is not the case in the present study. In this regard, it can be assumed that in the case of high efficiency devices, the PDT has a slightly different effect and that the increase of the QY is rather related to the increase of beneficial defects at the absorber surface. This assumption about surface defects, however, does not contradict the conclusions of ref. [12] where a PDT-related decrease of the detrimental defects in the bulk of the absorber was proposed based on different experimental and calculation approaches. The above mentioned surface beneficial defects are most probably related to copper vacancies (V_{Cu}) that contribute to radiative recombination and define the p-type conductivity of chalcopyrite-type compounds.[61] The increase of the beneficial defects also correlates with the aforementioned increase of the FWHM of the PL band after PDT, and is further confirmed by the correlation between the changes in the PL and Raman spectra: an inverse correlation of the relative PL QY is observed with the increasing relative intensity of the OVC Raman peaks (Figure S2c, Supporting Information), as well as a direct correlation of the QY with the increasing relative intensity of the defective chalcopyrite phase Raman peak (Figure S2d, Supporting Information). It is worth noticing that the observed PL band is related strictly to the emission of the CIGSe phase, while no PL emission of the OVC phase was observed in the analyzed samples which is usually blue-shifted.[63] Thus, the increase of the relative QY of the PL band with the increase of the temperature of the RbF source, that is explained by the increase of beneficial defects, is strongly connected to the changes occurring in the chalcopyrite phase, while changes in the OVC phase is a secondary associated effect. Finally, a clear direct correlation of the relative QY and the V_{oc} of the solar cells (Figure 4c) is also in accordance with such a model that explains the effect of PDT on the absorber surface. Similarly to the analysis performed above of the dependence of the V_{oc} on the OVC content, the linear fitting of the data in Figure 4c results in a higher R^2 value

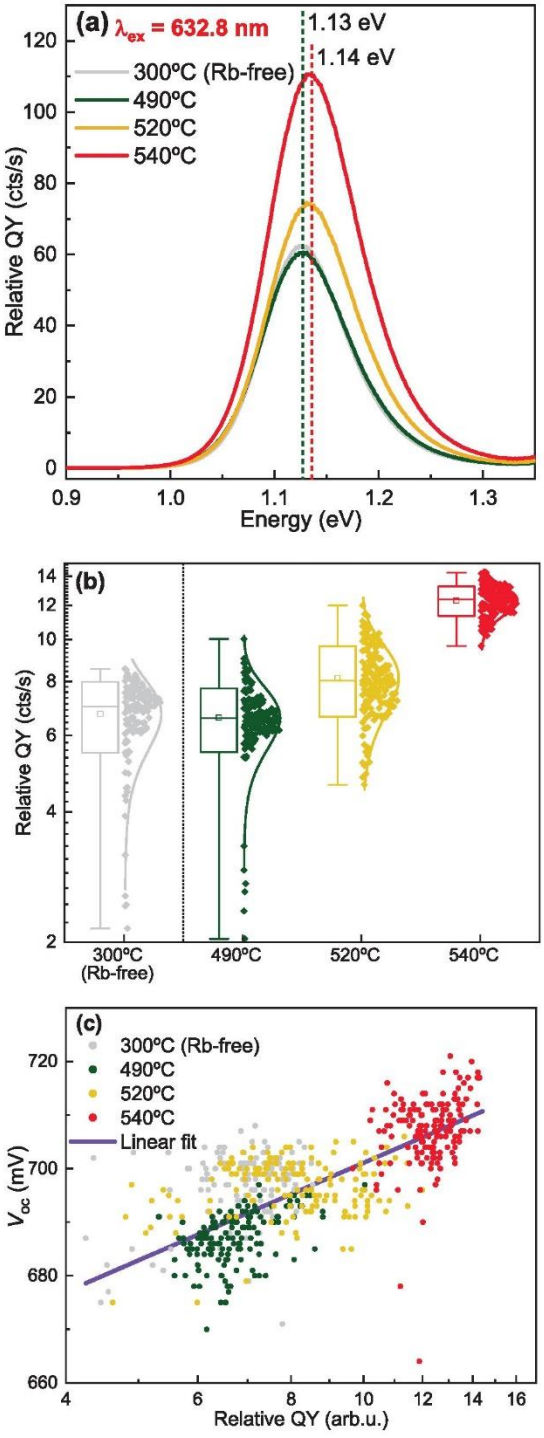

Figure 4. a) PL spectra of CIGSe-based devices exposed to different RbF-PDT temperature. b) Relative QY of the PL in function of the RbF-PDT source temperature. c) V_{oc} in function of the relative QY of the PL band.

ADVANCED SCIENCE NEWS
www.advancedsciencenews.com

ADVANCED ENERGY MATERIALS
www.advenergymat.de

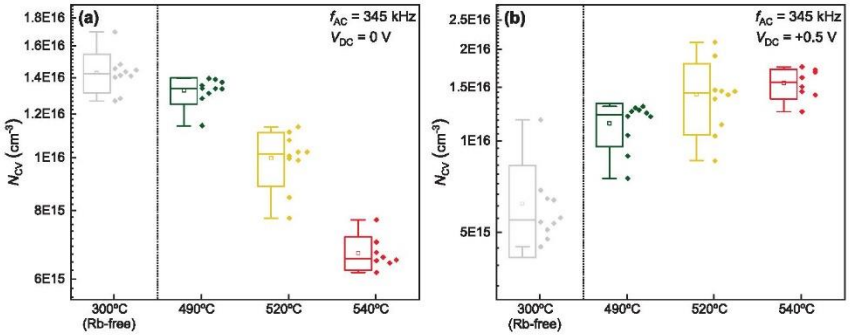

Figure 5. Variation of the apparent hole concentrations in cells exposed to different PDT measured by *C–V* a) without and b) with applied bias voltage.

when the Rb-free cells are not taken into account (0.63 vs 0.47, when all points are included in the fitting).

The variation in defect concentration was further investigated by studying the capacitance properties of representative solar cells from the different sets of samples exposed to different PDTs. Extracted from the capacitance–voltage (*C–V*) measurements, the values of the apparent hole concentration (see calculation details in the Supporting Information) showed a clear decrease with the increasing PDT source temperature (**Figure 5**a). These results, even if in accordance with several previously published results[19,64] and able to contribute to the observed decrease of the J_{sc} in the solar cells exposed to the PDT (Figure 1c), do not strictly support the previous conclusions regarding the increase of the beneficial defects (associated to an increase of V_{Cu}) since this would be expected to also increase the hole concentration. In order to define the origin of such inconsistence, the *C–V* measurements were performed by applying different bias voltages. The positive value of the bias voltage, which results in a decrease of the effective depletion width thus allowing to collect information closer to the absorber-buffer interface, shows an opposite dependence of the apparent hole concentration with the PDT source temperature (Figure 5b) compared to the non-bias voltage case (Figure 5a). This denotes that the effect of RbF-PDT in the hole concentration is different in the absorber bulk and at the surface. Further fine correlations of the apparent hole concentration at the absorber surface with the relative QY of the PL emission and with the amount of defective chalcopyrite phase found from Raman scattering analysis (Figure S3, Supporting Information) support the model proposed above based on the increase of defect concentration with the PDT that is originated by the redistribution of defects out of the OVC phase and, probably, also out from the absorber bulk to the chalcopyrite phase at the absorber surface.

The results and discussions presented here, that show the relatively high importance of surface modifications in the absorber layer due to PDT (mainly the absorber surface and close to surface layers are analyzed by the Raman and PL measurement conditions used, see Experimental Section), add new findings to the conclusions previously published in a review article co-authored by researchers from several groups.[12] In this review article the authors could not define any clear correlations between the absorber surface modifications and the beneficial effect of the alkali PDT, which has been overcome in the present work mainly thanks to the high statistics employed. Some publications by Kaufmann et al.[27,28] also show the importance of the absorber surface modifications, which, however, can have either a positive or negative effect on device performance, mainly depending on the CGI ratio. The analysis presented in this work does not exclude any beneficial effects of the alkali PDT on the CIGSe bulk, but allows concluding that the surface modifications, even if of high importance, are quite small when dealing with high efficiency devices, and their detection requires high statistics and complex data analysis. These are omitted by some of the researchers or are impossible to be implemented due to the complexity and time consuming nature of the applied characterization techniques. In this case, the spectroscopic approach proposed here, based on combined Raman and PL analysis, can be a key for the further development of research on complex semiconductor materials based on high statistics of experimental data.

2.3. Development of Process Monitoring Methodologies

From the analytical analysis of the data presented in the previous section, it is possible to propose a fast and non-destructive methodology for the monitoring of the RbF-PDT process and the prediction of the solar cell performance, specifically of the V_{oc}, at early stages of device manufacturing. In the following, the optimum V_{oc} is defined to be 705 mV and the objective of the process monitoring methodology is to be able to detect deviations of about ±2% from that value, with that V_{oc} range selected as the criterion for "high V_{oc}."

Regarding the analytical process monitoring methodology for V_{oc} prediction, it is proposed to use the high statistical analyses performed in this work with Raman and PL spectroscopies since they show a clear dependence of the V_{oc} with the analyzed parameters: relative amount of OVC phase (Raman) and relative QY (PL) (see Figures 2c,4c). However, both dependences present a relatively high dispersion that limits their independent use for the fine prediction of the V_{oc} (the R^2 value for the linear fitting of the results in both cases did not exceed 0.63). In order to overcome this limitation, the proposed process monitoring analytical methodology for predicting the solar cell V_{oc} is based on a more advanced correlation using the combination of both

ADVANCED SCIENCE NEWS
www.advancedsciencenews.com

ADVANCED ENERGY MATERIALS
www.advenergymat.de

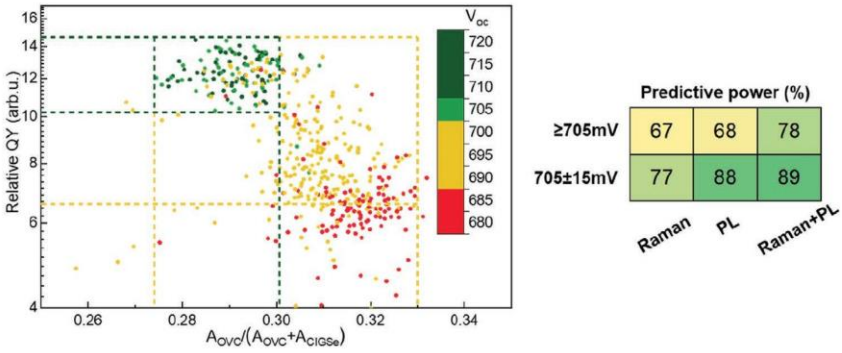

Figure 6. Left: 3D plot for the fine monitoring and prediction of V_{oc} value based on Raman and PL data. Right: comparison of the predictive power for two different criteria using separated Raman or PL data or a combination of both. See the main text for more detailed explanation.

parameters, the OVC content and the relative QY of the PL, in a 3D correlation graph (see **Figure 6**, third dimension for the V_{oc} represented by color). From the 3D correlation graph, two specific regions can be defined (green and orange dashed rectangles in Figure 6). The green rectangle contains mainly points associated to cells with $V_{oc} \geq 705$ mV while the orange rectangle contains cells with $V_{oc} = 705 \pm 15$ mV (i.e., inside the aforementioned ±2% limit of V_{oc}). For the orange rectangle, the statistical analysis yields a predictive power of the proposed combined methodology (when both Raman and PL data are taking into account) close to 89%, calculated as the percentage of the cells with targeted V_{oc} (705 ± 15 mV) that are inside the rectangle. In addition to this, the predictive power when using only Raman or PL data was also calculated and the obtained percentages are presented in the right panel of Figure 6. Here, it is seen that for the ±2% limit of V_{oc} (705 ± 15 mV), the use of only PL data provides a similar predictive power to the combined Raman and PL approach. However, for the stricter case of predicting cells with $V_{oc} \geq 705$ mV, the predictive power of employing the combined Raman and PL data is 10% (absolute) higher than when information of the separated spectroscopies is used. This may be due to the slightly different sensitivity of Raman and PL spectroscopies to changes at the absorber surface due to the PDT. Be as it may, the analysis presented here clearly demonstrates the potential of the combined Raman and PL approach for the fine prediction of the V_{oc} of the PV devices based solely on spectroscopic data.

Even though most of the evaluation steps of the analytical approach were performed in an automatic way (using the "spectrapepper" library),[65] some of them still require the implication of highly qualified trained specialists which imposes several limitations for applying this methodology for real in-line or on-line monitoring of a production process. To move further and to propose a more robust process monitoring methodology, the spectroscopic data obtained in the present study were used for the training and testing of a ML algorithm. As mentioned in Experimental Section, a principal component and linear discriminant analysis (PCLDA) algorithm was used as the most appropriate one for the defined task. The raw Raman and PL spectra were used as features for the algorithm, and two training instances were performed for two different target variables: i) PDT source temperature, and ii) V_{oc} of the final device.

The first selected target variable allows to establish a methodology to monitor the possible deviations of the process from the standard one. For this case, four classification groups were considered in accordance with the four RbF source temperatures used in manufacturing process of the samples employed in this work: 1) 300 °C (Rb-free); 2) 490 °C; 3) 520 °C; and 4) 540 °C. The application of the PCLDA algorithm allowed obtaining good testing scores for each group (**Figure 7**), showing their fine classification, and the possibility to use spectroscopic data for the monitoring of possible deviations in the PDT process.

For the second selected target variable, three main categories were defined for the analysis: 1) $V_{oc} \geq 705$ mV;

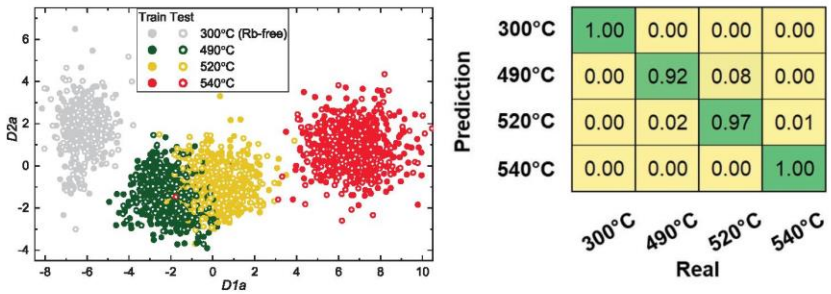

Figure 7. Results of the PCLDA algorithm using the PDT source temperature as target: (left) decision map and (right) confusion matrix for process prediction.

ADVANCED SCIENCE NEWS
www.advancedsciencenews.com

ADVANCED ENERGY MATERIALS
www.advenergymat.de

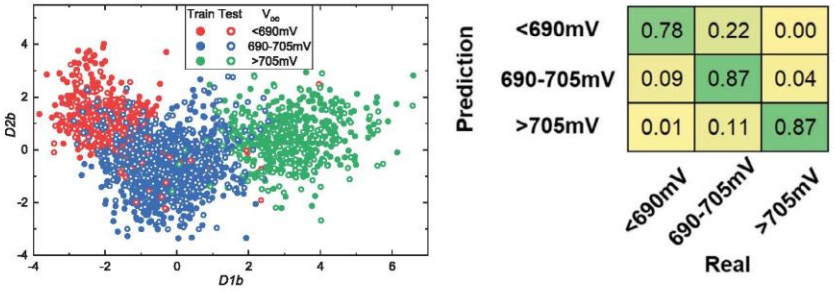

Figure 8. Results of the PCLDA algorithm using the V_{oc} as target: (left) decision map and (right) confusion matrix for V_{oc} prediction.

2) 705 > V_{oc} ≥ 690 mV; and 3) V_{oc} < 690 mV. These three categories correspond to the above defined limit of ±2% deviation from the optimal 705 mV (category 2 and 3) and deviations higher than 2% (category 1). The defined decision criteria (left panel in the **Figure 8**) allowed to classify with relatively high accuracy the test cells based only on their spectroscopic response; ≈95% of correct predictions for categories 2 and 3 (see right panel in Figure 8), that provides about ±2% maximum deviation from 705 mV. These results prove the possibility to combine spectroscopic techniques with ML algorithms for establishing a process monitoring methodology for a fine prediction of the V_{oc} value within a 2% error. However, the performance of the ML algorithm could be further improved employing a higher number of training data which would decrease the overfitting of the classified data and improve the test scores. Additionally, increasing the amount of applied characterization techniques would allow to add additional inputs for the ML algorithms (information about chemical composition, structural properties, etc.) which would certainly lead to the improvement of the predictive power of the methodology. Under these conditions, the main limitation for including further techniques in the ML algorithms in a certain application will be defined by its compatibility with process monitoring (high measurement speed, non-destructiveness, easy integration in industrial lines, etc.).

The applied PCLDA algorithm reduces the *n*-dimensional experimental spectroscopic data (n > 1500 for each cell, taking into account the information for each CCD pixel of the measured Raman and PL spectra) to a simpler 2D representation as shown in Figures 7,8. In most cases, this reduction of the dimensions leads to the loss of physical meaning of the discriminants calculated by the ML algorithm. However, the search of a possible physical meaning remains one of the key points in the application of self-learning ML algorithms for the development of materials science. From the two target variables used in the present study, the main interest lies at the discriminants that were obtained by the PCLDA algorithm from the classification of the V_{oc} (Figure 8). Correlating these two discriminants with different physical parameters discussed above it was found that the discriminant *D1b* correlates with both the relative OVC content and relative QY of the PL band (**Figure 9**a,b). This suggests that namely these two physical parameters extracted from the input data had a decisive effect on the ML results, and supports the monitoring methodology based on the analytical approach presented above (see Figure 6). The correlation of both parameters with the same *D1b* discriminant suggests that the variation of a similar property of the CIGSe-based solar cell lies behind the variations of these two parameters, in accordance with the conclusions made above in Section 2.2, and that is related to the formation of a defective chalcopyrite phase. Moreover, the continuous correlation of the V_{oc} and *D1b* was also established (Figure 9c), which allows not only to specify the classification group but to directly predict the numerical value of the V_{oc} for a solar cell. In comparison with directly employing the ML V_{oc} discretized group classification shown in Figure 8, this approach allows predicting the numerical value of the V_{oc} in a continuous range. However, it presents an overall lower predictive power (the R^2 value for the polynomial fitting in Figure 9c is equal to 0.68). Such a correlation with the *D1b* discriminant that is also assigned to the relative content of the defective chalcopyrite phase denotes the critical importance of changes in this phase at the absorber surface during the PDT process. However, it is worth noticing that for low V_{oc} values (<700 mV) there is a slightly higher deviation of the points from the proposed trend lines in Figure 9 (yellow dotted lines and solid black fitting line). The same feature can also be observed in the analytical analysis of some of the data (i.e., higher scattering of the points in Figures 4c,6 for V_{oc} < 700 mV values). This may suggest that there exist different mechanisms that lead to the improvement of the V_{oc} due to PDT for the very high and medium or low values of this parameter. As already mentioned above, the passivation effect of RbF-PDT of detrimental point defects was already established in the case of relatively low efficiency solar cells,[60,61] while an additional increase of the beneficial point defects is proposed in the present study. The combination of both mechanisms due to the RbF-PDT can occur in the cells with low or medium V_{oc}. Nevertheless, this hypothesis needs to be further evaluated to define a full picture of the effect of heavy alkalis on the surface and bulk of the chalcopyrite absorbers.

3. Conclusions

This work has presented the high potential of combining Raman and PL spectroscopies for the analysis of the effect of RbF-PDT on a high amount of high efficiency CIGSe solar cells which has allowed to reach to two important results. First, that

ADVANCED SCIENCE NEWS
www.advancedsciencenews.com

ADVANCED ENERGY MATERIALS
www.advenergymat.de

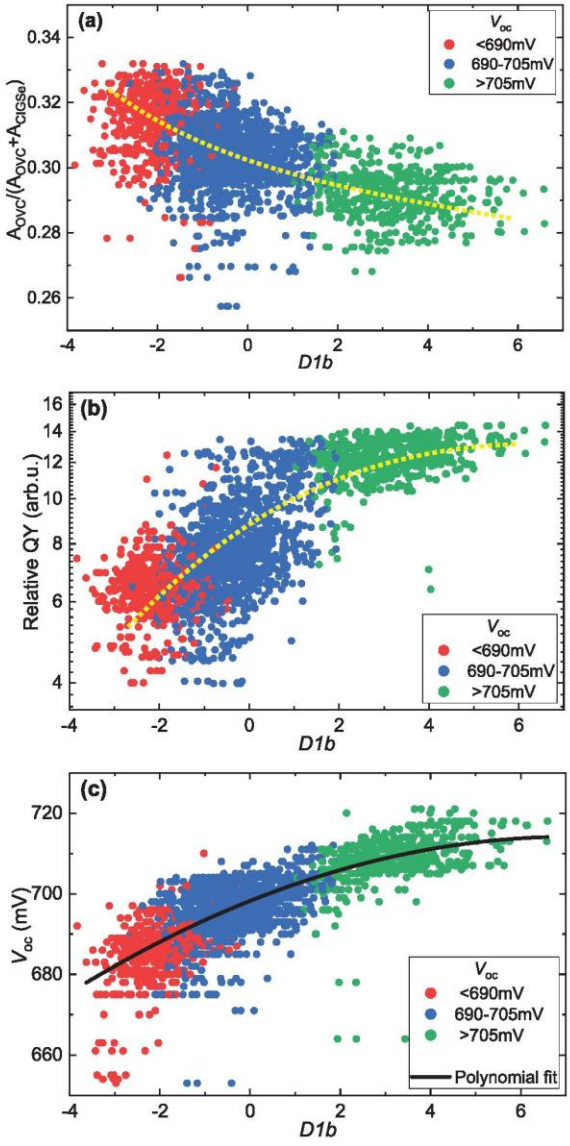

Figure 9. Correlation of the calculated *D1b* PCLDA discriminant with a) relative OVC content calculated from the Raman scattering analysis and with b) relative QY of the PL band. c) Continuous correlation of the V_{oc} with the *D1b* discriminant. The dotted yellow lines are only intended as a visual guide for the reader.

the surface modifications that occur in the CIGSe absorber layer of the high efficiency devices are of great relevance. This conclusion was made based on the advanced analysis of the spectroscopic data obtained under different measurement conditions combined with the electronic and optoelectronic information of the solar cells. As a result, an innovative model has been proposed in which the main driving force behind the improvement of the device performance due to RbF-PDT is related to the redistribution of defects between the OVC and chalcopyrite phases that leads to the formation of the so-called "defective chalcopyrite phase." All the applied techniques (Raman, PL, and *C*–*V*) support the observed effect of the defect redistribution at the absorber surface as result of PDT process, showing the importance of the formation of the defective chalcopyrite phase. However, the exact mechanism of its influence on the optoelectronic properties, mainly on the V_{oc}, of the solar cells still has to be defined and remains as a challenging tasks for the future studies of CIGSe-based devices. The second result of the performed study is related to the development of industry-compatible process monitoring methodologies for the assessment of the RbF-PDT process and prediction of the V_{oc} of the final devices. Both analytical and ML approaches were established for this task, resulting in process monitoring methodologies that allow to predict the V_{oc} with an error as small as ±2% and an efficacy ≈95%, and to have a precise control (with the test score ≥ 92%) of the PDT temperature. These results show the high potential of the combined Raman and PL spectroscopic techniques and advanced analysis to be used both for fundamental research and for the fast, non-destructive, and in situ monitoring of the CIGSe-based thin film solar cells production process. This represents a very powerful tool for the future development of this promising and environmentally-sustainable PV technology and for a more efficient and precise industrial manufacturing.

4. Experimental Section

$Cu(In,Ga)Se_2$ absorbers were deposited on Mo-coated soda-lime glass in a production-like in-line co-evaporation system for substrate sizes up to 30×30 cm^2 using a multi-stage process. Details of the process can be found in ref. [29]. All the samples were prepared in the same deposition process with different conditions only for the in situ alkali PDT realized by varying the RbF evaporation source temperature for different carriers in the continuous substrate flow of the inline-system with steps at 300 (relating to no RbF-PDT), 490, 520, and 540 °C.[66] As a very rough rule of thumb, it could be estimated that the difference in vapor pressure due to the different RbF source temperatures results in a twice thicker RbF layer for each temperature step (i.e., from 490 to 520 °C and from 520 to 540 °C).

The solar cells were finalized by a 50 nm thick chemical bath deposited CdS buffer layer, 35 nm thick i-ZnO as high resistive layer, 200 nm thick ZnO:Al as transparent front contact, and Ni/Al/Ni grids with ≈2.5 µm thickness. X-ray fluorescence measurements determined the chemical composition of the absorber with a [Ga]/([Ga] + [In]) ratio of about 0.30, a [Cu]/([Ga] + [In]) ratio of ≈0.80 (both with ≈0.01 error related to the uncertainty of the measurement system) and a thickness of ≈2.3 µm for all samples.

Each substrate was mechanically scribed into 1.0×0.5 cm^2 individual solar cells and no specific selection of the cells was performed for their analysis (i.e., all the different individual cells were employed for this study). Current–voltage (*I*–*V*) curves of the individual cells were measured with a WACOM AM1.5G solar simulator in four-point geometry at standard testing conditions and a silicon reference cell for calibration.

Raman spectroscopy and PL were employed to analyze the structural, compositional, and radiative properties of the CIGSe absorber. A special optical probe was developed at IREC to measure the Raman scattering and the PL spectra at the same point quasi-simultaneously using a large area spot (≈70 μm^2) in order to characterize a representative region of the CIGSe layer. The probe was coupled to high resolution FHR640

ADVANCED SCIENCE NEWS
www.advancedsciencenews.com

ADVANCED ENERGY MATERIALS
www.advenergymat.de

Horiba Jobin Yvon spectrometer and a CCD detector cooled to −130 °C for Raman spectra acquisition in back scattering configuration, and to a Sol 1.7 spectrometer from B&WTek with an InGaAs detector for acquiring the PL data in near-backscattering configuration. The simultaneous Raman and PL characterization was carried out under a 638 nm (solid state laser) excitation wavelength. Additionally, a solid state laser of 785 nm excitation wavelength (leading to quasi-resonant conditions with CIGSe) was used in order to complete the Raman characterization of the absorber layer. It was important to note that the strong PL signal arising from the samples under 785 nm excitation wavelength required special conditions and high acquisition times to obtain high quality Raman spectra preventing to measure the spectra of all the cells studied in this work in a reasonable time. Under this limitation, only ten representative cells for each RbF source temperature were analyzed with these excitation conditions. Laser power densities lower than 150 W cm^{-2} were selected for both excitation wavelengths to prevent any thermal effect on the samples. The Raman shift was calibrated using a monocrystalline Si reference by imposing the position of its main peak to 520 cm^{-1}, and the baseline was subtracted in the spectra prior to the analytical analysis using the "bspbaseline" function from the spectrapepper library.[65] It should be noted that for both 638 and 785 nm excitation wavelengths, the photon energies were higher than the band gap of the CIGSe absorber (≈1.2 eV, taking into account the measured amount of Ga)[67] leading to a high absorption coefficient and a low penetration depth providing information of mainly the surface (≈50 nm—expected penetration depth of 638 nm laser, taking into account the absorption coefficient of CIGSe)[68] and the subsurface (≈100 nm—expected penetration depth of 785 nm laser, taking into account the absorption coefficient of CIGSe)[68] region of the absorber. Thus, the Raman results presented in this work showed mainly the influence of RbF-PDT on the CIGSe absorber surface. Regarding PL, it was worth noticing that the specific conditions of the measurements and the applied system did not allow to directly measure the absolute QY of the emission band, but they allowed to define the relative QY, which showed the relative change from one measured point/sample to another. All the spectroscopic measurements were performed in four points for each cell, and the resulting spectra were averaged in one Raman and one PL spectrum per cell. These averaged spectra were used for the analytical analysis approach.

C–V profiling was performed with a Keysight E4990A Impedance Analyzer in the dark at room temperature. A 50 mV and 345 kHz AC signal was employed in accordance with previously reported *C–V* studies of CIGSe-based solar cells treated with heavy alkali PDT.[19,64]

A ML driven methodology, based on cascaded PCLDA algorithms, was employed to define a robust and easy-to-implement methodology for the monitoring of the PDT process and the prediction of solar cell performance. Both algorithms performed dimension reductions capable of translating high-dimensionality problems into a bi-dimensional one. Their combination provided several benefits, namely the detection of the most important dimensions for the data as a whole and then for each classification group, which provided improved classification results. More in detail, the PCLDA algorithm was selected since it allowed to reduce dimensionality not by deleting features but rather by performing linear combinations. In other words, this technique did not perform feature selection and preserves more of the information when the dimensionality was reduced, focusing more on feature extraction. It is worth mentioning that other dimension reduction algorithms could be also applied for the analysis performed in this work, and this could be a matter of future considerable investigations. In order to test and implement the ML-based PCLDA algorithms, the Python programming environment with the Scikit-Learn[69] and spectrapepper[65] (developed by IREC for spectral data conditioning and ML support) libraries were employed. As specified above, for each cell Raman and PL spectra were measured simultaneously under the 638 nm excitation conditions in four different points. All these individual spectra (4960 Raman and PL spectra in total) were used as input features, and they were randomly divided in 70% for training and 30% for testing. The PCLDA interface was done by, first, training PCA to reduce dimensionality to 400 and then LDA to translate these 400 dimensions into a 2D space. The test scores were calculated for each category separately by calculating the amount of correct predictions inside each category. This allowed to better understand the possible dependence of the predictive power of the PCLDA algorithm on the value of the V_{oc} and to estimate a possible methodology saturation. The fact that four points per cell were measured allowed to increase the amount of input data (in this case, no cell averaging was made) allowing to minimize the overfitting effect. Moreover, the fact of using raw Raman and PL spectra as input data allowed to consider that each pixel of the two detectors (1024 pixel in Raman CCD and 512 pixels in PL InGaAs detector) was a separate dimension, resulting in 1536-dimension data that were reduced to 2-dimensions by the PCLDA algorithm.

Supporting Information

Supporting Information is available from the Wiley Online Library or from the author.

Acknowledgements

This work is part of the R+D+I In4CIS projects Ref. PCI 2019-111837-2 (funded by MCIN/AEI/10.13039/5011000110033) and Ref. 03EE1020A (funded by the Federal Ministry for Economic Affairs and Energy), co-funded by the European Union. Project In4CIS was supported under the umbrella of SOLAR-ERA.NET Cofund 2 by "Agencia Estatal de Investigacion" (AEI, Spain), CDTI (Spain) and Projektträger Jülich (PtJ, Germany). SOLAR-ERA.NET was supported by the European Commission within the EU Framework Programme for Research and Innovation HORIZON 2020 (Cofund 2 ERA-NET Action, N° 786483). This work has received funding from the European Union's Horizon 2020 Fast Track to Innovation Programme under grant agreement no. 870004 (Solar-Win project). Authors from IREC belong to the SEMS (Solar Energy Materials and Systems) Consolidated Research Group of the "Generalitat de Catalunya" (Ref. 2017 SGR 862). M.G. acknowledges the financial support from Spanish Ministry of Science, Innovation and Universities within the Juan de la Cierva (IJC2018-038199-I) program.

Conflict of Interest

The authors declare no conflict of interest.

Data Availability Statement

The data that support the findings of this study are available from the corresponding author upon reasonable request.

Keywords

combinatorial analysis, $Cu(In,Ga)Se_2$ solar cells, machine learning, process monitoring, RbF treatments

Received: October 11, 2021
Revised: December 20, 2021
Published online: January 9, 2022

[1] M. Nakamura, K. Yamaguchi, Y. Kimoto, Y. Yasaki, T. Kato, H. Sugimoto, *IEEE J. Photovoltaics* **2019**, *9*, 1863.

[2] T. Feurer, P. Reinhard, E. Avancini, B. Bissig, J. Löckinger, P. Fuchs, R. Carron, T. P. Weiss, J. Perrenoud, S. Stutterheim, S. Buecheler, A. N. Tiwari, *Prog. Photovolt.* **2017**, *25*, 645.
[3] A. Chirilă, P. Reinhard, F. Pianezzi, P. Bloesch, A. R. Uhl, C. Fella, L. Kranz, D. Keller, C. Gretener, H. Hagendorfer, D. Jaeger, R. Erni, S. Nishiwaki, S. Buecheler, A. N. Tiwari, *Nat. Mater.* **2013**, *12*, 1107.
[4] P. Jackson, D. Hariskos, R. Wuerz, W. Wischmann, M. Powalla, *Phys. Status Solidi RRL* **2014**, *8*, 219.
[5] P. Jackson, R. Wuerz, D. Hariskos, E. Lotter, W. Witte, M. Powalla, *Phys. Status Solidi RRL* **2016**, *10*, 583.
[6] M. Edoff, T. Jarmar, N. S. Nilsson, E. Wallin, D. Hogstrom, O. Stolt, O. Lundberg, W. Shafarman, L. Stolt, *IEEE J. Photovoltaics* **2017**, *7*, 1789.
[7] L. M. Mansfield, R. Noufi, C. P. Muzzillo, C. DeHart, K. Bowers, B. To, J. W. Pankow, R. C. Reedy, K. Ramanathan, *IEEE J. Photovoltaics* **2014**, *4*, 1650.
[8] S. Zahedi-Azad, M. Maiberg, R. Clausing, R. Scheer, *Thin Solid Films* **2019**, *669*, 629.
[9] T. Kato, *Jpn. J. Appl. Phys.* **2017**, *56*, 04CA02.
[10] T. Feurer, F. Fu, T. P. Weiss, E. Avancini, J. Löckinger, S. Buecheler, A. N. Tiwari, *Thin Solid Films* **2019**, *670*, 34.
[11] T. Kato, J.-L. Wu, Y. Hirai, H. Sugimoto, V. Bermudez, *IEEE J. Photovoltaics* **2019**, *9*, 325.
[12] S. Siebentritt, E. Avancini, M. Bär, J. Bombsch, E. Bourgeois, S. Buecheler, R. Carron, C. Castro, S. Duguay, R. Félix, E. Handick, D. Hariskos, V. Havu, P. Jackson, H. Komsa, T. Kunze, M. Malitckaya, R. Menozzi, M. Nesladek, N. Nicoara, M. Puska, M. Raghuwanshi, P. Pareige, S. Sadewasser, G. Sozzi, A. N. Tiwari, S. Ueda, A. Vilalta-Clemente, T. P. Weiss, F. Werner, R. G. Wilks, W. Witte, M. H. Wolter, *Adv. Energy Mater.* **2020**, *10*, 1903752.
[13] P. Jackson, D. Hariskos, R. Wuerz, O. Kiowski, A. Bauer, T. M. Friedlmeier, M. Powalla, *Phys. Status Solidi RRL* **2015**, *9*, 28.
[14] T. Kodalle, L. Choubrac, L. Arzel, R. Schlatmann, N. Barreau, C. A. Kaufmann, *Sol. Energy Mater. Sol. Cells* **2019**, *200*, 109997.
[15] P. Pistor, D. Greiner, C. A. Kaufmann, S. Brunken, M. Gorgoi, A. Steigert, W. Calvet, I. Lauermann, R. Klenk, T. Unold, M.-C. Lux-Steiner, *Appl. Phys. Lett.* **2014**, *105*, 063901.
[16] T. P. Weiss, S. Nishiwaki, B. Bissig, R. Carron, E. Avancini, J. Löckinger, S. Buecheler, A. N. Tiwari, *Adv. Mater. Interfaces* **2018**, *5*, 1701007.
[17] D. Rudmann, D. Brémaud, H. Zogg, A. N. Tiwari, *J. Appl. Phys.* **2005**, *97*, 084903.
[18] A. Rockett, *Thin Solid Films* **2005**, *480*, 2.
[19] F. Pianezzi, P. Reinhard, A. Chirilă, B. Bissig, S. Nishiwaki, S. Buecheler, A. N. Tiwari, *Phys. Chem. Chem. Phys.* **2014**, *16*, 8843.
[20] D. Braunger, D. Hariskos, G. Bilger, U. Rau, H. W. Schock, *Thin Solid Films* **2000**, *361*, 161.
[21] D. Rudmann, D. Brémaud, A. F. da Cunha, G. Bilger, A. Strohm, M. Kaelin, H. Zogg, A. N. Tiwari, *Thin Solid Films* **2005**, *480*, 55.
[22] W. Li, X. Yan, A. G. Aberle, S. Venkataraj, *Sci. Rep.* **2019**, *9*, 2637.
[23] D. Hariskos, M. Powalla, *J. Mater. Res.* **2018**, *33*, 239.
[24] J. M. Raguse, C. P. Muzzillo, J. R. Sites, L. Mansfield, *IEEE J. Photovoltaics* **2017**, *7*, 303.
[25] R. Kormath Madam Raghupathy, T. D. Kühne, G. Henkelman, H. Mirhosseini, *Adv. Theory Simul.* **2019**, *2*, 1900036.
[26] T. Kodalle, T. Bertram, R. Schlatmann, C. A. Kaufmann, *IEEE J. Photovoltaics* **2019**, *9*, 1839.
[27] T. Kodalle, M. D. Heinemann, D. Greiner, H. A. Yetkin, M. Klupsch, C. Li, P. A. van Aken, I. Lauermann, R. Schlatmann, C. A. Kaufmann, *Sol. RRL* **2018**, *2*, 1800156.
[28] N. Maticiuc, T. Kodalle, B. Ümsür, T. Bertram, R. Wenisch, Y. Wang, I. Majumdar, H. A. Yetkin, D. Abou-Ras, N. Schäfer, C. A. Kaufmann, R. Schlatmann, I. Lauermann, *Sol. Energy Mater. Sol. Cells* **2021**, *226*, 111071.
[29] A. Kanevce, S. Paetel, D. Hariskos, T. Magorian Friedlmeier, *EPJ Photovoltaics* **2020**, *11*, 8.
[30] M. Powalla, S. Paetel, D. Hariskos, R. Wuerz, F. Kessler, P. Lechner, W. Wischmann, T. M. Friedlmeier, *Engineering* **2017**, *3*, 445.
[31] M. Park, S. Ahn, J. H. Yun, J. Gwak, A. Cho, S. Ahn, K. Shin, D. Nam, H. Cheong, K. Yoon, *J. Alloys Compd.* **2012**, *513*, 68.
[32] C. Insignares-Cuello, C. Broussillou, V. Bermúdez, E. Saucedo, A. Pérez-Rodríguez, V. Izquierdo-Roca, *Appl. Phys. Lett.* **2014**, *105*, 021905.
[33] R. Scheer, A. Pérez-Rodríguez, W. K. Metzger, *Prog. Photovolt.* **2010**, *18*, 467.
[34] I.-H. Choi, *Thin Solid Films* **2011**, *519*, 4390.
[35] F. Oliva, S. Kretzschmar, D. Colombara, S. Tombolato, C. M. Ruiz, A. Redinger, E. Saucedo, C. Broussillou, T. G. de Monsabert, T. Unold, P. J. Dale, V. Izquierdo-Roca, A. Pérez-Rodríguez, *Sol. Energy Mater. Sol. Cells* **2016**, *158*, 168.
[36] W. Witte, R. Kniese, M. Powalla, *Thin Solid Films* **2008**, *517*, 867.
[37] C. Insignares-Cuello, V. Izquierdo-Roca, J. López-García, L. Calvo-Barrio, E. Saucedo, S. Kretzschmar, T. Unold, C. Broussillou, T. Goislard de Monsabert, V. Bermudez, A. Pérez-Rodríguez, *Sol. Energy* **2014**, *103*, 89.
[38] W. Witte, R. Kniese, A. Eicke, M. Powalla, in *Proc. Fourth IEEE World Conf. Photovoltaic Energy Conversion*, IEEE, Piscataway **2006**, p. 553.
[39] X. Fontané, V. Izquierdo-Roca, L. Calvo-Barrio, A. Pérez-Rodríguez, J. R. Morante, D. Guettler, A. Eicke, A. N. Tiwari, *Appl. Phys. Lett.* **2009**, *95*, 261912.
[40] C.-M. Xu, X.-L. Xu, J. Xu, X.-J. Yang, J. Zuo, N. Kong, W.-H. Huang, H.-T. Liu, *Semicond. Sci. Technol.* **2004**, *19*, 1201.
[41] C.-M. Xu, W.-H. Huang, J. Xu, X.-J. Yang, J. Zuo, X.-L. Xu, H.-T. Liu, *J. Phys.: Condens. Matter* **2004**, *16*, 4149.
[42] C. Rincón, S. M. Wasim, G. Marín, J. M. Delgado, J. R. Huntzinger, A. Zwick, J. Galibert, *Appl. Phys. Lett.* **1998**, *73*, 441.
[43] K. Timmo, M. Kauk-Kuusik, M. Pilvet, M. Altosaar, M. Grossberg, M. Danilson, R. Kaupmees, V. Mikli, J. Raudoja, T. Varema, *Sol. Energy* **2018**, *176*, 648.
[44] M. Guc, E. Bailo, R. Fonoll-Rubio, F. Atlan, M. Placidi, P. Jackson, D. Hariskos, X. Alcobe, P. Pistor, I. Becerril-Romero, A. Perez-Rodriguez, F. Ramos, V. Izquierdo-Roca, *Acta Mater.* **2021**, *223*, 117507.
[45] D. Schmid, M. Ruckh, F. Grunwald, H. W. Schock, *J. Appl. Phys.* **1993**, *73*, 2902.
[46] X. Fontané, V. Izquierdo-Roca, L. Calvo-Barrio, J. Álvarez-Garcia, A. Pérez-Rodríguez, J. R. Morante, W. Witte, *Appl. Phys. Lett.* **2009**, *95*, 121907.
[47] T. Lepetit, S. Harel, L. Arzel, G. Ouvrard, N. Barreau, *Prog. Photovolt.* **2017**, *25*, 1068.
[48] S. Ishizuka, P. J. Fons, *Phys. Rev. Appl.* **2021**, *15*, 054005.
[49] E. Avancini, R. Carron, T. P. Weiss, C. Andres, M. Bürki, C. Schreiner, R. Figi, Y. E. Romanyuk, S. Buecheler, A. N. Tiwari, *Chem. Mater.* **2017**, *29*, 9695.
[50] N. Maticiuc, T. Kodalle, J. Lauche, R. Wenisch, T. Bertram, C. A. Kaufmann, I. Lauermann, *Thin Solid Films* **2018**, *665*, 143.
[51] P. Reinhard, B. Bissig, F. Pianezzi, E. Avancini, H. Hagendorfer, D. Keller, P. Fuchs, M. Döbeli, C. Vigo, P. Crivelli, S. Nishiwaki, S. Buecheler, A. N. Tiwari, *Chem. Mater.* **2015**, *27*, 5755.
[52] S. Ishizuka, N. Taguchi, J. Nishinaga, Y. Kamikawa, S. Tanaka, H. Shibata, *J. Phys. Chem. C* **2018**, *122*, 3809.
[53] T. Kodalle, H. A. Yetkin, A. V. Tovar, T. Bertram, R. Klenk, R. Schlatmann, C. A. Kaufmann, *IEEE J. Photovoltaics* **2021**, *11*, 232.
[54] P. Schöppe, S. Schönherr, P. Jackson, R. Wuerz, W. Wisniewski, M. Ritzer, M. Zapf, A. Johannes, C. S. Schnohr, C. Ronning, *ACS Appl. Mater. Interfaces* **2018**, *10*, 40592.

[55] M. Malitckaya, T. Kunze, H.-P. Komsa, V. Havu, E. Handick, R. G. Wilks, M. Bär, M. J. Puska, *ACS Appl. Mater. Interfaces* **2019**, *11*, 3024.
[56] I. Dirnstorfer, M. Wagner, D. M. Hofmann, M. D. Lampert, F. Karg, B. K. Meyer, *Phys. Status Solidi* **1998**, *168*, 163.
[57] J. Krustok, H. Collan, M. Yakushev, K. Hjelt, *Phys. Scr.* **1999**, *T79*, 179.
[58] E. Skidchenko, M. V. Yakushev, L. Spasevski, P. R. Edwards, M. A. Sulimov, R. W. Martin, *Phys. Solid State* **2019**, *61*, 918.
[59] O. M. Borodavchenko, V. D. Zhivulko, A. V. Mudryí, M. V. Yakushev, I. A. Mogilnikov, *Semiconductors* **2021**, *55*, 168.
[60] S. Ishizuka, N. Taguchi, P. J. Fons, *J. Phys. Chem. C* **2019**, *123*, 17757.
[61] H. Lee, Y. Jang, S.-W. Nam, C. Jung, P.-P. Choi, J. Gwak, J. H. Yun, K. Kim, B. Shin, *ACS Appl. Mater. Interfaces* **2019**, *11*, 35653.
[62] O. Nwakanma, S. Velumani, A. Morales-Acevedo, *Mater. Today Energy* **2021**, *20*, 100617.
[63] R. Kimura, T. Nakada, P. Fons, A. Yamada, S. Niki, T. Matsuzawa, K. Takahashi, A. Kunioka, *Sol. Energy Mater. Sol. Cells* **2001**, *67*, 289.
[64] S. Ishizuka, H. Shibata, J. Nishinaga, Y. Kamikawa, P. J. Fons, *Appl. Phys. Lett.* **2018**, *113*, 063901.
[65] E. Grau-Luque, F. Atlan, I. Becerril-Romero, A. Perez-Rodriguez, M. Guc, V. Izquierdo-Roca, *J. Open Source Softw.* **2021**, *6*, 3781.
[66] K. A. Sense, R. W. Stone, *J. Phys. Chem.* **1958**, *62*, 1411.
[67] Su-Huai Wei, S. B. Zhang, Alex Zunger, *Appl. Phys. Lett.* **1998**, *72*, 3199.
[68] S. Levcenko, G. Gurieva, E. J. Friedrich, J. Trigo, J. Ramiro, J. M. Merino, E. Arushanov, M. León, *Moldavian Journal of the Physical Science* **2010**, *9*, 148.
[69] F. Pedregosa, G. Varoquax, A. Gramfort, V. Michel, B. Thirion, O. Grisel, M. Blondel, P. Prettenhofer, R. Weiss, V. Dubourg, J. Vanderplas, A. Passos, D. Cournapeu, *J. Mach. Learn. Res.* **2011**, *12*, 2825.

ADVANCED ENERGY MATERIALS

Supporting Information

for *Adv. Energy Mater.,* DOI: 10.1002/aenm.202103163

Insights into the Effects of RbF-Post-Deposition Treatments on the Absorber Surface of High Efficiency Cu(In,Ga)Se_2 Solar Cells and Development of Analytical and Machine Learning Process Monitoring Methodologies Based on Combinatorial Analysis

Robert Fonoll-Rubio, Stefan Paetel, Enric Grau-Luque, Ignacio Becerril-Romero, Rafael Mayer, Alejandro Pérez-Rodríguez, Maxim Guc, and Victor Izquierdo-Roca**

WILEY-VCH

Supporting Information

Insights into the Effects of RbF-PDT on the Absorber Surface of High Efficiency CIGSe Solar Cells and Development of Analytical and Machine Learning Process Monitoring Methodologies Based on Combinatorial Analysis

Robert Fonoll-Rubio, Stefan Paetel, Enric Grau-Luque, Ignacio Becerril-Romero, Rafael Mayer, Alejandro Pérez-Rodríguez, Maxim Guc, Victor Izquierdo-Roca**

R. Fonoll-Rubio, E. Grau-Luque, I. Becerril-Romero, R. Mayer, A. Pérez-Rodríguez, M. Guc, V. Izquierdo-Roca
Catalonia Institute for Energy Research (IREC), Jardins de les Dones de Negre 1, 08930 Sant Adrià de Besòs-Barcelona, Spain
E-mail: vizquierdo@irec.cat, mguc@irec.cat

S. Paetel
Zentrum für Sonnenenergie- und Wasserstoff-Forschung, Baden-Württemberg (ZSW), Meitnerstr. 1, 70563 Stuttgart, Germany

A. Pérez-Rodríguez
Catalonia Institute for Energy Research (IREC), Jardins de les Dones de Negre 1, 08930 Sant Adrià de Besòs-Barcelona, Spain
Departament d'Enginyeria Electronica i Biomedica, IN2UB, Universitat de Barcelona, C/ Marti i Franques 1, 08028 Barcelona, Spain

Table S1. Optoelectronic parameters of the solar cells analyzed in the present study. It should be noted that the only parameter varied from sample to sample was the PDT source temperature indicated on the top of the table for each set. Further details on the device preparation process are presented in the *Experimental Details and Methods* section of the main text.

Nr.	PDT source T = 300 °C (Rb-free)				PDT source T = 490 °C				PDT source T = 520 °C				PDT source T = 540 °C			
	PCE (%)	FF (%)	Jsc (mA/cm²)	Voc (mV)	PCE (%)	FF (%)	Jsc (mA/cm²)	Voc (mV)	PCE (%)	FF (%)	Jsc (mA/cm²)	Voc (mV)	PCE (%)	FF (%)	Jsc (mA/cm²)	Voc (mV)
1	17.07	74.2	32.49	708	15.84	70.4	32.32	697	17.06	75.2	32.12	706	18.05	78.2	32.02	721
2	17.42	75.2	32.77	707	16.77	73.9	32.56	697	16.97	75	32.1	705	17.13	76.4	31.15	720
3	17.45	75.4	32.81	705	16.94	74.6	32.55	697	17.47	77.1	32.14	705	17.86	77.7	32.02	718
4	17.51	75.8	32.73	705	14.94	67	32.1	695	15.64	68.7	32.3	704	17.30	78.1	30.86	718
5	17.39	75.7	32.59	705	16.33	72.1	32.57	695	17.51	77.6	32.07	704	16.73	74.2	31.41	718
6	17.22	75.2	32.49	704	16.73	74.6	32.25	695	17.75	78.6	32.08	704	17.43	77.7	31.29	717
7	17.37	76.3	32.37	704	16.76	75.1	32.11	695	17.63	78.5	31.9	704	17.79	78.1	31.79	717
8	17.19	75.3	32.44	704	15.53	69.8	32.02	694	17.24	75.5	32.42	704	17.85	78.7	31.63	717
9	16.55	71.8	32.72	704	16.46	73.2	32.41	694	17.64	78.3	32.05	703	17.41	76.8	31.64	717
10	17.90	77.2	32.91	704	16.09	71.9	32.24	694	17.85	78.5	32.34	703	18.15	78.7	32.19	716
11	16.70	72.8	32.61	704	16.74	74.4	32.43	694	16.60	73.2	32.24	703	17.31	78	31.03	716
12	16.78	72.9	32.73	703	16.79	74.9	32.28	694	17.49	77	32.31	703	17.40	77.2	31.52	715
13	16.64	73.1	32.38	703	16.33	73.1	32.27	693	15.31	67.3	32.33	703	17.20	76	31.63	715
14	17.05	75	32.33	703	16.83	74.7	32.5	693	16.74	74.3	32.08	702	18.14	78.5	32.36	714
15	16.84	73.5	32.56	703	16.66	74.3	32.36	693	17.72	78.7	32.09	702	17.78	79.1	31.5	714
16	17.15	75.4	32.32	703	16.44	73.8	32.14	693	17.14	75.9	32.18	702	17.65	78.7	31.41	714
17	17.45	76.1	32.63	703	16.46	74	32.13	693	16.89	74.5	32.3	702	17.82	78.3	31.86	714
18	17.80	77	32.86	703	16.52	74.5	32.01	693	16.98	75.7	31.97	702	17.45	76.5	31.92	714
19	16.44	71.5	32.76	702	15.95	70.9	32.45	693	17.71	78.6	32.08	702	17.38	77.8	31.31	714
20	17.26	75.1	32.73	702	16.27	72.4	32.42	693	15.53	69.1	32.02	702	17.59	78.4	31.47	713
21	17.09	75.3	32.32	702	16.23	72.4	32.38	693	15.38	68.3	32.05	702	17.81	78.3	31.92	713
22	17.47	76.2	32.68	702	13.92	63.1	31.85	692	14.97	66.4	32.15	701	17.38	77.3	31.54	713
23	16.82	73.2	32.74	702	16.10	71.7	32.43	692	16.11	71.6	32.09	701	17.80	77.7	32.15	713
24	16.61	73.6	32.19	701	16.15	72.6	32.14	692	15.82	70.1	32.22	701	16.47	75	30.81	713
25	16.98	74.9	32.38	701	16.56	73.4	32.56	692	17.45	77.6	32.09	701	17.49	78.4	31.32	712
26	16.63	73.1	32.46	701	15.76	70.3	32.43	692	16.77	74.4	32.17	701	17.48	77.1	31.83	712
27	16.38	71.9	32.51	701	16.57	73.7	32.48	692	17.59	77.8	32.26	701	17.74	77.7	32.06	712
28	16.88	74.5	32.32	701	16.67	74.8	32.2	692	17.22	76.5	32.13	701	17.68	78.2	31.73	712
29	17.25	74.7	32.93	701	16.83	74.6	32.57	692	17.48	78.4	31.82	701	17.52	77.9	31.6	712
30	17.21	75.5	32.52	701	15.48	70.6	31.74	691	17.68	78.3	32.23	701	17.08	76.7	31.28	712

Nr.	PDT source T = 300 °C (Rb-free)				PDT source T = 490 °C				PDT source T = 520 °C				PDT source T = 540 °C			
	PCE (%)	FF (%)	J_{SC} (mA/cm²)	V_{OC} (mV)	PCE (%)	FF (%)	J_{SC} (mA/cm²)	V_{OC} (mV)	PCE (%)	FF (%)	J_{SC} (mA/cm²)	V_{OC} (mV)	PCE (%)	FF (%)	J_{SC} (mA/cm²)	V_{OC} (mV)
31	16.69	73.8	32.28	701	15.51	69.9	32.12	691	17.64	77.8	32.35	701	17.75	78.4	31.81	712
32	16.94	74.9	32.27	701	15.63	71	31.85	691	16.99	76.7	31.6	701	17.61	78	31.7	712
33	17.15	75.9	32.24	701	15.97	71.7	32.25	691	16.07	70.5	32.5	701	17.68	78.4	31.7	712
34	17.18	75.4	32.5	701	16.24	72.5	32.4	691	17.28	77.2	31.94	701	17.87	77.9	32.24	712
35	17.12	75.1	32.56	701	15.42	69	32.36	691	16.27	72.4	32.05	701	17.25	76.1	31.83	712
36	16.82	73.4	32.7	701	15.11	67.4	32.48	691	14.68	65.8	31.84	701	17.00	76.6	31.18	712
37	17.07	75.1	32.43	701	16.81	75.1	32.4	691	14.57	65	31.98	701	17.02	77.1	31.03	711
38	17.12	74.6	32.76	701	16.52	73.2	32.68	691	15.40	68.2	32.28	700	17.54	77.7	31.75	711
39	17.44	75.3	33.02	701	16.52	73.3	32.62	691	17.47	77.5	32.19	700	17.77	77.9	32.08	711
40	17.09	74.6	32.66	701	16.73	75.2	32.19	691	16.81	75	32.04	700	17.55	78.3	31.54	711
41	16.62	73.2	32.4	701	16.92	75.4	32.46	691	17.38	77.7	31.94	700	17.60	77.7	31.84	711
42	17.14	75.4	32.42	701	16.81	76.6	31.77	691	17.33	78	31.77	700	17.80	78.6	31.83	711
43	16.46	72.4	32.44	700	16.46	75.8	31.41	691	17.06	76.1	32.03	700	17.82	79	31.72	711
44	16.58	73.2	32.32	700	14.82	67.5	31.85	690	17.44	77.6	32.12	700	17.67	78.4	31.68	711
45	16.04	70.1	32.66	700	15.52	70.5	31.9	690	17.46	77.6	32.14	700	17.80	78.5	31.91	711
46	16.83	73.9	32.54	700	15.48	70.3	31.93	690	17.53	77.5	32.3	700	17.86	78.1	32.17	711
47	17.29	75.9	32.56	700	16.16	72.6	32.26	690	17.57	78.2	32.09	700	17.54	78.5	31.44	711
48	17.24	75.3	32.7	700	15.15	67.6	32.47	690	16.33	73.2	31.85	700	17.72	78.6	31.7	711
49	17.13	74.6	32.81	700	16.03	70.9	32.77	690	17.33	76.6	32.32	700	17.50	77.1	31.92	711
50	16.53	72.7	32.52	700	16.56	74.5	32.25	690	17.37	77.4	32.04	700	17.31	75.8	32.14	711
51	16.44	72.1	32.55	700	16.49	74.3	32.17	690	17.39	77.1	32.21	700	17.65	77.9	31.91	710
52	16.15	71.6	32.21	700	16.18	73.5	31.89	690	14.31	63.6	32.12	700	17.62	78	31.86	710
53	16.59	73.3	32.31	700	16.60	74.6	32.24	690	14.33	63.7	32.19	699	17.64	78.7	31.59	710
54	17.33	76.2	32.49	700	16.63	75.2	32.07	690	15.42	68.3	32.29	699	17.74	78.4	31.88	710
55	17.35	76.1	32.54	700	15.96	71.7	32.23	690	15.50	68.8	32.26	699	17.77	78.4	31.94	710
56	17.22	75.9	32.39	700	16.36	73.5	32.27	690	15.56	69.1	32.18	699	17.89	78.4	32.11	710
57	16.89	74.3	32.52	699	15.79	71.4	32.09	689	17.40	78.3	31.77	699	15.15	67.4	31.66	710
58	17.07	74	32.99	699	14.27	64.9	31.9	689	17.08	76.5	31.91	699	17.09	76.1	31.61	710
59	17.08	75.5	32.36	699	14.42	64.7	32.35	689	17.15	77.1	31.84	699	17.69	78.2	31.9	709
60	17.20	75.6	32.53	699	16.49	73.8	32.44	689	17.08	75.8	32.22	699	17.28	78.1	31.24	709
61	16.89	75.3	32.07	699	16.68	75.5	32.04	689	17.26	76.5	32.29	699	17.62	78.5	31.68	709
62	17.07	75	32.56	699	16.58	73.9	32.54	689	17.03	75.8	32.14	699	17.32	76.3	31.99	709
63	17.18	75.2	32.7	699	16.48	73.5	32.54	689	15.87	71.2	31.87	699	17.81	78.1	32.16	709
64	17.10	74.7	32.78	699	15.98	72.7	31.86	689	17.42	77.7	32.07	699	17.67	78.5	31.76	709
65	16.53	72.4	32.66	699	16.55	74.3	32.35	689	15.18	67.2	32.34	699	18.00	78.7	32.23	709

Nr.	PDT source T = 300 °C (Rb-free)				PDT source T = 490 °C				PDT source T = 520 °C				PDT source T = 540 °C			
	PCE (%)	FF (%)	J_{SC} (mA/cm²)	V_{OC} (mV)	PCE (%)	FF (%)	J_{SC} (mA/cm²)	V_{OC} (mV)	PCE (%)	FF (%)	J_{SC} (mA/cm²)	V_{OC} (mV)	PCE (%)	FF (%)	J_{SC} (mA/cm²)	V_{OC} (mV)
66	17.43	76.3	32.68	699	16.36	74.4	31.92	689	16.99	75.6	32.13	699	17.28	78.1	31.24	709
67	17.09	75.8	32.23	699	15.64	70.9	31.99	689	16.97	75.7	32.07	699	17.33	76	32.15	709
68	17.24	76.4	32.26	699	15.16	67.9	32.45	688	13.63	61.8	31.58	699	17.57	76.5	32.4	709
69	16.86	74.8	32.26	698	16.37	72.8	32.71	688	13.78	62.3	31.65	699	16.88	76.6	31.07	709
70	16.86	74.5	32.41	698	15.57	69.8	32.38	688	13.95	62.2	32.09	699	16.96	75.4	31.76	709
71	17.09	75	32.65	698	16.34	73.7	32.25	688	16.04	72.2	31.83	698	17.56	77.8	31.87	708
72	17.29	75.8	32.69	698	16.21	72.6	32.46	688	17.20	77.6	31.73	698	17.43	76.8	32.04	708
73	17.19	75.2	32.77	698	16.47	73.8	32.43	688	17.24	77.9	31.72	698	17.35	78.2	31.34	708
74	16.84	74.2	32.51	698	16.47	74.6	32.09	688	17.48	77.8	32.21	698	17.54	78	31.75	708
75	16.41	71.9	32.72	698	15.86	71.8	32.12	688	16.92	74.5	32.52	698	17.02	75.8	31.7	708
76	15.80	70.2	32.29	697	15.87	72.2	31.98	688	16.73	74.4	32.22	698	17.67	78.6	31.77	708
77	16.90	74.1	32.73	697	15.07	69.2	31.68	687	16.99	75.3	32.3	698	17.80	78.4	32.08	708
78	16.79	75	32.11	697	14.63	66.8	31.86	687	17.21	77.1	31.98	698	17.64	77.9	32	708
79	16.99	75.7	32.21	697	14.38	65.5	31.98	687	14.95	65.9	32.52	698	17.82	78.3	32.14	708
80	17.07	74.9	32.69	697	16.37	74	32.2	687	13.85	62.8	31.58	698	17.06	76.8	31.38	708
81	17.45	76.4	32.76	697	16.23	72.1	32.75	687	13.95	62	32.23	698	17.36	76.4	32.09	708
82	17.25	77.1	32.09	697	15.05	67.9	32.26	687	13.99	62.4	32.1	698	17.06	76.6	31.47	708
83	15.06	66.1	32.75	696	16.11	72.5	32.31	687	15.26	68.2	32.08	697	17.34	77.7	31.6	707
84	16.53	73.1	32.47	696	16.15	72.2	32.53	687	13.63	60.7	32.21	697	17.16	78.2	31.03	707
85	16.82	74.1	32.58	696	15.92	72.2	32.09	687	14.97	67	32.13	696	17.10	76.4	31.65	707
86	15.59	68.4	32.76	696	15.93	72.9	31.8	687	15.34	68.6	32.13	696	17.61	78.3	31.78	707
87	17.06	75.4	32.51	696	16.03	73.3	31.82	687	15.26	68.5	32.01	696	17.36	77.7	31.61	707
88	17.16	75.6	32.61	696	15.83	71.9	32.05	687	16.43	74.6	31.68	696	16.65	74.8	31.5	707
89	16.51	72.1	32.89	696	14.09	64	32.12	686	16.94	76.8	31.71	696	17.21	77.2	31.55	707
90	16.75	73.8	32.59	696	15.71	70.8	32.34	686	13.98	62.8	32.01	696	16.29	72.3	31.89	707
91	17.15	76.9	32.06	696	16.21	72.8	32.46	686	13.85	62	32.08	696	17.60	77.4	32.16	707
92	16.26	72.5	32.26	695	16.00	71.3	32.71	686	16.66	75.9	31.54	696	17.33	76.8	31.9	707
93	16.58	74	32.24	695	15.42	69.3	32.43	686	17.20	77.2	32.01	696	17.50	77.1	32.09	707
94	17.00	74.5	32.86	695	16.08	71.5	32.74	686	13.21	59.2	32.08	696	16.87	75.9	31.44	707
95	17.44	76.6	32.72	695	15.60	71	32	686	13.42	60	32.15	696	17.61	76.9	32.38	707
96	16.40	73.4	32.17	694	15.34	70	31.98	686	14.64	65.4	32.23	695	17.42	77	31.99	707
97	15.21	66.9	32.77	694	15.78	70.8	32.53	686	15.93	71.1	32.25	695	13.73	61.9	31.4	707
98	16.99	74.8	32.71	694	15.89	72.1	32.11	686	14.60	65.7	31.99	695	16.72	75.8	31.19	707
99	15.75	70.6	32.17	694	15.29	69.2	32.2	686	16.95	75.9	32.13	695	16.38	74.5	31.09	707
100	16.59	73.9	32.38	693	15.02	67.8	32.33	686	16.06	72.2	32	695	17.38	77.1	31.91	706

Nr.	PDT source T = 300 °C (Rb-free)				PDT source T = 490 °C				PDT source T = 520 °C				PDT source T = 540 °C			
	PCE (%)	FF (%)	J_{SC} (mA/cm²)	V_{OC} (mV)	PCE (%)	FF (%)	J_{SC} (mA/cm²)	V_{OC} (mV)	PCE (%)	FF (%)	J_{SC} (mA/cm²)	V_{OC} (mV)	PCE (%)	FF (%)	J_{SC} (mA/cm²)	V_{OC} (mV)
101	16.86	75.3	32.34	692	13.35	61.5	31.72	685	13.36	60.6	31.72	695	17.61	77.7	32.11	706
102	16.19	71.4	32.78	692	14.59	66.4	32.1	685	13.28	59.9	31.87	695	17.35	77.7	31.66	706
103	13.88	61.7	32.51	692	15.36	70.2	31.92	685	16.98	76.9	31.79	695	15.04	66.9	31.86	706
104	15.11	66.6	32.79	692	14.35	65.2	32.14	685	16.83	76.7	31.56	695	17.00	76.5	31.49	706
105	16.22	71.4	32.84	692	14.77	66.9	32.23	685	13.54	61.9	31.48	695	16.58	74.8	31.4	706
106	17.21	75.5	32.95	692	14.84	66.9	32.39	685	13.74	61.5	32.16	695	17.32	76.9	31.92	706
107	17.11	76.1	32.51	691	14.86	66.4	32.66	685	15.54	72.1	31.08	694	17.52	78.1	31.76	706
108	17.16	75.8	32.77	691	15.56	69.6	32.68	685	15.92	73.3	31.25	694	17.50	76.8	32.28	706
109	15.85	71.5	32.08	691	15.42	69.6	32.33	685	16.00	72	32.03	694	16.55	74.4	31.48	706
110	14.83	66.2	32.46	690	16.18	73.2	32.27	685	14.45	65.2	31.96	694	17.28	76.9	31.85	706
111	17.04	76.2	32.51	688	15.99	72.6	32.13	685	15.21	68.3	32.11	694	17.32	77.3	31.81	705
112	15.06	67.1	32.62	688	15.63	71.5	31.9	685	16.01	72.2	31.94	694	17.45	77.4	31.95	705
113	15.98	71	32.79	687	14.43	65.3	32.23	685	14.79	66.9	31.86	694	17.80	78.4	32.17	705
114	16.48	75.4	31.85	687	14.04	64.1	32.04	684	15.74	71	31.94	694	17.38	77.7	31.74	705
115	14.48	64.6	32.68	686	14.84	67.5	32.14	684	16.37	73.8	31.98	694	17.15	75.8	32.11	705
116	13.66	61.5	32.44	685	14.65	66.1	32.42	684	16.30	73.6	31.92	694	17.37	77.2	31.97	704
117	16.86	75.4	32.63	685	14.58	65.6	32.51	684	16.76	75.7	31.93	694	17.59	77.8	32.1	704
118	16.74	75.5	32.35	685	14.90	66.9	32.54	684	16.97	76.7	31.92	694	17.68	78.6	31.95	704
119	15.05	68.6	32.02	685	16.00	73.6	31.78	684	15.86	72.5	31.55	693	17.52	78.2	31.79	704
120	13.83	62.5	32.45	682	15.05	68.9	31.92	684	15.66	72	31.42	693	17.28	76.9	31.93	704
121	15.66	72.1	31.87	682	15.68	71.5	32.05	684	14.59	66.8	31.49	693	16.87	75.9	31.56	704
122	13.37	60.7	32.36	681	15.81	72.1	32.05	684	14.67	66.3	31.93	693	16.93	77.4	31.05	704
123	14.41	65.1	32.62	679	13.85	63.5	31.92	683	15.93	72.3	31.81	693	17.44	76.8	32.22	704
124	16.24	74	32.42	677	14.12	64.8	31.91	683	13.40	60.9	31.74	693	17.42	77.2	32.03	704
125	13.21	59.7	32.79	675	14.30	65.4	31.98	683	13.57	62.3	31.41	693	17.57	77.4	32.22	704
126	15.10	69.5	32.17	675	15.83	70.8	32.74	683	13.41	60.2	32.1	693	17.48	77.1	32.17	704
127	14.05	64.2	32.58	671	15.50	70.2	32.34	683	14.96	66.9	32.29	692	17.31	77.1	31.94	703
128	13.99	65.1	32.43	663	15.91	72.3	32.19	683	14.75	65.7	32.43	692	17.14	77.5	31.48	703
129	11.26	52.1	32.73	661	13.88	63.4	32.14	682	15.09	68.2	31.98	692	17.37	77	32.09	703
130	15.42	73.4	32.1	654	15.08	67.7	32.67	682	15.39	69.5	32.01	692	17.13	77.1	31.6	703
131	13.95	66.6	32.09	653	13.36	60.7	32.31	681	15.70	70.5	32.16	692	17.10	75.6	32.17	703
132	12.60	61.1	31.84	647	15.26	68.1	32.91	681	14.43	68.9	30.26	692	14.82	66.2	31.85	703
133	13.43	67.7	31.67	627	14.24	64.3	32.52	681	13.51	61.8	31.63	692	17.01	76.2	31.83	702
134	13.23	65.3	32.42	625	15.31	70.5	31.9	680	13.26	60.7	31.54	692	17.32	77.3	31.91	702
135	12.90	66.4	31.51	616	15.11	69.7	31.87	680	14.72	67.4	31.62	691	17.30	77.2	31.92	702

Nr.	PDT source T = 300 °C (Rb-free)				PDT source T = 490 °C				PDT source T = 520 °C				PDT source T = 540 °C			
	PCE (%)	FF (%)	J_{SC} (mA/cm²)	V_{OC} (mV)	PCE (%)	FF (%)	J_{SC} (mA/cm²)	V_{OC} (mV)	PCE (%)	FF (%)	J_{SC} (mA/cm²)	V_{OC} (mV)	PCE (%)	FF (%)	J_{SC} (mA/cm²)	V_{OC} (mV)
136	10.86	59.3	31.7	577	15.53	71	32.19	680	15.25	69.7	31.65	691	17.44	77.1	32.21	702
137	10.47	58.3	31.35	573	14.01	64.1	32.12	680	14.43	65.1	32.09	691	16.94	77.4	31.21	702
138	10.28	56.4	32.18	566	14.00	63.8	32.31	680	14.34	64.6	32.13	691	17.51	77.4	32.23	702
139	10.23	58.8	31.71	549	14.31	65.7	32.05	680	15.26	69.9	31.59	691	17.00	77.4	31.33	701
140	8.23	48.6	32.57	520	14.68	67.5	31.99	680	15.01	67.5	32.19	691	17.23	78	31.52	701
141					14.86	68.7	31.78	680	15.72	70.8	32.09	691	17.17	78	31.41	701
142					13.66	64.9	31.02	679	15.25	68.8	32.1	691	16.76	75.6	31.63	701
143					13.52	62.9	31.7	678	15.43	69.2	32.27	691	17.02	76	31.93	701
144					14.42	66	32.24	678	13.07	59	32.02	691	16.67	75.7	31.45	701
145					15.38	71.5	31.71	678	14.93	67.5	32.04	690	16.15	71.6	32.19	701
146					14.16	65.4	31.93	678	14.99	70	31.03	690	14.86	67.4	31.47	701
147					13.68	64	31.56	677	14.62	65.9	32.23	689	17.42	77.2	32.23	700
148					12.95	60.7	31.6	675	15.81	71.9	31.98	688	17.06	77.1	31.63	700
149					14.95	69.3	31.97	675	14.76	66.8	32.1	688	17.16	77.6	31.62	700
150					13.62	62.7	32.14	675	13.39	61.2	31.83	688	15.27	69.9	31.26	699
151					13.02	64	30.19	675	16.63	75.6	31.94	688	14.91	66.8	32	698
152					14.46	67.6	31.93	670	13.85	63.5	31.78	687	16.67	76.8	31.14	697
153					11.00	56.1	29.93	655	13.69	62.9	31.76	685	16.62	74.7	31.94	697
154					7.63	37.9	32.03	628	13.53	61.5	32.09	685	16.66	76.6	31.24	696
155					9.61	47.8	32.02	627	11.60	53.1	32.14	679	14.95	67.1	32.02	696
156					10.79	55.2	31.7	617	13.28	61.3	32.1	675	15.15	70.6	30.8	696
157					9.15	46.4	32.21	611	12.79	59	32.11	675	13.90	63.4	31.79	690
158					5.03	27.2	32.16	576	6.03	33.3	31.96	567	12.24	57.1	31.64	678
159					8.27	55.7	32.43	458	4.44	25.9	31.21	550	8.54	40.5	31.79	664
160					2.57	23.5	30.73	356	5.41	40	31.28	432	4.65	43.6	30.2	353

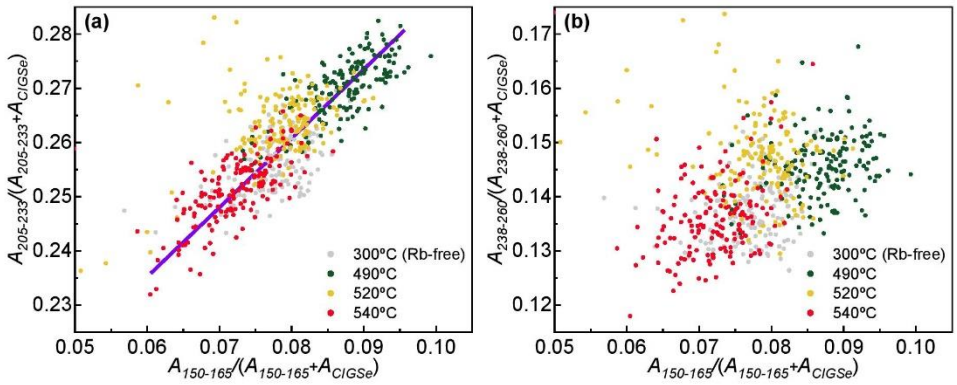

Figure S1. Relative integrated intensity of the Raman peaks in the spectral ranges (a) 205 – 233 cm^{-1} and (b) 238 – 260 cm^{-1} in function of relative integrated intensity of the peaks in the range 150 – 165 cm^{-1} range.

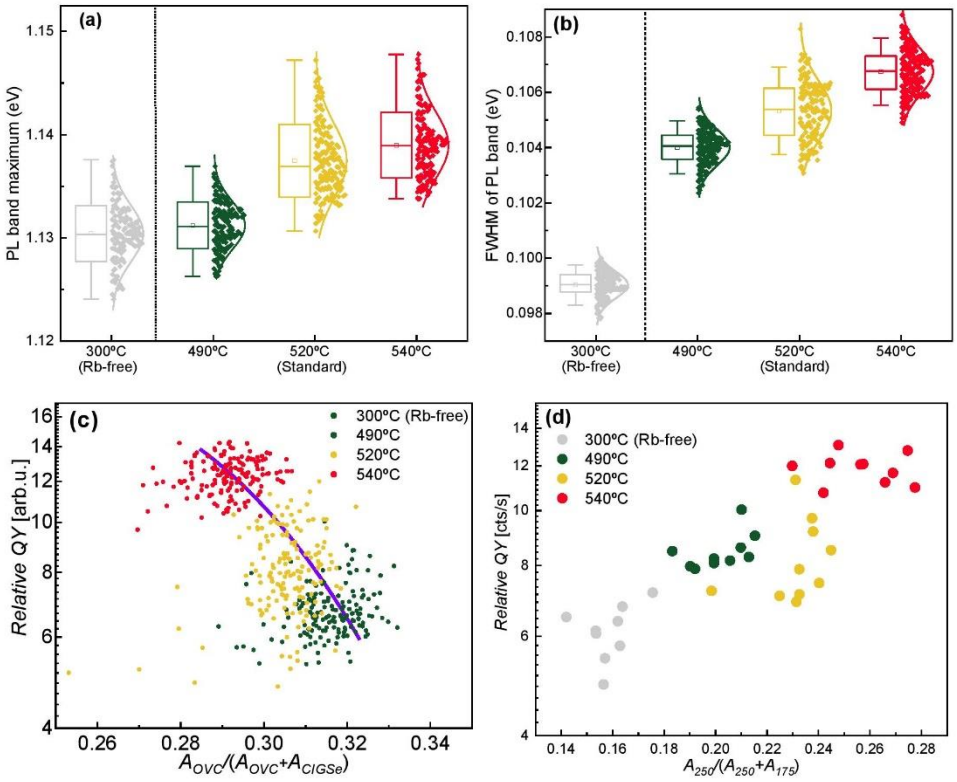

Figure S2. (a) Position of the PL band maximum in function of the RbF-PDT source temperature. (b) Full width at the half maximum (FWHM) of the PL band in function of the RbF-PDT source temperature. (c) Relative quantum yield (QY) of the PL band in function of the relative integrated intensity of the Raman peak at 250 cm^{-1} (spectra measured under 785 nm excitation). (d) Correlation of the relative QY of the PL band with the relative integrated intensity of the OVC-related Raman peaks.

The apparent hole concentration is extracted from the C-V measurements by employing the following relationship:[1,2]

$$N_{CV} = \frac{2}{q\varepsilon_S\varepsilon_0 A^2} \cdot \left[\frac{-1}{\frac{d\left(\frac{1}{C^2}\right)}{dV}} \right],$$

where N_{CV} is the apparent hole concentration, q is the elementary charge, ε_S is the CIGSe permittivity,[3-5] ε_o is the vacuum permittivity, A is the area of the solar cell, and $d(1/C^2)/dV$ is the first derivative of the square capacitance inverse in function of the bias voltage.

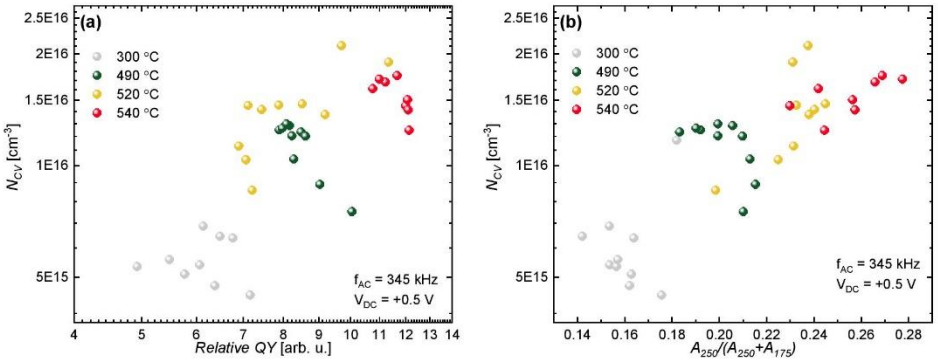

Figure S3. Apparent hole concentration at the absorber surface (0.5V of applied bias voltage) in function of (a) the relative QY of the PL emission and (b) the amount of defect chalcopyrite phase found from Raman scattering analysis.

References

[1] A.R. Peaker, V.P. Markevich, J. Coutinho, J. Appl. Phys. **2018**, 123, 161559.

[2] N. Christoforou, J.D. Leslie, S. Damaskinos, Can. J. Phys. **1987**, 65, 966.

[3] F. Werner, T. Bertram, J. Mengozzi, S. Siebentritt, Thin Solid Films **2017**, 633, 222.

[4] H. Heriche, Z. Rouabah, N. Bouarissa, Int. J. Hydrogen Energy **2017**, 42, 9524.

[5] S. Oladapo, B.M. Soucase, B. Aka, IOSR J. Appl. Phys. **2016**, 08, 01.

3.7. Article 6: Characterization of the Stability of Indium Tin Oxide and Functional Layers for Semitransparent Back-Contact Applications on $Cu(In,Ga)Se_2$ Solar Cells

RESEARCH ARTICLE

Solar RRL

www.solar-rrl.com

Characterization of the Stability of Indium Tin Oxide and Functional Layers for Semitransparent Back-Contact Applications on $Cu(in,Ga)Se_2$ Solar Cells

Robert Fonoll-Rubio, Marcel Placidi,* Torsten Hoelscher, Angelica Thomere, Zacharie Jehl Li-Kao, Maxim Guc, Victor Izquierdo-Roca, Roland Scheer, and Alejandro Pérez-Rodríguez*

Herein, a detailed study of the stability of different ITO-based back-contact configurations (including bare ITO contacts and contacts functionalized with nanometric Mo, $MoSe_2$, and MoS_2 layers) under the coevaporation processes developed for the synthesis of high-efficiency $Cu(In,Ga)Se_2$ (CIGSe) solar cells is reported. The results show that bare ITO layers can be used as efficient back contacts for coevaporation process temperatures of 480 °C. However, higher temperatures produce an amorphous In–Se phase at the ITO surface that reduces the contacts transparency in the visible region. This is accompanied by degradation of the solar cells' efficiency. Inclusion of a Mo functional layer leads to the formation of a $MoSe_2$ interfacial phase during the coevaporation process, which improves the cells' efficiency, achieving device efficiencies similar to those obtained with reference solar cells fabricated with standard Mo back contacts. Optimization of the initial Mo layer thickness improves the contact transparency, achieving contacts with an optical transparency of 50% in the visible region. This is accompanied by a relevant decrease in back reflectivity in the CIGSe devices, confirming the potential of these contact configurations for the development of semitransparent CIGSe devices with improved optical aesthetic quality without compromising the device performance.

1. Introduction

Thin-film photovoltaics (PV) presents numerous advantages such as low material usage, fabrication versatility, and easy integration (e.g., building-integrated PV [BIPV], wearables, internet of things, etc.). Among the nontoxic thin-film absorbers, $Cu(In,Ga)Se_2$ (CIGSe) has achieved the highest energy conversion efficiency (23.35%) at the laboratory scale[1] and it has been proven viable for large-scale industrial development.[2] Thus, technologies based on CIGSe play an important role in the democratization and integration of PV through mass production of cheap and efficient solar cell devices.

There exists a growing interest in CIGSe solar cells grown on transparent and semitransparent back contacts as this configuration offers different applications such as bifacial devices,[3–7] semitransparent BIPV,[8] and tandem solar cells.[9–12] Focusing on BIPV, it is predicted to achieve a relevant share of the total PV production of electricity in the next years, leading to strong interest in the recent years in the development of semitransparent PV solutions that will allow to achieve a relevant increase in the surface available in the buildings for the generation of BIPV electricity.[8,13] PV can be an integral part of windows,[14] skylights,[15] agrovoltaics,[16] glass-based facades,[17] and other related structures. Currently, semitransparent BIPV products based on amorphous silicon (a-Si) are being commercialized.[8,14,18,19] However, the energy conversion efficiency of a-Si solar cells was stuck around 10%.[18,20,21] Crystalline Si may

R. Fonoll-Rubio, M. Placidi, A. Thomere, M. Guc, V. Izquierdo-Roca, A. Pérez-Rodríguez
Catalonia Institute for Energy Research (IREC)
Jardins de les Dones de Negre 1
08930 Sant Adrià de Besòs-Barcelona, Spain
E-mail: rfonoll@irec.cat; marcel.placidi@upc.edu

The ORCID identification number(s) for the author(s) of this article can be found under https://doi.org/10.1002/solr.202101071.

DOI: 10.1002/solr.202101071

M. Placidi, Z. J. Li-Kao
Electronic Engineering Department
Polytechnic University of Catalonia (UPC)
Campus Besòs, Av. d'Eduard Maristany, 16, 08930 Barcelona, Spain

T. Hoelscher, R. Scheer
Institute of Physics
Martin-Luther-University (MLU)
von-Danckelmann-Platz, 3, 06120 Halle, Germany

A. Pérez-Rodríguez
IN2UB
Departament d'Enginyeria Electrònica i Biomèdica
Universitat de Barcelona
Carrer de Martí i Franquès 1, 08028 Barcelona, Spain

ADVANCED SCIENCE NEWS
www.advancedsciencenews.com

Solar RRL
www.solar-rrl.com

also be a candidate for BIPV applications due to its high energy conversion efficiency and high level of technological maturity,[18] even if it lacks the potential advantages of thin-film PV technologies for the design of customized modules adapted to the characteristics of the BIPV element. So, CIGSe absorbers offer an alternative for the BIPV market that promises higher efficiencies than a-Si, while keeping the advantages of thin-film PV.

When the solar cell absorber is of opaque thickness, which is the case of high-efficiency CIGSe, the semitransparency of the device is achieved by means of spatial segmentation,[13,22,23] consisting of removing parts of the absorber layer from selected areas. Thus, solar light is absorbed in the regions with the remaining absorber and it is transmitted in the regions where the absorber has been removed. Increasing the space between the absorption regions increases the transparency of the device, but this strategy is limited by the loss of short-circuit current density (J_{SC}) due to reduced photoactive material[13,22] and thus a trade-off efficiency/transparency has to be chosen depending on the final application.

The typical architecture of CIGSe devices consists of a soda-lime glass (SLG) substrate (3 mm), molybdenum back contact (800 nm), CIGSe absorber layer (2 μm), CdS buffer layer (10–60 nm), zinc oxide (i:ZnO), and a transparent conductive oxide (TCO) such as indium tin oxide (ITO) or aluminum-doped zinc oxide (AZO) window layers.[24–27] However, the replacement of the Mo back contact by semitransparent contact configurations based on the use of TCOs, such as ITO, offers different advantages. First, a metallic back contact, such as Mo, reflects the light at the back surface and, in combination with the glass substrate, generates a "mirror effect" when looking at the module from the substrate side, that is, people see their own reflection in the module back side, which compromises the aesthetic quality of the devices for semitransparent BIPV applications. Taking this into account, TCOs provide a drastic reduction of the back-contact reflectance, which improves the aesthetical quality of BIPV products viewed from the interior of the building by avoiding the mirror effect, a relevant point to ensure a higher level of acceptance of these solutions in the BIPV market. In addition, using a transparent back contact allows also to simplify the segmentation process, as in this case only the CIGSe and upper layers have to be removed in the light-transmitting regions. Finally, the use of semitransparent back contacts allows also the development of nonsegmented semitransparent devices that are based on the use of semitransparent absorbers (including wide-bandgap and/or ultrathin absorbers). This is strongly relevant for the development of devices with higher transparency levels and very high optical quality. Availability of optimal semitransparent back contacts is also required for the development of bifacial devices with improved efficiency, as well as for the development of higher-efficiency tandem device configurations using a wide-bandgap chalcogenide top cell.

Replacement of Mo by a semitransparent back contact in chalcopyrite devices has already been demonstrated using ITO,[9,28–31] fluorine-doped SnO_2 (FTO),[9,28,32] AZO,[28,33] and hydrogen-doped In_2O_3 (IOH).[34,35] In some of these cases, high-efficiency devices were obtained by applying bare ITO with a CIGSe coevaporation deposition temperature of 520 °C (efficiency of 15.2%)[28] or bare IOH with a coevaporation deposition temperature of 550 °C (up to 16.1% efficiency in $(Ag,Cu)(In,Ga)Se_2$ devices and 11% in $Cu(In,Ga)Se_2$ devices).[34,35] Nevertheless, in the case of CIGSe absorbers on ITO back contacts, the formation of a Ga_2O_3 layer at the TCO/CIGSe interface has been reported by Nakada et al. for deposition temperatures higher than 520 °C,[9,28] and such a layer has been associated with the deterioration of the device performance due to increased resistivity. To solve this problem, implementation of an intermediate functional layer (FL), such as Mo, between the TCO back contact and the CIGSe absorber has been proposed to avoid the formation of the Ga_2O_3 layer.[9] While the implementation of an FL on TCO back contacts is no novelty, the impact of the absorber fabrication process on the back contact and on the optical properties of the FL/TCO back-contact structure has not been deeply studied. Only a deterioration of the transparency of the ITO back contact is reported after deposition of a $CuGaSe_2$ absorber film,[31] but no systematic analysis is made on the impact of these processes on the optical characteristics of the back contact. Optimization of these processes requires for back-contact configurations to keep a high degree of transparency and good electrical properties after fabrication of the solar cell, and this implies the need for a systematic analysis of the impact of the processes on the optical and electrical characteristics of the back-contact configurations.

In this framework, this work reports a detailed study of the stability of ITO-based back-contact configurations under the coevaporation processes that are developed for the synthesis of high-efficiency CIGSe solar cells. Previous works developed on chalcogenide device technologies closely related to CIGSe as kesterites ($Cu_2ZnSn(S,Se)_4$ compounds) have shown the potential of nanometric chalcogenide FLs such as $MoSe_2$ on TCO-based back contacts for the achievement of high-efficiency devices.[36] In this work, different bare ITO, ITO/Mo, ITO/$MoSe_2$, and ITO/MoS_2 back-contact configurations have been studied as the function of both the CIGSe synthesis temperature and the thickness of the FLs, and we have analyzed the impact of such back contacts on the optoelectronic properties of the CIGSe solar cells. The results show that bare ITO layers can be used as efficient back contacts for coevaporation process temperatures of 480 °C. However, higher process temperatures lead to the formation of an amorphous In–Se phase at the ITO surface that reduces drastically both the transparency of the contacts in the visible region and the efficiency of solar cells. Inclusion of Mo FL leads to the formation of $MoSe_2$ interfacial phase during the coevaporation process, and the presence of this phase has been observed to improve significantly the efficiency of the cells, achieving device efficiencies similar to those obtained with reference solar cells fabricated with standard Mo back contacts. Optimization of the thickness of the initial Mo layer also allows to improve the contact transparency, achieving contacts with an optical transparency of 50% in the visible region. This is also accompanied by a relevant decrease in back reflectivity in the CIGSe devices, confirming the potential of these contact configurations for the development of semitransparent CIGSe devices with improved optical aesthetic quality without compromising the device performance. Further optimization of the processes is required to achieve higher AVT values as required for higher-transparency devices and high-efficiency tandem device configurations. This gives interest to further research on alternative FLs as those based on MoO_3 nanometric layers, which show

ADVANCED SCIENCE NEWS
www.advancedsciencenews.com

Solar RRL
www.solar-rrl.com

interesting optical properties as recently reported from first simulation studies.[37]

2. Results and Discussion

2.1. Impact of Coevaporation Process Temperatures on ITO and ITO/$MoSe_2$ Back Contacts

The substitution of the standard metallic Mo back contact by semitransparent ITO and ITO/$MoSe_2$ back contacts was studied at different temperatures of the CIGSe coevaporation process to determine the impact of the temperature on such back contacts. In this section, and for all the process temperatures, $MoSe_2$ was obtained by depositing an ultrathin Mo metallic layer with a nominal thickness of 20 nm on the surface of the ITO contact, and this Mo layer was selenized in situ during the CIGSe coevaporation process.

Figure 1a shows the average visible transmittance (AVT), which is defined in **Equation (1)** in the Experimental Section, of mechanically exposed ITO and ITO/$MoSe_2$ back contacts as a function of the coevaporation process temperature. Reference (as-grown) ITO layers have a high level of transparency with a value of AVT around 80%. However, processing of the CIGSe layer leads to a decrease in AVT of the bare ITO back contact with the processing temperature, down to a value of 43% for the highest process temperature of 625 °C. In the case of the ITO/$MoSe_2$ back contacts, the AVT is much lower than the value obtained on the corresponding bare ITO back contact with the same CIGSe processing temperature, showing a minimum value of 22% for the lowest processing temperature of 480 °C. In this case, increasing the processing temperature leads to a gradual increase in AVT of the exposed contact, in contrast with the process temperature dependence obtained on the bare ITO back contacts.

Figure 1b shows the relative energy conversion efficiencies of CIGSe devices with ITO and ITO/$MoSe_2$ back contacts as a function of the coevaporation process temperature by normalizing to the efficiency achieved with a reference CIGSe single cell processed in the very same batch and using a standard Mo back contact. It can be observed that the relative efficiency of the device with bare ITO back contact notably decreases with temperature, while the relative efficiency of the device with ITO/$MoSe_2$ back contact tends to increase when increasing the temperature. At highest temperatures, the relative efficiency of the device with ITO/$MoSe_2$ back contact is much higher than that of the device with bare ITO back contact.

Current density–voltage (J–V) curves are shown in Figure S1, Supporting Information, for the different temperatures. Table S1, Supporting Information, summarizes the main optoelectronic parameters of the devices. A clear current blocking behavior can be observed at 540 °C on the bare ITO sample, with a roll-over effect (current saturation at high forward bias).[38] This observation is discussed at the end of this section. So, in the case of bare ITO contacts, the worsening of the optical transparency is also accompanied by worsening of the optoelectronic properties of the CIGSe solar cells fabricated with these contacts. Only for the lowest process temperature of 480 °C, the solar cell shows a relative efficiency which corresponds to more than 80% of the efficiency achieved in the Mo-based reference devices. This, together with the high transparency of the layer (of 79%, as shown in Figure 1a), gives interest to the use of bare ITO back contacts for the fabrication of semitransparent CIGSe devices. However, the efficiency of the devices is limited by the low value of the process temperature, that is below 500 °C, and the efficiency of the reference solar cells produced with this process is of the order of 10% (Table S1, Supporting Information).

Achievement of high-efficiency CIGSe devices normally requires the use of process temperatures higher than 500 °C[39–42] and this is in particular the case with the baseline process using the Mo substrate, as described in the study by Jarzembowski et al.[43] This allows to increase the efficiency of the reference cells to values up to 15.6% (Table S1, Supporting Information). As shown in Figure 1b, the inclusion of an interfacial $MoSe_2$ layer between the CIGSe absorber and the ITO back contact allows to achieve contacts with good electrical properties, obtaining relative efficiency values higher than 80% obtained with the devices processed at 540 and 625 °C. However, the improvement of the optoelectronic properties is

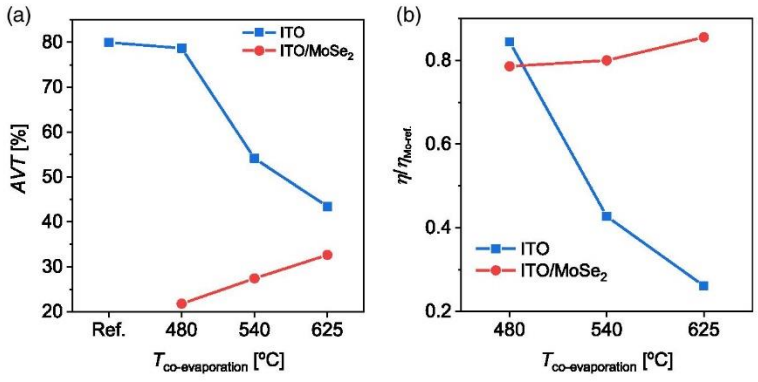

Figure 1. a) AVT of exposed ITO and ITO/$MoSe_2$ back contacts on glass substrate as a function of the coevaporation process temperature. Back contacts are exposed by mechanical removal of CIGSe and upper layers. b) Normalized energy conversion efficiency of CIGSe devices with ITO and ITO/$MoSe_2$ back contacts as a function of the coevaporation process temperature. Energy conversion efficiency values are normalized to those of a CIGSe device with a standard Mo back contact synthesized in the very same batch.

ADVANCED SCIENCE NEWS
www.advancedsciencenews.com

Solar RRL
www.solar-rrl.com

compromised by a strong reduction of the optical transparency with respect to that achieved with the bare ITO back contacts.

Figure 2 shows Raman spectra obtained on the exposed bare ITO and ITO/$MoSe_2$ back-contact surfaces as a function of the co-evaporation process temperature using 785 nm excitation wavelength. On the one hand, the Raman spectra (blue line) from the bare ITO back contacts are characterized by the presence of broad bands, and the most intense ones are located in between 400 and 600 cm^{-1} spectral region (with peaks at 433 and 550 cm^{-1}) and in between 200 and 300 cm^{-1} spectral region (with a peak at 225 cm^{-1}). Increasing the process temperature leads to a relevant increase in the intensity of the Raman bands. The presence of these bands indicates the formation of a surface phase that is likely located at the CIGSe/ITO interface, and the width of these Raman bands indicates a low level of crystallinity for this phase. In consideration with Figure 1a, the presence of this phase is likely responsible for the degradation of the transparency of the ITO layers. Increasing the processing temperature leads to an increase in the formation of this phase, as shown by the relevant increase in intensity of the Raman bands in the measured spectra, and this likely leads to the observed strong decrease in AVT of the bare ITO back contact with increasing processing temperature in Figure 1a.

The detected broad bands appear within the spectral regions that are characteristic of amorphous In–Se phases.[44–47] For the same chemical composition, Raman spectra of amorphous phases change notably with respect to the spectra of crystalline phases.[44,48] It has been reported that the amorphous In_2Se_3 presents a broad band with a peak at 255 cm^{-1} and a broad band with a peak at 490 cm^{-1},[44] while In_xSe_{1-x} presents a broad band with a peak that ranges from 190 to 255 cm^{-1} depending on the In/Se ratio.[46] According to this, the Raman bands observed in Figure 2 for bare ITO back contacts have been attributed to the presence of an amorphous In–Se phase, and the composition of this phase is responsible of the changes of the bands in relation to those characteristic from stoichiometric In_2Se_3. This means that the surface of the ITO back contact is selenized during the coevaporation process, forming an amorphous In–Se phase at the ITO/CIGSe interface that reduces the transparency of the back contact and degrades the optoelectronic properties of the device. It is not known whether Sn or Ga atoms are incorporated into this amorphous phase. The presence of some CIGSe contribution to the Raman peak located at ≈175 cm^{-1} from residual CIGSe on the exposed back contact after the segmentation process cannot be excluded. However, the dependence of the intensity of this peak with the coevaporation process temperature strongly suggests this peak to be mainly related to the amorphous In–Se phase. This also agrees with the absence of this peak in the Raman spectra from the samples processed at 480°C, where formation of the In–Se phase does not take place.

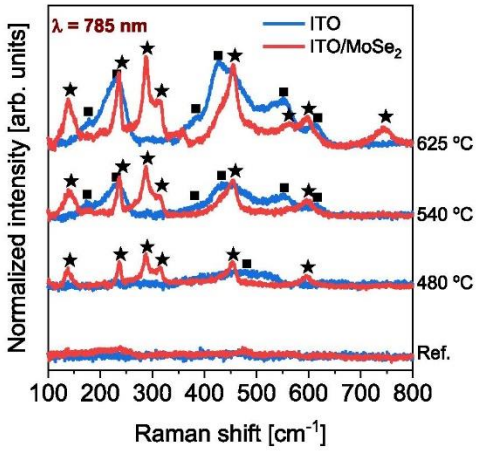

Figure 2. Raman spectra obtained on exposed bare ITO and ITO/$MoSe_2$ back contacts as a function of the coevaporation process temperature using 785 nm excitation wavelength. Star symbols indicate Raman peaks related to vibrational modes of $MoSe_2$ phase[51] and square symbols indicate Raman peaks related to an amorphous In–Se phase.[44–47] The spectra are normalized to the noise of the baseline.

The detected Raman peaks do not correspond to the reported ones for Ga_2O_3 phase,[49,50] whose formation was suggested when growing CIGSe on ITO back contacts at high temperatures[9,28]; however, these results do not discard the Ga_2O_3 formation, as the used excitation wavelength is not optimum for the Raman detection of this phase.

On the other hand, the Raman spectra (red line) measured on the exposed ITO/$MoSe_2$ contacts show the presence of the Raman peaks characteristic of the $MoSe_2$ phase.[51] Note that the relative intensity of the peaks can be influenced using resonant excitation conditions,[51] possible preferential orientation of the $MoSe_2$ layer,[52] and/or by the nanometric thickness of this layer.[53] These measurements confirm the formation of $MoSe_2$ interfacial phase during the CIGSe coevaporation process due to the in situ selenization of the ultrathin Mo layer deposited on the ITO. Increasing the process temperature leads to an increase in the intensity of the peaks, and this is likely due to an increased thickness of the $MoSe_2$ layer formed during the process, in spite of the same thickness of the Mo layer in the as-grown ITO/Mo contacts. This indicates that for these process conditions the initial Mo layer is not fully selenized and there is a remaining Mo layer that is located between the $MoSe_2$ layer and the ITO contact. The presence of this Mo metallic layer would explain the strong decrease of the transparency of these contacts with respect to the bare ITO ones, as shown in Figure 1a. Increasing the process temperature leads to a decrease in the remaining Mo layer, related to the increase in the thickness of the $MoSe_2$ layer, and this explains the increase in transparency of these contacts with the process temperature.

Summarizing the impact of the CIGSe coevaporation process temperature on the semitransparent back contacts, it has been observed that bare ITO back contacts have an AVT of 79% after the coevaporation temperature at 480 °C and produce solar cells with relative efficiencies which correspond to more than 80% of the efficiency achieved using a standard Mo back contact. However, increasing the process temperature results in selenization of the ITO back contact, thus forming an amorphous In–Se at the back interface that decreases the AVT of the back contact and the efficiencies (mainly due to the V_{OC} and fill factor (FF)) of the devices. The presence of the In–Se phase could be responsible for a Schottky barrier at the back interface and would explain the roll-over effect observed.[38] At 625 °C, the J–V curve is perfectly linear, and the device behaves like a photoresistor. Such an

ADVANCED SCIENCE NEWS
www.advancedsciencenews.com

Solar RRL
www.solar-rrl.com

observation can be related to either a high series resistance or low shunt resistance. As current and voltage are only marginally affected, it is currently not possible to discriminate between both hypotheses without additional material characterization. A thick, insulating, InSe layer could lead to a strong series resistance, while a small shunt resistance could be ascribed to process imperfections (pinholes) or metallic phases bypassing the p–n junction. In consequence, bare ITO does not appear suitable as a back contact for CIGSe devices fabricated at process temperatures of 540 °C or higher. At such high temperatures, the application of an ultrathin Mo layer on the ITO, that is selenized during the coevaporation process, thus forming an ITO/$MoSe_2$ back contact, prevents the degradation of both the transparency and the optoelectronic properties when increasing the process temperature, as clearly seen in the *J*–*V* curves. With this ITO/$MoSe_2$ back contact, relative efficiencies higher than 80% of those of a reference CIGSe device with a standard Mo back contact are achieved. However, though it is not degraded with process temperature, a remaining Mo layer reduces the optical transparency of the back contact, so it must be optimized for ensuring its viability for BIPV applications.

2.2. Thickness Control of FL on the ITO-Based Back Contacts Processed at 625 °C

According to the experimental data described in the previous section, optimization of the transparency of the ITO/$MoSe_2$ back contacts could be achieved by suitable tuning of the thickness of the initial Mo layer deposited onto the ITO back contact, trying to avoid the presence of a residual Mo metallic layer in the processed devices. To clarify this, the impact of the thickness of the initial Mo FL on the characteristics of the contacts has been investigated, using initial Mo FLs with nominal thicknesses between 10 nm and 30 nm. For the devices analyzed in this section, the CIGSe absorbers were grown using a coevaporation process temperature of 625 °C, which allows to achieve higher device efficiency values.

Figure 3 shows the AVT values measured after the solar cell process of the different mechanically exposed ITO/$MoSe_2$ back contacts as a function of the initial Mo FL nominal thickness. As shown in this figure, decreasing the thickness of the Mo initial layer down to 10 nm allows to achieve, after the coevaporation process, a relevant increase in the transparency of the ITO/$MoSe_2$ contact selenized in situ (with an AVT value of 52%). This is likely related to the full selenization of the initial Mo layer. The transparency of this contact is also higher than the transparency achieved with the bare ITO contact (of about 43%). This suggests that the $MoSe_2$ interfacial layer that is formed in situ during the coevaporation process prevents the formation of a-In–Se phase on the ITO surface; in this case, the loss of transparency in relation to the bare ITO as-deposited layer is likely related to optical absorption in the nanometric $MoSe_2$ layer. Increasing the thickness of the initial Mo layer leads to a strong decrease in transparency, and this has been attributed to the presence of a remaining unreacted metallic Mo layer between the $MoSe_2$ layer and the ITO back contact for the FLs obtained with thicker Mo layers. This interpretation is supported by the Raman measurements performed on these layers, as shown later. It is worth noting that, even in the case of the fully selenized ITO/$MoSe_2$ back contact, no peeling problems were observed after CIGSe deposition. This might be related to the formation of a $MoSe_2$ layer with the crystalline *c*-axis parallel to the substrate.[54]

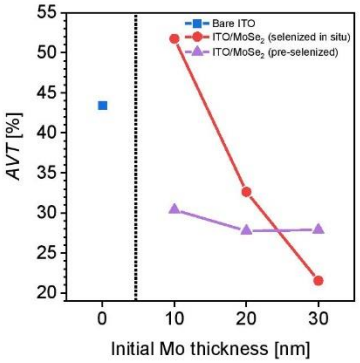

Figure 3. AVT after the coevaporation process of exposed ITO/$MoSe_2$ back contacts as a function of the nominal thickness of the initial Mo layer. The AVT of an exposed bare ITO back contact processed with the same conditions is included.

Synthesizing the $MoSe_2$ layer before the CIGSe coevaporation process leads to contacts with a transparency value that does not depend on the thickness of the layer. However, in this case, the transparency achieved is much lower than that obtained with the Mo thinnest layer that is selenized in situ during the coevaporation process, as the transparency values are in the range 28–30%. This behavior has been attributed to a degradation of the ITO surface during the selenization process that is performed before the coevaporation of the CIGSe absorber. This process is performed at a temperature of 500 °C during strongly selenizing conditions, which would explain the formation of ITO selenized phases at the surface of the ITO back contact.

Table 1 shows the average reflectance values measured in the visible spectral region on the back glass surface of the CIGSe devices fabricated with different ITO/$MoSe_2$ back contacts produced with an initial Mo layer thickness of 20 nm. The table shows also the values measured on the back glass surface from reference cells fabricated with a standard Mo back contact and from cells fabricated with a bare ITO back contact. It can be observed that the reflectance is reduced from a high value of 43.4% for standard Mo back contact to 9.1% for ITO/$MoSe_2$ back contact that is selenized in situ during the coevaporation process. In addition, the reflectance of the ITO/$MoSe_2$ back contact can be further reduced from 9.1% to 6.9% if the nanometric Mo layer is preselenized before the coevaporation process. Finally, a bare ITO back contact offers the lowest reflectance with 6.4%. This confirms the interest of these contact configurations for the

Table 1. Average reflectance measured in the visible spectral region (380–780 nm) from the back glass surface of CIGSe cells produced with different back-contact configurations.

Back contact	Glass/Mo (ref.)	Bare ITO	ITO/$MoSe_2$ (selenized in situ)	ITO/$MoSe_2$ (pre-selenized)
R [%]	43.4	6.4	9.1	6.9

ADVANCED SCIENCE NEWS
www.advancedsciencenews.com

Solar RRL
www.solar-rrl.com

improvement of the aesthetic quality of the CIGSe semitransparent devices, eliminating the "mirror effect" characteristic of the Mo back contact.

Figure 4a shows the Raman spectra measured with the 532 nm excitation wavelength at the back interface of CIGSe solar cells produced with ITO/$MoSe_2$ back contacts that are selenized in situ during the coevaporation process for different nominal thicknesses of the initial Mo layer. These spectra have been measured with the laser excitation spot on the back surface of the SLG substrate on complete solar cells. This has allowed to avoid potential damage effects in the measurements related to the mechanical removal of the CIGSe and upper layers. The presence of the peak at 238 cm^{-1} indicates that the Mo layers are always selenized, forming $MoSe_2$ at the CIGSe/back-contact interface.[51] However, the decrease of the absolute intensity of both the 176 and the 238 cm^{-1} peaks with the increase in the thickness of the initial Mo layer suggests the presence of a remaining metallic Mo that is likely located below the $MoSe_2$ layer. The thickness of this Mo metallic region increases with the nominal thickness of the initial Mo layer. This is in agreement with the observed decrease of the AVT for increasing thickness of the initial Mo layer shown in Figure 3. Figure 4b shows the Raman spectra measured in the same conditions from CIGSe solar cells with ITO/$MoSe_2$ back contacts that were preselenized

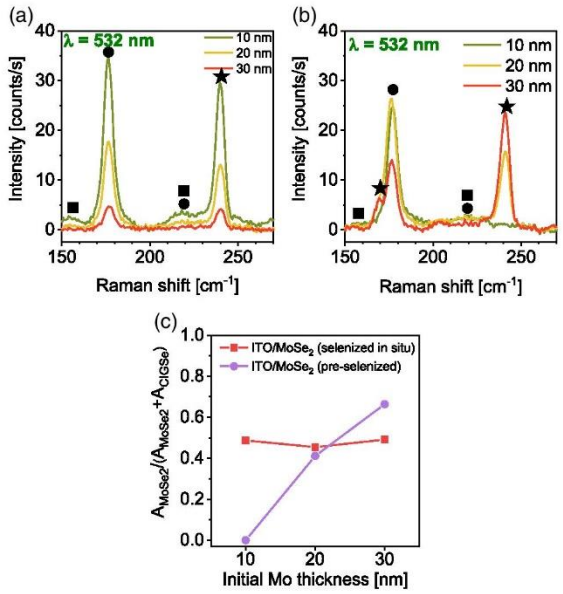

Figure 4. Raman spectra obtained using 532 nm excitation wavelength at the back interface of CIGSe solar cells synthesized at 625 °C with a) ITO/$MoSe_2$ (selenized in situ) and b) ITO/$MoSe_2$ (pre-selenized) back contacts for different initial Mo layers. Circle symbols indicate Raman peaks related to CIGSe vibrational modes, star symbols indicate peaks related to $MoSe_2$ vibrational modes, and square symbol indicates peaks related to vibrational modes of the CIGSe-ordered vacancy compounds. The back CIGSe/FL/ITO interface was analyzed by measuring the spectra with the laser spot on the back surface of the devices as the 532 nm wavelength was able to penetrate through the glass substrate. c) Relative area of the $MoSe_2$-related Raman peaks versus thickness of the initial Mo layer.

before the coevaporation deposition of the CIGSe layer. The presence of $MoSe_2$ (238 cm^{-1} peak)[51] is detected for samples with 20 and 30 nm initial Mo thickness, but not in the case of the 10 nm initial Mo layer. In this case, the thickness of the $MoSe_2$ FL is too low for efficient detection of the $MoSe_2$ peaks. Figure 4c shows the relative intensity of the $MoSe_2$ Raman peaks versus the nominal thickness of the initial Mo layer for all the processed ITO/$MoSe_2$ back contacts. For the $MoSe_2$ layers selenized in situ during the coevaporation process, the relative intensity of the $MoSe_2$ peaks is constant, which confirms that the thickness of the $MoSe_2$ layer produced during the coevaporation process is determined by the process parameters (i.e., the substrate temperature) but does not depend on the thickness of the initial Mo layer. This explains why for the thicker layers an unreacted metallic Mo layer remains below the selenized layer. This contrasts with the behavior observed for the $MoSe_2$ layers preselenized before the coevaporation process, where there is an increase in the thickness of the $MoSe_2$ layer with the thickness of the initial Mo layer.

Figure 5a shows the normalized energy conversion efficiencies of the CIGSe devices with different ITO-based back contacts as a function of the thickness of the initial Mo layer. It can be observed that in all cases there is relevant improvement in the efficiency of the devices in relation to the efficiency achieved using a bare ITO back contact. The highest efficiency values are achieved for the thickest initial Mo layers. Contrary to the case of the process temperature impact, the relative efficiency increase with increasing initial Mo layer thickness is due to an increase in J_{SC}, as shown in Figure 5b, while the V_{OC} and the FF remain more or less constant despite the thickness increase of the initial Mo layer (not shown). In the case of the Mo layers that are selenized in situ during the coevaporation process, the J_{SC} increase, and thus the relative efficiency increase, are likely related to the presence of a thicker Mo metallic layer below the $MoSe_2$ one, and this determines reduction of the sheet resistance of the back contact. In the case of the $MoSe_2$ layer that is selenized before the coevaporation process, this could be related to higher thickness of the $MoSe_2$ layer ensuring better coverage of the CIGSe/back-contact interface. Nevertheless, for all the investigated thicknesses of the initial Mo layer, the relative efficiency of the cells is higher than 80% of the efficiency of the reference CIGSe cells fabricated with a standard Mo back contact. This demonstrates the feasibility of these back-contact configurations to obtain devices with efficiencies similar to those achieved with standard Mo back contacts.

In addition to ITO/$MoSe_2$ back contacts, ITO/MoS_2 contacts have also been studied. Figure S2, Supporting Information, shows the AVT values obtained on contacts processed with MoS_2 FL. Use of a MoS_2 FL gives AVT and reflectance (see Table S2, Supporting Information) values similar to those obtained with the $MoSe_2$ layers selenized before the coevaporation process, even if in this case the AVT tends to decrease with the thickness in the FL. This behavior has been related to the existence of partial sulfurization of the initial Mo layer, which leads to a Mo metallic layer that is not selenized during the coevaporation process. This interpretation is supported by the Raman measurements (Figure S3, Supporting Information), which suggest a constant thickness of the MoS_2 layer independent of the initial thickness of the Mo layer. This behavior indicates the need to optimize the sulfurization process to ensure full sulfurization

ADVANCED SCIENCE NEWS
www.advancedsciencenews.com

Solar RRL
www.solar-rrl.com

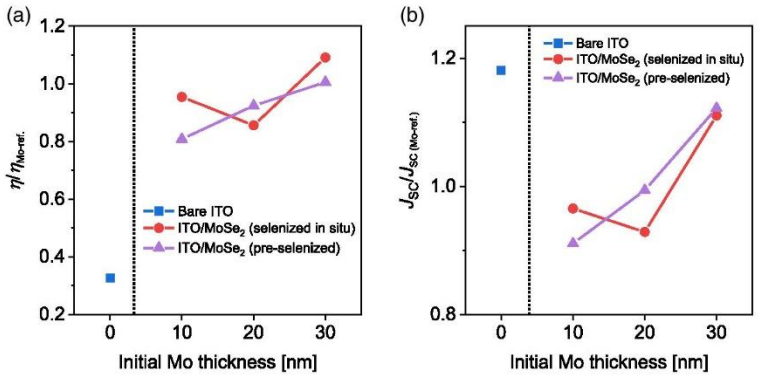

Figure 5. Normalized a) energy conversion efficiency and b) short-circuit current density of CIGSe devices with different ITO-based back contacts as a function of the thickness of the initial Mo layer. Optoelectronic parameters are normalized to those of a CIGSe device with a standard Mo back contact synthesized at the same conditions.

of the initial Mo layer. The presence of this Mo metallic region below the MoS_2 layer explains the low AVT values achieved within these contacts. On the other hand, the cells fabricated with the ITO/MoS_2 back contacts show device efficiencies similar to those achieved with ITO/$MoSe_2$ back contacts, as shown in Figure S4, Supporting Information.

Summarizing the impact of the FL thickness on the semitransparent back contacts, it has been observed that, when selenizing the Mo layer applied on the ITO in situ during the coevaporation process, reducing the initial Mo layer thickness down to 10 nm allows to achieve an AVT of 52% while keeping energy conversion efficiency very close to that obtained with a standard Mo back contact. In this case, increasing the initial Mo layer thickness only increases the remaining metallic Mo layer thickness, not the $MoSe_2$ one, which drastically reduces the AVT of the back contact. If the initial Mo layer is preselenized before the CIGSe coevaporation process, the thickness of the formed $MoSe_2$ layer can be controlled by tuning the initial Mo layer thickness; however, this strategy produces low AVT values due to degradation of the ITO back contact during the preselenization process.

3. Conclusion

In conclusion, bare ITO layers can be used as back contacts with high transparency (close to 80%) in CIGSe devices coevaporated at temperatures $T \leq 480\,^{\circ}C$. However, higher process temperatures lead to a partial selenization effect of the surface of the ITO layer, with the formation of an amorphous In–Se phase. This secondary phase leads to degradation of both the transparency in the visible region of the contacts and can also contribute to the observed degradation of the efficiency of the solar cells. This compromises the suitability of bare ITO back contacts for high-efficiency CIGSe semitransparent devices.

Inclusion of $MoSe_2$ or MoS_2 FLs on the surface of the ITO back contact allows a relevant improvement of the efficiency of the cells, leading to device efficiencies similar to those achieved with standard Mo back contacts, but processes have to be finely tuned to avoid the presence of a remaining metallic Mo layer that would degrade the transparency of the contacts. In addition, ITO/$MoSe_2$ back contacts obtained by selenizing the Mo deposited layer before the CIGSe coevaporation process lead to low AVT values. This has been attributed to the deterioration of the ITO surface due to selenization of ITO as well. By tuning the thickness of the initial Mo layer to ensure its full selenization, AVT values up to 50% have been achieved using a 10 nm Mo FL that is selenized in situ during the coevaporation process. Finally, we are able to show that replacing the standard Mo back contact by ITO-based back contacts with and without FLs leads to a drastic decrease in the reflectance at the back surface of our devices, avoiding the "back-mirror" effect that hinders the aesthetic quality of CIGSe semitransparent devices fabricated with standard Mo back contacts.

4. Experimental Section

The synthesis process started with the sputtering deposition (Alliance Concept CT100) of the ITO (800 nm thick, sheet resistance $\approx 5\ \Omega/\square$) back contact on a SLG substrate laminated with a 100 nm SiN_x diffusion barrier. Then, a very thin layer of Mo (with a nominal thickness between 10 nm and 30 nm) was deposited by sputtering (Alliance Concept AC450).

Two strategies were used to obtain the ITO/$MoSe_2$ back contact. In the first case, the Mo layer deposited on ITO was selenized in situ during the CIGSe coevaporation process. In the second case, Mo was specifically selenized before the CIGSe coevaporation process. For the ITO/MoS_2 back contact, a similar procedure as in the latter case was followed. Selenization/sulfurization processes were both done within a tubular furnace and reactive annealing was performed at 500 °C under an Ar atmosphere with a pressure of 1 bar and with the presence of elemental Se or S. The CIGSe coevaporation consisted of a three-stage process, described in the study by Jarzembowski et al,[43] with the second stage performed at very high temperature, that is, at 480, 540, or 625 °C for the first experiment (synthesis temperature variation) and fixed at 625 °C for the second one (FL thickness variation). Na was incorporated at the end of the growth process through NaF postdeposition treatment; this alkali incorporation strategy was previously optimized on Mo/glass substrates having an alkali-barrier layer, and the same process was transferred to the transparent substrates. The absorber layers were then completed into devices by depositing first a 50 nm-thick CdS layer (made by chemical bath deposition) and

ADVANCED SCIENCE NEWS
www.advancedsciencenews.com

Solar RRL
www.solar-rrl.com

followed with a 100–250 nm-thick i-ZnO/ITO window layer (Alliance Concept EVA 450) and a Ni/Al/Ni metal grid (E-gun Telemark 247).

Raman spectroscopy measurements were performed in a backscattering configuration though a probe designed at IREC using 532 and 785 nm lasers. The measurement spot size was ≈100 and 50 µm, respectively. For 785 nm excitation, an iHR 320 monochromator from Horiba Jobin Yvon coupled with a charge-coupled device (CCD) detector was used; for 532 nm excitation, a fHR 640 monochromator from Horiba Jobin Yvon coupled with an InGaAs detector was used. To avoid the presence of thermal effects in the spectra, excitation power density was kept below 50 W cm^{-2} in the laser spot. The measurements were performed at different surfaces of the samples. 1) The surface of exposed ITO-based back contacts was analyzed after performing mechanical removal of the CIGSe and upper layers in selected regions by scratching. To check if the process induced additional damage, selected samples were removed using a developed lift-off process using a microscope slide and an adhesive epoxy. [55] 2) The back CIGSe/FL/ITO interface was analyzed by measuring the spectra with the laser spot on the back surface of the devices as the used wavelengths were able to penetrate through the glass substrate. Configuration (2) had the advantage that measurements were not affected by potential damage effects related to the removal of the CIGSe top layer but were compromised by a lower signal-to-noise ratio.

Transmittance measurements were performed on the exposed regions of the ITO-based back contacts, after mechanical removal of the CIGSe and upper layers, using an light-emitting diode table and an iHR 320 monochromator from Horiba Jobin Yvon coupled with a CCD detector. The measurement spot size was ≈1 mm. Transmittance of exposed ITO-based back contacts was measured by illuminating the samples from the bottom side and the transmitted light was collected at the top side of the samples. The obtained transmittance spectra allowed to calculate the AVT, which is defined in Equation (1)

$$\mathrm{AVT} = \frac{\int_{\lambda_1}^{\lambda_2} T(\lambda)P(\lambda)S(\lambda)d\lambda}{\int_{\lambda_1}^{\lambda_2} P(\lambda)S(\lambda)d\lambda} \quad (1)$$

where λ is the wavelength, $T(\lambda)$ is the spectral transmissivity of the device evaluated, $P(\lambda)$ is the photopic response, $S(\lambda)$ is the solar photon flux (AM1.5G), and (λ_1, λ_2) is the integral range.[13,56,57] Analyzing the 435–670 nm range was sufficient to cover over 99% of the visible light spectrum[57]; in this work, the 380–780 nm range was analyzed as it was the optimum detection range of the system.

Reflectance measurements were performed using a Lambda 950 UV/VIS spectrometer from PerkinElmer coupled with a 150 mm integrating sphere from the same company. The total reflectance of the back contacts was measured from the glass substrate side, at regions where the CIGSe absorber was not removed. Average reflectance was also calculated in the 380–780 nm spectral range as the arithmetic mean of the reflectance values measured at each wavelength.

Optoelectronic properties of the solar cells were measured with a home-built sun simulator in a four-wire configuration. For electrical probing and sensing, a Keithley 2400 source meter was utilized. The electrical characterization of the solar cells took place under standard testing conditions (STCs), using a 3350 K tungsten halogen lamp calibrated to an intensity of 1 sun equivalent light.

Supporting Information

Supporting Information is available from the Wiley Online Library or from the author.

Acknowledgements

This work was part of the R+D+i Cell2Win project ref. PID 2019-104372RB-C31 funded by MCIN/AEI/10.13039/5011000110033 and the R+D+i MasterPV project ref. PCI 2018-092945 funded by MCIN/AEI/10.13039/5011000110033 and cofunded by the European Union. Project MasterPV was supported under the umbrella of SOLAR-ERA.NET and cofunded by "Agencia Estatal de Investigacion" (AEI, Spain), CDTI (Spain), and BMWi/PTJ (Germany, FKZ 0324230). SOLAR-ERA.NET was supported by the European Commission within the EU Framework Programme for Research and Innovation HORIZON 2020 (cofunded by ERA-NET Action, N° 691664). Authors from IREC belong to the Solar Energy Materials and Systems (SEMS) Consolidated Research Group of the "Generalitat de Catalunya" (ref. 2017 SGR 862). M.P. and M.G. acknowledge the financial support from Spanish Ministry of Science, Innovation and Universities within the Ramón y Cajal (RYC-2017–23758) and Juan de la Cierva (IJC2018–038199-I) programs, respectively. The authors would like to thank Thomas Schneider for his help in manufacturing CIGSe solar cells.

Conflict of Interest

The authors declare no conflict of interest.

Data Availability Statement

The data that support the findings of this study are available from the corresponding author upon reasonable request.

Keywords

CIGSe solar cells, Raman spectroscopy, semitransparent back contacts, transmittances spectroscopy

Received: December 20, 2021
Revised: February 15, 2022
Published online: May 6, 2022

[1] M. Nakamura, K. Yamaguchi, Y. Kimoto, Y. Yasaki, T. Kato, H. Sugimoto, *IEEE J. Photovoltaics* **2019**, *9*, 1863.
[2] T. Feurer, P. Reinhard, E. Avancini, B. Bissig, J. Löckinger, P. Fuchs, R. Carron, T. P. Weiss, J. Perrenoud, S. Stutterheim, S. Buecheler, A. N. Tiwari, *Prog. Photovoltaics Res. Appl.* **2017**, *25*, 645.
[3] N. Cavallari, F. Pattini, S. Rampino, F. Annoni, M. Barozzi, M. Bronzoni, E. Gilioli, E. Gombia, C. Maragliano, M. Mazzer, G. Pepponi, G. Spaggiari, R. Fornari, *Appl. Surf. Sci.* **2017**, *412*, 52.
[4] M. J. Shin, A. Lee, A. Cho, K. Kim, S. K. Ahn, J. H. Park, J. Yoo, J. H. Yun, J. Gwak, D. Shin, I. Jeong, J.-S. Cho, *Nano Energy* **2021**, *82*, 105729.
[5] M. Mazzer, S. Rampino, G. Spaggiari, F. Annoni, D. Bersani, F. Bissoli, M. Bronzoni, M. Calicchio, E. Gombia, A. Kingma, F. Pattini, E. Gilioli, *Sol. Energy Mater. Sol. Cells* **2017**, *166*, 247.
[6] A. Mavlonov, T. Nishimura, J. Chantana, Y. Kawano, T. Masuda, T. Minemoto, *Sol. Energy* **2020**, *211*, 1311.
[7] Y.-J. Hsiao, T.-J. Hsueh, J.-M. Shieh, Y.-M. Yeh, C.-C. Wang, B.-T. Dai, W.-W. Hsu, J.-Y. Lin, C.-H. Shen, C. W. Liu, C. Hu, F.-L. Yang, in *2011 Int. Electron Devices Meet.*, IEEE, Washington **2011**, 36.5.1.
[8] M. Saifullah, S. Ahn, J. Gwak, S. Ahn, K. Kim, J. Cho, J. H. Park, Y. J. Eo, A. Cho, J.-S. Yoo, J. H. Yun, *J. Mater. Chem. A* **2016**, *4*, 10542.
[9] T. Nakada, Y. Hirabayashi, T. Tokado, D. Ohmori, T. Mise, *Sol. Energy* **2004**, *77*, 739.
[10] Z. Yu, M. Leilaeioun, Z. Holman, *Nat. Energy* **2016**, *1*, 16137.
[11] M. Elbar, S. Tobbeche, A. Merazga, *Sol. Energy* **2015**, *122*, 104.
[12] S. Ishizuka, *Phys. Status Solidi A* **2019**, *216*, 1800873.
[13] C. J. Traverse, R. Pandey, M. C. Barr, R. R. Lunt, *Nat. Energy* **2017**, *2*, 849.

[14] T. Miyazaki, A. Akisawa, T. Kashiwagi, *Renewable Energy* **2005**, *30*, 281.
[15] D. H. W. Li, T. N. T. Lam, K. L. Cheung, *Energy Convers. Manage.* **2009**, *50*, 1981.
[16] C. J. M. Emmott, J. A. Röhr, M. Campoy-Quiles, T. Kirchartz, A. Urbina, N. J. Ekins-Daukes, J. Nelson, *Energy Environ. Sci.* **2015**, *8*, 1317.
[17] R. Ciriminna, F. Meneguzzo, L. Albanese, M. Pagliaro, *Green* **2015**, *5*, 73.
[18] B. Petter Jelle, C. Breivik, H. Drolsum Røkenes, *Sol. Energy Mater. Sol. Cells* **2012**, *100*, 69.
[19] J.-H. Yoon, J. Song, S.-J. Lee, *Sol. Energy* **2011**, *85*, 723.
[20] M. A. Green, E. D. Dunlop, J. Hohl-Ebinger, M. Yoshita, N. Kopidakis, X. Hao, *Prog. Photovoltaics Res. Appl.* **2021**, *29*, 657.
[21] T. Matsui, A. Bidiville, K. Maejima, H. Sai, T. Koida, T. Suezaki, M. Matsumoto, K. Saito, I. Yoshida, M. Kondo, *Appl. Phys. Lett.* **2015**, *106*, 053901.
[22] Z. Li, T. Ma, H. Yang, L. Lu, R. Wang, *Sol. RRL* **2021**, *5*, 2000614.
[23] T. Sidali, A. Bou, D. Coutancier, E. Chassaing, B. Theys, D. Barakel, R. Garuz, P.-Y. Thoulon, D. Lincot, *EPJ Photovoltaics* **2018**, *9*, 2.
[24] D. Lee, K. Yong, *Korean J. Chem. Eng.* **2013**, *30*, 1347.
[25] M. Sibinski, K. Znajdek, *Solar Cells - Thin-Film Technologies*, InTech, London, United Kingdom **2011**.
[26] S. Calnan, *Coatings* **2014**, *4*, 162.
[27] N. Khoshsirat, N. A. M. Yunus, *Nanoelectronics and Materials Development*, InTech, London, United Kingdom **2016**.
[28] T. Nakada, *Thin Solid Films* **2005**, *480–481*, 419.
[29] Y. Li, G. Yin, M. Schmid, *Sol. Energy Mater. Sol. Cells* **2022**, *234*, 111431.
[30] K. Kim, W. N. Shafarman, *Nano Energy* **2016**, *30*, 488.
[31] S. Nishiwaki, S. Siebentritt, P. Walk, M. Ch Lux-Steiner, *Prog. Photovoltaics Res. Appl.* **2003**, *11*, 243.
[32] W. Ohm, W. Riedel, U. Aksunger, D. Greiner, C. A. Kaufmann, M. C. Lux-Steiner, S. Gledhill, in *2015 IEEE 42nd Photovolt. Spec. Conf.*, IEEE, New Orleans, LA **2015**, p. 1.
[33] J. Mattheis, P. J. Rostan, U. Rau, J. H. Werner, *Sol. Energy Mater. Sol. Cells* **2007**, *91*, 689.
[34] J. Keller, N. Shariati Nilsson, A. Aijaz, L. Riekehr, T. Kubart, M. Edoff, T. Törndahl, *Prog. Photovoltaics Res. Appl.* **2018**, *26*, 159.
[35] J. Keller, W.-C. Chen, L. Riekehr, T. Kubart, T. Törndahl, M. Edoff, *Prog. Photovoltaics Res. Appl.* **2018**, *26*, 846.
[36] I. Becerril-Romero, D. Sylla, M. Placidi, Y. Sánchez, J. Andrade-Arvizu, V. Izquierdo-Roca, M. Guc, A. Pérez-Rodríguez, S. Grini, L. Vines, B. Pusay, R. Almache, J. Puigdollers, P. Pistor, E. Saucedo, M. Espíndola-Rodríguez, *ACS Appl. Mater. Interfaces* **2020**, *12*, 33656.
[37] K. J. Tiwari, S. Giraldo, M. Placidi, A. Gon Medaille, A. Thomere, S. Resalati, E. Saucedo, Z. Jehl Li-Kao, *Sol. RRL* **2021**, *5*, 2100202.
[38] R. Scheer, H.-W. Schock, *Chalcogenide Photovoltaics: Physics, Technologies, and Thin Film Devices*, Wiley-VCH Verlag GmbH & Co. KGaA, Weinheim, Germany **2011**.
[39] W. Li, L. Yao, K. Li, X. Li, B. Yang, S. Xu, S. Shi, C. Yi, M. Chen, Y. Feng, W. Li, Z. Lu, C. Yang, *ACS Appl. Energy Mater.* **2020**, *3*, 4201.
[40] D. Rudmann, D. Brémaud, A. F. da Cunha, G. Bilger, A. Strohm, M. Kaelin, H. Zogg, A. N. Tiwari, *Thin Solid Films* **2005**, *480–481*, 55.
[41] P. Jackson, R. Wuerz, D. Hariskos, E. Lotter, W. Witte, M. Powalla, *Phys. Status Solidi RRL* **2016**, *10*, 583.
[42] T. Kato, J.-L. Wu, Y. Hirai, H. Sugimoto, V. Bermudez, *IEEE J. Photovoltaics* **2019**, *9*, 325.
[43] E. Jarzembowski, M. Maiberg, F. Obereigner, K. Kaufmann, S. Krause, R. Scheer, *Thin Solid Films* **2015**, *576*, 75.
[44] J. Weszka, P. Daniel, A. Burian, A. M. Burian, A. T. Nguyen, *J. Non-Cryst. Solids* **2000**, *265*, 98.
[45] C.-H. Ho, *Sci. Rep.* **2015**, *4*, 4764.
[46] I. Watanabe, T. Yamamoto, *Jpn. J. Appl. Phys.* **1985**, *24*, 1282.
[47] J. Weszka, P. Daniel, A. M. Burian, *Acta Phys. Pol. A* **2000**, *98*, 619.
[48] P. Pistor, R. Caballero, D. Hariskos, V. Izquierdo-Roca, R. Wächter, S. Schorr, R. Klenk, *Sol. Energy Mater. Sol. Cells* **2009**, *93*, 148.
[49] C. Kranert, C. Sturm, R. Schmidt-Grund, M. Grundmann, *Sci. Rep.* **2016**, *6*, 35964.
[50] Y. Wang, N. Li, P. Duan, X. Sun, B. Chu, Q. He, *J. Nanomater.* **2015**, *2015*, 1.
[51] D. Nam, J.-U. Lee, H. Cheong, *Sci. Rep.* **2015**, *5*, 17113.
[52] T. Sekine, M. Izumi, T. Nakashizu, K. Uchinokura, E. Matsuura, *J. Phys. Soc. Japan* **1980**, *49*, 1069.
[53] M. Placidi, M. Dimitrievska, V. Izquierdo-Roca, X. Fontané, A. Castellanos-Gomez, A. Pérez-Tomás, N. Mestres, M. Espindola-Rodriguez, S. López-Marino, M. Neuschitzer, V. Bermudez, A. Yaremko, A. Pérez-Rodríguez, *2D Mater.* **2015**, *2*, 035006.
[54] C. M. Ruiz, A. Pérez-Rodríguez, J. Arbiol, J. R. Morante, V. Bermúdez, *Phys. Status Solidi A* **2015**, *212*, 61.
[55] J. Andrade-Arvizu, R. F. Rubio, V. Izquierdo-Roca, I. Becerril-Romero, D. Sylla, P. Vidal-Fuentes, Z. J. Li-Kao, A. Thomere, S. Giraldo, K. Tiwari, S. Resalati, M. Guc, M. Placidi, *ACS Appl. Mater. Interfaces* **2022**, *14*, 1177.
[56] C. Yang, D. Liu, M. Bates, M. C. Barr, R. R. Lunt, *Joule* **2019**, *3*, 1803.
[57] R. R. Lunt, *Appl. Phys. Lett.* **2012**, *101*, 043902.

WILEY-VCH

Supporting Information

Characterization of the stability of ITO and functional layers for semitransparent back contact applications on CIGSe solar cells

Robert Fonoll-Rubio, Marcel Placidi*, Torsten Hoelscher, Angelica Thomere, Zacharie Jehl Li-Kao, Maxim Guc, Victor Izquierdo-Roca, Roland Scheer, Alejandro Pérez-Rodríguez*

R. Fonoll-Rubio, M. Placidi, A. Thomere, M. Guc, V. Izquierdo-Roca, A. Pérez-Rodríguez
Catalonia Institute for Energy Research (IREC), Jardins de les Dones de Negre 1, 08930 Sant Adrià de Besòs-Barcelona, Spain
E-mail: rfonoll@irec.cat

M. Placidi, Z. Jehl Li-Kao
Electronic Engineering Department, Polytechnic University of Catalonia (UPC), Campus Besòs, Av. d'Eduard Maristany, 16, 08930 Barcelona, Spain
E-mail: marcel.placidi@upc.edu

T. Hoelscher, R. Scheer
Martin-Luther-University (MLU), von-Danckelmann-Platz, 3, 06120 Halle, Germany

A. Pérez-Rodríguez
IN^{2}UB, Departament d'Enginyeria Electrònica i Biomèdica, Universitat de Barcelona, Carrer de Martí i Franquès 1, 08028, Barcelona, Spain

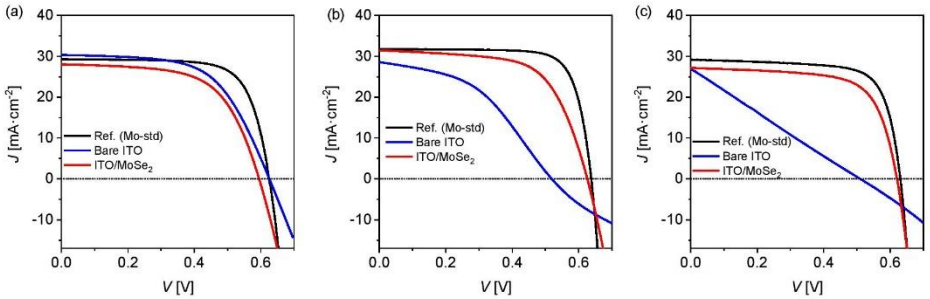

Figure S1. Current density as a function of the applied bias voltage of CIGSe solar cells synthesized at co-evaporation process temperatures of (a) 480ºC, (b) 540ºC, and (c) 625ºC. Different back contacts were employed: a standard Mo back contact (reference), a bare ITO back contact, and an ITO/$MoSe_2$ back contact.

Table S1. Short-circuit current density, open-circuit voltage, fill factor, and energy conversion efficiency of CIGSe solar cells with different back contacts as a function of the co-evaporation process temperature. The employed back contacts were a standard Mo back contact (reference), a bare ITO back contact, and an ITO/$MoSe_2$ back contact.

T [ºC]	J_{SC} [mA·cm^{-2}]			V_{OC} [mV]			FF [%]			η [%]		
	Ref.	Bare ITO	ITO/$MoSe_2$	Ref.	Bare ITO	ITO/$MoSe_2$	Ref.	Bare ITO	ITO/$MoSe_2$	Ref.	Bare ITO	ITO/$MoSe_2$
480	29.30	30.34	28.05	624	626	595	72.61	59.13	61.17	13.28	11.22	10.21
540	31.75	28.58	31.44	638	519	626	76.96	44.02	63.28	15.59	6.53	12.46
625	29.18	26.97	27.15	631	510	621	72.96	24.59	68.30	13.43	3.38	11.51

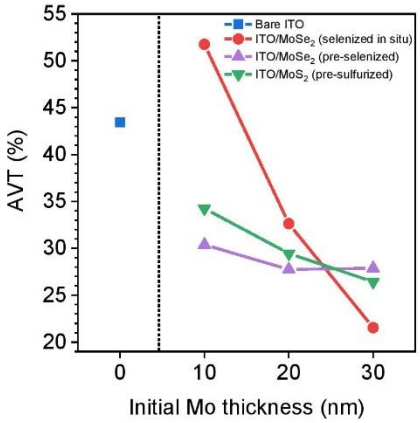

Figure S2. AVT of different exposed ITO-based back contacts on glass substrate in function of the nominal thickness of the initial Mo layer. Back contacts are exposed by mechanical removal of CIGSe and upper layers.

Table S2. Average reflectance in the visible light spectrum (380–780 nm) of different exposed ITO-based back contacts obtained with a Mo layer thickness of 20 nm, measured from the glass substrate side. Reflectance of a standard Mo back contact is included.

Back contact	Glass/Mo (ref.)	Bare ITO	ITO/$MoSe_2$ (selenized in situ)	ITO/$MoSe_2$ (pre-selenized)	ITO/MoS_2 (pre-sulfurized)
R [%]	43.4	6.4	9.1	6.9	8.3

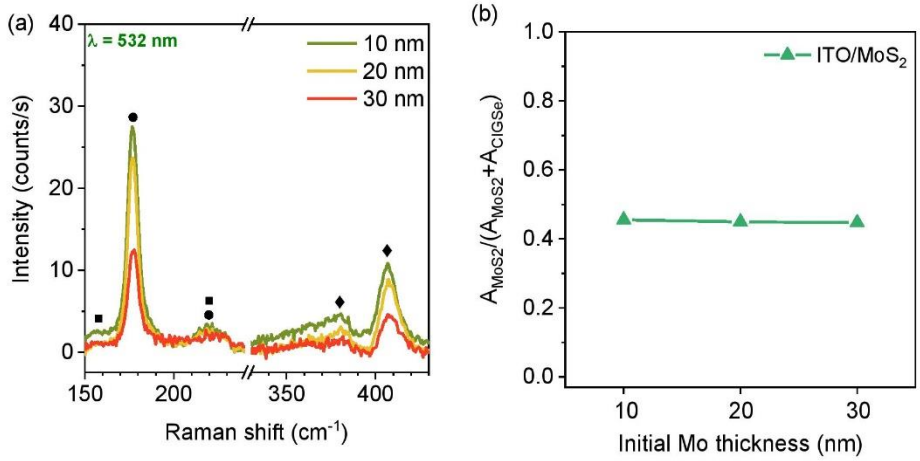

Figure S3. (a) Raman spectra obtained using 532 nm excitation wavelength at the back interface of CIGSe solar cells synthesized at 625ºC with pre-sulfurized ITO/MoS_2 back contacts for different thicknesses of the initial Mo layer. Spectra are obtained by measuring through the glass substrate of the devices. Circle symbols indicate Raman peaks related to CIGSe vibrational modes, square symbols indicate peaks related to vibrational modes of CIGSe ordered vacancy compounds, and diamond symbols indicate peaks related to MoS_2 vibrational modes. (b) Relative area of MoS_2-related Raman peaks in function of thickness of initial Mo layer.

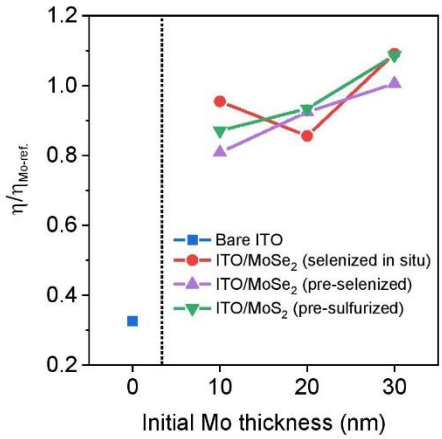

Figure S4. Normalized energy conversion efficiencies of CIGSe devices with different ITO-based back contacts in function of the thickness of the initial Mo layer. Efficiencies are

normalized to the energy conversion efficiency of a CIGSe device with a standard Mo back contact synthesized at the same conditions.

Chapter 4: Conclusions and outlook

The main objective of this thesis is the development of advanced characterization methodologies based on Raman scattering suitable for the deep characterization of the interfaces in high efficiency (chalcopyrites) and emerging sustainable (kesterites) thin film chalcogenide solar cells, with the aim to achieve a deeper understanding of the critical influence of the interfaces on the performance of the devices. This objective is in line with one of the main research lines of the SEMS group in IREC related to the advanced characterization of materials for PV application and of solar cell devices. Moreover, during the implementation of the thesis, and being influenced by its results, a new research line of the group "Process monitoring of the materials and devices quality" was formulated in its final shape. This objective of the thesis was achieved by analyzing the front interface between the absorber and the buffer layer and the back interface between the absorber and the back contact in kesterite and chalcopyrite-based thin film solar cells by means of Raman scattering in combination with different characterization techniques such as PL, transmittance, capacitance spectroscopies, and electron microscopy. Based on the obtained results of the performed advanced characterizations, six articles were published in high impact peer-review journals that constitute the core of the present thesis.

On the one hand, kesterite absorbers had been studied for some years and many fundamental properties of the kesterite compounds were already known at the start of the thesis, but the performance achieved by the corresponding solar cells is still far below the one achieved by other materials used in thin film solar cells (CIGSe, CdTe). In this regard, further identification and understanding of the limitations of this technology was needed, and a complex approach in characterization of the photovoltaic devices is one of the possible ways to push forward this promising technology. Taking this into account, in the first experiment of this thesis, a deep analysis of the formation of defects in the different regions of a high efficiency CZTSe device was performed by a combination of advanced electron microscopy and spectroscopic techniques at the macro, micro and nanoscale. It revealed, for the first time, direct evidence of the presence of twinning defects in the bulk, of micro and nano-voids at the back interface, and confirmed the presence of a widely-suspected high density of defects at the front interface. The defects formed at the front interface have been identified as the main source of V_{OC} deficit limiting the performance

of these devices, although the issues observed in the bulk and at the back interface also represent important drawbacks for device performance. This article showed a good practice in the comprehensive analysis of complex systems as thin film solar cells, addressing the different regions where the defects can appear. Moreover, it allowed comparing the effect of the bulk of the absorber with the effect of its interfaces on the solar cell performance, showing the critical importance of a specific focus on the device interfaces. The second experiment of this thesis complemented the first one by making a characterization of the absorber layers at different depths using the Raman spectroscopy that provided a relative profile of defects in CZTSe kesterite. Here, the stepwise Br_2-based chemical etching was used to access different depths of the absorber, and the obtained results confirm the suitability of Raman spectroscopy to make a comprehensive and relevant analysis of the kesterite based absorbers. The third experiment focused on the analysis of the back interface of the CZTSe absorber using mechanical lift-off techniques. Namely, a novel approach based on the formation of a nanometric layer of CGSe at the back interface was analyzed, and the performed studies show how the presence of this layer prevents the formation of voids at the back interface (which in the first article was identified as one of the limiting factor for the efficiency of kesterite based devices) and, as result, improved the optoelectronic properties. In the fourth experiment, Raman spectroscopy was employed as easy and fast technique to demonstrate the achievement of anionic compositional gradients from the front to the back interfaces in different kesterite absorbers, which was proposed as a way to restrain the defect formation, and to optimize the band alignment with carrier-selective contacts. Taking into account all the results involving characterization of the kesterite based materials and of the absorber interfaces in the thin film devices based on them, this thesis represents a step forward in the comprehension of the main limitations in the kesterite solar cells and opens the way to identify new solutions to further develop this technology and pushing it towards higher performances. In addition, it also presents innovative strategies based on back interface engineering and band gap engineering to overcome the current relatively low device efficiencies, and it shows that spectroscopic techniques alone allow evaluating such strategies. On the other hand, combination of the spectroscopic techniques, especially Raman spectroscopy, with other, more complex techniques can provide a full picture of the main limitations that appear in such a complex system as a thin film solar cell. Further studies involving kesterite-based PV devices should be aimed to the development of strategies that favor a formation pathway avoiding the formation of volatile phases at the

back interface, which would minimize the appearance of large voids, and to the development of passivation and etching strategies that eliminate the high density of defects at the front interface, resulting in a better band alignment with buffer layers. Additionally, the strong inhomogeneity in the chemical composition of the bulk of the grains should be a matter of further studies in this technology.

On the other hand, chalcopyrite absorbers are a more mature technology, and devices based on them had achieved the highest performance among thin film solar cells. However, their contribution to the global PV production is far below the technology based on crystalline Si, and a further optimization of the processes at industrial scale is required. In the recent years, PDT process with heavy alkali elements was found to have a beneficial effect on the efficiency of CIGSe-based devices, but the nature of this positive influence remained a matter of discussion. In the fifth experiment of this thesis, Raman spectroscopy applied to a high amount of individual cells (>600 cells) allowed to identify very small variations at the front interface of the absorber when varying the conditions of the PDT process. This has allowed to identify the main driving force behind the improvement of the device performance in CIGSe-based solar cells due to RbF-PDT as related to the redistribution of defects between the OVC and chalcopyrite phases that leads to the formation of a so-called "defective chalcopyrite phase" in the surface region of the absorbers. In addition, an industry-compatible process monitoring methodology has been developed based on the analytical methodologies applied in this work, for the quality control assessment of the RbF-PDT processes, with the prediction of the V_{OC} of the final devices at an early production stage. The sixth experiment of this thesis was focused on widening the application routes of CIGSe-based solar cells towards the semitransparent technologies and on studying the influence of the absorber deposition conditions on the transparent back contacts. It was shown that the application of functional layers such as $MoSe_2$ and MoS_2 on the surface of ITO back contacts is required to avoid a degradation of its optical transparency and of the device performance at high co-evaporation process temperatures, which is relevant for the future development of this technology in different applications such as BIPV, tandem solar cells, and bifacial solar cells. This study also showed that the replacement of the standard Mo back contact by ITO-based back contacts reduces the reflectance at the back surface of the devices, which improves the aesthetic quality of CIGSe-based semitransparent devices and facilitates its integration in BIPV applications. The obtained results demonstrate the importance of

characterizing the back interface after the absorber synthesis instead of limiting the study to the as-deposited back contact. Taking into account the results involving characterization of chalcopyrite materials and interfaces in the devices based on them, this thesis contributes to deepen in the understanding of the great relevance of interface modifications in CIGSe-based solar cells in the performance of the devices. Additionally, it provides a powerful tool as methodology for the PDT process monitoring for the future transfer of these processes from the lab scale (cell level) to the industrial scale (module level), looking forward a more efficient and precise industrial manufacturing. Further investigation is needed to define the exact mechanism of the RbF-PDT influence on the optoelectronic properties of CIGSe-based solar cells and, in the case of semitransparent back contacts, to achieve higher transparency values as required for higher-transparency devices and high-efficiency tandem device configurations.

In addition to the specific knowledge regarding kesterite and chalcopyrite absorbers, the characterization strategies employed in this thesis can be applied to other thin film solar cell technologies. Globally, the results presented in this thesis show the high potential of combining different characterization techniques both for fundamental research and for the fast, non-destructive, and in situ monitoring of thin film solar cells production process. Furthermore, aiming beyond the PV field, this thesis provides examples of advanced characterization studies of a complex system (similar to the thin film solar cell) that may help to build up the full picture of processes, mechanisms and limitations in multilayer-based devices for a broad spectrum of readers and researchers.

Bibliography

1 D. Adam, *Nature*, 2021, **597**, 462–465.

2 *bp Statistical Review of World Energy*, 2021.

3 N. Abas, A. Kalair and N. Khan, *Futures*, 2015, **69**, 31–49.

4 B. H. Kreps, *Am. J. Econ. Sociol.*, 2020, **79**, 695–717.

5 S. Manabe, *Tellus A Dyn. Meteorol. Oceanogr.*, 2019, **71**, 1620078.

6 S. VijayaVenkataRaman, S. Iniyan and R. Goic, *Renew. Sustain. Energy Rev.*, 2012, **16**, 878–897.

7 M. Kampa and E. Castanas, *Environ. Pollut.*, 2008, **151**, 362–367.

8 D. J. Hill, *Nat. Mater.*, 2008, **7**, 680–682.

9 C. L. Smith and S. Cowley, *Philos. Trans. R. Soc. A Math. Phys. Eng. Sci.*, 2010, **368**, 1091–1108.

10 J. Mohtasham, *Energy Procedia*, 2015, **74**, 1289–1297.

11 L. El Chaar, L. A. Lamont and N. El Zein, *Renew. Sustain. Energy Rev.*, 2011, **15**, 2165–2175.

12 M. Pogson, A. Hastings and P. Smith, *GCB Bioenergy*, 2013, **5**, 513–524.

13 J. R. Oakleaf, C. M. Kennedy, S. Baruch-Mordo, J. S. Gerber, P. C. West, J. A. Johnson and J. Kiesecker, *Sci. Data*, 2019, **6**, 101.

14 E. Verdolini, F. Vona and D. Popp, *Bridging the Gap: Do Fast Reacting Fossil Technologies Facilitate Renewable Energy Diffusion?*, Cambridge, MA, 2016.

15 In *Physics of Semiconductor Devices*, Kluwer Academic Publishers, Boston, pp. 1–49.

16 T. Soga, in *Nanostructured Materials for Solar Energy Conversion*, Elsevier, 2006, pp. 3–43.

17 P. Rappaport, *Sol. Energy*, 1959, **3**, 8–18.

18 T. Kirchartz and U. Rau, in *Advanced Characterization Techniques for Thin Film Solar Cells*, Wiley, 2011, pp. 1–32.

19 J. Nelson, *The Physics of Solar Cells*, PUBLISHED BY IMPERIAL COLLEGE PRESS AND DISTRIBUTED BY WORLD SCIENTIFIC PUBLISHING CO., 2003.

20 A. L. Fahrenbruch and R. H. Bube, in *Fundamentals of Solar Cells*, Elsevier, 1983, pp. 210–244.

21 T. Kirchartz, K. Ding and U. Rau, in *Advanced Characterization Techniques for Thin Film Solar Cells*, Wiley-VCH Verlag GmbH & Co. KGaA, Weinheim, Germany, 2016, pp. 41–69.

22 E. T. Efaz, M. M. Rhaman, S. Al Imam, K. L. Bashar, F. Kabir, M. E. Mourtaza, S. N. Sakib and F. A. Mozahid, *Eng. Res. Express*, 2021, **3**, 032001.

23 A. Slaoui, *EPJ Web Conf.*, 2017, **148**, 00007.

24 M. A. Green, E. D. Dunlop, J. Hohl-Ebinger, M. Yoshita, N. Kopidakis, K. Bothe, D. Hinken, M. Rauer and X. Hao, *Prog. Photovoltaics Res. Appl.*, 2022, **30**, 687–701.

25 T. Feurer, P. Reinhard, E. Avancini, B. Bissig, J. Löckinger, P. Fuchs, R. Carron, T. P. Weiss, J. Perrenoud, S. Stutterheim, S. Buecheler and A. N. Tiwari, *Prog. Photovoltaics Res. Appl.*, 2017, **25**, 645–667.

26 V. Bermudez and A. Perez-Rodriguez, *Nat. Energy*, 2018, **3**, 466–475.

27 J. Yan and B. R. Saunders, *RSC Adv.*, 2014, **4**, 43286–43314.

28 G. Conibeer, *Mater. Today*, 2007, **10**, 42–50.

29 D. Mora-Herrera, M. Pal and J. Santos-Cruz, *Sol. Energy*, 2021, **220**, 316–330.

30 M. Nakamura, K. Yamaguchi, Y. Kimoto, Y. Yasaki, T. Kato and H. Sugimoto, *IEEE J. Photovoltaics*, 2019, **9**, 1863–1867.

31 A. Jahagirdar, A. Kadam and N. Dhere, in *2006 IEEE 4th World Conference on Photovoltaic Energy Conference*, IEEE, 2006, pp. 557–559.

32 R. Scheer, L. Messmann-Vera, R. Klenk and H.-W. Schock, *Prog. Photovoltaics*

Res. Appl., 2012, **20**, 619–624.

33 L. Weinhardt, D. Hauschild and C. Heske, *Adv. Mater.*, 2019, **31**, 1806660.

34 W. Jaegermann, A. Klein and T. Mayer, *Adv. Mater.*, 2009, **21**, 4196–4206.

35 O. Gunawan, T. K. Todorov and D. B. Mitzi, *Appl. Phys. Lett.*, 2010, **97**, 233506.

36 D. A. R. Barkhouse, O. Gunawan, T. Gokmen, T. K. Todorov and D. B. Mitzi, *Prog. Photovoltaics Res. Appl.*, 2012, **20**, 6–11.

37 J. J. Scragg, T. Ericson, X. Fontané, V. Izquierdo-Roca, A. Pérez-Rodríguez, T. Kubart, M. Edoff and C. Platzer-Björkman, *Prog. Photovoltaics Res. Appl.*, 2014, **22**, 10–17.

38 M. Gloeckler and J. R. Sites, *Thin Solid Films*, 2005, **480**–**481**, 241–245.

39 C. Platzer-Björkman, T. Törndahl, D. Abou-Ras, J. Malmström, J. Kessler and L. Stolt, *J. Appl. Phys.*, 2006, **100**, 044506.

40 Z.-K. Yuan, S. Chen, H. Xiang, X.-G. Gong, A. Walsh, J.-S. Park, I. Repins and S.-H. Wei, *Adv. Funct. Mater.*, 2015, **25**, 6733–6743.

41 H. Xie, Y. Sáncheza, P. Tang, M. Espíndola-Rodríguez, M. Guc, L. Calvo-Barrio, S. López-Marino, Y. Liu, J. R. Morante, A. Cabot, V. Izquierdo-Roca, J. Arbiol, A. Pérez-Rodríguez and E. Saucedo, *Sol. RRL*, 2018, 1800279.

42 Y. Sánchez, M. Espíndola-Rodríguez, H. Xie, S. López-Marino, M. Neuschitzer, S. Giraldo, M. Dimitrievska, M. Placidi, V. Izquierdo-Roca, F. A. Pulgarín-Agudelo, O. Vigil-Galán and E. Saucedo, *Sol. Energy Mater. Sol. Cells*, 2016, **158**, 138–146.

43 T. Negami, Y. Hashimoto and S. Nishiwaki, *Sol. Energy Mater. Sol. Cells*, 2001, **67**, 331–335.

44 L. Yin, G. Cheng, Y. Feng, Z. Li, C. Yang and X. Xiao, *RSC Adv.*, 2015, **5**, 40369–40374.

45 M. E. Erkan, V. Chawla and M. A. Scarpulla, *J. Appl. Phys.*, 2016, **119**, 194504.

46 S. López-Marino, Y. Sánchez, M. Placidi, A. Fairbrother, M. Espindola-Rodríguez, X. Fontané, V. Izquierdo-Roca, J. López-García, L. Calvo-Barrio, A.

Pérez-Rodríguez and E. Saucedo, *Chem. - A Eur. J.*, 2013, **19**, 14814–14822.

47 S. López-Marino, M. Placidi, A. Pérez-Tomás, J. Llobet, V. Izquierdo-Roca, X. Fontané, A. Fairbrother, M. Espíndola-Rodríguez, D. Sylla, A. Pérez-Rodríguez and E. Saucedo, *J. Mater. Chem. A*, 2013, **1**, 8338.

48 G. Brammertz, M. Buffière, S. Oueslati, H. ElAnzeery, K. Ben Messaoud, S. Sahayaraj, C. Köble, M. Meuris and J. Poortmans, *Appl. Phys. Lett.*, 2013, **103**, 163904.

49 J. J. Scragg, J. T. Wätjen, M. Edoff, T. Ericson, T. Kubart and C. Platzer-Björkman, *J. Am. Chem. Soc.*, 2012, **134**, 19330–19333.

50 S. Lopez-Marino, M. Espíndola-Rodríguez, Y. Sánchez, X. Alcobé, F. Oliva, H. Xie, M. Neuschitzer, S. Giraldo, M. Placidi, R. Caballero, V. Izquierdo-Roca, A. Pérez-Rodríguez and E. Saucedo, *Nano Energy*, 2016, **26**, 708–721.

51 S. Wang, S. Gao, D. Wang, Z. Jiang, J. Ao, Z. Zhou, S. Liu, Y. Sun and Y. Zhang, *Sol. RRL*, 2019, **3**, 1800236.

52 M. Bär, S. Nishiwaki, L. Weinhardt, S. Pookpanratana, W. N. Shafarman and C. Heske, *Appl. Phys. Lett.*, 2008, **93**, 042110.

53 T. Dullweber, O. Lundberg, J. Malmström, M. Bodegård, L. Stolt, U. Rau, H. W. Schock and J. H. Werner, *Thin Solid Films*, 2001, **387**, 11–13.

54 R. Klenk, *Thin Solid Films*, 2001, **387**, 135–140.

55 T. Gokmen, O. Gunawan and D. B. Mitzi, *Appl. Phys. Lett.*, 2014, **105**, 033903.

56 L. Zhang, T. Li, Y. Chen, W. Pang, M. Qu, X. Song, Y. Zhang and H. Yan, *J. Mater. Sci. Mater. Electron.*, 2018, **29**, 3482–3491.

57 K. Sardashti, R. Haight, T. Gokmen, W. Wang, L.-Y. Chang, D. B. Mitzi and A. C. Kummel, *Adv. Energy Mater.*, 2015, **5**, 1402180.

58 A. Kanevce, I. Repins and S.-H. Wei, *Sol. Energy Mater. Sol. Cells*, 2015, **133**, 119–125.

59 M. Courel, J. A. Andrade-Arvizu and O. Vigil-Galán, *Solid. State. Electron.*, 2015, **111**, 243–250.

60 W. Wang, M. T. Winkler, O. Gunawan, T. Gokmen, T. K. Todorov, Y. Zhu and D. B. Mitzi, *Adv. Energy Mater.*, 2014, **4**, 1301465.

61 I. D. Olekseyuk, L. D. Gulay, I. V. Dydchak, L. V. Piskach, O. V. Parasyuk and O. V. Marchuk, *J. Alloys Compd.*, 2002, **340**, 141–145.

62 Y. Gong, Y. Zhang, Q. Zhu, Y. Zhou, R. Qiu, C. Niu, W. Yan, W. Huang and H. Xin, *Energy Environ. Sci.*, 2021, **14**, 2369–2380.

63 M. He, C. Yan, J. Li, M. P. Suryawanshi, J. Kim, M. A. Green and X. Hao, *Adv. Sci.*, 2021, **8**, 2004313.

64 S. Giraldo, Z. Jehl, M. Placidi, V. Izquierdo-Roca, A. Pérez-Rodríguez and E. Saucedo, *Adv. Mater.*, 2019, **31**, 1806692.

65 C. Persson, *J. Appl. Phys.*, 2010, **107**, 053710.

66 C. Wang, S. Chen, J.-H. Yang, L. Lang, H.-J. Xiang, X.-G. Gong, A. Walsh and S.-H. Wei, *Chem. Mater.*, 2014, **26**, 3411–3417.

67 H. Katagiri, N. Sasaguchi, S. Hando, S. Hoshino, J. Ohashi and T. Yokota, *Sol. Energy Mater. Sol. Cells*, 1997, **49**, 407–414.

68 S. Ebnesajjad, in *Surface Treatment of Materials for Adhesive Bonding*, Elsevier, 2014, pp. 39–75.

69 B. D. Fahlman, in *Materials Chemistry*, Springer Netherlands, Dordrecht, 2018, pp. 643–741.

70 F. Pianezzi, P. Reinhard, A. Chirilă, B. Bissig, S. Nishiwaki, S. Buecheler and A. N. Tiwari, *Phys. Chem. Chem. Phys.*, 2014, **16**, 8843.

71 S. Ishizuka, H. Shibata, J. Nishinaga, Y. Kamikawa and P. J. Fons, *Appl. Phys. Lett.*, 2018, **113**, 063901.

72 J. Álvarez-García, V. Izquierdo-Roca, P. Pistor, T. Schmid and A. Pérez-Rodríguez, in *Advanced Characterization Techniques for Thin Film Solar Cells*, Wiley-VCH Verlag GmbH & Co. KGaA, Weinheim, Germany, 2016, pp. 469–499.

73 W. Witte, R. Kniese, A. Eicke and M. Powalla, in *2006 IEEE 4th World Conference on Photovoltaic Energy Conference*, IEEE, 2006, pp. 553–556.

74 W. Witte, R. Kniese and M. Powalla, *Thin Solid Films*, 2008, **517**, 867–869.

75 M. Guc, M. Neuschitzer, D. Hariskos, A. Bauer, W. Witte, W. Hempel, L. Calvo-Barrio, P. Pistor, A. Perez-Rodriguez and V. Izquierdo-Roca, *RSC Adv.*, 2016, **6**, 24536–24542.

76 M. Guc, D. Hariskos, L. Calvo-Barrio, P. Jackson, F. Oliva, P. Pistor, A. Perez-Rodriguez and V. Izquierdo-Roca, *Sci. Rep.*, 2017, **7**, 1144.

77 E. Garcia-Llamas, M. Guc, I. V. Bodnar, X. Fontané, R. Caballero, J. M. Merino, M. León and V. Izquierdo-Roca, *J. Alloys Compd.*, 2017, **692**, 249–256.

78 M. Dimitrievska, A. Fairbrother, E. Saucedo, A. Pérez-Rodríguez and V. Izquierdo-Roca, *Sol. Energy Mater. Sol. Cells*, 2016, **149**, 304–309.

79 M. Dimitrievska, H. Xie, A. Fairbrother, X. Fontané, G. Gurieva, E. Saucedo, A. Pérez-Rodríguez, S. Schorr and V. Izquierdo-Roca, *Appl. Phys. Lett.*, 2014, **105**, 031913.

80 M. Dimitrievska, G. Gurieva, H. Xie, A. Carrete, A. Cabot, E. Saucedo, A. Pérez-Rodríguez, S. Schorr and V. Izquierdo-Roca, *J. Alloys Compd.*, 2015, **628**, 464–470.

81 S. Schorr, G. Gurieva, M. Guc, M. Dimitrievska, A. Pérez-Rodríguez, V. Izquierdo-Roca, C. S. Schnohr, J. Kim, W. Jo and J. M. Merino, *J. Phys. Energy*, 2019, **2**, 012002.

82 M. Dimitrievska, A. Fairbrother, A. Pérez-Rodríguez, E. Saucedo and V. Izquierdo-Roca, *Acta Mater.*, 2014, **70**, 272–280.

83 M. Dimitrievska, S. Giraldo, P. Pistor, E. Saucedo, A. Pérez-Rodríguez and V. Izquierdo-Roca, *Sol. Energy Mater. Sol. Cells*, 2016, **157**, 462–467.

84 M. Dimitrievska, F. Oliva, M. Guc, S. Giraldo, E. Saucedo, A. Pérez-Rodríguez and V. Izquierdo-Roca, *J. Mater. Chem. A*, 2019, **7**, 13293–13304.

85 M. Dimitrievska, A. Fairbrother, E. Saucedo, A. Pérez-Rodríguez and V. Izquierdo-Roca, *Appl. Phys. Lett.*, 2015, **106**, 073903.

86 P. A. Fernandes, P. M. P. Salomé and A. F. da Cunha, *J. Alloys Compd.*, 2011, **509**, 7600–7606.

87 M. Dimitrievska, H. Xie, A. J. Jackson, X. Fontané, M. Espíndola-Rodríguez, E. Saucedo, A. Pérez-Rodríguez, A. Walsh and V. Izquierdo-Roca, *Phys. Chem. Chem. Phys.*, 2016, **18**, 7632–7640.

88 A. Fairbrother, X. Fontané, V. Izquierdo-Roca, M. Espíndola-Rodríguez, S. López-Marino, M. Placidi, L. Calvo-Barrio, A. Pérez-Rodríguez and E. Saucedo, *Sol. Energy Mater. Sol. Cells*, 2013, **112**, 97–105.

89 X. Fontané, L. Calvo-Barrio, V. Izquierdo-Roca, E. Saucedo, A. Pérez-Rodriguez, J. R. Morante, D. M. Berg, P. J. Dale and S. Siebentritt, *Appl. Phys. Lett.*, 2011, **98**, 181905.

90 C. Insignares-Cuello, C. Broussillou, V. Bermúdez, E. Saucedo, A. Pérez-Rodríguez and V. Izquierdo-Roca, *Appl. Phys. Lett.*, 2014, **105**, 021905.

91 F. Oliva, S. Kretzschmar, D. Colombara, S. Tombolato, C. M. Ruiz, A. Redinger, E. Saucedo, C. Broussillou, T. G. de Monsabert, T. Unold, P. J. Dale, V. Izquierdo-Roca and A. Pérez-Rodríguez, *Sol. Energy Mater. Sol. Cells*, 2016, **158**, 168–183.

92 S. Giraldo, E. Saucedo, M. Neuschitzer, F. Oliva, M. Placidi, X. Alcobé, V. Izquierdo-Roca, S. Kim, H. Tampo, H. Shibata, A. Pérez-Rodríguez and P. Pistor, *Energy Environ. Sci.*, 2018, **11**, 582–593.

93 A. Hernández-Martínez, M. Placidi, L. Arqués, S. Giraldo, Y. Sánchez, V. Izquierdo-Roca, P. Pistor, M. Valentini, C. Malerba and E. Saucedo, *ACS Appl. Energy Mater.*, 2018, **1**, 1981–1989.

94 M. Neuschitzer, K. Lienau, M. Guc, L. C. Barrio, S. Haass, J. M. Prieto, Y. Sanchez, M. Espindola-Rodriguez, Y. Romanyuk, A. Perez-Rodriguez, V. Izquierdo-Roca and E. Saucedo, *J. Phys. D. Appl. Phys.*, 2016, **49**, 125602.

95 Z. Tong, C. Yan, Z. Su, F. Zeng, J. Yang, Y. Li, L. Jiang, Y. Lai and F. Liu, *Appl. Phys. Lett.*, 2014, **105**, 223903.

96 M. Neuschitzer, J. Marquez, S. Giraldo, M. Dimitrievska, M. Placidi, I. Forbes, V. Izquierdo-Roca, A. Pérez-Rodriguez and E. Saucedo, *J. Phys. Chem. C*, 2016, **120**, 9661–9670.

97 F. Harrou, Y. Sun, A. S. Hering, M. Madakyaru and A. Dairi, in *Statistical Process Monitoring Using Advanced Data-Driven and Deep Learning Approaches*,

Elsevier, 2021, pp. 1–17.

98 B. Sopori, Yi Zhang, Wei Chen and J. Madjdpour, in *Conference Record of the Twenty-Eighth IEEE Photovoltaic Specialists Conference - 2000 (Cat. No.00CH37036)*, IEEE, pp. 120–123.

99 B. Dietzek, D. Cialla, M. Schmitt and J. Popp, 2018, pp. 47–68.

100 D. J. Gardiner, in *Practical Raman Spectroscopy*, Springer Berlin Heidelberg, Berlin, Heidelberg, 1989, pp. 1–12.

101 A. Pinczuk and E. Burstein, 1983, pp. 23–78.

102 In *The Raman Effect*, John Wiley & Sons, Ltd, Chichester, UK, pp. 49–84.

103 R. S. Mulliken, *J. Chem. Phys.*, 1955, **23**, 1997–2011.

104 R. S. Mulliken, *J. Chem. Phys.*, 1956, **24**, 1118–1118.

105 J. E. White, *J. Chem. Educ.*, 1967, **44**, 128.

106 M. Guc, S. Levcenko, I. V. Bodnar, V. Izquierdo-Roca, X. Fontane, L. V. Volkova, E. Arushanov and A. Pérez-Rodríguez, *Sci. Rep.*, 2016, **6**, 19414.

107 D. L. Rousseau, R. P. Bauman and S. P. S. Porto, *J. Raman Spectrosc.*, 1981, **10**, 253–290.

108 D. F. Shriver and J. B. R. Dunn, *Appl. Spectrosc.*, 1974, **28**, 319–323.

109 A. Paudel, D. Raijada and J. Rantanen, *Adv. Drug Deliv. Rev.*, 2015, **89**, 3–20.

110 M. J. Pelletier and C. C. Pelletier, in *Encyclopedia of Analytical Science*, Elsevier, 2005, pp. 94–104.

111 R. Hui, in *Introduction to Fiber-Optic Communications*, Elsevier, 2020, pp. 125–154.

112 T. Unold and L. Gütay, in *Advanced Characterization Techniques for Thin Film Solar Cells*, Wiley, 2011, pp. 151–175.

113 A. Höpe, 2014, pp. 179–219.

114 R. R. Lunt, *Appl. Phys. Lett.*, 2012, **101**, 043902.

115 C. Streli, P. Wobrauschek and P. Kregsamer, in *Encyclopedia of Spectroscopy and*

Spectrometry, Elsevier, 1999, pp. 2478–2487.

116 M. Klenk, O. Schenker, U. Probst and E. Bucher, *Sol. Energy Mater. Sol. Cells*, 1999, **58**, 299–319.

117 E. von Hauff, *J. Phys. Chem. C*, 2019, **123**, 11329–11346.

118 J. Heath and P. Zabierowski, in *Advanced Characterization Techniques for Thin Film Solar Cells*, Wiley-VCH Verlag GmbH & Co. KGaA, Weinheim, Germany, 2016, pp. 93–119.

119 D. Abou-Ras, M. Nichterwitz, M. J. Romero and S. S. Schmidt, in *Advanced Characterization Techniques for Thin Film Solar Cells*, Wiley, 2011, pp. 299–345.

120 TEM-UCA, EJE-Z – TEM-UCA development software for Electron Microscopy, http://www2.uca.es/dept/cmat_qinor/catalisis/tem-uca-server.htm.

121 S. Bernal, F. . Botana, J. . Calvino, C. López-Cartes, J. . Pérez-Omil and J. . Rodríguez-Izquierdo, *Ultramicroscopy*, 1998, **72**, 135–164.

122 Journal Citation Reports, https://jcr.clarivate.com/jcr/home.

123 L. Grenet, M. A. A. Suzon, F. Emieux and F. Roux, *ACS Appl. Energy Mater.*, 2018, **1**, 2103–2113.

124 S. Chen, A. Walsh, X.-G. Gong and S.-H. Wei, *Adv. Mater.*, 2013, **25**, 1522–1539.

125 T. Gokmen, O. Gunawan, T. K. Todorov and D. B. Mitzi, *Appl. Phys. Lett.*, 2013, **103**, 103506.

126 H. Xie, Y. Sánchez, S. López-Marino, M. Espíndola-Rodríguez, M. Neuschitzer, D. Sylla, A. Fairbrother, V. Izquierdo-Roca, A. Pérez-Rodríguez and E. Saucedo, *ACS Appl. Mater. Interfaces*, 2014, **6**, 12744–12751.

127 O. Lundberg, M. Edoff and L. Stolt, *Thin Solid Films*, 2005, **480**–**481**, 520–525.

128 J. Dietrich, D. Abou-Ras, T. Rissom, T. Unold, H.-W. Schock and C. Boit, *IEEE J. Photovoltaics*, 2012, **2**, 364–370.

129 S. H. Sohn, N. S. Han, Y. J. Park, S. M. Park, H. S. An, D.-W. Kim, B. K. Min and J. K. Song, *Phys. Chem. Chem. Phys.*, 2014, **16**, 27112–27118.

130 S. Bag, O. Gunawan, T. Gokmen, Y. Zhu, T. K. Todorov and D. B. Mitzi, *Energy*

Environ. Sci., 2012, **5**, 7060.

131 T. Ratz, G. Brammertz, R. Caballero, M. León, S. Canulescu, J. Schou, L. Gütay, D. Pareek, T. Taskesen, D.-H. Kim, J.-K. Kang, C. Malerba, A. Redinger, E. Saucedo, B. Shin, H. Tampo, K. Timmo, N. D. Nguyen and B. Vermang, *J. Phys. Energy*, 2019, **1**, 042003.

132 P. Jackson, R. Wuerz, D. Hariskos, E. Lotter, W. Witte and M. Powalla, *Phys. status solidi - Rapid Res. Lett.*, 2016, **10**, 583–586.

133 S. Zahedi-Azad, M. Maiberg, R. Clausing and R. Scheer, *Thin Solid Films*, 2019, **669**, 629–632.

134 S. Siebentritt, E. Avancini, M. Bär, J. Bombsch, E. Bourgeois, S. Buecheler, R. Carron, C. Castro, S. Duguay, R. Félix, E. Handick, D. Hariskos, V. Havu, P. Jackson, H. Komsa, T. Kunze, M. Malitckaya, R. Menozzi, M. Nesladek, N. Nicoara, M. Puska, M. Raghuwanshi, P. Pareige, S. Sadewasser, G. Sozzi, A. N. Tiwari, S. Ueda, A. Vilalta-Clemente, T. P. Weiss, F. Werner, R. G. Wilks, W. Witte and M. H. Wolter, *Adv. Energy Mater.*, 2020, **10**, 1903752.

135 N. Cavallari, F. Pattini, S. Rampino, F. Annoni, M. Barozzi, M. Bronzoni, E. Gilioli, E. Gombia, C. Maragliano, M. Mazzer, G. Pepponi, G. Spaggiari and R. Fornari, *Appl. Surf. Sci.*, 2017, **412**, 52–57.

136 M. Saifullah, S. Ahn, J. Gwak, S. Ahn, K. Kim, J. Cho, J. H. Park, Y. J. Eo, A. Cho, J.-S. Yoo and J. H. Yun, *J. Mater. Chem. A*, 2016, **4**, 10542–10551.

137 T. Nakada, Y. Hirabayashi, T. Tokado, D. Ohmori and T. Mise, *Sol. Energy*, 2004, **77**, 739–747.

138 T. Nakada, *Thin Solid Films*, 2005, **480**–**481**, 419–425.

139 R. Fonoll-Rubio, J. Andrade-Arvizu, J. Blanco-Portals, I. Becerril-Romero, M. Guc, E. Saucedo, F. Peiró, L. Calvo-Barrio, M. Ritzer, C. S. Schnohr, M. Placidi, S. Estradé, V. Izquierdo-Roca and A. Pérez-Rodríguez, *Energy Environ. Sci.*, 2021, **14**, 507–523.

140 K. J. Tiwari, R. Fonoll Rubio, S. Giraldo, L. Calvo-Barrio, V. Izquierdo-Roca, M. Placidi, Y. Sanchez, A. Pérez-Rodríguez, E. Saucedo and Z. Jehl Li-Kao, *Appl. Surf. Sci.*, 2021, **540**, 148342.

141 S. Giraldo, R. Fonoll-Rubio, Z. Jehl Li-Kao, Y. Sánchez, L. Calvo-Barrio, V. Izquierdo-Roca, A. Pérez-Rodríguez and E. Saucedo, *Prog. Photovoltaics Res. Appl.*, 2021, **29**, 334–343.

142 J. Andrade-Arvizu, R. F. Rubio, V. Izquierdo-Roca, I. Becerril-Romero, D. Sylla, P. Vidal-Fuentes, Z. J. Li-Kao, A. Thomere, S. Giraldo, K. Tiwari, S. Resalati, M. Guc and M. Placidi, *ACS Appl. Mater. Interfaces*, 2022, **14**, 1177–1186.

143 R. Fonoll-Rubio, S. Paetel, E. Grau-Luque, I. Becerril-Romero, R. Mayer, A. Pérez-Rodríguez, M. Guc and V. Izquierdo-Roca, *Adv. Energy Mater.*, 2022, 2103163.

144 R. Fonoll-Rubio, M. Placidi, T. Hoelscher, A. Thomere, Z. J. Li-Kao, M. Guc, V. Izquierdo-Roca, R. Scheer and A. Pérez-Rodríguez, *Sol. RRL*, 2022, 2101071.